

NOV 29 1977

**NASA TECHNICAL NOTE**



**NASA TN D-8449**

**NASA TN D-8449**

**COMPLETED  
ORIGINAL**

**PERFORMANCE OF TWIN  
TWO-DIMENSIONAL WEDGE NOZZLES  
INCLUDING THRUST VECTORING  
AND REVERSING EFFECTS AT  
SPEEDS UP TO MACH 2.20**

*Francis J. Capone and Donald L. Maiden  
Langley Research Center  
Hampton, Va. 23665*

1. Report No. NASA TN D-8449		2. Government Accession No.		3. Recipient's Catalog No.	
4. Title and Subtitle PERFORMANCE OF TWIN TWO-DIMENSIONAL WEDGE NOZZLES INCLUDING THRUST VECTORING AND REVERSING EFFECTS AT SPEEDS UP TO MACH 2.20				5. Report Date July 1977	
				6. Performing Organization Code	
7. Author(s) Francis J. Capone and Donald L. Maiden				8. Performing Organization Report No. L-11277	
				10. Work Unit No. 505-11-23-02	
9. Performing Organization Name and Address NASA Langley Research Center Hampton, VA 23665				11. Contract or Grant No.	
				13. Type of Report and Period Covered Technical Note	
12. Sponsoring Agency Name and Address National Aeronautics and Space Administration Washington, DC 20546				14. Sponsoring Agency Code	
15. Supplementary Notes					
16. Abstract  An investigation was conducted in the Langley 16-foot transonic tunnel and in the Langley 4-foot supersonic pressure tunnel to determine the performance characteristics of twin nonaxisymmetric or two-dimensional nozzles with fixed shrouds and variable-geometry wedges. The effects of thrust vectoring, reversing, and installation of various tails were also studied. The investigation was conducted statically and at flight speeds up to a Mach number of 2.20. The total-pressure ratio of the simulated jet exhaust was varied up to approximately 26 depending on Mach number. The Reynolds number per meter varied up to $13.20 \times 10^6$ . An analytical study was made to determine the effect on calculated wave drag by varying the mathematical model used to simulate the nozzle jet-exhaust plume.					
17. Key Words (Suggested by Author(s)) Two-dimensional wedge nozzles Thrust reversing nozzle Vectoring nozzle Twin nozzles				18. Distribution Statement Unclassified - Unlimited  Subject Category 02	
19. Security Classif. (of this report) Unclassified	20. Security Classif. (of this page) Unclassified	21. No. of Pages 188	22. Price* \$7.50		



# PERFORMANCE OF TWIN TWO-DIMENSIONAL WEDGE NOZZLES INCLUDING THRUST

## VECTERING AND REVERSING EFFECTS AT SPEEDS UP TO MACH 2.20

Francis J. Capone and Donald L. Maiden  
Langley Research Center

### SUMMARY

The performance characteristics of twin two-dimensional nozzles, each having a fixed shroud and a variable-geometry wedge, have been determined in the Langley 16-foot transonic tunnel and in the Langley 4-foot supersonic pressure tunnel. The effects of various tail installations, thrust vectoring, and reversing were also studied. The investigation was conducted statically and at flight speeds up to Mach 2.20. The nozzle pressure ratio of the simulated jet exhaust was varied up to 26, and the Reynolds number per meter was varied depending on Mach number up to  $13.20 \times 10^6$ . An analytical study was made to determine the effect on calculated wave drag by varying the mathematical model used to simulate the nozzle jet-exhaust plume.

The results showed that aeropropulsion performance with the twin-nozzle installation (tails off) was nearly identical to that with a single-nozzle installation for a dry power setting at the same internal expansion area ratio. This similarity indicates little or no twin-engine installation penalty for nozzles of this type. The thrust-minus-afterbody drag performance of the twin-nozzle installation is significantly higher than the performance achieved with twin axisymmetric nozzle installations at speeds greater than a Mach number of 0.8. Significant jet-induced lift can be obtained on aft-mounted lifting surfaces using a cambered two-dimensional wedge centerbody to vector jet exhaust thrust downward. However, thrust-minus-drag performance is degraded up to 14 and 43 percent of ideal gross thrust for wedge angles of  $12^\circ$  and  $24^\circ$ , respectively. The two-dimensional wedge nozzle with reverser panels exhibited very effective static or in-flight thrust reversing characteristics. However, care must be exercised when integrating tail surfaces because of the potential for losses in stability and control effectiveness. The values of analytically determined supersonic wave drag are highly dependent upon the mathematical model used to simulate the nozzle jet-exhaust plume. The results indicate that different mathematical models are needed to simulate jet-off and power-on conditions.

### INTRODUCTION

Multimission military aircraft are usually required to operate at subsonic to supersonic speeds over a wide range of engine pressure ratios. The attainment of high performance is dependent upon the minimization of interference effects resulting from the integration of the propulsion system into the airframe. Past aircraft have been built with axisymmetric nozzles because of their higher internal performance and their ease of mating to the engine-augmentor duct. However, the installation of twin engines with axisymmetric nozzles

usually results in the aircraft having large boattailed "gutter" interfairing or base regions between the nozzles. These regions, as well as the nozzle boattail, tail surfaces, and booms are subject to adverse interference effects, especially if the external flow separates from the afterbody near the nozzle exits (refs. 1 to 3).

If properly integrated with the airframe, two-dimensional wedge nozzles can offer improved aeropropulsion performance by eliminating the large boattail gutters or base regions between the engine nacelles; elimination of tail support booms may also be possible. The two-dimensional wedge nozzle offers additional advantages in that it can be adapted for in-flight thrust vectoring and/or thrust reversing, the benefits of which are discussed in references 4 and 5, respectively. Although the two-dimensional nozzle may be heavier than an axisymmetric nozzle, the wedge centerbody can be used as a carry-through structure for the horizontal tails to reduce aircraft weight.

Because of the potential advantages offered by the two-dimensional wedge nozzle, the Langley Research Center has undertaken a two-phase experimental program to evaluate the aeropropulsion performance characteristics of these nozzles. The first phase, conducted on an isolated single-engine configuration, investigated two nozzle concepts and the effects of several geometric variables such as internal expansion area ratio, cowl boattail angle, and wedge half-angle on nozzle performance. Results from these investigations, presented in references 6 and 7 and summarized in reference 8, indicated performance comparable to that of axisymmetric nozzles at transonic speeds.

The second phase of the experimental program was conducted on a twin-engine propulsion simulator with twin two-dimensional wedge nozzles, and results for this phase are reported herein. The objectives of this investigation were to determine the effects of twin-nozzle installation and tail interference on nozzle and afterbody performance and to assess the in-flight thrust vectoring and reversing characteristics of this unique nozzle. This investigation was conducted in the Langley 16-foot transonic tunnel and in the Langley 4-foot supersonic pressure tunnel at speeds up to Mach 2.20 over a range of nozzle pressure ratios. A brief summary of the results of this investigation are presented in references 8 and 9.

## SYMBOLS

All force and moment coefficients are referred to the body-axis system except lift and drag, which are referred to the stability-axis system. The moment reference center was located at fuselage station 73.10 cm, the location which corresponds to the force-balance pitch center. At static conditions, ambient pressure is substituted for free-stream dynamic pressure.

- $A_e$  nozzle exit area,  $\text{cm}^2$   
 $A_{e,x}$  area of theoretically fully expanded flow at wedge tip,  $\text{cm}^2$   
 $A_m$  model maximum cross-sectional area, 284.784  $\text{cm}^2$

$A_{\text{seal}}$	cross-sectional area enclosed by seal strip, 266.000 cm <sup>2</sup>
$A_t$	nozzle throat area, cm <sup>2</sup>
$C_{D,a}$	afterbody drag coefficient, $\frac{D_a}{q_\infty A_m}$
$C_{D,f}$	skin friction drag coefficient, $\frac{D_f}{q_\infty A_m}$
$C_{D,int}$	interference drag coefficient
$C_{D,w}$	wave drag coefficient, $\frac{D_w}{q_\infty A_m}$
$\Delta C_{D,int}$	incremental interference drag coefficient
$C_{F,i}$	ideal isentropic gross thrust coefficient, $\frac{F_i}{q_\infty A_m}$
$C_{(F-D)}$	thrust-minus-drag coefficient, $\frac{F - D}{q_\infty A_m}$
$C_{F,j}$	nozzle thrust coefficient measured at static conditions, $\frac{F_j}{p_a A_m}$
$C_L$	total lift coefficient including thrust component on metric portion of model, $\frac{\text{Lift}}{q_\infty A_m}$
$C_{L,o}$	jet-off lift coefficient
$\Delta C_L$	incremental lift coefficient, $C_L - C_{L,o}$
$C_l$	rolling-moment coefficient on metric portion of model, $\frac{\text{Rolling moment}}{q_\infty A_m l}$
$C_m$	total pitching-moment coefficient including component due to thrust measured on metric portion of model, $\frac{\text{Pitching moment}}{q_\infty A_m l}$
$C_{m,j}$	jet pitching-moment coefficient measured at static conditions, $\frac{\text{Jet pitching moment}}{p_a A_m l}$
$C_{N,j}$	jet normal-force coefficient measured at static conditions, $\frac{\text{Jet normal force}}{p_a A_m}$

$C_n$	yawing-moment coefficient measured on metric portion of model, $\frac{\text{Yawing moment}}{q_\infty A_{ml}}$
$C_y$	side-force coefficient measured on metric portion of model, $\frac{\text{Side force}}{q_\infty A_m}$
$c$	chord, cm
$\bar{c}$	horizontal or vertical tail mean geometric chord, cm
$D$	total drag of model on metric portion of model, N
$D_a$	total afterbody drag on model aft of FS 68.58 (see fig. 2) including tail surfaces, N
$D_f$	external skin friction drag, N
$D_{int}$	interference drag due to tail surface, N
$D_n$	total nozzle drag on portion of model aft of FS 112.65, N
$D_w$	wave drag, N
$F$	thrust along stability axis, N
$F_A$	axial force, N
$F_{A,bal}$	resultant axial force measured by balance, positive upstream, N
$F_{A,mom}$	momentum tare axial force due to bellows, N
$F_g$	gross thrust, N
$F_i$	ideal isentropic gross thrust, N
$F_j$	thrust along body axis, N
$l$	reference length, 1.0 cm
$M$	free-stream Mach number
$N_{Re}$	Reynolds number per meter
$p_a$	ambient pressure, Pa
$\bar{p}_{es}$	average external static pressure at external seal, Pa
$\bar{p}_i$	average internal static pressure, Pa
$p_{t,j}$	average jet total pressure, Pa

$P_{t,\infty}$	free-stream stagnation pressure, Pa
$P_\infty$	free-stream static pressure, Pa
$q_\infty$	free-stream dynamic pressure, Pa
$T_t$	free-stream stagnation temperature, K
$x, z$	airfoil ordinates, cm
$\alpha$	angle of attack, deg
$\delta_h$	horizontal-tail deflection, deg
$\delta_j$	effective jet turning angle at static conditions, deg
$\delta_r$	rudder deflection, deg
$\delta_v$	single vertical-tail deflection, deg
$\delta_w$	resultant wedge camber angle (fig. 5(a)), deg
$\phi$	resultant thrust reverser angle (fig. 5(c)), deg

Subscripts:

F	forward thrust mode
R	reverser thrust mode

Abbreviations:

ASME	American Society of Mechanical Engineers
DPR	design nozzle pressure ratio
FS	fuselage station, cm

## APPARATUS AND PROCEDURE

### Model

General arrangement.— A photograph of the model without tails is shown in figure 1. The overall arrangement of the model including the propulsion simulation system is presented in figure 2.

The fuselage had essentially rectangular cross sections with rounded corners. The body lines were chosen so as to enclose the internal propulsion system, to provide a length of constant cross-sectional area, and to fair into the nozzle at FS 112.65 cm. The maximum width and height of the body were 22.86 cm and 12.7 cm, respectively, and the maximum body cross-sectional area was

284.78 cm<sup>2</sup>. A 0.125-cm annular gap (metric break) between the fixed forebody and the remainder of the body was required to prevent fouling between the non-metric and the metric portions of the model. A flexible teflon strip inserted into slots was used as a seal to prevent external flow into the model. The low coefficient of friction of teflon minimized restraint between the metric and non-metric portions of the model. Only that portion of the configuration aft of the metric break at FS 68.58 cm is supported by the force balance and hereinafter force and moment data are presented for this portion of the model.

Twin-jet propulsion simulation system.- A sketch of the twin-jet propulsion simulation system is presented in figure 2. The propulsion system internal performance characteristics are given in reference 10.

An external high-pressure air system provides a continuous flow of clean, dry air at a controlled temperature of about 306 K. This high-pressure air is brought through the support strut by six tubes into a high-pressure chamber. (See fig. 2.) Here, the air is divided into two separate flows and is passed through flow control valves. These manually preset valves are used to balance the exhaust-nozzle total pressure to agree to within less than 0.2 percent of each other (ref. 10). As shown in figure 3, the air in each supply pipe is then discharged perpendicular to the model axis through eight sonic nozzles equally spaced around the supply pipe. This method is designed to eliminate any transfer of axial momentum as the air is passed from the nonmetric to the metric portion of the model. Two flexible metal bellows are used as seals and serve to compensate the axial forces caused by pressurization. The cavity between the supply pipe and bellows is vented to model internal pressure. This system is identical to the system of reference 10 except that the separate thrust balance was eliminated for the present investigation.

Basic nozzle concept.- Figure 4(a) shows a sketch of the basic variable-geometry, two-dimensional nozzle with a collapsing wedge centerbody and a fixed-cowl afterbody. Results from isolated single nacelle tests with this nozzle concept are presented in reference 7. The wedge geometry for a flight nozzle would be varied by unique scissor-type linkages and hinges (ref. 11) which allow the nozzle exit area to be varied independently of the nozzle throat area. The mechanism also allows for internal expansion area ratio variation by providing throat transfer capability, that is, the transfer of the nozzle throat to the nozzle exit plane, to maintain high performance at low nozzle pressure ratios. For afterburner power, the wedge is collapsed to obtain the desired area ratio. Other features and a brief description of the design method used to define the internal contour lines of this nozzle are discussed in references 7 and 12. This nozzle concept is similar to but differs from the concept reported in reference 6 in that the configuration of reference 6 featured a collapsing wedge with a translating shroud for internal expansion area ratio variation.

Basic nozzle configurations.- The basic nozzle/afterbody design shown in figure 4(a) was based on the single-engine fixed-cowl concept of reference 7 with the afterbody having 10° boattail at the cowl trailing edge. Based on the data available from reference 7, only one nozzle simulating a dry power (non-after burning) setting was chosen to be tested as a twin-engine configuration. This nozzle with a 9.2° plug angle and  $A_e/A_t = 1.287$  was selected because it was shown to have superior transonic performance. Two nozzles simulating after-



burner power settings with internal expansion area ratios of 1.100 (tested at  $M = 2.20$  only) and 1.393 were also tested as shown in figure 4(a).

Alternate nozzle concept and configuration.- Some limited tests were conducted with an alternate nozzle shown in the sketch of figure 4(b) and the photograph of figure 4(c). This nozzle concept has a collapsing wedge made in two segments so that the wedge angle of the collapsing segment downstream from the dry power nozzle throat was  $15^\circ$ . The wedge fixed segment (FS 132.08 cm to FS 139.86 cm for the wind-tunnel model) has a  $6^\circ$  angle which results in a discontinuity along the wedge surface for the dry power setting. The throat area location is fixed, and the internal expansion area ratio is provided by small rotating flaps. The design philosophy for this nozzle concept was to shorten the overall length of the wedge and hence to lighten the structural weight and to reduce surface area to be cooled. For the wind-tunnel model, the internal expansion area ratio was 1.100 for both dry and afterburner power.

Thrust vectoring configuration.- To study the capability of the basic two-dimensional wedge nozzle to vector thrust by cambering the wedge, thrust vectoring configurations were tested for wedge-vectoring angles of  $12^\circ$  and  $24^\circ$  (fig. 5(a)). Vectoring was accomplished only with the nozzle in the dry power position. The same mechanisms used for varying nozzle throat and exit area are employed to camber the wedge (ref. 11). Photographs of the nozzle with the two vector angles are presented in figure 5(b).

Thrust reversing configurations.- During this investigation, an in-flight thrust reverser with two reverser-panel positions (ref. 11) was studied on the dry power nozzle as indicated in figure 5(c). Photographs of the reversing configuration with the single vertical tail installation are presented in figure 5(d). One reverser position represented a nominal 50-percent deployment which symmetrically directed the exhaust  $62.8^\circ$  from the horizontal plane as shown in figure 5(c). The other position represented a nominal 100-percent deployment which directed the exhaust forward or at an angle of  $134.8^\circ$  (fig. 5(c)). The 50-percent deployed reverser was intended to simulate a thrust-spoiler position.

Tail surfaces.- The model was tested with an all-movable horizontal tail in combination with either a single tail or twin vertical tails as indicated in the sketch of figure 6(a) and the photographs of figure 6(b). The geometrical characteristics of the horizontal, single, and twin vertical tails are presented in figure 7. The tails also had similar airfoil geometry.

The horizontal tails were installed adjacent to the nozzle two-dimensional wedge on the model center line with the quarter-chord of the mean geometric chord (of exposed panel) nearly aligned with the nozzle exit plane (fig. 7(a)). Horizontal-tail deflection angle was varied from  $-4^\circ$  to  $8^\circ$ .

The single vertical tail (fig. 7(b)) was mounted on the model center line, and the twin vertical tails (fig. 7(c)) were installed canted outboard  $15^\circ$  to the vertical plane that intersected the outside wall of the internal flow duct. The single tail and twin vertical tails were sized to have the same tail volume which is typical of twin-engine fighter airplanes. Both tails had full span rudders with the rudder hinge line located at 0.7c. The rudder was tested at

deflection angles of  $0^\circ$  and  $10^\circ$ . In addition, provisions were made to test the single vertical tail as all movable with the hinge line at  $0.3\bar{c}$ . The all-movable vertical tail was tested at  $0^\circ$  and  $6^\circ$ .

### Wind Tunnel and Support System

This investigation was conducted in the Langley 16-foot transonic tunnel and in the Langley 4-foot supersonic pressure tunnel. The Langley 16-foot transonic tunnel is a single-return atmospheric wind tunnel with a slotted octagonal test section and continuous air exchange. The wind tunnel has continuously variable airspeed up to a Mach number of 1.30. Test-section plenum suction is used for speeds above a Mach number of 1.10. A complete description of the wind tunnel and operating characteristics can be found in reference 13. The Langley 4-foot supersonic pressure tunnel is a single-return, continuous-flow wind tunnel with a stagnation-pressure range of 27.58 kPa to 206 kPa and a stagnation-temperature range from 310 K to 322 K. By use of flexible tunnel-nozzle walls fitted to a calibrated contour, the tunnel Mach number can be varied from 1.25 to 2.20. A brief description of the Langley 4-foot supersonic pressure tunnel is given in reference 14.

The model was supported in the Langley 16-foot transonic tunnel by a sting strut as shown in figure 1. The strut had a  $45^\circ$  leading- and trailing-edge sweep, a 50.8-cm chord, and a 5-percent-thick hexagonal airfoil in the streamwise direction. The model blockage ratio was 0.0015 (ratio of model cross-sectional area to test-section area), and the maximum blockage ratio including the support system was 0.0020. Strut interference effects are considered to be small on this model afterbody because of the low boattail angle (ref. 15). A similar strut without the sting was used in the Langley 4-foot supersonic pressure tunnel installation to mount the model on the wind-tunnel center line from one of the wind-tunnel sidewalls. The same twin-jet propulsion simulation system including the force balance was used in both wind tunnels. Both wind tunnels also have similar air supplies, control equipment, and data recording systems.

### Test Conditions

Tests were conducted in the Langley 16-foot transonic tunnel at Mach numbers from 0 to 1.30 and in the Langley 4-foot supersonic pressure tunnel at Mach numbers of 0 and 2.20. The ratio of jet total pressure to free-stream static pressure varied depending on Mach number from jet off to approximately 26. For the performance portion of this investigation, the angle of attack was nominally held at a  $0^\circ$  angle of attack with actual angles of attack ranging from 0 to  $-0.10^\circ$ . For the thrust vectoring tests, there was an additional small decrease in angle of attack as pressure ratio was increased because of the method of model support and the manner in which data were obtained. Normally, the model support pitch angle is fixed as pressure ratio is increased. This decrease in  $\alpha$  can be as much as  $1.0^\circ$  at the higher pressure ratios and Mach numbers for configurations with the  $24^\circ$  vectored wedge and horizontal tail deflected ( $+\delta_h$ ).

The average Reynolds number per meter, free-stream dynamic pressure, stagnation pressure, and stagnation temperature are summarized in the following table:

M	$N_{Re}$ per meter	$q_\infty$ , kPa	$P_{t,\infty}$ , kPa	$T_t$ , K
0.40	$8.20 \times 10^6$	10.14	101.01	302
.60	10.43	19.92	101.01	316
.80	12.30	29.78	101.01	323
.90	12.63	33.92	101.01	329
.95	12.80	35.71	101.01	331
1.20	13.12	41.92	101.01	344
1.30	13.20	42.95	101.01	350
2.20	13.12	39.37	124.11	314
2.20	16.40	51.99	165.47	322

At  $M = 2.20$ , all tests were conducted at  $N_{Re} = 13.12 \times 10^6$  except as noted on data figures.

All tests were conducted with 0.25-cm-wide boundary-layer transition strips consisting of No. 100 silicon carbide grit sparsely distributed in a thin film of lacquer. These strips were located 2.54 cm from the tip of the forebody nose and on both surfaces of the horizontal and vertical tails at 5 percent of the root chord to 10 percent of the tip chord in accordance with the recommendations of references 16 and 17.

#### Instrumentation

External aerodynamic and internal nozzle forces and moments were measured by an internal, six-component strain-gage balance. Eight external static pressures were measured at the sealed metric break at approximately FS 68.58 cm. Four of these pressure orifices were located on the nonmetric forebody, and four were located on the metric afterbody at meridian angles. All these orifices were spaced every  $90^\circ$ . These pressure measurements were used to correct the measured axial forces for pressure-area force tares. Four internal pressures were measured in the vicinity of the sealed metric break, and four internal pressures were located inside the model cavity at approximately FS 112.00 cm. One internal pressure measurement was made near the nose of the model. These pressures were also used to determine pressure-area force tares.

A turbine flowmeter (external to the wind tunnel) was used to measure total mass-flow rate to the nozzles. In addition, the pressure and temperature in each supply pipe was measured prior to discharge of the flow through the eight sonic nozzles in order to determine mass-flow rate to each nozzle. These flow measurements were used independently to check the mass-flow rate as determined by the flowmeter. The two flow measurements usually agreed to within 1/2 percent of each other. Flow conditions in each nozzle were determined from a rake located at FS 104.52 cm (fig. 2). Each rake contained 10 total pressure

probes and two total temperature (chromel-alumel thermocouples) probes. All pressures were measured with individual pressure transducers. At each test condition, approximately 10 samples of data were recorded on magnetic tape over a period of about 10 sec. The average of the 10 samples was used for computational purposes.

## DATA REDUCTION PROCEDURE

### Data Adjustments

External aerodynamic and internal forces and moments were measured by an internal six-component force balance. Because the center line of the force balance was located above the jet center line (fig. 2), a force and moment interaction between the bellows flow transfer system (fig. 3) and force balance existed. Consequently, single and combined calibration loadings of normal force and pitching moment were made with and without the jets operating with an ASME calibration nozzle. These calibrations were performed with the jets operating because this condition gives a more realistic effect of pressurizing the bellows than does capping off the nozzles and pressurizing the flow system. However, loadings were also done in the axial-force direction with the flow system capped off and pressurized, and this method indicated no effect on the axial force measured by the balance. Thus, in addition to the usual balance interaction corrections applied for a single force balance under combined loads, another set of interactions for the combined loading effect of the balance with the bellows system were made to the data from this investigation.

Angle of attack  $\alpha$  was determined by applying deflection terms due to model and balance bending under aerodynamic load to the sting pitch angle. Calibrations were made with the propulsion simulation system in place to account for any restraints that might occur across the force balances. It should also be noted that some difference in angle between the nonmetric and metric portions of the model exists because of balance deflection alone, especially during vectoring operation at  $\delta_w = 24^\circ$ . No adjustment has been made for wind-tunnel flow angularity (approximately  $0.1^\circ$  for most sting-supported models in the Langley 16-foot transonic tunnel).

Gross thrust-minus-axial force was computed from the following relationship:

$$(F_g - F_A) = F_{A,bal} + (\bar{p}_{es} - p_\infty)(A_m - A_{seal}) + (\bar{p}_1 - p_\infty)A_{seal} - F_{A,mom}$$

where  $F_{A,bal}$  (positive upstream) includes all pressure and viscous forces, internal and external, on both the afterbody and the thrust system. The second and third terms account for the metric break seal rim pressure forces and interior pressure forces, respectively. In terms of an axial-force coefficient, the second term ranges from -0.0001 to -0.0007, and the third term varies  $\pm 0.0075$ , depending upon Mach number. The fourth term, which ideally should be zero, is a momentum tare correction and is a function of the average bellows internal pressure. At an internal pressure of 1380 kPa (corresponding to  $p_{t,j}/p_\infty \approx 4.0$ ), this tare is approximately 5 percent of the maximum static thrust, and its repeatability is 0.25 percent of the maximum static thrust. This tare results from high internal velocities in the bellows area where the flow is being



ejected radially. This condition causes a pressure differential to exist between the ends of the bellows. The momentum tare force was determined from calibrations prior to and after the wind-tunnel tests with the standard calibration nozzles of reference 10. The iris-convergent nozzles of reference 3 were also tested to ascertain whether this tare was invariant with nozzle throat area because of the large difference in throat area between the dry power and afterburner power nozzle settings for the current investigation. The results indicated no effect of variation of throat area on this tare force.

#### Performance Parameters

The basic performance parameter used for the presentation of results is the aeropropulsion thrust ratio  $(F - D_a)/F_1$  which is the ratio of actual nozzle thrust-minus-afterbody drag to the ideal nozzle thrust where

$$F - D_a = (F - D) + D_f$$

The friction drag  $D_f$  for this parameter is calculated for that portion of the model from FS 68.58 cm to FS 80.77 cm by the method of reference 18. The results (body alone) contained herein are, therefore, directly comparable with those of reference 3.

The ratio of actual thrust-minus-nozzle drag to ideal thrust  $(F - D_n)/F_1$  is next determined by adding to  $F - D$  the skin friction drag on that portion of the model from FS 68.58 cm to FS 112.65 cm or

$$(F - D_n) = (F - D) + D_f$$

This term is applicable only to the configuration without tails and is used for comparisons between the data of the current investigation and the data of references 6 and 7.

#### Tail Interference Parameters

Since one of the objectives of this investigation was to assess the installation effects of the tails on performance, an incremental tail interference parameter is defined simply as

$$\Delta \left( \frac{F - D_{int}}{F_1} \right) = \left( \frac{F - D_a}{F_1} \right)_{\text{tails on}} - \left( \frac{F - D_a}{F_1} \right)_{\text{body alone}} + \left( \frac{D_f + D_w}{F_1} \right)_{\text{tails}}$$

where  $D_f$  is the skin friction drag on the tails. The wedge and internal side-plate skin friction drag is charged to nozzle performance. For Mach numbers greater than 1.00, the wave drag  $D_w$  is also included and is computed by the method of reference 19. For Mach numbers less than 1.00,  $D_w$  is assumed to be zero. The tail interference drag coefficient is then

$$\Delta C_{D,int} = \Delta \left( \frac{F - D_{int}}{F_1} \right) \frac{F_1}{Q_\infty A_m}$$

Note that no adjustments have been made to the friction drag to account for profile effects. Also included in the tail interference parameters is the increase in drag due to compressibility effects, especially in the drag rise. This effect is included since there are no suitable means to account for such terms.

### Thrust Vectoring Parameters

From the measured axial and normal components of the jet resultant force, determined at static conditions for each vectored nozzle configuration, an effective jet turning angle is defined as

$$\delta_j = \tan^{-1} \frac{C_{N,j}}{C_{F,j}}$$

These static components of the jet resultant force were also used to determine the thrust contribution to lift at forward speeds. This assumes no effect of the external flow on the jet turning characteristics. As shown in reference 10, the external flow can affect jet turning.

The effect of thrust vectoring on thrust-minus-drag performance is determined by

$$\Delta \left( \frac{F - D}{F_1} \right) = \left( \frac{F - D}{F_1} \right)_{\delta_w} - \cos \delta_j \left( \frac{F - D}{F_1} \right)_{\delta_w=0}$$

Note that a component of drag  $D \cos \delta_j$  has been subtracted. This procedure is not absolutely correct but was done in this manner because the drag cannot be separated from the thrust-minus-drag term.

## DISCUSSION

### Static Performance

The static performance characteristics for both the basic and alternate two-dimensional wedge twin-nozzle configurations are presented in figure 8. Also shown is the static performance for the single-engine nozzle taken for the model with  $A_e/A_t = 1.300$  from reference 7. The twin-nozzle performance was slightly lower (less than 1/2 percent) than the single-nozzle static performance. This difference is within the accuracy band of the two different propulsion simulation systems. The "dip" in the basic nozzle, dry power wedge performance at a nozzle pressure ratio of 4.5 with the twin-nozzle model may be caused by shock interactions that reduce pressures acting on the external wedge surface. This characteristic was not discovered during the investigation of reference 7 because data were not obtained at a nozzle pressure ratio of 4.5. The maximum obtainable pressure ratio, at static conditions, for the nozzle with the afterburner power setting was limited by the maximum flow rate of the system.



A comparison of twin- and single-engine two-dimensional wedge nozzle performances at a nozzle pressure ratio of 2.6 (corresponding to take-off conditions) is presented in figure 9. Also shown for comparison are the performances of the axisymmetric convergent nozzles ( $A_e/A_t = 1.000$ ) from references 15 and 20. Since peak nozzle performance is dependent on the nozzle internal expansion area ratio, only nozzles with the same  $A_e/A_t$  are directly comparable at this selected nozzle pressure ratio. Note also that most of the area ratios for the nozzles (both dry and afterburner power) of the present investigation are much higher than necessary for static take-off conditions ( $A_e/A_t = 1.050$ ). Thus, performance at the selected pressure ratio is low when compared with nozzles with lower internal expansion area ratios. The lower performance is primarily a result of overexpansion losses ( $A_e/A_t$  too large) since the two-dimensional nozzles with the lower  $A_e/A_t$  approach the performance of a near-ideal axisymmetric nozzle.

### Aeropropulsion Performance

The variation of the thrust-minus-afterbody drag ratio with jet nozzle pressure ratio at several Mach numbers for the basic nozzle at dry and afterburner power settings is presented in figure 10. The large decrease in performance at supersonic speeds results from an increase in drag due to supersonic wave drag. A comparison of the aeropropulsion performance of the basic and alternate nozzle concepts is presented in figures 11 and 12 for the dry and afterburner power settings, respectively. These data are directly comparable to the data in reference 3. Figures 13 and 14 present thrust-minus-nozzle drag ratio for the same model configurations as presented in figures 11 and 12. The results from reference 7 for  $A_e/A_t = 1.100$  and  $A_e/A_t = 1.300$  are also included (fig. 13). As can be seen, there is a large decrease in performance for the alternate nozzle in the dry power setting when compared with the basic nozzle (fig. 11) or with the results of reference 7 for  $A_e/A_t = 1.100$ . The decrease in performance is attributed to separated flow on the wedge. At Mach numbers from 0.80 to 0.95, the alternate nozzle at afterburner power setting had higher performance than the basic nozzle up to a nozzle pressure ratio of about 3.6 (fig. 14). This higher performance would be expected since the internal area ratio was less. Supersonic performance was much less than the basic nozzle.

The variation of ideal thrust coefficient  $C_{F,i}$  with jet total pressure for the nozzle with both power settings is presented in figure 15 for all the test Mach numbers. These data are presented for reference only. Figure 16 presents a schedule of the nozzle pressure ratio with Mach number for a typical high-performance, low-bypass ratio turbofan engine. Also shown is the internal expansion area ratio, based on one-dimensional theoretical flow analysis, required for optimum exhaust flow expansion for an air jet at this specified pressure ratio schedule. Reference to the scheduled pressure ratio is made during subsequent discussion of the test results.

A summary of the aeropropulsion performance (thrust-minus-nozzle drag ratio) of the current investigation and of references 6 and 7 are given in figure 17. Performances for nozzles with several internal area expansion ratios are presented at scheduled pressure ratios in order to compare single- and twin-nozzle configurations at the same  $A_e/A_t$  ratio and to illustrate the effect of

Mach number on performance of a nozzle with fixed  $A_e/A_t$ . It should be noted that the performance shown has not been optimized for the single or the twin nozzle. Optimum thrust-minus-drag performance at a particular Mach number is generally obtained by adjusting the internal expansion area ratio  $A_e/A_t$  in order to match the scheduled operating pressure ratio. For example, for the scheduled pressure ratio of figure 16, an internal expansion area ratio of 1.140 is required at  $M = 0.60$ ; at  $M = 0.90$ ,  $A_e/A_t = 1.240$  is needed. In actual operation, wedge geometry would be continuously varied (within mechanical restrictions) to optimize performance at each flight Mach number. Thus, a comparison of the performance for a nozzle with different values of  $A_e/A_t$  at a particular Mach number only indicates which nozzle gave the better performance. Reference 8 points out that peak in-flight nozzle performance (for single nozzle) appeared to occur at higher nozzle pressure ratios than indicated by one-dimensional flow analysis. This result indicates that the two-dimensional wedge nozzles probably should be designed to operate slightly underexpanded.

A comparison of the dry power performance of the single-engine two-dimensional wedge nozzle ( $A_e/A_t = 1.300$ ) from reference 7 with the basic nozzle of the present study ( $A_e/A_t = 1.287$ ) at Mach numbers below 1.00, indicates that the twin-nozzle performance is essentially equal to the single-nozzle performance (fig. 17). The fact that the performance is the same (or higher) represents a reversal of the traditional trend of installation penalties associated with twin-nozzle configurations. The reason for the higher twin-nozzle performance is attributed to an approximate 25-percent reduction of external wetted area obtained by joining the twin nozzles. It should be noted that part of the twin-engine installation penalty for axisymmetric nozzles can be attributed to the boattail gutter or base between the engines. A comparison of the thrust-minus-pressure drag (removing the external friction drag of the nozzles) indicates that the twin-nozzle installation does have a slight pressure drag penalty at  $M = 0.90$  and  $0.95$ . However, the reduction in wetted area for the twin-nozzle installation more than compensates for the pressure drag penalty by a reduction in friction drag.

The basic twin-nozzle performance level at  $M = 1.20$  was about 2 percent lower than the single-nozzle model performance ( $A_e/A_t = 1.30$ ). This loss in performance for the twin-nozzle installation is attributed to an increase in wave drag due to the two different model configurations tested. The maximum cross-sectional area and the overall length of both models were nearly the same. However, the twin-nozzle model closure rate was higher than that for the single-nozzle model, a difference which resulted in increased twin afterbody supersonic wave drag. This would probably not result in a properly designed twin-engine fighter airplane. The differences in performance noted for the single- and twin-nozzle configurations are nearly constant over the pressure ratio test range (ref. 8).

#### Twin Two-Dimensional and Axisymmetric Nozzle Comparisons

Comparisons of aeropropulsion performance between the twin two-dimensional wedge nozzle installation of the present investigation and the twin axisymmetric nozzle installations are presented in figures 18 to 23. All the axisymmetric data were obtained from the parametric investigation of reference 3 which

studied the effects of nozzle design, power setting, afterbody shape, and nozzle lateral shaping on performance. The results of reference 3 indicate that the best subsonic performance for an axisymmetric installation was obtained on a clean afterbody with close-spaced circular-arc iris-convergent nozzles installed. These data are compared with the present model in figure 18. Also included from reference 3 are the data for an afterbody with short horizontal stabilizer actuator fairings and short blunt engine interfairings (referred to as "short booms") and an afterbody similar to a current twin-jet fighter aircraft which had a long engine interfairing and long horizontal stabilizer actuator fairings (referred to as "long booms"). All three afterbodies from reference 3, chosen for this comparison, had the same nozzle lateral spacing.

Since the axisymmetric nozzle configurations were slightly wider than the two-dimensional wedge nozzle afterbody, the closure area ratio  $(A_m - A_t)/A_m$  was also higher. This condition could slightly favor the aeropropulsion performance of the axisymmetric installations at subsonic speeds since more pressure recovery is possible. However, at supersonic speeds, the configurations with the higher closure ratios would have greater supersonic wave drag. In addition, the nozzle internal expansion area ratios of the two-dimensional and axisymmetric installations are different. A conservative comparison to determine the level of performance of the two-dimensional wedge nozzle in relation to the axisymmetric nozzle installation is to compare peak nozzle-afterbody performance since most of the axisymmetric nozzle peak internal performance can be shifted to a different nozzle pressure ratio by varying the internal expansion area ratio.

As seen in figure 18, the twin two-dimensional wedge nozzle performance at  $M = 0.90$  is higher than the clean afterbody with close-spaced iris-convergent nozzles. This is significant for practical configurations since the addition of booms and interfairings causes performance penalties which, as figure 18 shows, can be large. Booms to support horizontal tails may not be necessary for the integrated design of the twin two-dimensional nozzle as illustrated in the sketch and photographs showing tail installation of figure 6. Similar results are shown for comparisons with other nozzle types, such as axisymmetric convergent-divergent nozzles (fig. 19), axisymmetric blow-in-door nozzles (fig. 20), and axisymmetric plug nozzles (fig. 21). Note that the internal expansion area ratio for each axisymmetric nozzle was 1.000. If this ratio was increased to 1.300 to approximate the two-dimensional wedge nozzles, then the axisymmetric nozzle performance would be increased by about 2 percent at a nozzle pressure ratio of 6.00.

For afterburner power at Mach numbers up to 1.20 (fig. 22), the two-dimensional wedge nozzle again exhibits higher performance at  $M \geq 0.90$  when compared with the axisymmetric convergent-divergent nozzles with similar expansion area ratios. The best axisymmetric nozzle installation performance with afterburner power setting was obtained with the convergent-divergent nozzle (ref. 3), partly because of the lower nozzle boattail angle. This figure also indicates that some beneficial effect has occurred for the afterbody of reference 3 with the long booms since this configuration had better performance with the afterburning convergent-divergent nozzles than either the clean or short boom configuration. This beneficial interference probably results from a positive pressure field acting in the vicinity of the booms and interfairings. In



addition, this afterbody had a  $M = 1.20$  design area distribution which should give near-optimum performance at this Mach number. It should be noted that the impact of nozzle cooling requirements on the installed nozzle-afterbody performance has not been included in the afterburner power performance comparison and must be evaluated for absolute performance levels.

Twin two-dimensional wedge nozzle and twin axisymmetric nozzle performances are compared at  $M = 2.20$  in figure 23. Performances are shown for dry and both afterburner power settings from the present investigation. Only performances for each of the nozzle types with the clean close-spaced afterbody from reference 3 are presented since the differences in performance for the other two afterbodies were generally less than 1-percent ideal gross thrust at pressure ratios greater than 10. The afterburner power, two-dimensional wedge nozzles, with  $A_e/A_t = 1.100$  and  $A_e/A_t = 1.393$ , have superior performance characteristics over axisymmetric nozzle types at pressure ratios up to 19 and 22, respectively. The poor performance of the iris-convergent nozzle is expected since this nozzle type has no internal or external expansion surfaces and thus characteristically exhibits a large underexpansion loss in performance at supersonic speeds. At a typical engine-operating pressure ratio of 14, the twin two-dimensional wedge nozzle at dry power has a 2.5- to 3.5-percent lower performance than the other types of axisymmetric nozzles at afterburner power. Although most current aircraft do not cruise at supersonic speeds at dry power, future aircraft may do so because of the higher thrust-weight ratios of advanced aircraft. If supersonic, dry power cruise is desired, the two-dimensional wedge nozzle appears to be an attractive installation because of its high performance at transonic and supersonic speeds.

### Effects of Tail Surfaces

Effects with power off.— The variations of jet-off afterbody drag coefficient with Mach number for the model with both the dry power and afterburner power wedges for the basic nozzle are presented in figure 24. Also shown are the computed skin friction drag coefficients  $C_{D,f}$  for the various combinations of tail surfaces. Since the internal nozzle surfaces (that is, wedge and sideplates) are charged to the nozzle internal performance, skin friction drag is the same for either power setting for a particular configuration.

At Mach numbers below 0.80, the increase in drag caused by adding the various tail surfaces results primarily from the difference in skin friction drag. At  $M = 0.90$  and  $0.95$ , installation of the tail surfaces also results in tail interference drag. At supersonic speeds, the configuration with twin vertical tails has slightly lower jet-off drag than with the single vertical tail. A subsequent discussion shows that this difference in drag is caused by the lesser wave drag of the twin vertical tails.

Effects with power.— Figure 25 presents the effects of horizontal-tail deflection on the variation of the aeropropulsion performance parameter with nozzle pressure ratio for the basic dry power nozzle. There is a decrease which varies with Mach number in  $(F - D_a)/F_1$  because of adding the horizontal tail at  $\delta_h = 0^\circ$ . As expected, deflection of the horizontal tail results in further reductions in performance because of increases in tail drag due to tail lift.

The effects of adding either the single or twin vertical tails with the horizontal tail at  $\delta_h = 0^\circ$  for both the dry and afterburner power nozzles are presented in figures 26 to 28. Note that unlike the case for the dry power nozzle, the model was not tested with only the horizontal tail with the afterburner power setting at  $A_e/A_t = 1.393$  for  $M < 1.20$ . At subsonic speeds, the penalty in performance for the twin vertical-tail installation is greater than that for the single vertical tail for either nozzle power setting. (See, for example, fig. 26(b) or 27(a).) The decrease in performance results not only from a small increase in friction drag but also from adverse tail interference effects from the twin vertical tail installation. Flow visualization photographs obtained at  $M = 0.90$  (presented in fig. 29) show that the twin vertical tails were not aligned with the local afterbody flow streamlines and thus wake disturbances from the twin vertical tails could affect flow on the afterbody cowl boat-tail. These wake disturbances could be minimized when the installation of the twin vertical tails is tailored by adjusting the toe-in and cant angles. The aeropropulsion performance at supersonic Mach numbers is essentially the same for both vertical-tail installations (figs. 26(c), 27(b), and 28), a similarity which indicates that the increase in drag due to friction for the twin verticals is offset by a decrease in wave drag.

The dry power wedge, tails-off configuration was also tested at a Reynolds number per meter of  $16.40 \times 10^6$  at  $M = 2.20$ . These data are indicated by the flagged symbols in figure 28. The differences shown are due only to the differences in skin friction drag that result from the difference in the two Reynolds numbers. When the friction drag is subtracted, there is no effect on aeropropulsion performance because of this change in Reynolds number.

Subsonic tail interference.— Since one of the advantages cited for the twin two-dimensional wedge nozzle is improved airframe-propulsion system integration (elimination of gutters, nozzle bases, etc.), it becomes of interest to assess the interference effects, especially at high subsonic speeds, of a typical tail installation for a twin-engine fighter airplane. To determine either of the two interference parameters defined in the section entitled "Data Reduction Procedure," skin friction drag coefficients already presented in figure 24 are used.

The variation of tail interference incremental drag coefficient  $\Delta C_{p,int}$  with pressure ratio for Mach numbers from 0.40 to 0.95 is presented in figure 30. Note that the parameter  $\Delta C_{p,int}$  implies no effect of the external flow on nozzle internal performance; the differences noted are charged to external flow interference effects. The solid symbols represent jet-off values. The effect of power is generally beneficial for the dry power wedge since the jet-on values of  $\Delta C_{p,int}$  are usually somewhat lower than the jet-off values. For both nozzle power settings, the differences between jet-off and jet-on values are generally small. These differences probably indicate that the magnitude of tail interference is due mainly to external aerodynamic interference that results from the tail installation. Again, this finding is consistent with the concept of improved integration afforded by the twin two-dimensional wedge nozzle inasmuch as there are no projected surfaces affected by potential pressure gradients induced by the jet exhaust.

The variation of the tail interference parameter  $\Delta\left(\frac{F - D_{int}}{F_1}\right)$  with nozzle pressure ratio is presented only for  $M = 0.90$  and  $M = 0.95$  in figure 31 since, for lower Mach numbers, these values are generally less than 1 percent of ideal gross thrust. Note that even at  $M = 0.90$ , the decrement in performance for the single vertical-tail installation is less than 1 percent of ideal gross thrust for both nozzle power settings. The difference in levels of the tail interference parameter between the dry and afterburner power setting is due primarily to the difference in ideal gross thrust which is the denominator of this parameter. Figure 30 indicated approximately the same levels of incremental interference drag for both nozzle power settings.

Supersonic tail interference.- The tail interference parameter  $\Delta\left(\frac{F - D_{int}}{F_1}\right)$  and the tail interference incremental drag  $\Delta C_{D,int}$  were determined at supersonic speeds using wave drag computed with the no-wedge mathematical model as outlined in the appendix. These results are presented in figure 32. The data indicate that at  $M = 1.20$ , the nozzle with the dry power wedge had about twice as much tail interference drag as it had with the afterburner wedge. At  $M = 2.20$ , the nozzle with the afterburner wedge had more than doubled the amount of interference drag noted for the dry power wedge. Since the experimental setup had only one force balance and no external pressure instrumentation, it cannot be ascertained whether these differences for the two power settings are caused by changes in nozzle internal performance or the external flow characteristics.

Figure 33 summarizes tail interference drag at both jet-off and at scheduled pressure ratio conditions. This figure indicates that interference drag due to various tail installations results from external aerodynamic flow interaction effects at jet-off conditions. Power effects are small and usually beneficial. Figure 33 also shows the results from reference 2 for a single-engine configuration with axisymmetric nozzles in both dry and afterburner power settings. These data were taken from the configuration with staggered tails. The similarity of that configuration to the present one comes from the location of the vertical tail with respect to the horizontal tails. The results show similar tail interference characteristics at the scheduled pressure ratio.

A comparison of the effects of tail installation on tail interference is shown in figure 34. These data show that tail interference drag generally increases with increasing number of tail surfaces, particularly in the subsonic cruise Mach number range.

### Thrust Vectoring Characteristics

Recent two-dimensional nozzle studies have shown that thrust vectoring can significantly increase the maneuverability of a fighter airplane. If the lifting surfaces are properly integrated with the vectoring nozzle, jet-induced lift forces equal to or greater than the thrust lift vector can be achieved together with substantial reductions in external drag (refs. 4 and 10). It should also be noted that thrust vectoring can be effective at low speeds where the lower dynamic pressure tends to make aerodynamic control surfaces less effective. For



a twin-engine aircraft, asymmetrical thrust vectoring for roll control could be used in those situations where flow separation may render roll control devices ineffective.

In order to study the capability of the two-dimensional wedge nozzle in vectoring thrust by cambering the wedge, thrust vectoring configurations were tested with wedge-vectoring deflection angles of  $12^\circ$  and  $24^\circ$  with the nozzle in the dry power configuration only, as shown in figures 5(a) and 5(b).

The static performance characteristics for the nozzle with wedge angles of  $12^\circ$  and  $24^\circ$  are presented in figure 35. The static turning angle  $\delta_j$  is seen to increase with increasing pressure ratio for both wedge angles until maximum static turning occurs at a nozzle pressure ratio of 4.0. The decrease in static turning at pressure ratios greater than 4.0 is probably caused by the separation of the jet flow over the upper aft portion of the wedge, and the separation probably occurs at the second hinge point. Only the jet normal force  $C_{N,j}$  and pitching moment  $C_{m,j}$  are affected by this flow separation.

Nozzle thrust ratio characteristics for the wedge angles of  $12^\circ$  and  $24^\circ$  are also shown in figure 35. The dashed lines represent computed values of thrust ratio with no turning loss for each of the respective wedge deflections. Static turning losses up to 0.8 percent for the  $12^\circ$  wedge and 2.5 percent for the  $24^\circ$  wedge occur. Note that although static turning was maximum at a nozzle pressure ratio of about 4, the minimum turning losses for the nozzle with both wedges occurred at a ratio of about 4.6 which was the nozzle design pressure ratio. The static turning losses affect vectoring performance at forward speeds, a characteristic that is discussed later in this report. However, it should be noted that no attempt was made to optimize plug vectoring geometry for minimum losses.

The effects of thrust vectoring on the longitudinal aerodynamic characteristics are presented in figures 36 to 40 for both wedge angles and for the various horizontal- and vertical-tail installations. These figures present the basic data for that effect measured on the entire metric portion of the model. The data include thrust-minus-drag coefficient  $C_{(F-D)}$ , total lift coefficient  $C_L$ , and total pitching moment  $C_m$ .

In general, figures 36 to 40 show an increase in lift coefficient with increasing pressure ratio for a particular configuration. This increase in  $C_L$  is the result of the contribution of both jet lift and jet-induced supercirculation lift. The increase in lift is accompanied by a decrease in pitching moment. Thrust-minus-drag coefficient varies almost linearly with pressure ratio. At a constant pressure ratio, the differences in  $C_{(F-D)}$  noted for different configurations are usually caused by the differences in drag.

Lift augmentation characteristics for the nozzle with the  $12^\circ$  and  $24^\circ$  wedges are summarized in figure 41. The variation of incremental lift  $\Delta C_L$  with nozzle pressure is shown where  $\Delta C_L$  is simply the difference between lift at some power-on and jet-off condition. Also shown is the computed jet lift which is determined by using the static data of figure 35. This calculation assumes no effect of the external flow on the nozzle internal performance or nozzle turning characteristics. The difference between  $\Delta C_L$  and the jet lift is then the jet-induced supercirculation lift. In general, maximum incremental lift occurred

between pressure ratios of 4.0 to 4.5, which is approximately where maximum static turning occurred.

The jet-induced supercirculation lift is generally equal to or greater than the jet lift for the body alone configuration for both wedge angles of  $12^\circ$  and  $24^\circ$  at  $M = 0.80$  and  $0.90$ . (See fig. 41.) This lift augmentation performance (jet-induced supercirculation lift) is superior to the wings-off performance of the two-dimensional convergent nozzle configuration of reference 10. However, good lift augmentation performance for a wedge nozzle would be expected since this nozzle closely resembles a blown flap (blowing over and under a wing trailing-edge flap), and the wedge aerodynamic lift is added onto the jet lift.

Additional increases in jet-induced supercirculation lift result from the addition of the horizontal tail and also from the increase in horizontal-tail deflection from  $-4^\circ$  to  $8^\circ$ . The increase in induced lift due to horizontal-tail deflection is caused by an increase in effective tail angle of attack as the horizontal tail operates in the jet-induced upwash flow field, even though the relative angle between the vectored jet exhaust and the horizontal tail decreases with increasing  $\delta_h$ . Some additional benefit may also result because, for higher values of  $\delta_h$ , the trailing edge of the horizontal tail is more favorably located with respect to the vectored jet exhaust, specifically the lower half of the jet exhaust. The effect of adding vertical tails is small for  $\delta_w = 12^\circ$  and negligible for  $\delta_w = 24^\circ$  (fig. 41).

The effect of thrust vectoring on incremental aeropropulsion performance (thrust minus drag) is summarized in figure 42 for the nozzle with the  $12^\circ$  and  $24^\circ$  wedges. An incremental thrust-minus-drag ratio, defined in the section entitled "Data Reduction Procedure," is used where a negative value indicates a loss in performance. For the two-dimensional wedge nozzle, the losses indicated are due partly to an increase in the drag of the wedge which resembles a speed brake and thrust spoiler when in a vectored mode.

Losses in performance for the nozzle alone range from about 1.5 to 14 percent for  $\delta_w = 12^\circ$  and from 8 to 43 percent for  $\delta_w = 24^\circ$  depending upon Mach number and nozzle pressure ratio. The minimum loss of 1.5 percent occurred for  $\delta_w = 12^\circ$  at  $M = 0.60$  and at a nozzle pressure ratio of 4.5 which was also approximately the pressure ratio at which static turning losses were minimum (fig. 35(a)). The effect of the various tail installations is small except for the  $12^\circ$  wedge with  $\delta_h = -4^\circ$  and  $8^\circ$ , vertical tails off.

#### Thrust Reversing Characteristics

The maneuvering benefits to be derived from in-flight thrust reversing or thrust modulation are discussed in reference 5. A thrust reversing system can easily be incorporated into the two-dimensional wedge nozzle by installation of reverser panels as previously described in figures 5(c) and 5(d). During the present investigation, two reverser-panel positions were studied with the nozzle in the dry power setting only. One position ( $\phi = 62.8^\circ$ ) represented a 50-percent deployment of the reverser, and the other position ( $\phi = 134.8^\circ$ ) represented a 100-percent deployment.

Static-thrust characteristics for the two reverser positions tested are presented in figure 43. These results are typical for current thrust reverser configurations (refs. 21 to 23). The effects of thrust reversing on the aerodynamic characteristics of the configuration tested are presented in figures 44 to 49. Figure 44 presents basic reverser longitudinal aerodynamic performances for  $\phi = 62.8^\circ$  and  $134.8^\circ$ , tails off and for  $\phi = 134.8^\circ$  with  $\delta_h = \pm 4^\circ$  with the twin vertical tails. The effects of rudder deflection for both single and twin vertical tails on the aerodynamic characteristics are presented in figures 45 and 46 for  $\phi = 62.8^\circ$  and in figures 47 and 48 for  $\phi = 134.8^\circ$ . The horizontal-tail deflection was  $0^\circ$  for these cases.

Reverser effectiveness.- The effect of nozzle pressure ratio on thrust reverser effectiveness for the Mach numbers tested is presented in figure 50 for the model with the single vertical tail, and  $\delta_h = 0^\circ$ . These results are typical. This figure shows the ratio of thrust-minus-drag coefficient for the reverser deployed to thrust minus drag for the reverser stowed (forward thrust mode). As can be seen, there is a decrease in reverser effectiveness as nozzle pressure ratio increases and an increase in effectiveness as Mach number increases. The increase in reverser effectiveness with Mach number is a result of the base drag acting on the reverser panels when they are deployed. (See fig. 5(c).) Base drag on the reverser panels, determined from static pressure measurements, was nearly constant with nozzle pressure ratio (ref. 8). In addition, some additional pressure drag, which was not determined, probably acts on that portion of the wedge behind the reverser panels. (See fig. 5(c).) Thrust modulation performance as a function of percent reverser deployment is presented in figure 51. Also shown are the results from reference 21 for an axisymmetric nozzle in-flight thrust reverser installed on a single-engine fighter airplane with a single vertical tail. The two-dimensional wedge nozzle configuration is a more effective thrust reverser, especially when deployed 50 percent. The increase in effectiveness probably results from the base drag generated by the reverser panels of the wedge nozzle concept. Reference 24 indicates that for  $M < 1.00$ , deploying a thrust reverser can provide greater longitudinal deceleration control than that provided by a typical speedbrake and, unlike the speedbrake, the thrust reverser also remains effective at very low speeds.

Longitudinal characteristics.- The effect of thrust reversing on the longitudinal characteristics can be seen by examining the basic lift and pitching-moment data of figures 44 to 48. However, it is difficult to relate pitching-moment coefficients to typical airplane quantities because of the chosen reference dimensions and moment reference center. Wing reference areas of typical twin-engine fighter aircraft are approximately 10 times maximum cross-sectional area. Thus, by dividing the lift coefficients presented in figures 44 to 48 by 10, one can obtain typical airplane lift coefficients which are used in the following discussion. In general, at  $\alpha = 0^\circ$ , thrust reversal at  $\phi = 62.8^\circ$  and  $\phi = 134.8^\circ$  had only a small effect on lift coefficient. Thrust reversing with the single vertical-tail installation usually resulted in a small increase in  $C_L$  (less than 0.05 airplane  $C_L$ ), an increase also reflected as a slight nose-down pitching moment. There is little or no effect on  $C_L$  for the model with the twin vertical tails. (See, for example, fig. 45(c) for  $M = 0.60$ ,  $\alpha = 0^\circ$ ,  $\delta_r = 0^\circ$ , single vertical tail; or fig. 48(e) for  $M = 0.80$ ,  $\alpha = 0^\circ$ ,  $\delta_r = 0^\circ$ , twin vertical tails.)

Examination of the lift characteristics at  $\alpha = 8^\circ$  (figs. 44 to 48) indicates a substantial decrease in lift coefficient during reverse thrust operation. These results are summarized in figure 52 where the ratio of  $C_L$  at reverse thrust conditions to  $C_L$  at forward thrust is shown as a function of Mach number at the scheduled pressure ratio. Figure 52 indicates a 33- to 46-percent loss in lift for  $\phi = 62.8^\circ$  and as much as a 100-percent loss in tail lift for  $\phi = 134.8^\circ$ . The loss in lift at  $\alpha = 8^\circ$ , during reverser operation, is probably caused by lateral spreading of the exhaust flow over the inboard rear portion of the horizontal tail, a condition which results in premature flow separation. A loss in stability and control effectiveness will probably occur; however, insufficient information is available to ascertain the magnitude of such losses. Proper integration of the reverse thrust system with the airframe-control surfaces must be accomplished to avoid this problem.

Rudder effectiveness.- The effect of thrust reversing on rudder effectiveness for both vertical-tail installations is presented in figure 53. At 100-percent reverser deployment, there is a complete loss of rudder effectiveness for the single vertical. Such loss occurs when the reverse exhaust flow washes both sides of the single vertical tail. This problem is not as severe with the twin vertical-tail installation since only one side of each of the twin vertical tails is severely affected by the exhaust flow. Reference 22 indicates losses in rudder effectiveness similar to those with the present twin vertical-tail installation even though the airplane configuration of reference 22 had a single vertical tail. However, the reverse jet exhaust described in reference 22 was directed forward on either side of the vertical tail at  $62.5^\circ$  from the vertical tail plane, and thus the vertical tail was not directly washed by the jet exhaust. Figure 53 also indicates that loss of lateral control effectiveness can be alleviated by use of an all-movable vertical tail.

## CONCLUSIONS

An investigation was conducted in the Langley 16-foot transonic tunnel and the Langley 4-foot supersonic pressure tunnel to determine the performance characteristics of twin two-dimensional variable-geometry wedge nozzles. The effects of thrust vectoring, reversing, and various tail installations were studied. The investigation was conducted statically and at flight speeds up to a Mach number of 2.20. The jet total-pressure ratio of the simulated exhaust was varied up to approximately 26 depending on Mach number. An analytical study was made to determine the effect on calculated wave drag by varying the mathematical model used to simulate the nozzle jet-exhaust plume. The results of this investigation indicate the following conclusions:

1. No twin-engine installation penalty was indicated since the twin-nozzle aeropropulsion performance (thrust minus drag) nearly equaled the performance of a single-nozzle installation for a dry power setting at the same internal expansion area ratio.

2. The thrust-minus-afterbody drag performance of the twin two-dimensional wedge nozzle installation is significantly higher than the performance achieved with twin axisymmetric nozzle installations for speeds greater than Mach 0.80.



3. Interference drag due to various tail installations resulted from external aerodynamic flow interaction effects. Power effects were small and usually beneficial.

4. Significant jet-induced lift can be obtained on aft-mounted lifting surfaces using a cambered two-dimensional wedge centerbody to vector jet-exhaust thrust downward. However, thrust-minus-drag performance is degraded up to 14 and 43 percent of ideal gross thrust for wedge angles of  $12^\circ$  and  $24^\circ$ , respectively.

5. The two-dimensional wedge nozzle with reverser panels exhibited effective static and in-flight thrust reversing characteristics. However, care must be exercised when integrating tail surfaces because of the potential for losses in stability and control effectiveness.

6. The values of analytically determined supersonic wave drag are dependent upon the mathematical model chosen to describe the geometry of the two-dimensional wedge nozzle. The results indicate that different mathematical models are needed to simulate jet-off and power-on conditions.

Langley Research Center  
National Aeronautics and Space Administration  
Hampton, VA 23665  
May 4, 1977

## APPENDIX

### SUPERSONIC TAIL INTERFERENCE

At supersonic speeds, the wave drag of the configuration must be determined to ascertain the tail interference parameters. (See section entitled "Data Reduction Procedure.") However, the determination of the wave drag by analytical methods requires an accurate description of the configuration (ref. 19) since wave drag is computed on the equivalent area distribution of the configuration. If local aft-end slopes are not excessive, the computation of wave drag for configurations with axisymmetric nozzles is amenable to current analytic techniques (ref. 19) because the area distribution discontinuities caused by the inlet and exit of the propulsion installation are eliminated by the assumption that cylinders are extended upstream or downstream to infinity from the discontinuities. Thus, the jet exhausting from the axisymmetric nozzle is simulated (neglecting entrainment) at the design pressure ratio with a plume that is neither overexpanded nor underexpanded. However, the two-dimensional wedge nozzle (or some other nozzle with external expansion ramps) is not as conducive to modeling the jet flow as the axisymmetric nozzle. In fact, the computed wave drag is strongly dependent upon the mathematical model chosen to represent the physical jet exhausting from the nozzle.

One limitation of the theoretical method of reference 19 is that it can only represent the engine exhaust by a cylindrical stream tube extended to infinity. For the nonplug axisymmetric nozzle, the jet-off case is computed as though the engine were at the design pressure ratio. However, since the pressure of the exhaust gases at the nozzle exit is generally different from ambient pressure, the jet tends either to plume or to contract on leaving the nozzle. Furthermore, the shape of the plume downstream of the nozzle exit is affected by viscous mixing between the jet exhaust and the external stream. In principle, these deviations of the jet exhaust from a cylindrical stream tube can result in aerodynamic interference on adjacent airframe surfaces. While the shape of the pluming jet exhaust can be described analytically and can be included in the configuration description, two additional mutual interference terms, one of which would be erroneous, would be calculated by the method of reference 19. The first is the interference effect of the jet plume on the aircraft, and the second is the interference of the aircraft on the plume. The first term is of course real, but the second interference term is not felt by the aircraft. The second interference term cannot be isolated in the calculation and thus cannot be corrected for.

A brief analytical study, therefore, has been undertaken by using the method of reference 19 to calculate wave drag for the present configuration. For this study, a total of five different mathematical models were used to describe the nozzle and jet-exhaust flow. Computer-generated drawings (ref. 25) of these configurations are presented in figure 54. Alterations to the mathematical models were only made downstream of the nozzle exit or from FS 127.00 cm. The model with the actual dry power wedge downstream from the nozzle exit (FS 127.00 cm) is shown in figure 54(a). The jet exhaust is shown by the open area in the end view and thus would be represented as four rectangular boxes extending downstream to infinity. Figure 54(b) shows the mathematical model



## APPENDIX

with the afterburner power wedge and the larger jet-exhaust area. It should be noted that wave drag is computed on the wedge centerbodies since the wedges are included in the equivalent area distribution of the configuration. These two mathematical models are probably not representative of the actual flow at either jet-off or jet-on conditions.

Two mathematical models were then employed to simulate the jet exhaust. The first, identified as simulated jet plume and shown in figure 54(c), assumes a jet boundary equal to the height of the nozzle sideplates with the resulting jet area starting at FS 144.78 cm (located at the end of the wind-tunnel model). It should be noted that wave drag is computed on this assumed shape because the assumed shape is included in the equivalent area distribution. The other model is defined as no-wedge and is presented in figure 54(d). In this model, the entire wedge is submerged into the jet flow beginning at the nozzle exit (FS 127.00 cm) and no wave drag is computed for either the wedge or jet plume. This procedure results in a mathematical model with the largest jet area and should provide an approximation of afterbody drag when wedge performance is not charged to external performance, and the nozzle is operating at near-design pressure ratio.

Finally, an attempt was made to simulate the jet-off wake of the actual wind-tunnel model. This simulation is illustrated in figure 54(e) as a wake impinging at FS 137.16 cm where the wake boundary is simulated by a solid body represented by a plane which begins at the nozzle exit at FS 127.00 cm and impinges on the dry power wedge. Cases were computed where the wake impinges the wedge at FS 132.08 cm to FS 142.24 cm in 2.54-cm increments. Only the case for wake impinging at FS 137.66 cm is shown in figure 54(e). Note that no jet area is associated with these cases and, as for the simulated jet plume model, wave drag is computed on the simulated wake surface. The resulting cross-sectional area distributions for  $M = 1.20$  for some of the mathematical models used in this analysis are given in figure 55.

A comparison of the wave drag coefficients computed for the mathematical models without tail surfaces is presented in figure 56. Wave drag was computed only at  $M = 1.20$  and  $M = 2.20$ . The model with no wedge has the least wave drag, but this would be expected since this configuration has the largest jet area (fig. 55) and hence the lowest amount of projected boattail area. The computed wave drag for the dry power wedge and simulated jet plume are nearly equal because they fortuitously have similar cross-sectional area distributions (fig. 55). The cross-hatched area data represent the range of computed wave drag for simulated jet-off wake represented by the series of solid bodies intersecting the dry power wedge (fig. 56).

The skin friction drag coefficients for the model without tail surfaces (fig. 24) are added to the computed wave drag coefficients, and these results, also shown in figure 56, are compared with the measured jet-off drag coefficients  $C_{D,a}$  for the nozzle with both the dry and afterburner power wedges. It should be noted that  $C_{D,a}$  includes drag on the wedge surfaces. Also shown is the jet-on drag coefficient (at scheduled pressure ratio) for the dry power nozzle at  $M = 1.20$ . The determination of power-on drag coefficient is dependent upon known static-thrust characteristics. (See section entitled "Data Reduction Procedure.") These thrust characteristics were not determined to suffi-

## APPENDIX

ciently high nozzle pressure ratios for the afterburner nozzle because of air supply limitations.

The best agreement with the measured jet-off data is obtained with the dry power wedge or simulated jet plume mathematical models of the configuration. This agreement implies that the simulated jet plume model (used hereinafter for jet-off analysis) may represent the actual jet-off wake more closely than those models chosen for jet-off wake simulation since all the cases computed for wake impingement on the wedge had a much higher computed value for wave plus skin friction drag than the measured jet-off drag coefficients. Because the computed values are higher, the mathematical models for simulated jet-off wake are not considered in the remaining analysis.

Wave drag coefficients were computed for the remaining mathematical models with various combinations of tail surfaces, and these results are presented in figure 57. The appropriate skin friction drag coefficients from figure 24 are added to the computed wave drag values, and the incremental interference drag coefficient  $\Delta C_{p,int}$  is computed by the method outlined in the data reduction section. Since  $\Delta C_{p,int}$  is dependent on the amount of wave drag removed from the measured total drag coefficient (see section entitled "Data Reduction Procedure"), the sensitivity of  $\Delta C_{p,int}$  to the mathematical model used in the calculation is shown in figure 58. Typical results are shown for the configuration with twin vertical tails  $\delta_h = 0^\circ$  at jet-off conditions and at the scheduled nozzle pressure ratio of figure 16.

As can be seen in figure 58, the largest differences between computed values of the incremental interference drag coefficient (using the various mathematical models) occur at  $M = 1.20$ . Differences between  $\Delta C_{p,int}$  for the various mathematical models ( $M = 1.20$ ) range up to a factor of 5; the largest occurs between the jet plume model and the no-wedge mathematical model for the jet-on, dry power wedge case. These same values of  $\Delta C_{p,int}$  vary from 0.5 percent of ideal gross thrust (jet plume) to about 3 percent of ideal gross thrust (no wedge). Although the same large differences caused by different mathematical models occur at  $M = 2.20$ , the maximum value of  $\Delta C_{p,int}$  (for no-wedge, jet-on, dry power case) represents only 0.8 percent of ideal gross thrust at  $M = 2.20$ ; for the afterburner wedge, the values of  $\Delta C_{p,int}$ , both jet off and at the scheduled pressure ratio, were not sensitive to the mathematical model chosen (all values shown are about 1.5 percent ideal gross thrust).

Thus, some rationale together with intuitive engineering judgment must be applied when attempting to calculate wave drag for configurations which have two-dimensional wedge nozzles. For the jet-off condition, the simulated jet plume mathematical model was chosen since it yielded results comparable with measured jet-off drag and could possibly represent the actual flow conditions. The larger discrepancy between calculated and measured drag at  $M = 1.20$  (see fig. 56) is probably caused when the equivalent body of the configuration departs from slender body definitions. This departure would affect the calculated wave drag more at  $M = 1.20$  than at  $M = 2.20$  (ref. 19).

For jet-on conditions, a comparison of the scheduled pressure ratio with the nozzle design pressure ratio (fig. 16) indicates to some extent the differences in jet plume shape. The design nozzle pressure ratios for the nozzle with

## APPENDIX

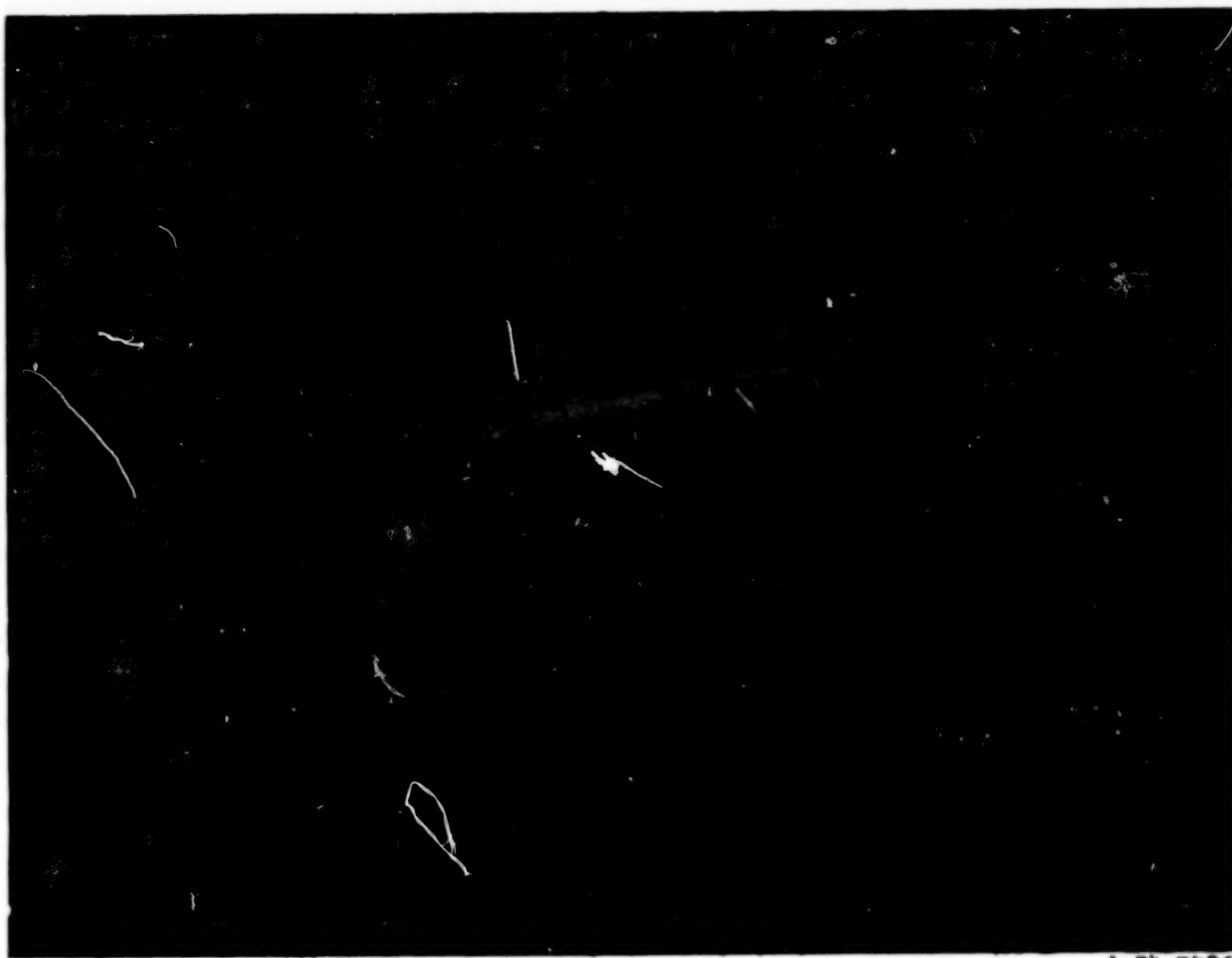
the dry power ( $A_e/A_t = 1.287$ ) and afterburner power ( $A_e/A_t = 1.393$ ) wedges are 4.6 and 5.4, respectively. Since at  $M = 1.20$ , the scheduled pressure ratio is 5.9, the nozzle with both power settings is slightly underexpanded, and both plumes diverge slightly at this Mach number. However, the difference between the scheduled and the two design pressure ratios is such that the plume shapes are very nearly the same. At  $M = 2.20$ , the nozzle is underexpanded for both power settings. However, at this Mach number, the values of  $\Delta C_{p,int}$  are nearly the same regardless of the mathematical model chosen; such similarity indicates that jet plume shape has little effect at this Mach number. Since the tail interference results at subsonic speeds indicate little or no effect of power, primarily because of the cleaner nozzle installation (fig. 30), it is further assumed that similar results would be attained at supersonic speeds which are indicated at  $M = 2.20$ . Therefore, this assumption permits wave drag at jet-on conditions to be computed by using the no-wedge model; these results are then used for further analysis.

# REFERENCES

1. Runckel, Jack F.: Interference Between Exhaust System and Afterbody of Twin-Engine Fuselage Configurations. NASA TN D-7525, 1974.
2. Berrier, Bobby L.: Effect of Nonlifting Empennage Surfaces on Single-Engine Afterbody/Nozzle Drag at Mach Numbers From 0.5 to 2.2. NASA TN D-8326, 1977.
3. Mercer, Charles E.; and Berrier, Bobby L.: Effect of Afterbody Shape, Nozzle Type, and Engine Lateral Spacing on the Installed Performance of a Twin-Jet Afterbody Model. NASA TM X-1855, 1969.
4. Capone, Francis J.: Supercirculation Effects Induced by Vectoring a Partial-Span Rectangular Jet. J. Aircraft, vol. 12, no. 8, Aug. 1975, pp. 633-638.
5. Linderman, D. L.; and Mount, J. S.: Development of an In-Flight Thrust Reverser for Tactical/Attack Aircraft. AIAA Paper No. 70-699, June 1970.
6. Maiden, Donald L.: Performance of an Isolated Two-Dimensional Variable-Geometry Wedge Nozzle With Translating Shroud and Collapsing Wedge at Speeds Up to Mach 2.01. NASA TN D-7906, 1975.
7. Maiden, Donald L.: Performance of an Isolated Two-Dimensional Wedge Nozzle With Fixed Cowl and Variable Wedge Centerbody at Mach Numbers Up to 2.01. NASA TN D-8218, 1976.
8. Maiden, Donald L.; and Petit, John E.: Investigation of Two-Dimensional Wedge Exhaust Nozzles for Advanced Aircraft. J. Aircraft, vol. 13, no. 10, Oct. 1976, pp. 809-816.
9. Capone, Francis J.: Summary of Propulsive-Lift Research in the Langley 16-Ft Transonic Tunnel. J. Aircraft, vol. 13, no. 10, Oct. 1976, pp. 803-808.
10. Capone, Francis J.: The Effects on Propulsion-Induced Aerodynamic Forces of Vectoring a Partial-Span Rectangular Jet at Mach Numbers From 0.40 to 1.20. NASA TN D-8039, 1975.
11. Goetz, Gerald F.; Young, John H.; and Paloza, J. Lawrence: A Two-Dimensional Airframe Integrated Nozzle Design With Inflight Thrust Vectoring and Reversing Capabilities for Advanced Fighter Aircraft. AIAA Paper No. 76-626, July 1976.
12. Goetz, G. F.; and Petit, J. E.: Integrated Nozzle Development Program, Transition Study Test Report. No. D180-15443 (Contract No. N00140-73-C-0027), Boeing Co.
13. Corson, Blake W., Jr.; Runckel, Jack F.; and Jgoe, William B.: Calibration of the Langley 16-Foot Transonic Tunnel With Test Section Air Removal. NASA TR R-423, 1974.

14. Schaefer, William T., Jr.: Characteristics of Major Active Wind Tunnels at the Langley Research Center. NASA TM X-1130, 1965.
15. Reubush, David E.; and Runckel, Jack F.: Effect of Fineness Ratio on the Boattail Drag of Circular-Arc Afterbodies Having Closure Ratios of 0.50 With Jet Exhaust at Mach Numbers up to 1.30. NASA TN D-7192, 1973.
16. Braslow, Albert L.; and Knox, Eugene C.: Simplified Method for Determination of Critical Height of Distributed Roughness Particles for Boundary-Layer Transition at Mach Numbers From 0 to 5. NACA TN 4363, 1958.
17. Braslow, Albert L.; Hicks, Raymond M.; and Harris, Roy V., Jr.: Use of Grit-Type Boundary-Layer-Transition Trips on Wind-Tunnel Models. NASA TN D-3579, 1966.
18. Peterson, John B., Jr.: A Comparison of Experimental and Theoretical Results for the Compressible Turbulent-Boundary-Layer Skin Friction With Zero Pressure Gradient. NASA TN D-1795, 1963.
19. Harris, Roy V., Jr.: An Analysis and Correlation of Aircraft Wave Drag. NASA TM X-947, 1964.
20. Reubush, David E.: Effects of Fineness and Closure Ratios on Boattail Drag of Circular-Arc Afterbody Models With Jet Exhaust at Mach Numbers up to 1.30. NASA TN D-7163, 1973.
21. Maiden, Donald L.; and Mercer, Charles E.: Performance Characteristics of a Single-Engine Fighter Model Fitted With an In-Flight Thrust Reverser. NASA TN D-6460, 1971.
22. Mercer, Charles E.; and Maiden, Donald L.: Effects of an In-Flight Thrust Reverser on the Stability and Control Characteristics of a Single-Engine Fighter Airplane Model. NASA TN D-6886, 1972.
23. Petit, John E.; and Scholey, Michael B.: Thrust Reverser and Thrust Vectoring Literature Review. Tech. Rep. AFAPL-TR-73-11, U.S. Air Force, Apr. 1972. (Available from DDC as AD 749 476.)
24. Hiley, P. E.; Wallace, H. W.; and Booz, D. E.: Nonaxisymmetric Nozzles Installed in Advanced Fighter Aircraft. J. Aircraft, vol. 13, no. 12, Dec. 1976, pp. 1000-1006.
25. Craidon, Charlotte B.: Description of a Digital Computer Program for Airplane Configuration Plots. NASA TM X-2074, 1970.





L-74-7486

Figure 1.- Photograph showing installation of model in the Langley 16-foot transonic tunnel.



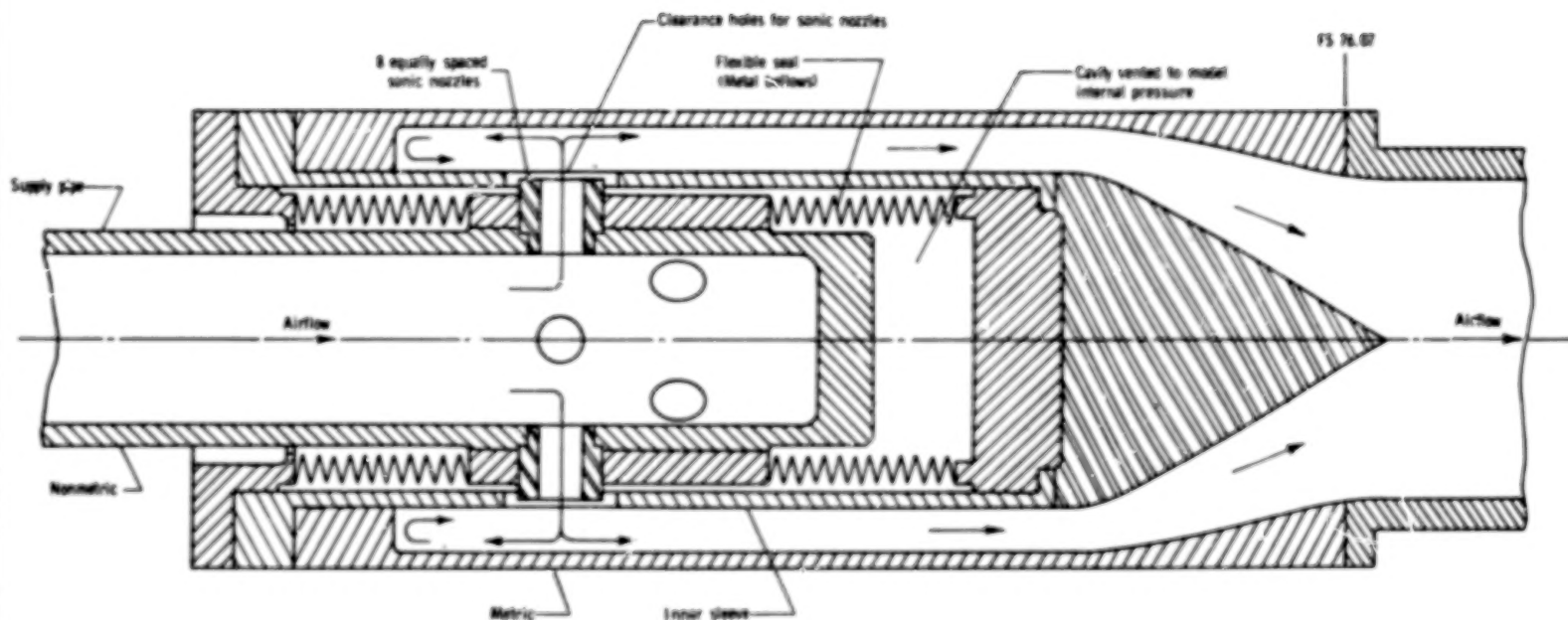
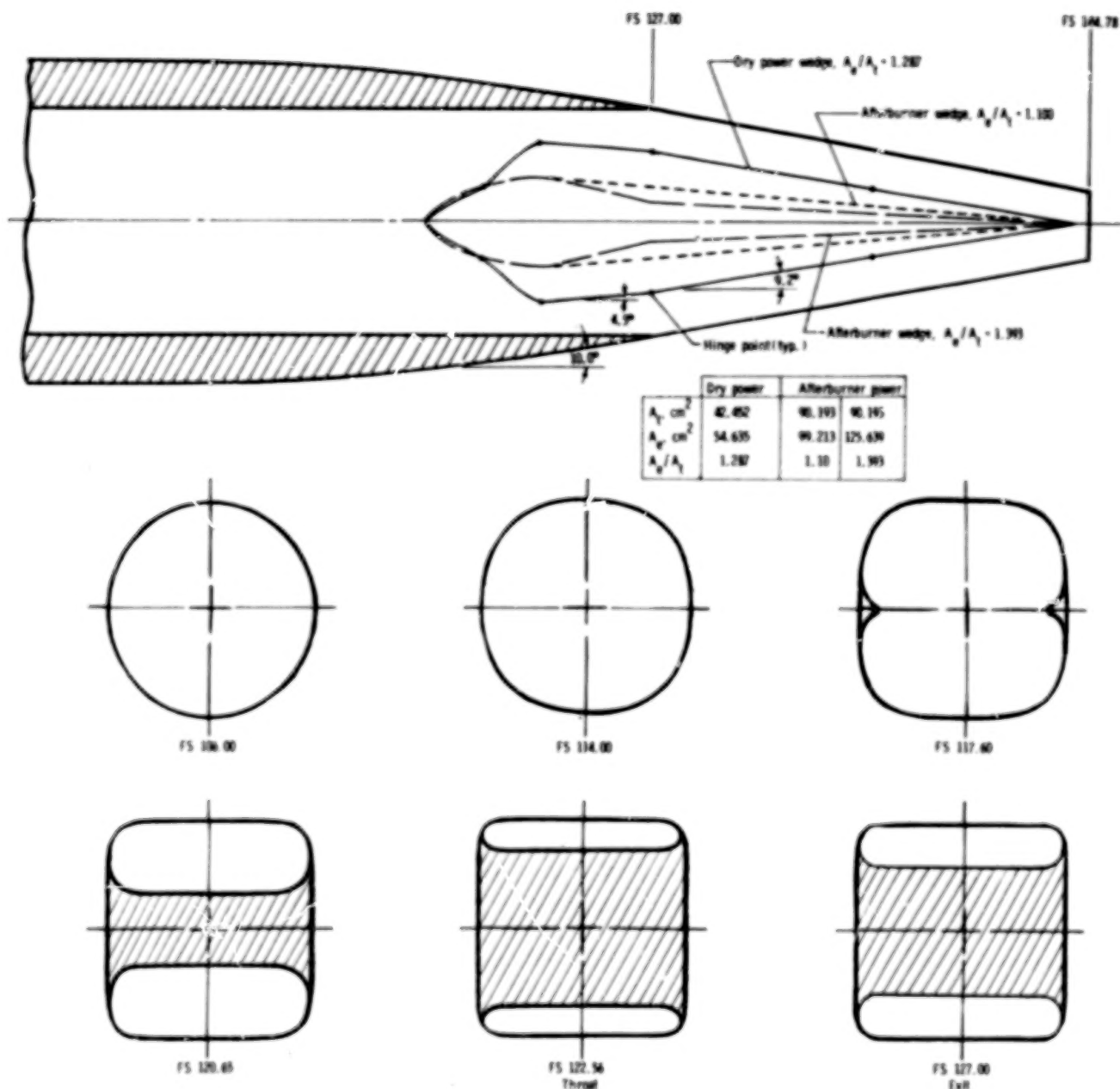
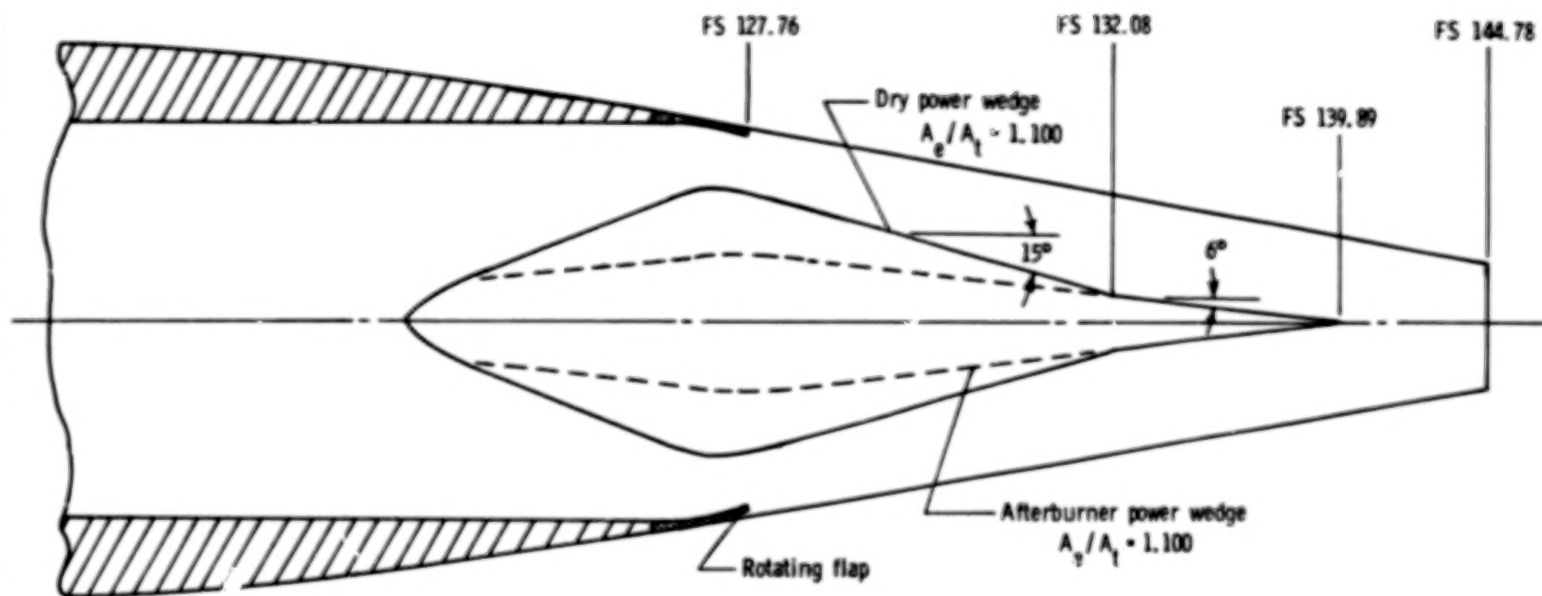


Figure 3.- Details of bellows arrangement used to transfer air from nonmetric to metric portions of model.



(a) Basic nozzle. Sections are shown for dry power wedge only.

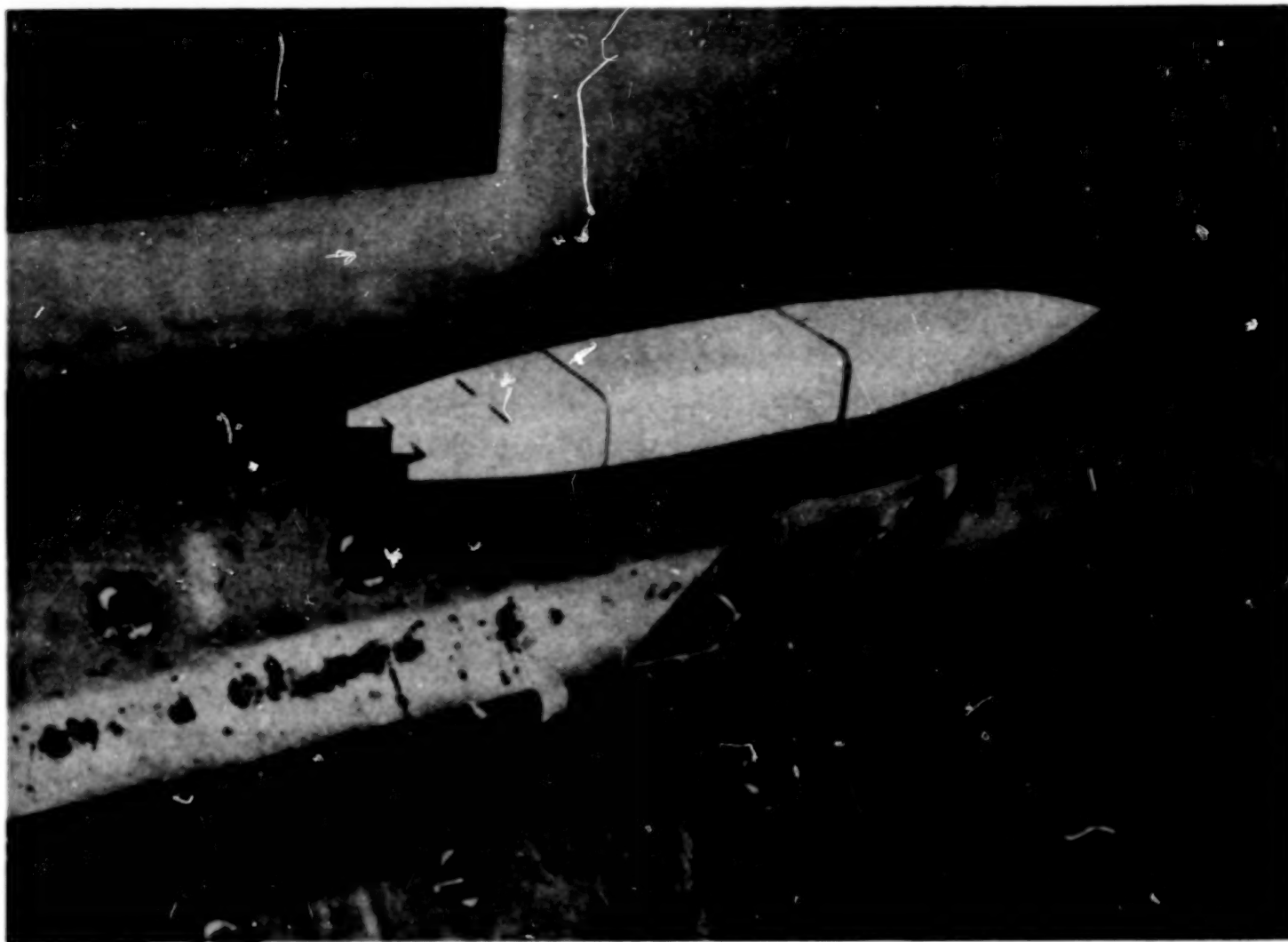
Figure 4.- Nozzle details. All dimensions are in centimeters unless otherwise noted.



(b) Alternate nozzle concept.

Figure 4.- Continued.

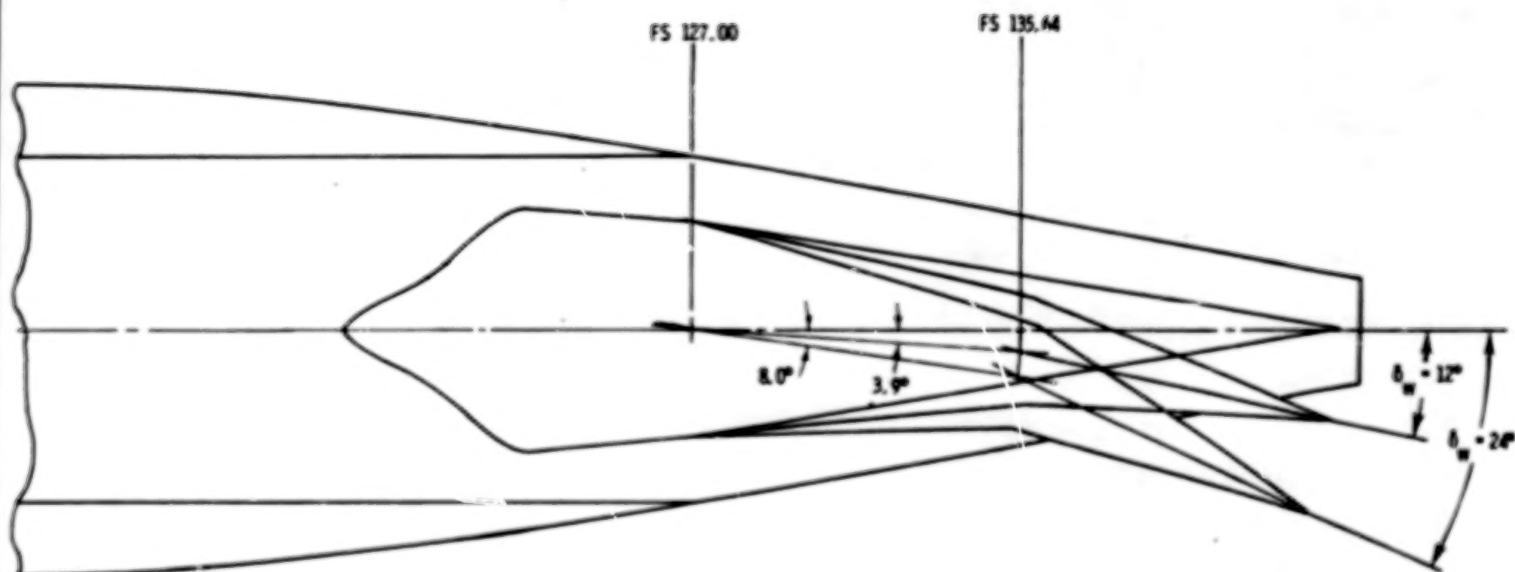




L-74-7476

(c) Photograph of alternate nozzle, dry power wedge.

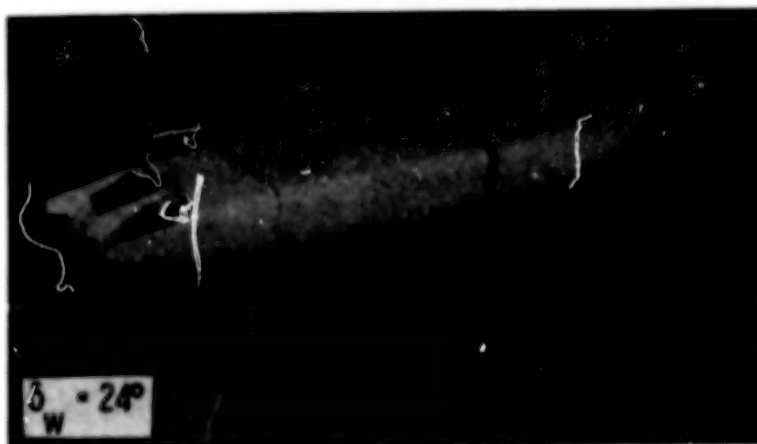
Figure 4.- Concluded.



(a) Vectoring modes.

Figure 5.- Details of dry power nozzles showing vectoring or reversing modes.  
All dimensions are in centimeters unless otherwise noted.

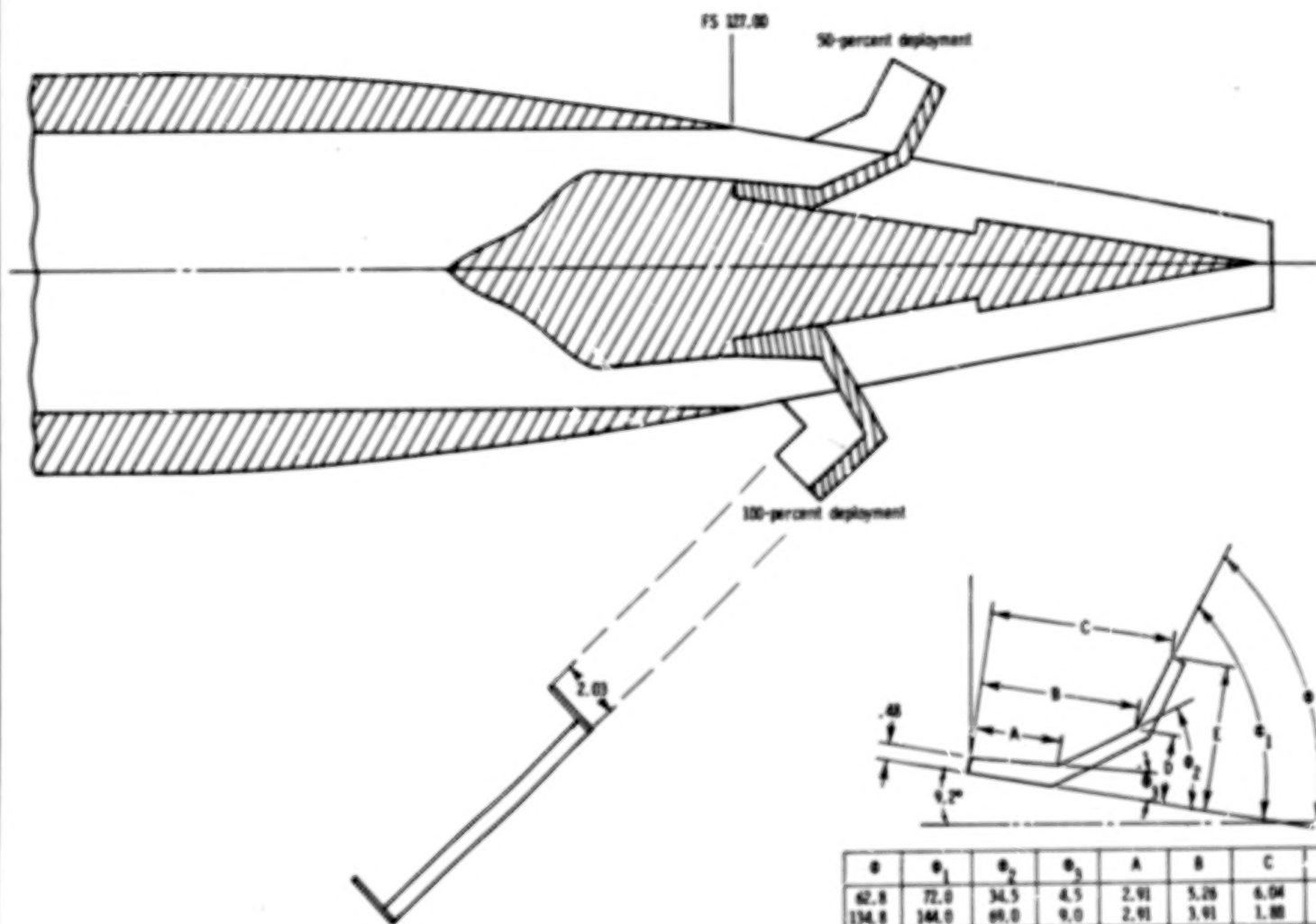
36



L-77-202

(b) Vectoring modes.

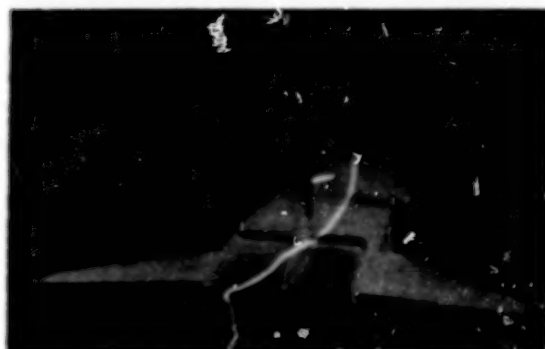
Figure 5.- Continued.



(c) Schematic of reversing modes.

Figure 5.- Continued.

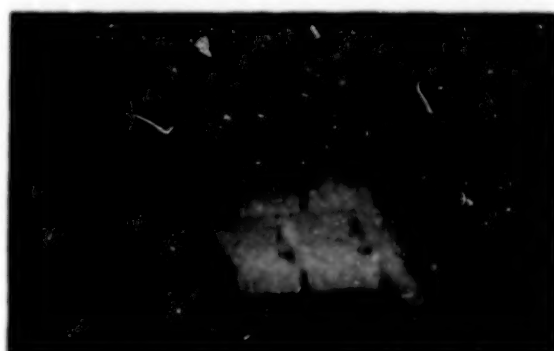




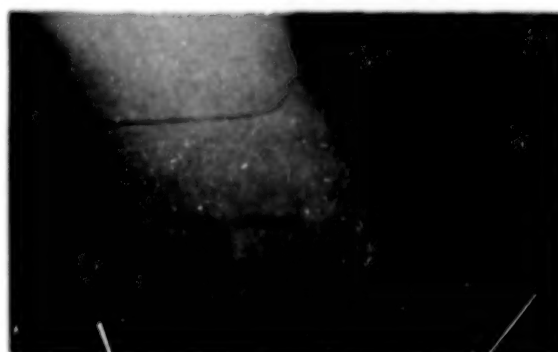
$\phi = 0^\circ$



$\phi = 62.8^\circ$



$\phi = 134.8^\circ$

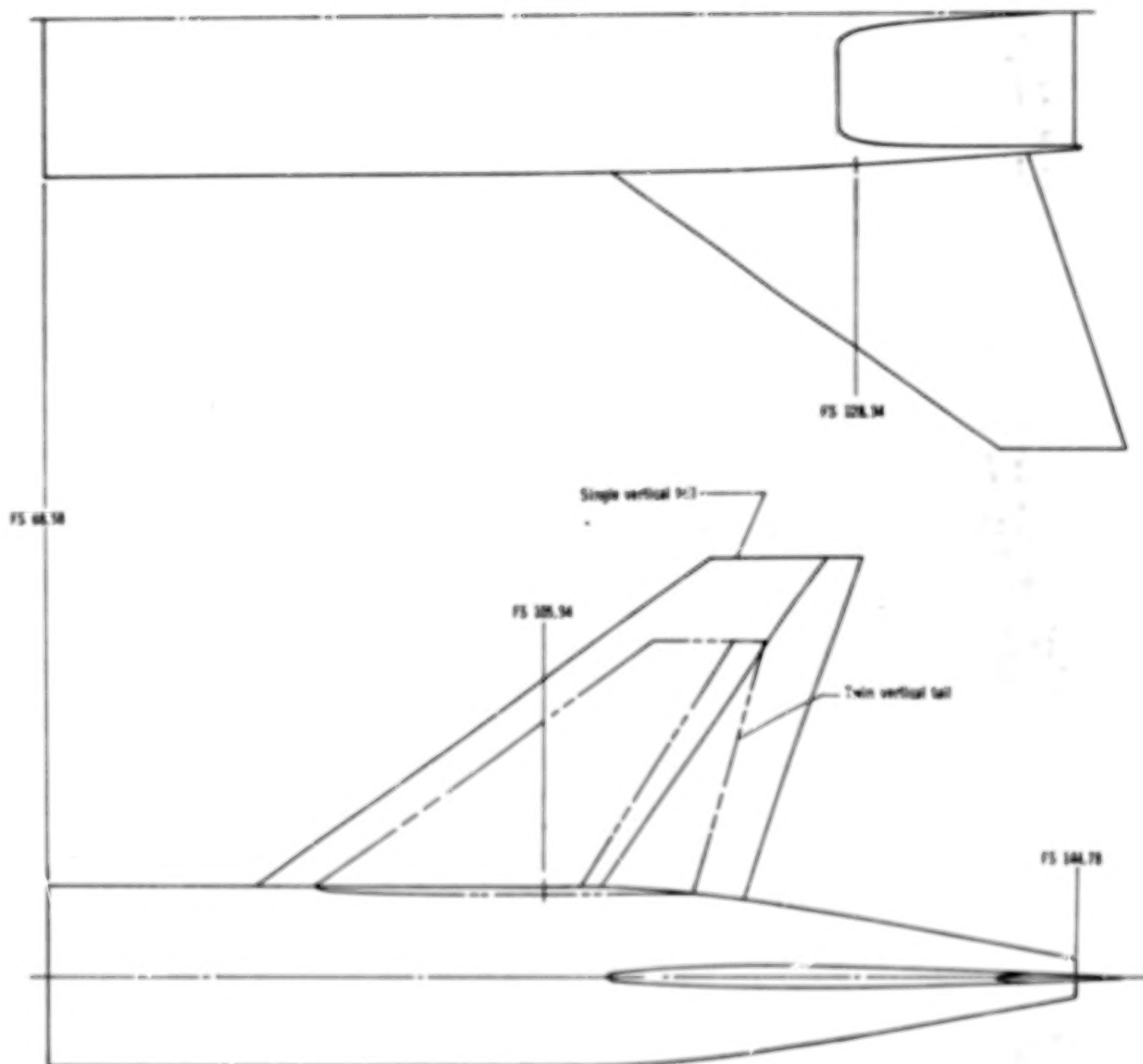


$\phi = 62.8^\circ$

L-77-203

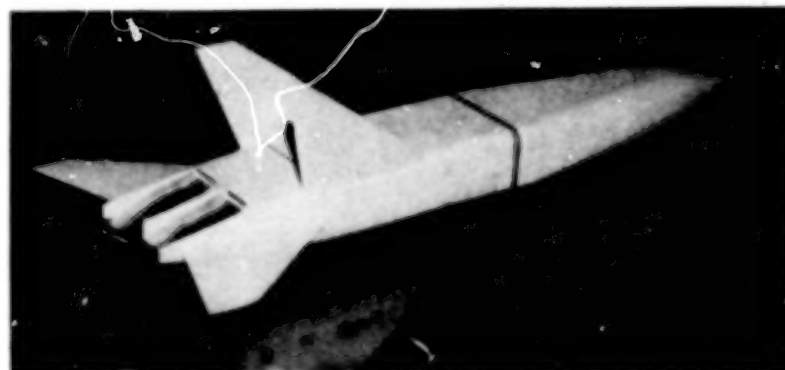
(d) Photographs of reversing modes.

Figure 5.- Concluded.



(a) Installation.

Figure 6.- Installation and reference planforms of tail surfaces. All dimensions are in centimeters unless otherwise noted.



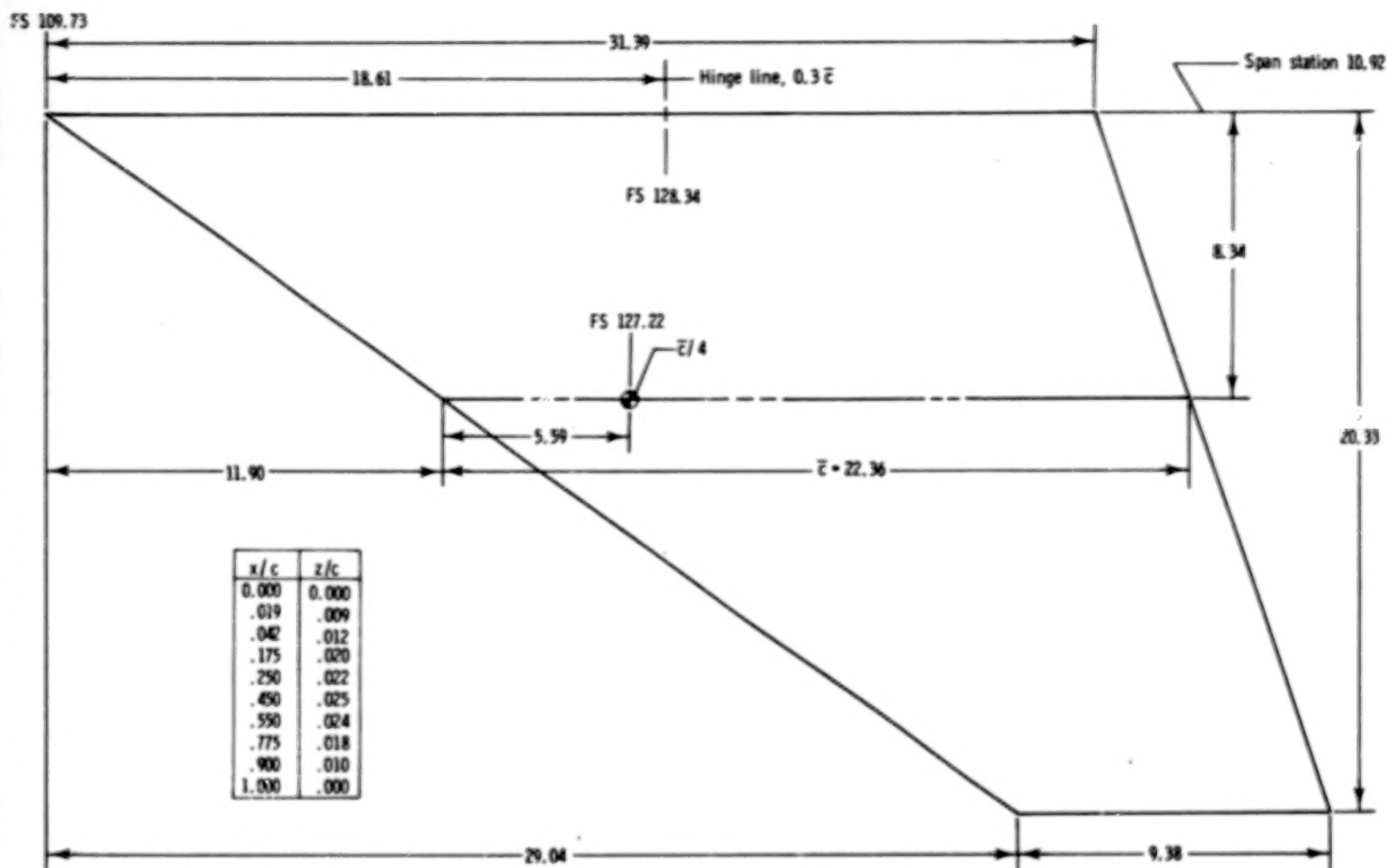
$\delta_w = 0^\circ$

$\delta_w = 12^\circ$

L-77-204

(b) Photographs showing various tail installations.

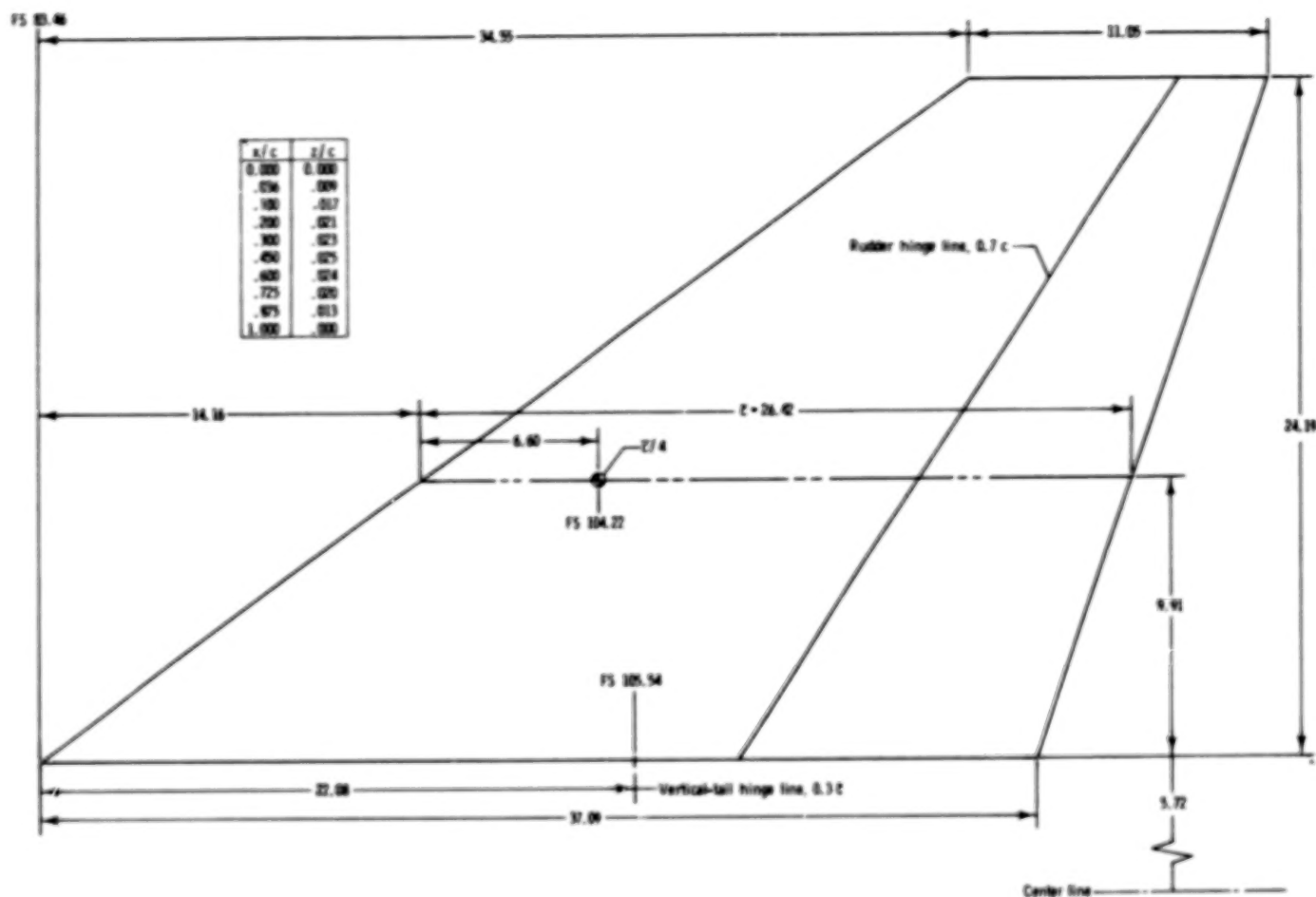
Figure 6.- Concluded.



(a) Horizontal tail, reference planform.

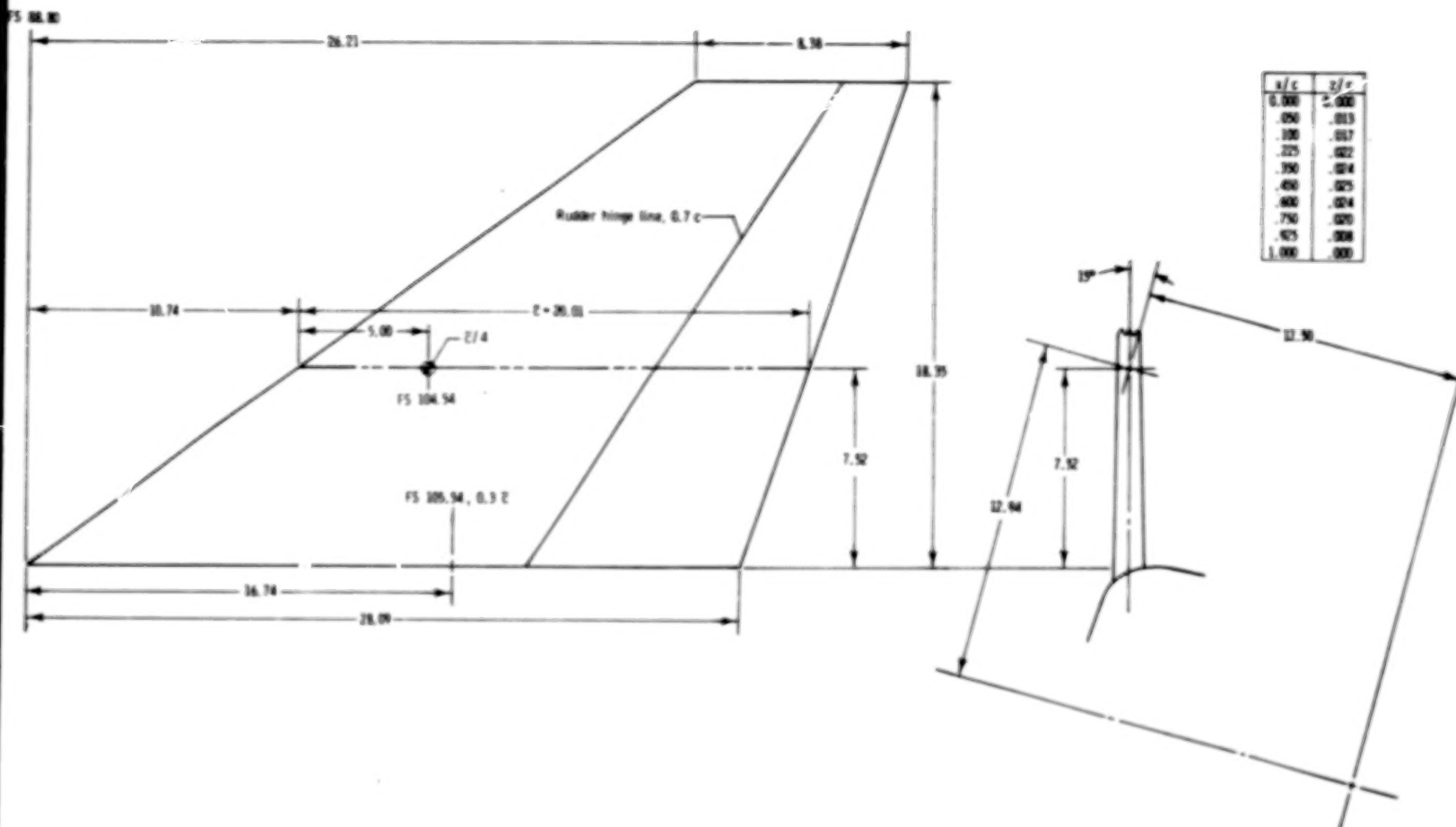
Figure 7.- Geometrical characteristics of tail surfaces. All dimensions are in centimeters unless otherwise noted.





(b) Single vertical tail, reference planform.

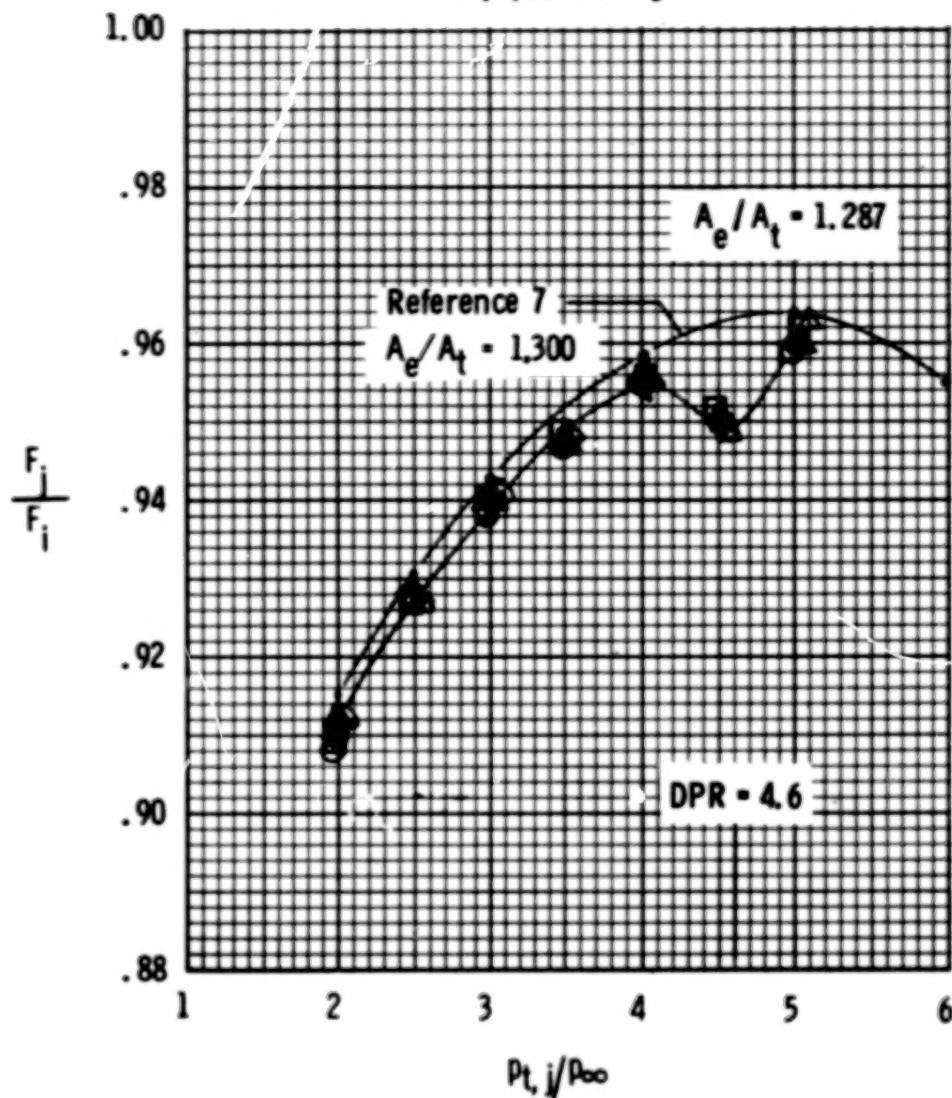
Figure 7.- Continued.



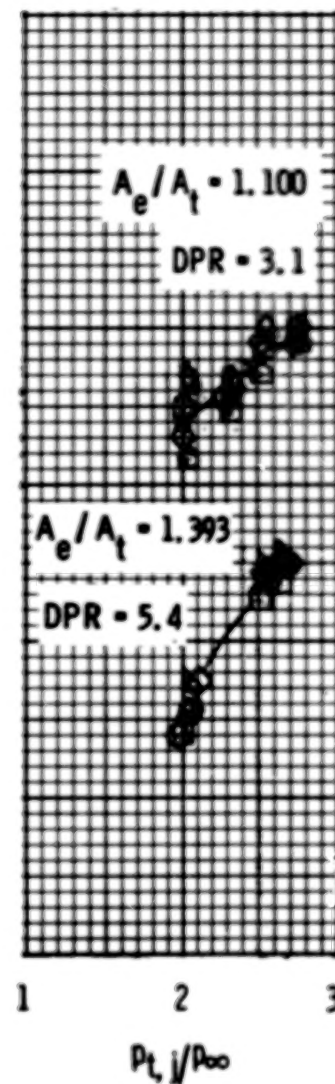
(c) Twin vertical tail, reference planform.

Figure 7.- Concluded.

Dry power wedge



Afterburner power wedge

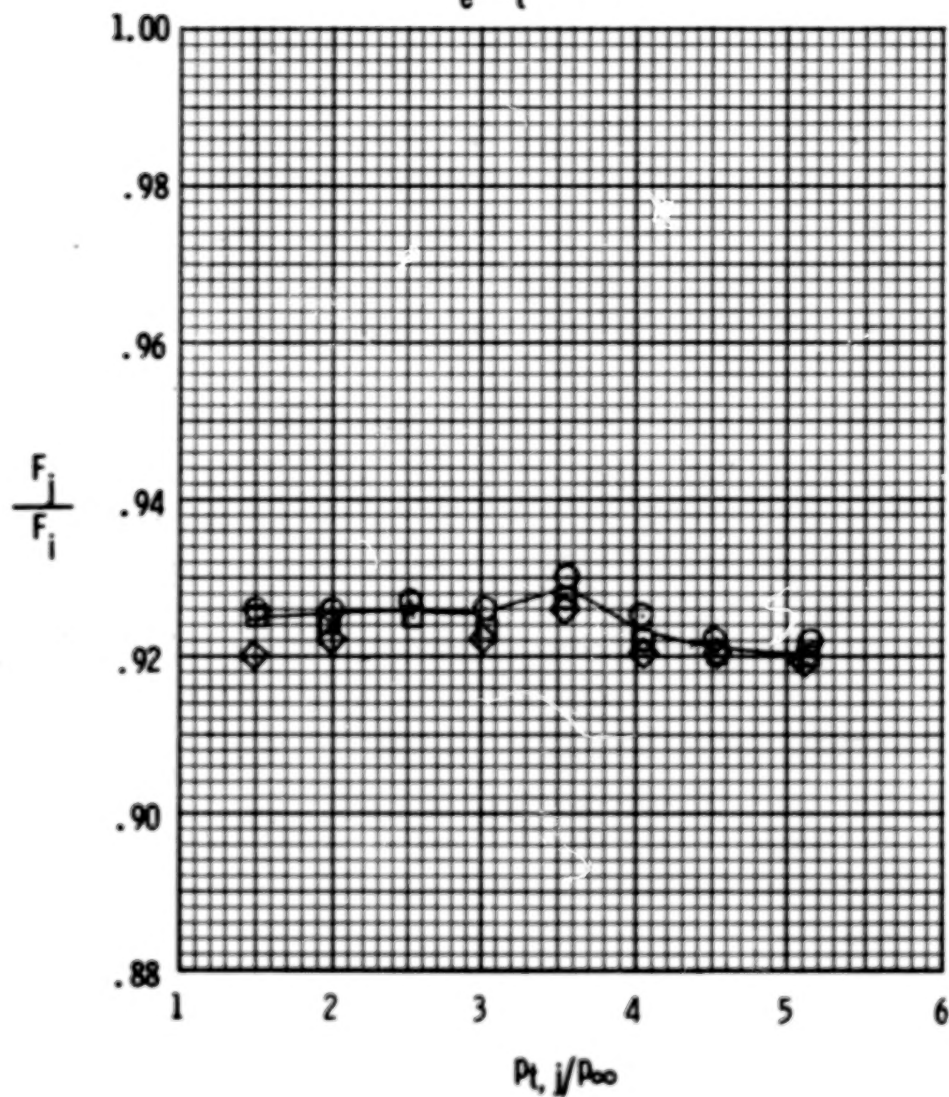


(a) Basic nozzle, Langley 16-foot transonic tunnel.

Figure 8.- Static performance characteristics of basic and alternate two-dimensional wedge nozzle configurations. Symbols represent several static runs.

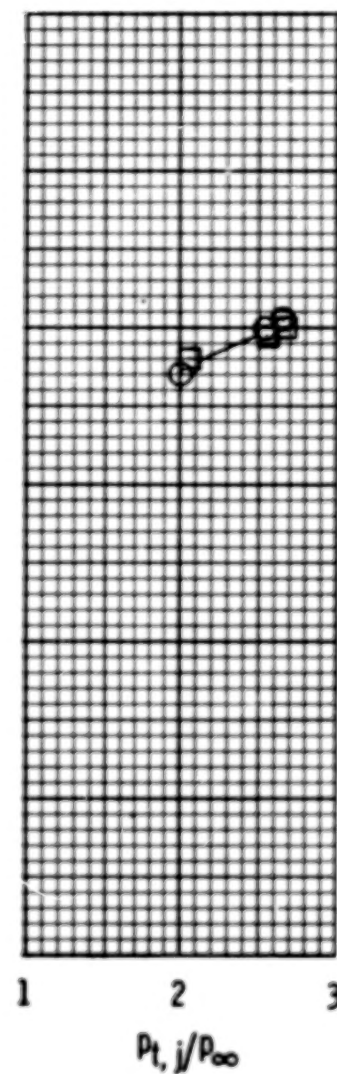
Dry power wedge

$$A_e / A_t = 1.100$$



Afterburner power wedge

$$A_e / A_t = 1.100$$



(b) Alternate nozzle.

Figure 8.- Concluded.

46.

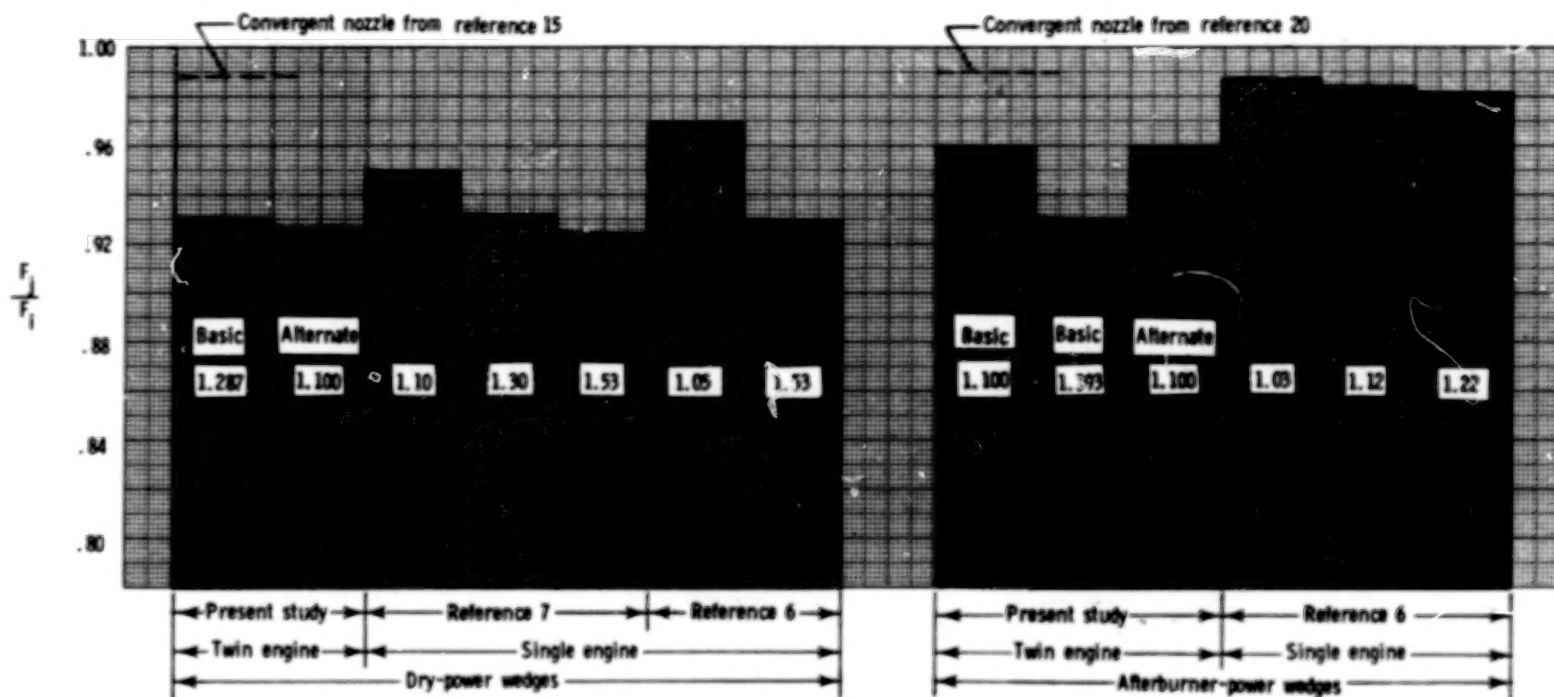
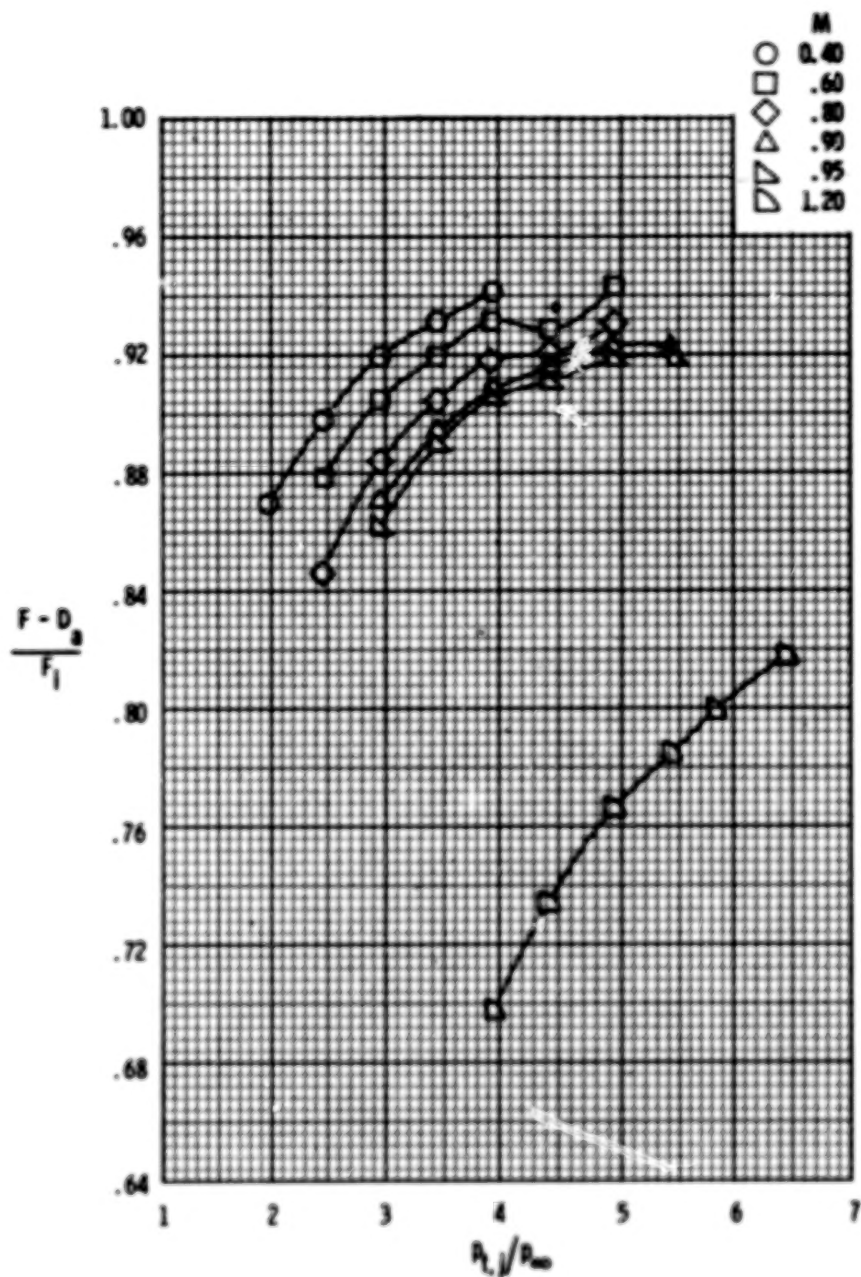


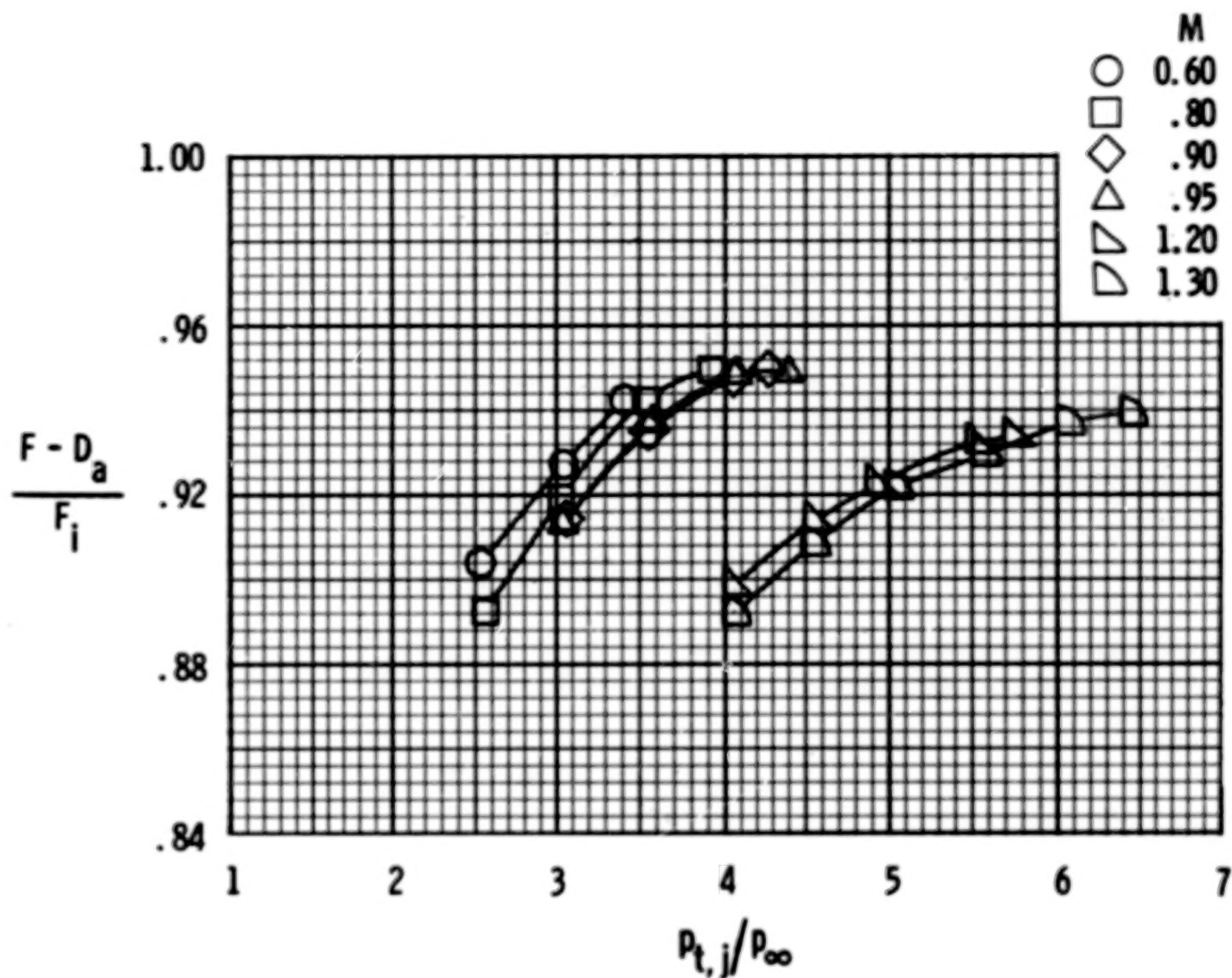
Figure 9.- Comparison of twin- and single-engine two-dimensional wedge nozzle static takeoff performance. Nozzle exit-area expansion ratio indicated on each data bar.  $P_{t,j}/P_{\infty} = 2.6$ .



(a) Dry power nozzle.

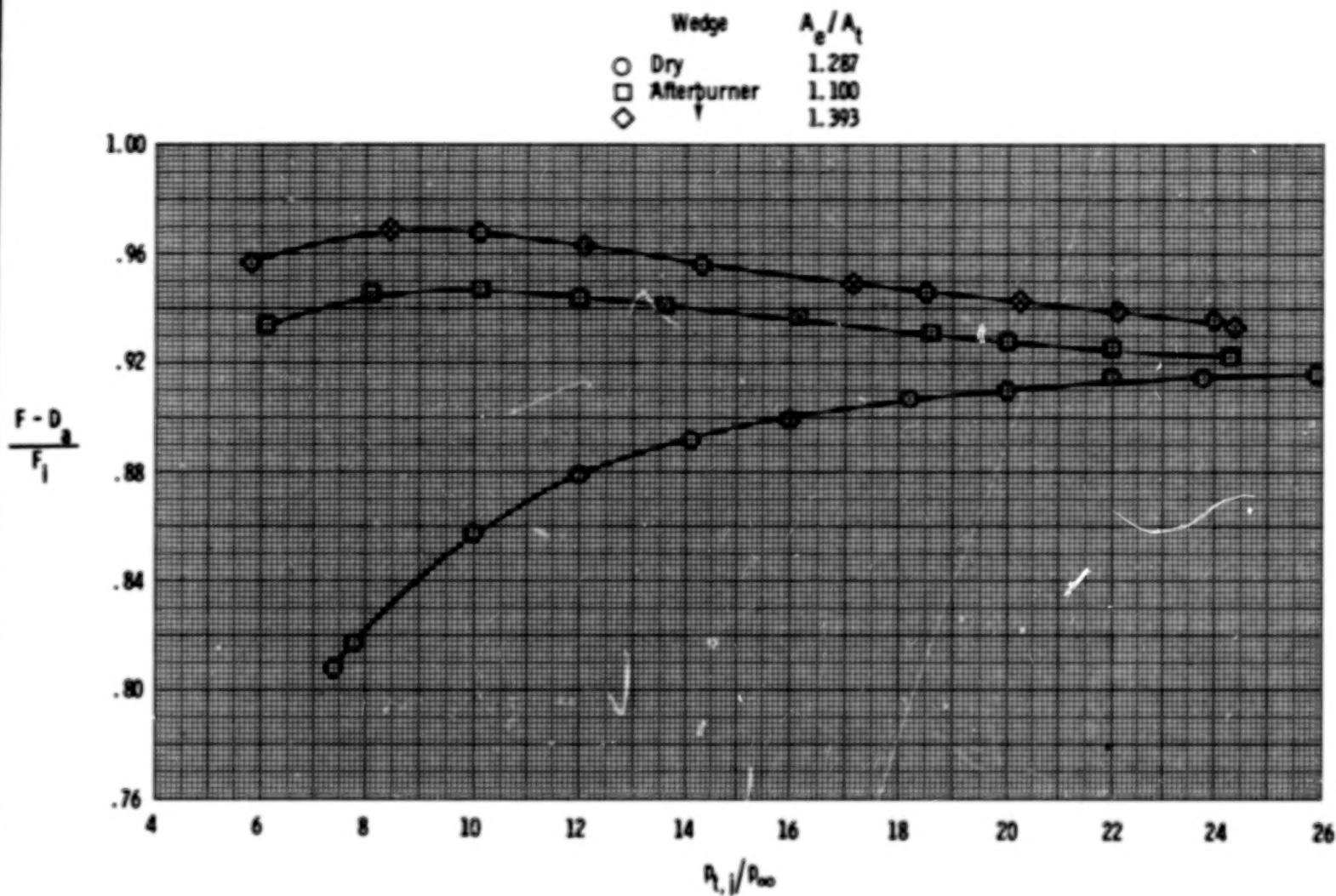
Figure 10.- Variation of aeropropulsion performance with nozzle pressure ratio for basic nozzle. Tails off.





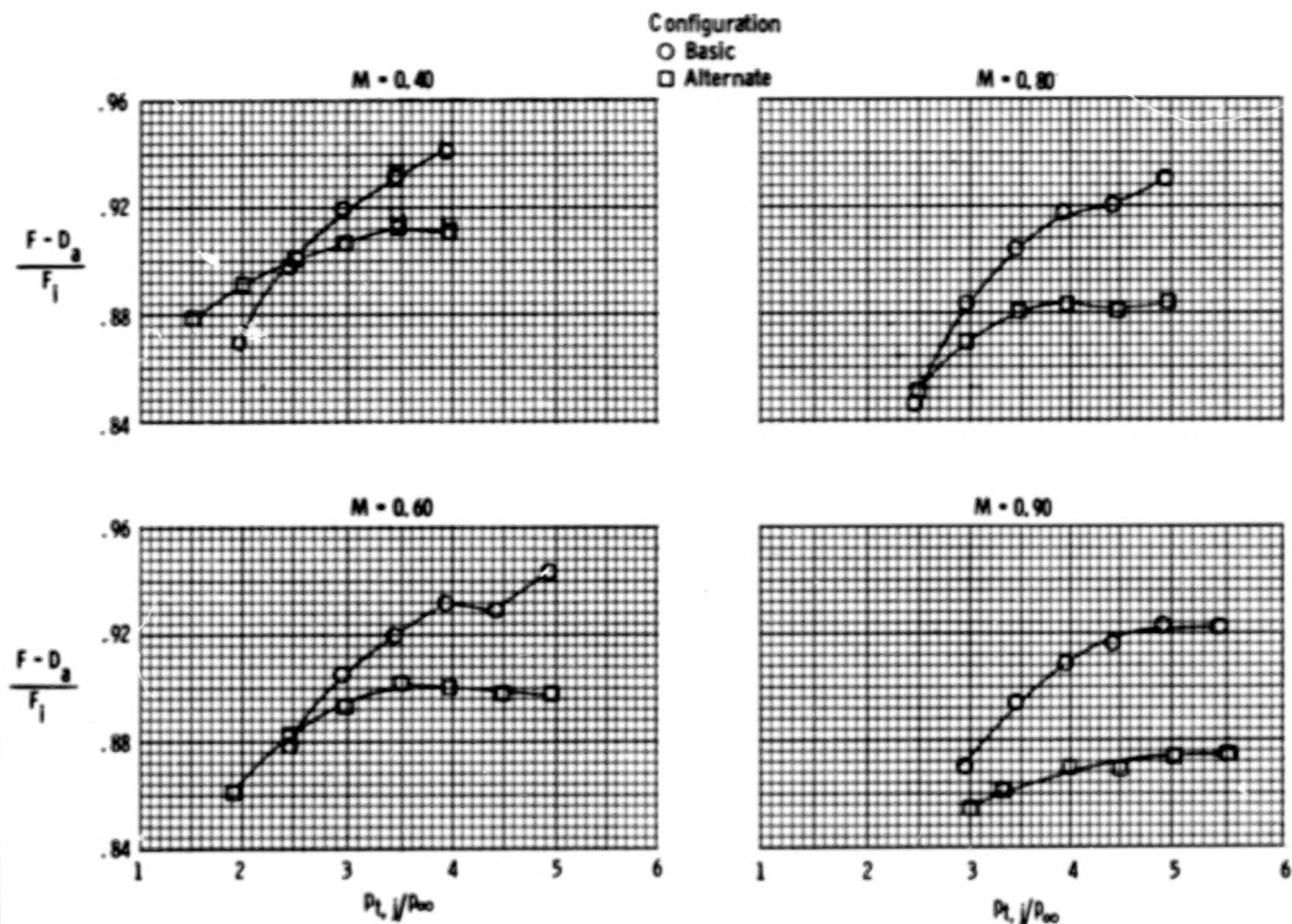
(b) Afterburner power nozzle.

Figure 10.- Continued.



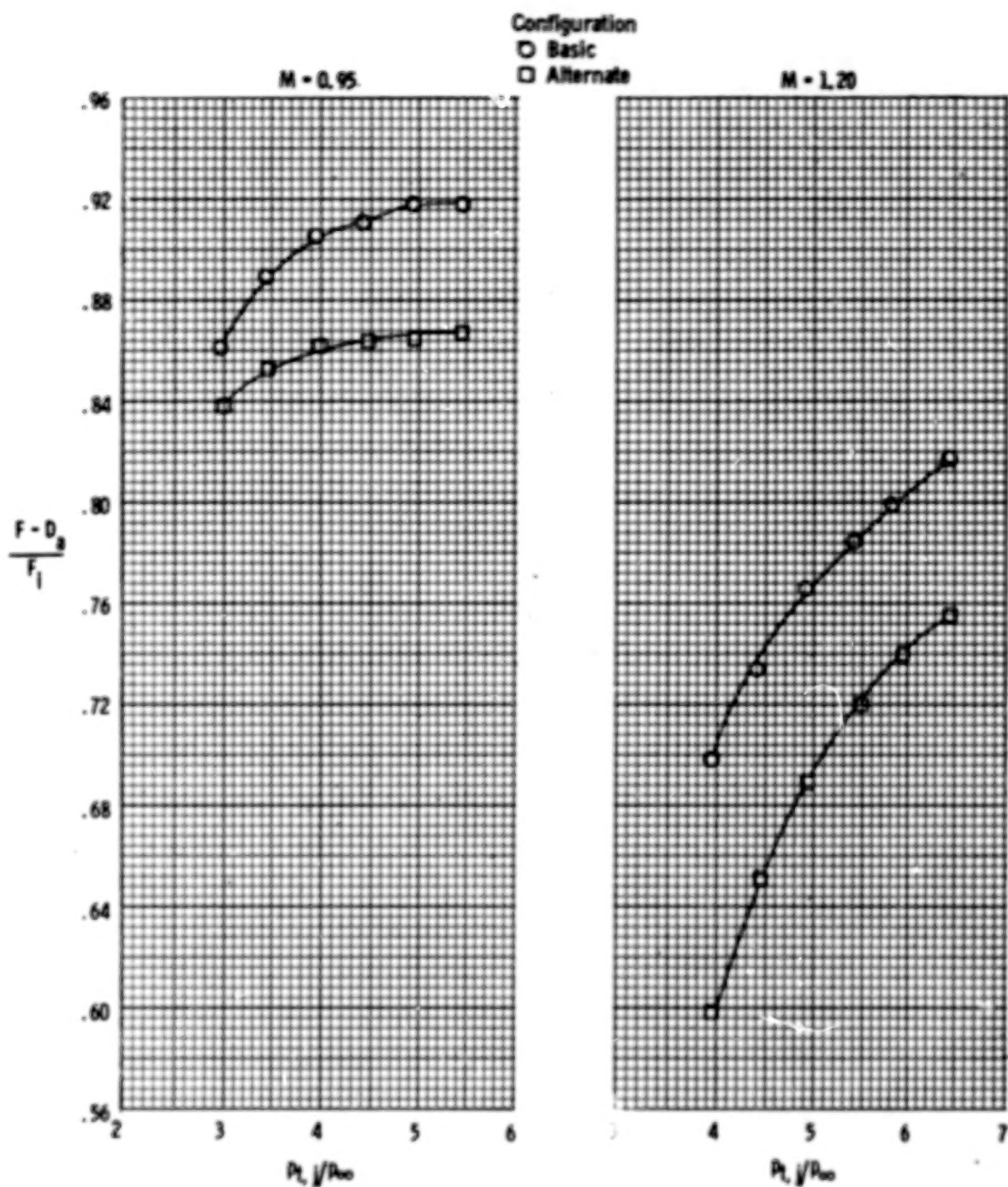
(c)  $M = 2.20$ .

Figure 10.- Concluded.

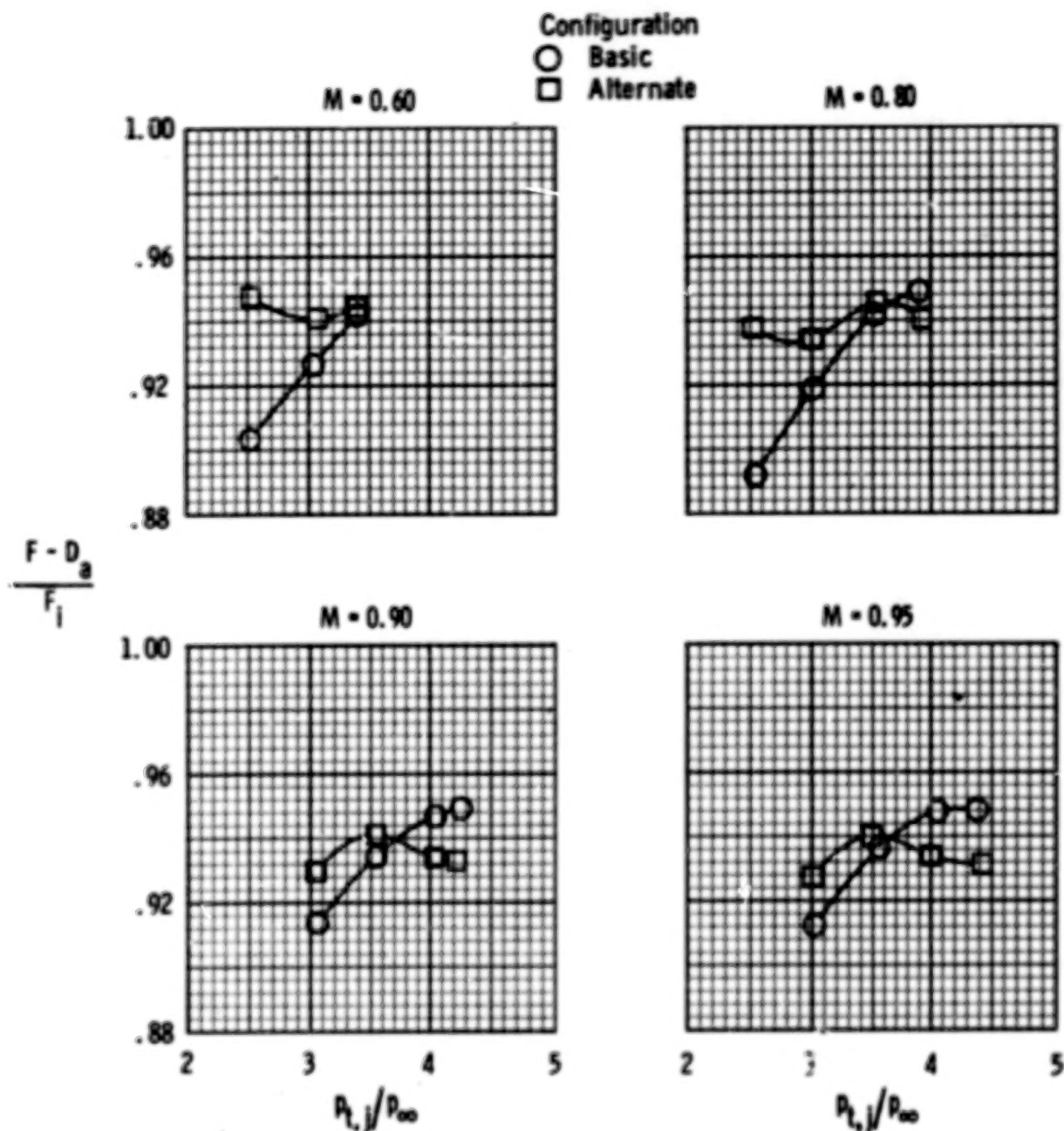


(a)  $M = 0.40$  to  $0.90$ .

Figure 11.- Comparison of aeropropulsion performance of alternate nozzle configuration with basic dry power nozzle. Tails off.



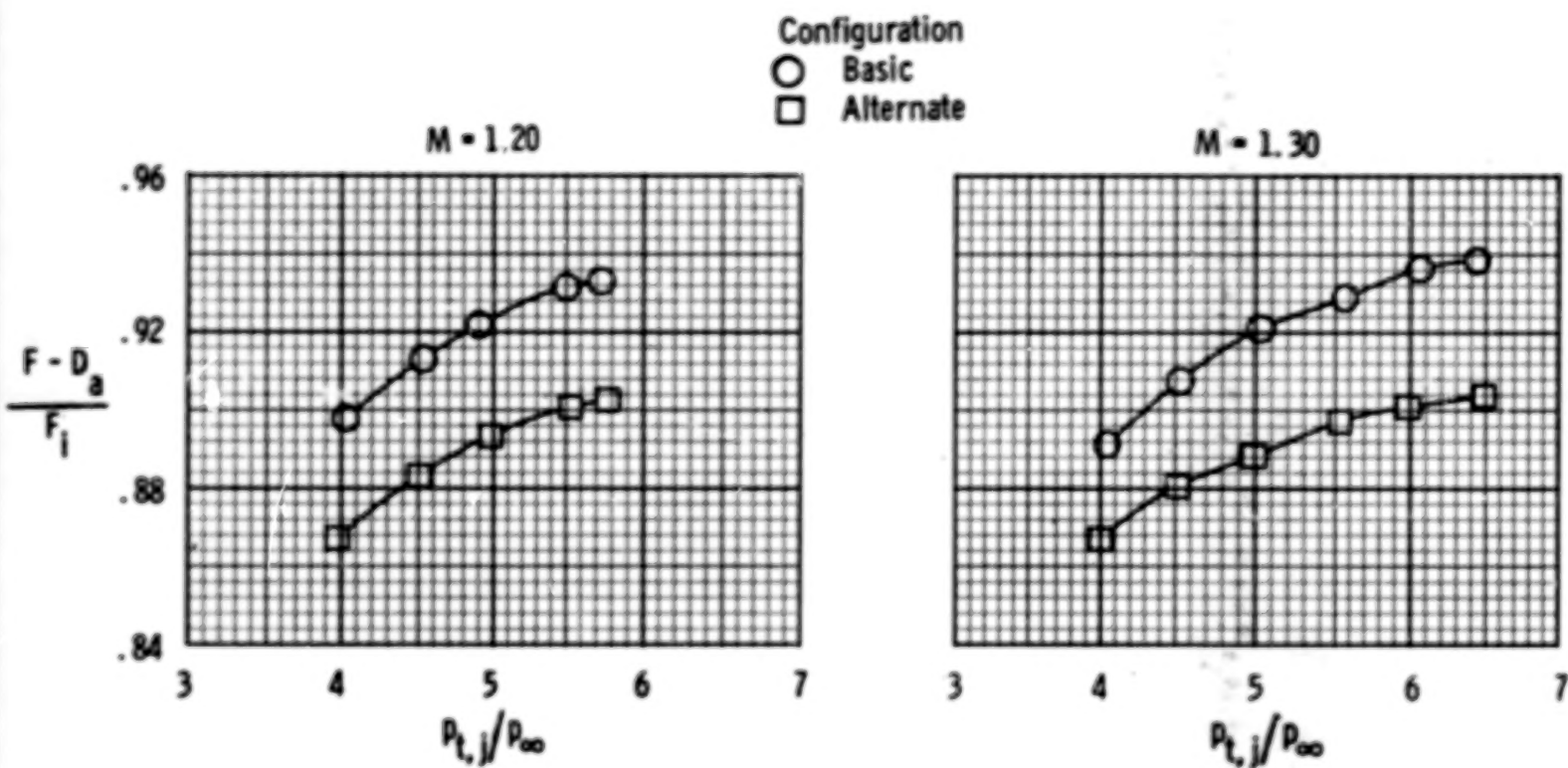
(b)  $M = 0.95$  and  $1.20$ .



(a)  $M = 0.60, 0.80, 0.90,$  and  $0.95$ .

Figure 12.- Comparison of aeropropulsion performance of alternate nozzle configuration with basic afterburner power nozzle. Tails off.





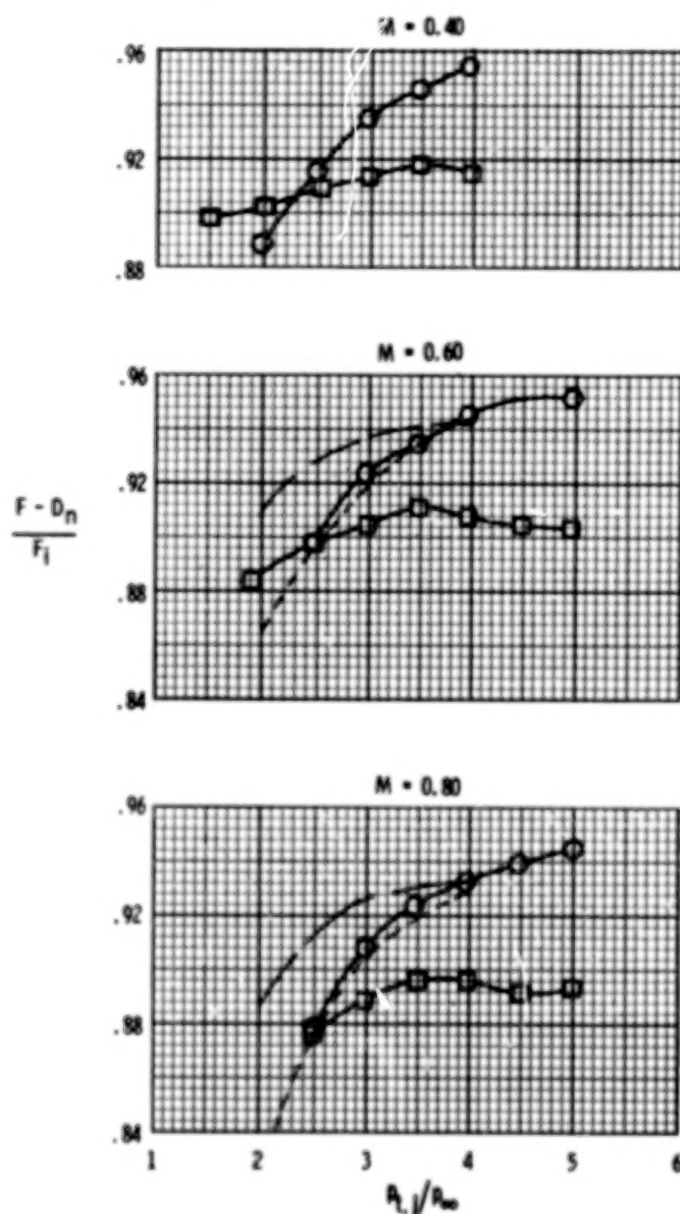
(b)  $M = 1.20$  and  $1.30$ .

Figure 12.- Concluded.

54.



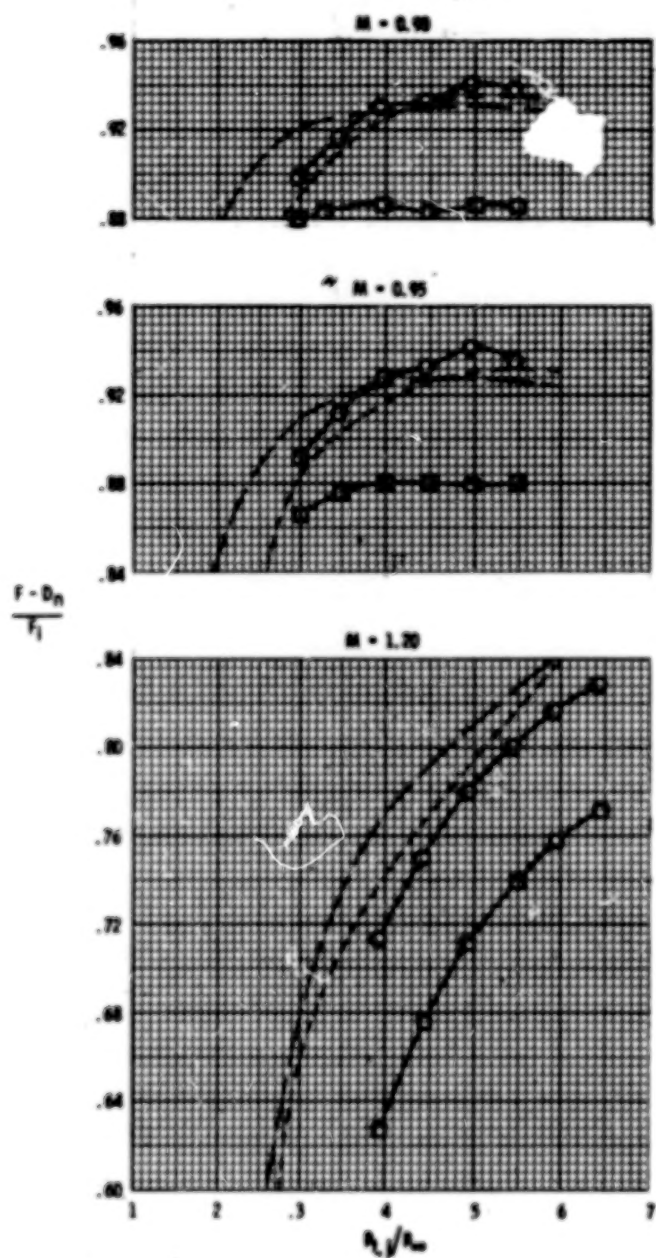
Model	Reference	$A_0/A_t$
○ Twin	Present study	1.287-Basic
□ Twin	Present study	1.100-Alternate
— Single	Reference 7	1.10
- - - Single	Reference 7	1.30



(a)  $M = 0.40, 0.60, \text{ and } 0.80$  at  $\alpha = 0^\circ$ .

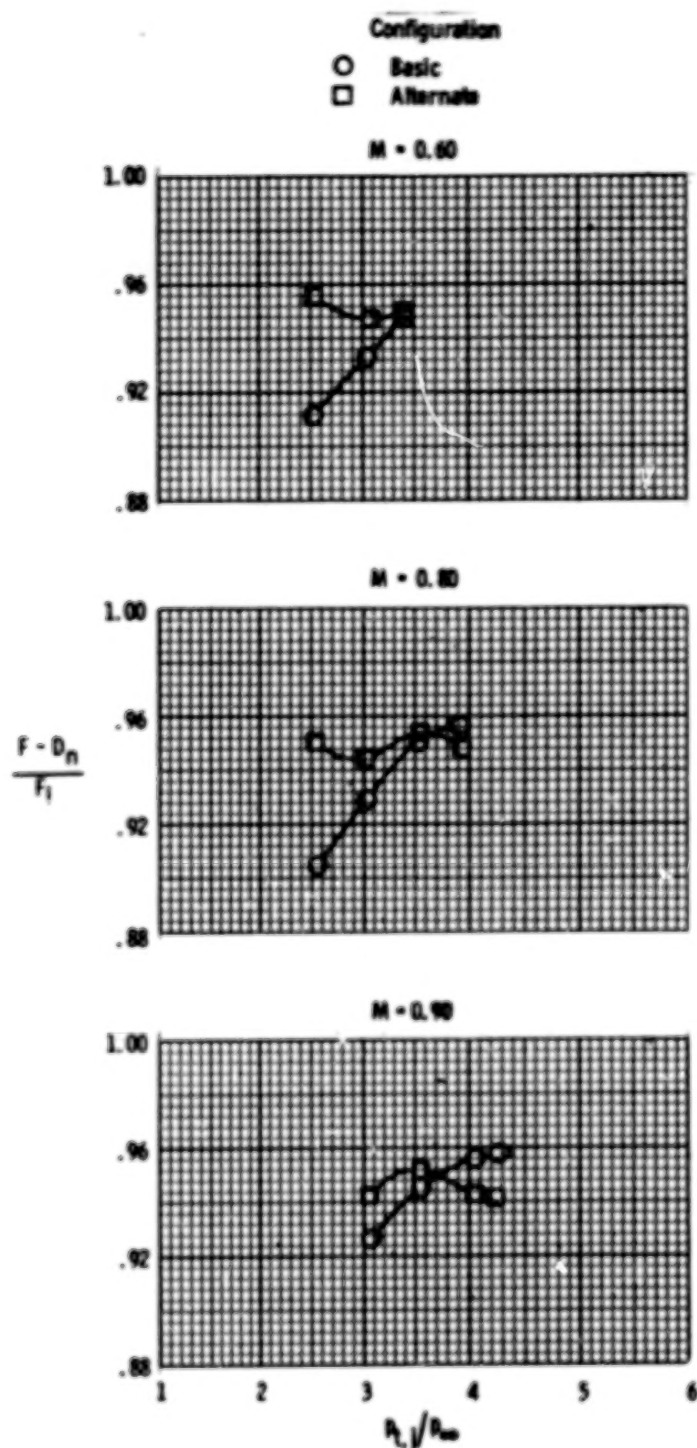
Figure 13.- Comparison of aeropropulsion performance of basic and alternate nozzles at dry power settings.

Model	Reference	$A_0/A_1$
○ Test	Present study	1.20-Basic
□ Test	Present study	1.20-Alternate
— Single	Reference 7	1.20
- - - Single	Reference 7	1.20



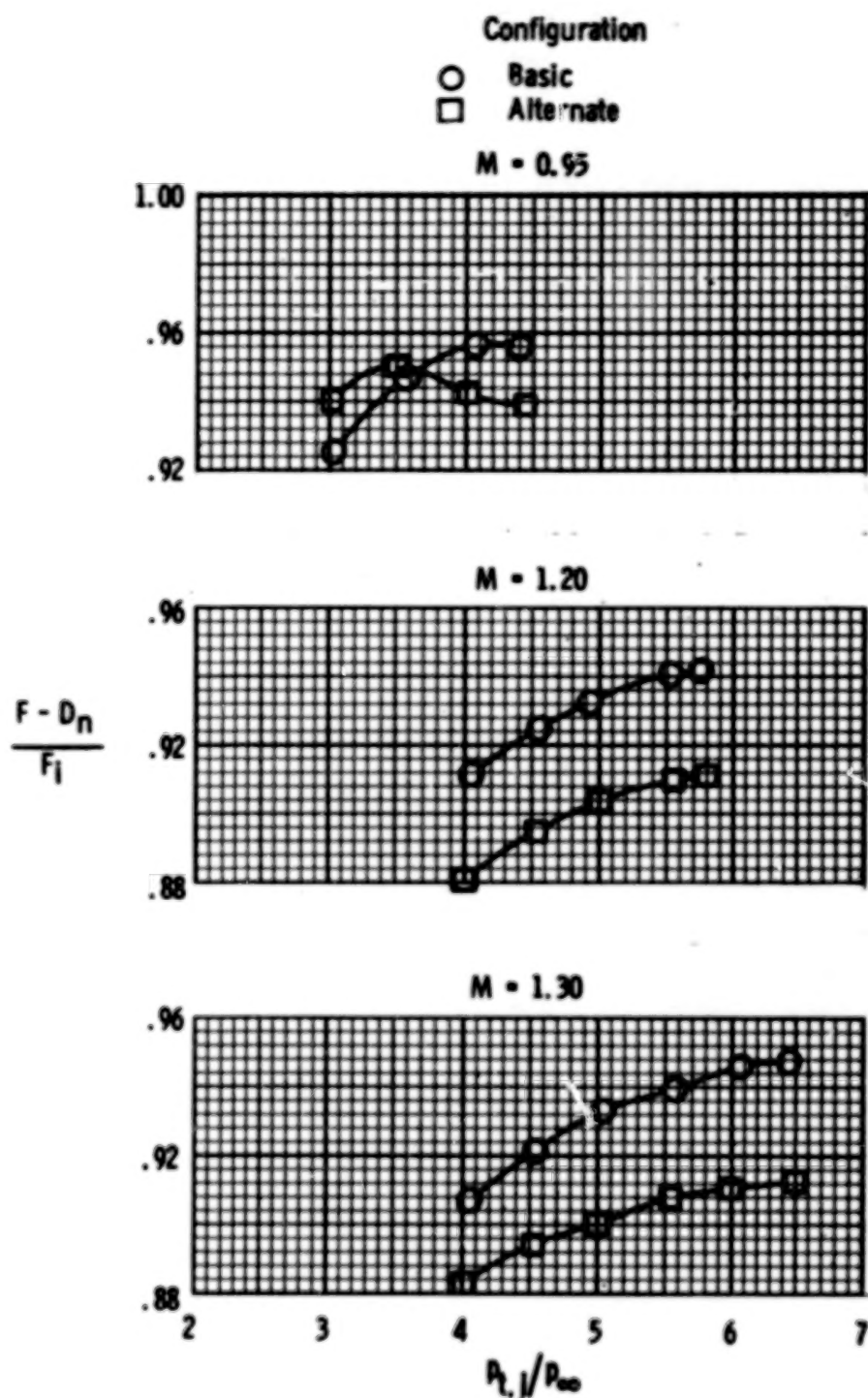
(b)  $M = 0.90, 0.95,$  and  $1.20$  at  $\alpha = 0^\circ$ .

Figure 13.- Concluded.



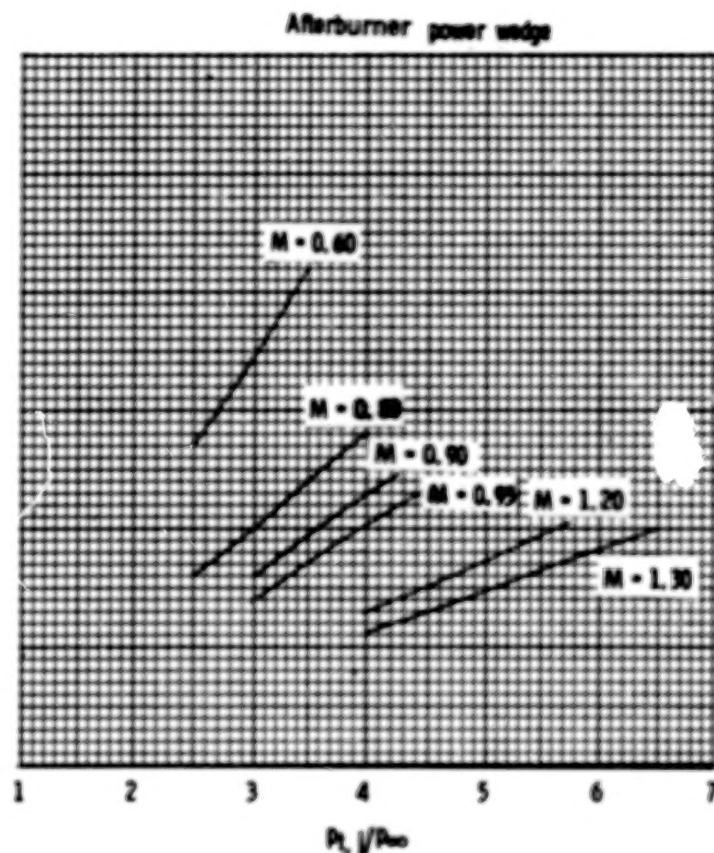
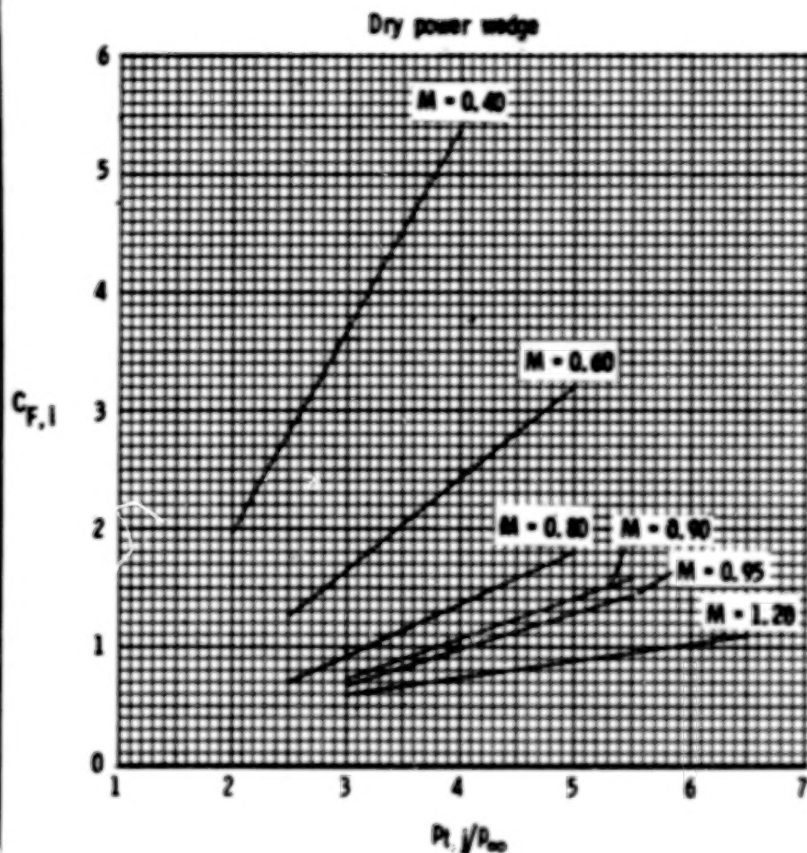
(a)  $M = 0.60, 0.80, \text{ and } 0.90$  at  $\alpha = 0^\circ$ .

Figure 14.- Comparison of aeropropulsion performance of basic and alternate nozzles at afterburning power setting.



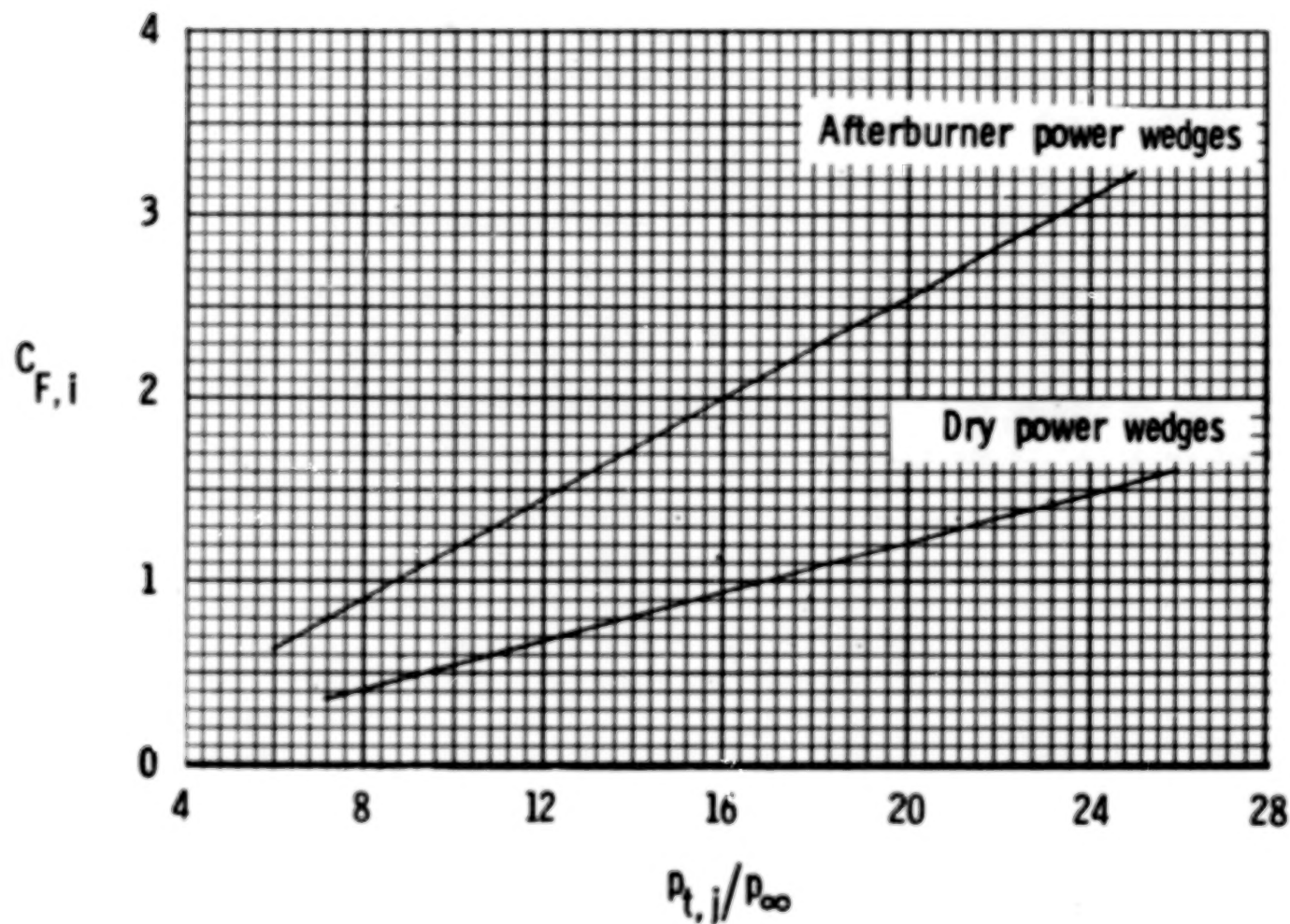
(b)  $M = 0.95, 1.20, \text{ and } 1.30$  at  $\alpha = 0^\circ$ .

Figure 14.- Concluded.



(a)  $M = 0.40$  to  $1.30$ .

Figure 15.- Variation of aerodynamic ideal thrust coefficient with jet total-pressure ratio.



(b)  $M = 2.20$ .

Figure 15.- Concluded.



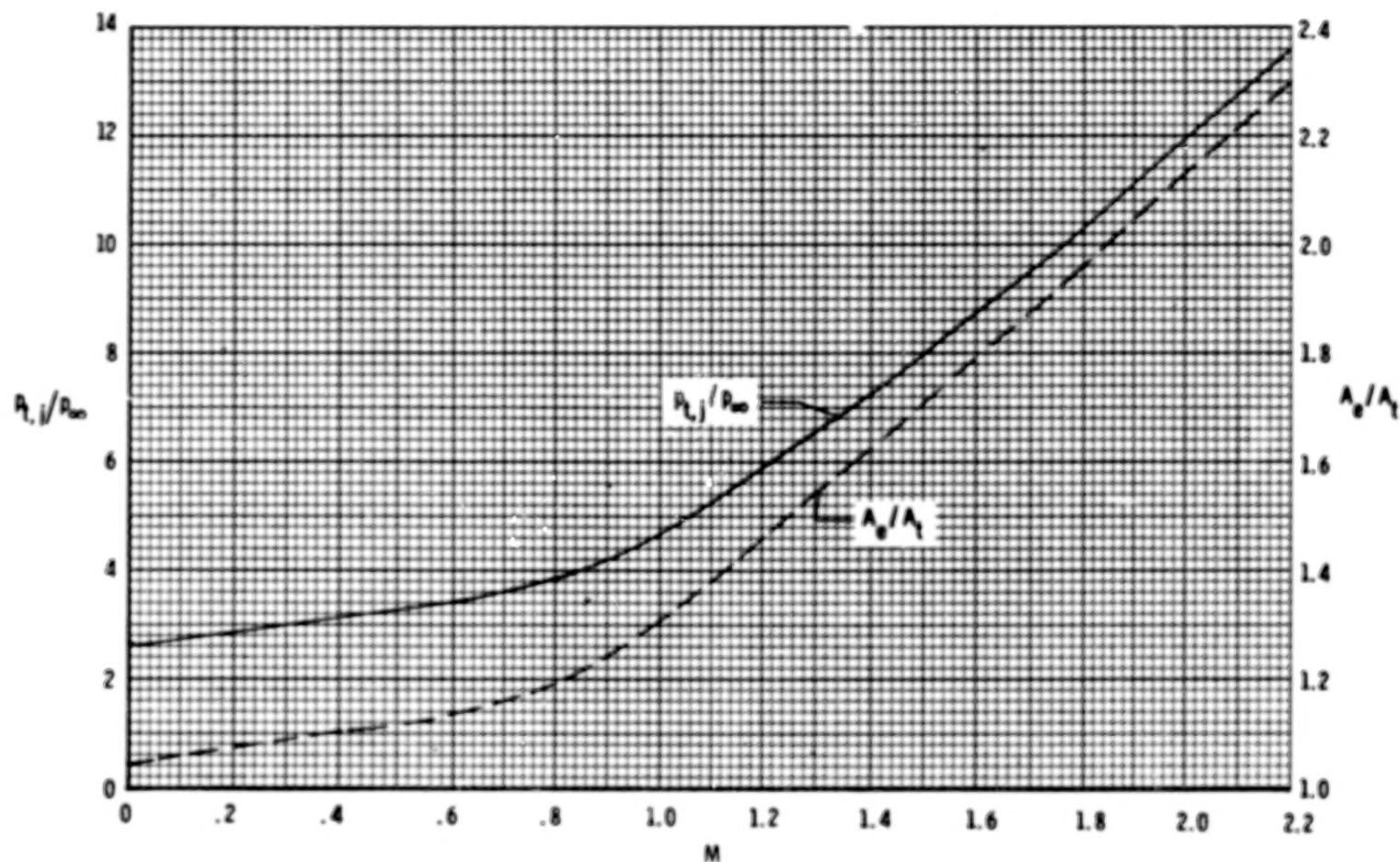


Figure 16.- Typical schedule of advanced-engine total pressure ratio with Mach number and corresponding internal expansion area ratio.

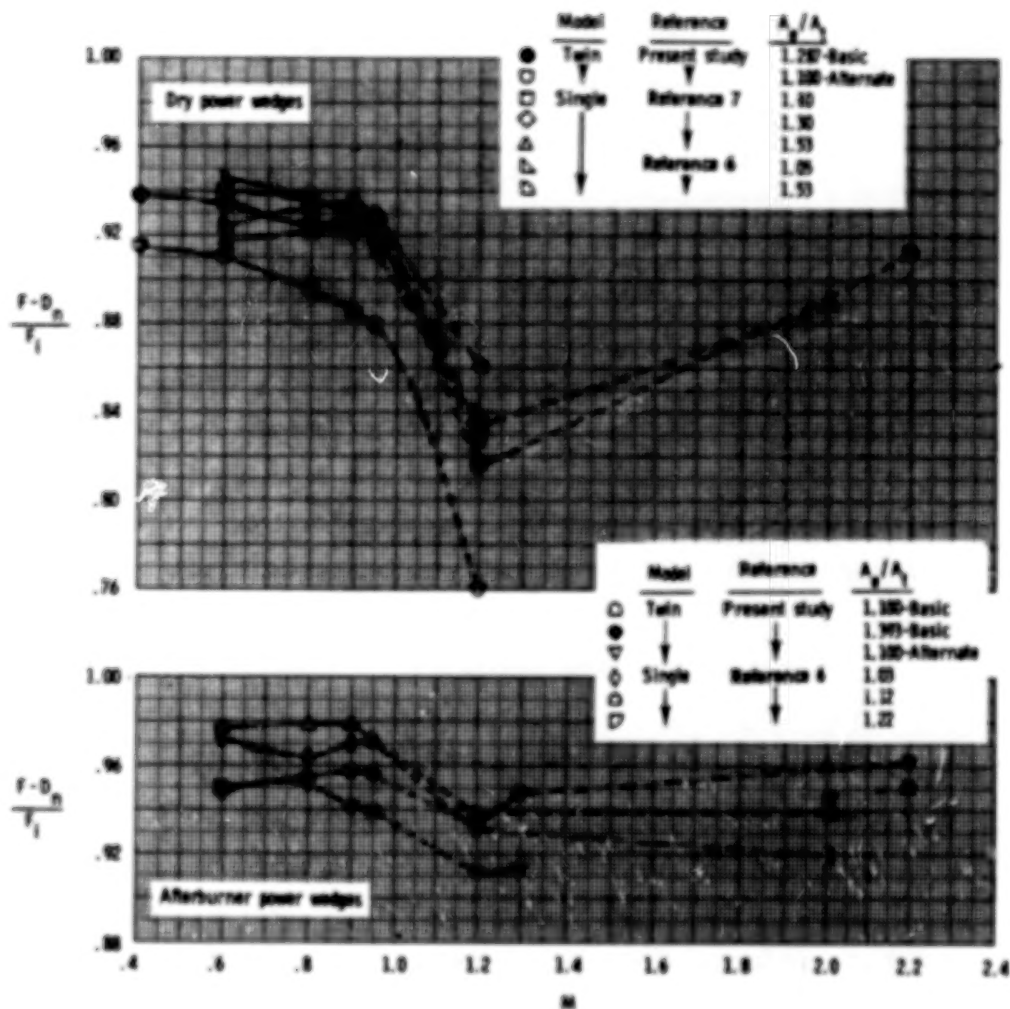
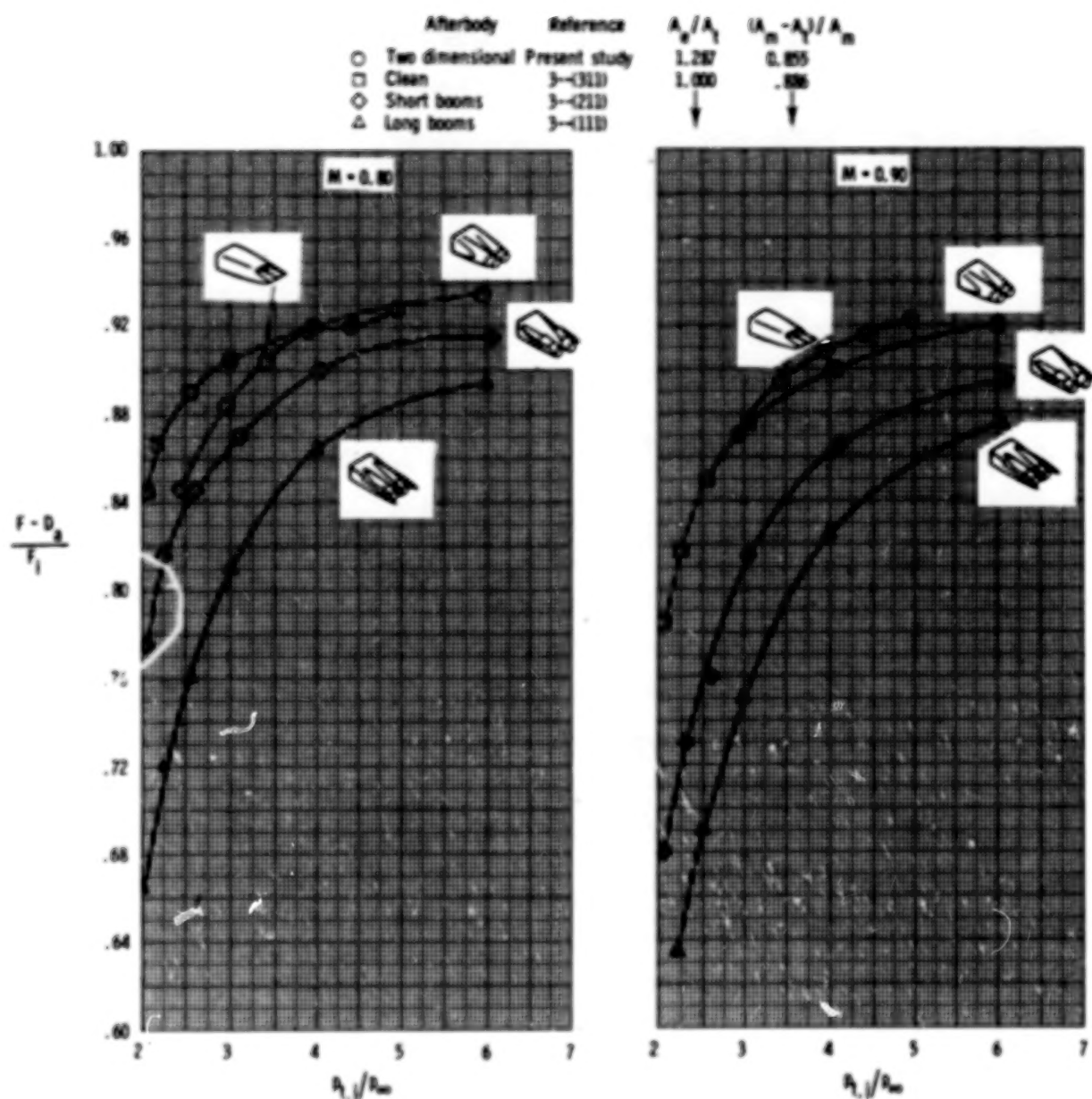


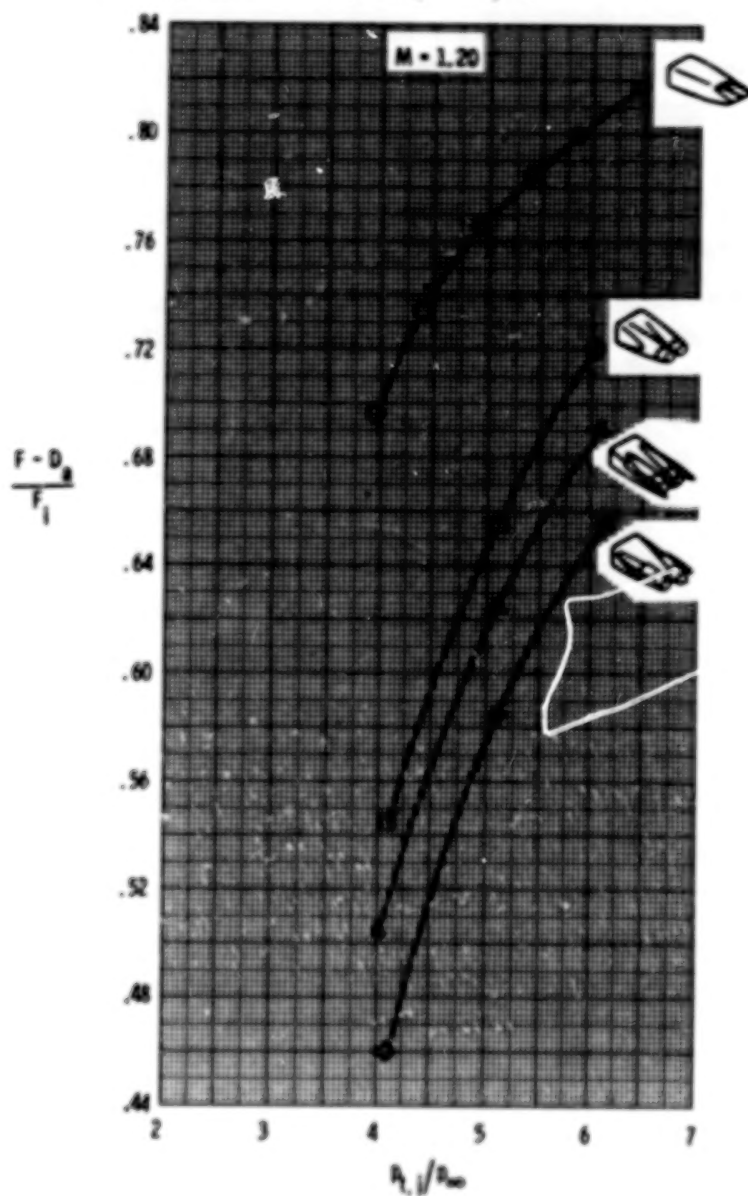
Figure 17.- Summary of single and twin two-dimensional wedge nozzle performance at flight Mach numbers for scheduled pressure ratio.



(a)  $M = 0.80$  and  $0.90$ .

Figure 18.- Comparison of twin two-dimensional wedge nozzle and twin axisymmetric iris-convergent nozzle performance; dry power, close spaced. Parenthetical number refers to configuration of reference 3.

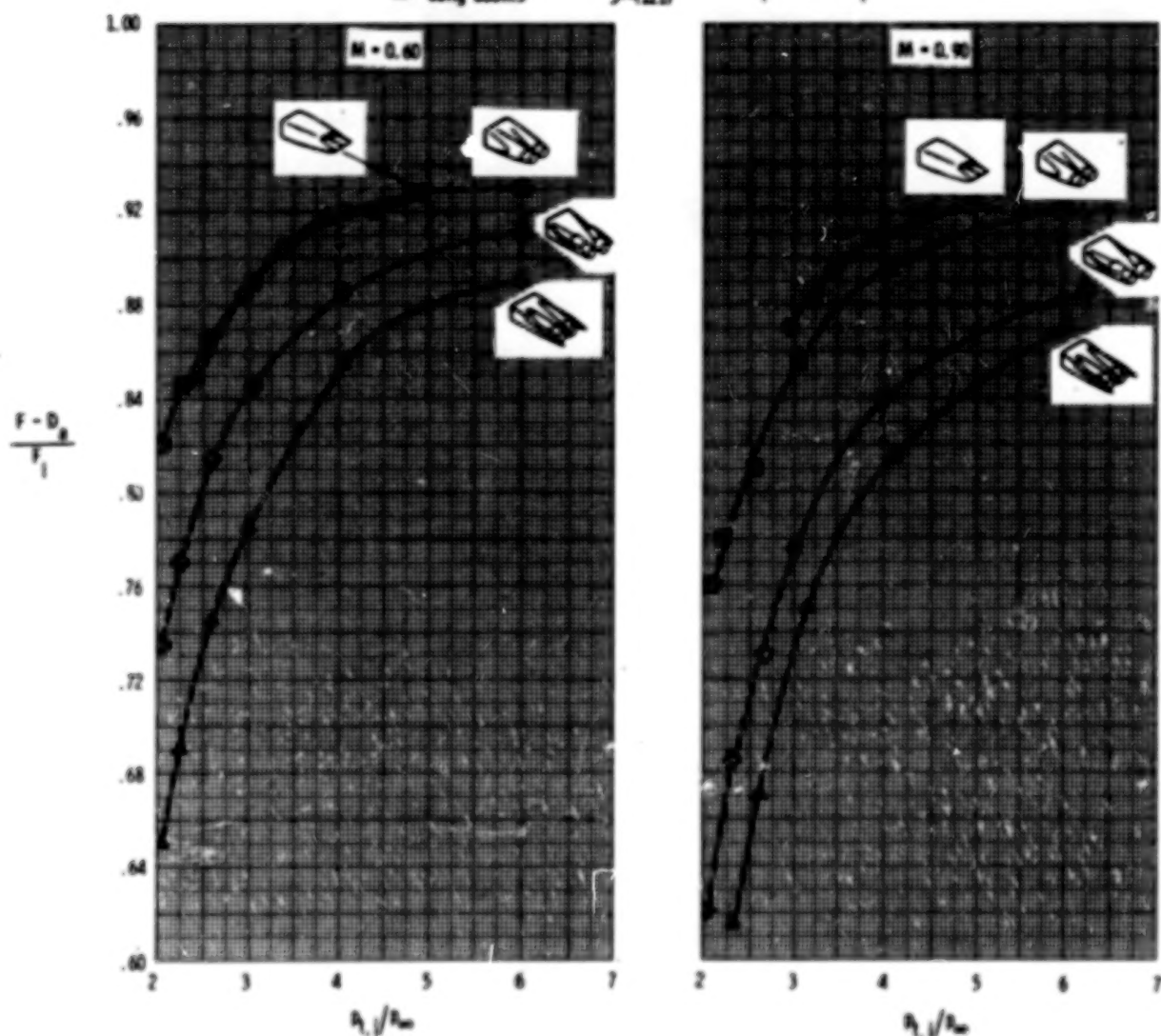
Afterbody	Reference	$A_0/A_1$	$(A_m - A_0)/A_m$
○ Two dimensional	Present study	1.287	0.855
□ Clean	3-(311)	1.000	.886
◇ Short booms	3-(211)	↓	↓
△ Long booms	3-(111)	↓	↓



(b)  $M = 1.20$ .

Figure 18.- Concluded.

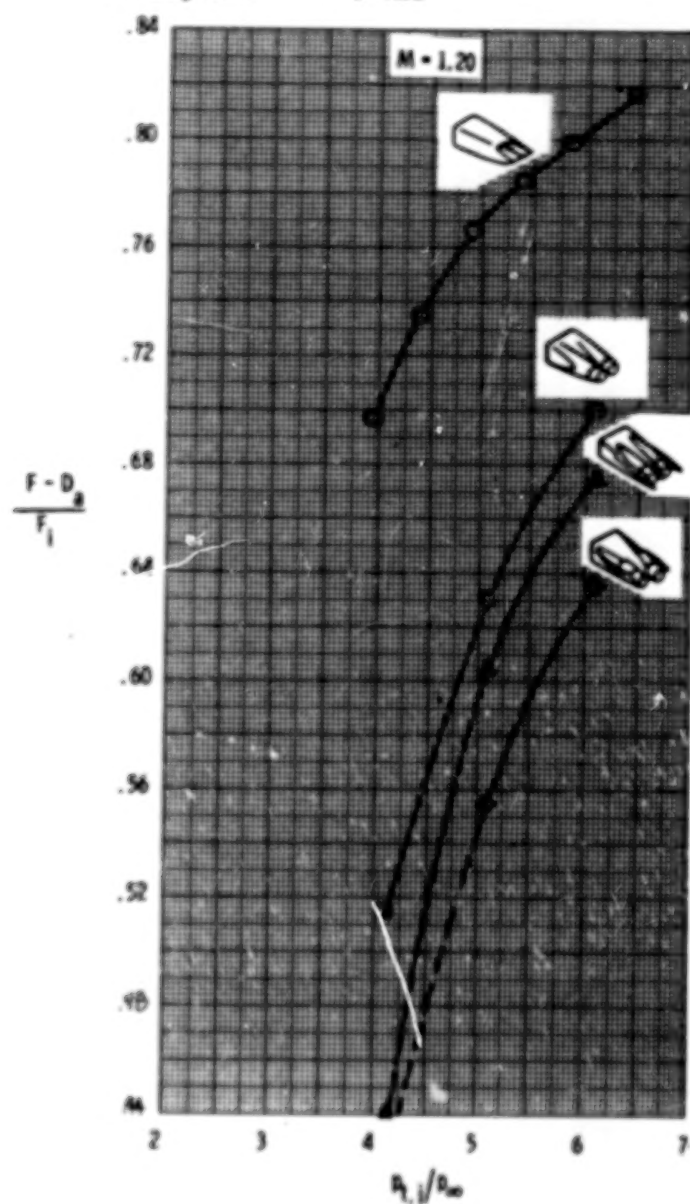
Afterbody	Reference	$A_e/A_t$	$(A_m - A_t)/A_m$
○ Two dimensional	Present study	1.287	0.855
□ Clean	3-(323)	1.852	.886
○ Short booms	3-(223)	↓	↓
△ Long booms	3-(123)	↓	↓



(a)  $M = 0.60$  and  $0.90$ .

Figure 19.- Comparison of twin two-dimensional wedge nozzle and twin axisymmetric convergent-divergent nozzle performance; dry power, close spaced. Parenthetical number refers to configuration of reference 3.

Afterbody	Reference	$A_b/A_t$	$(A_m - A_t)/A_m$
○ Two dimensional	Present study	1.287	0.855
□ Clean	3-(321)	1.000	.886
◇ Short booms	3-(221)	↓	↓
△ Long booms	3-(121)	↓	↓

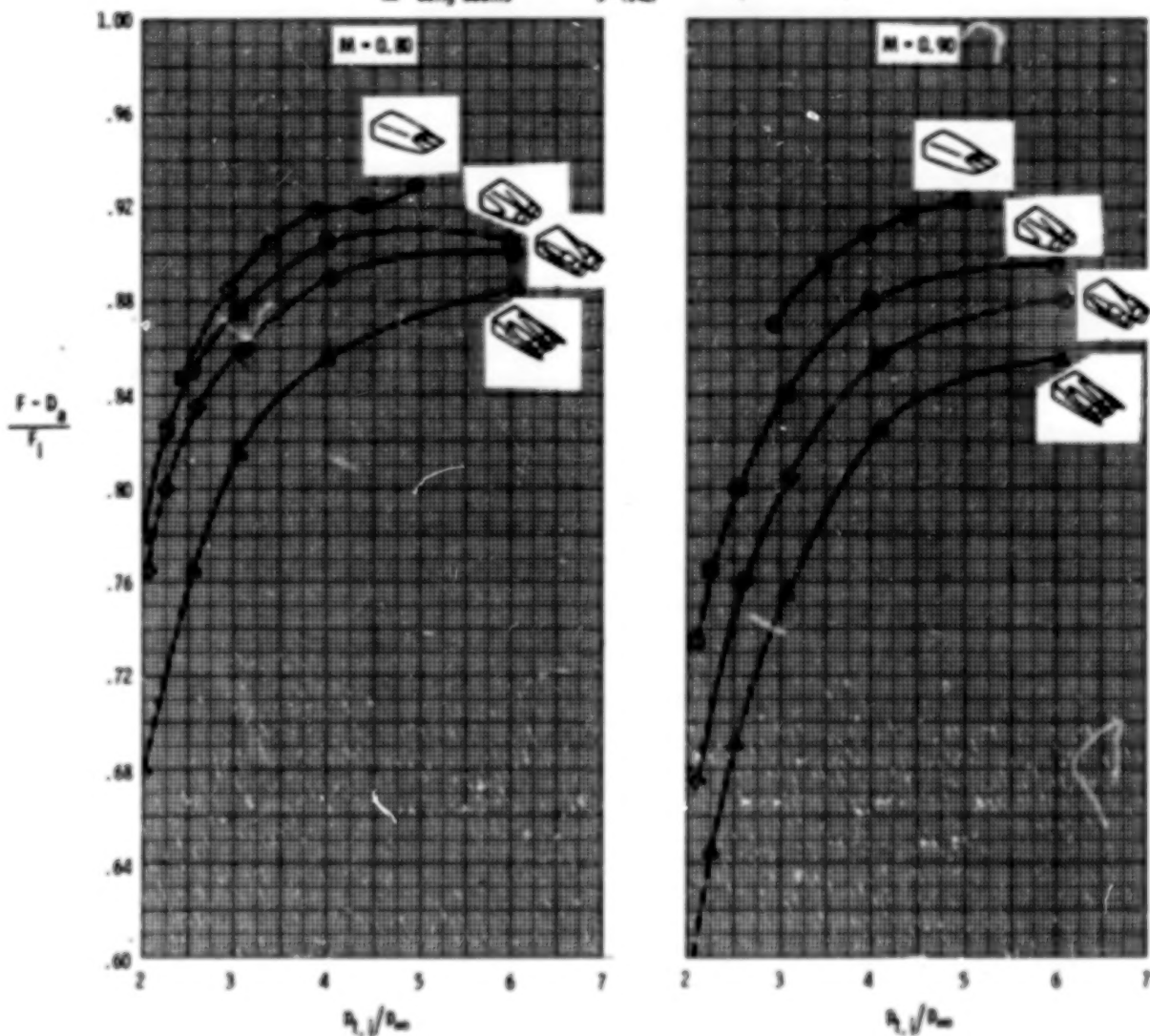


(b)  $M = 1.20$ .

Figure 19.- Concluded.



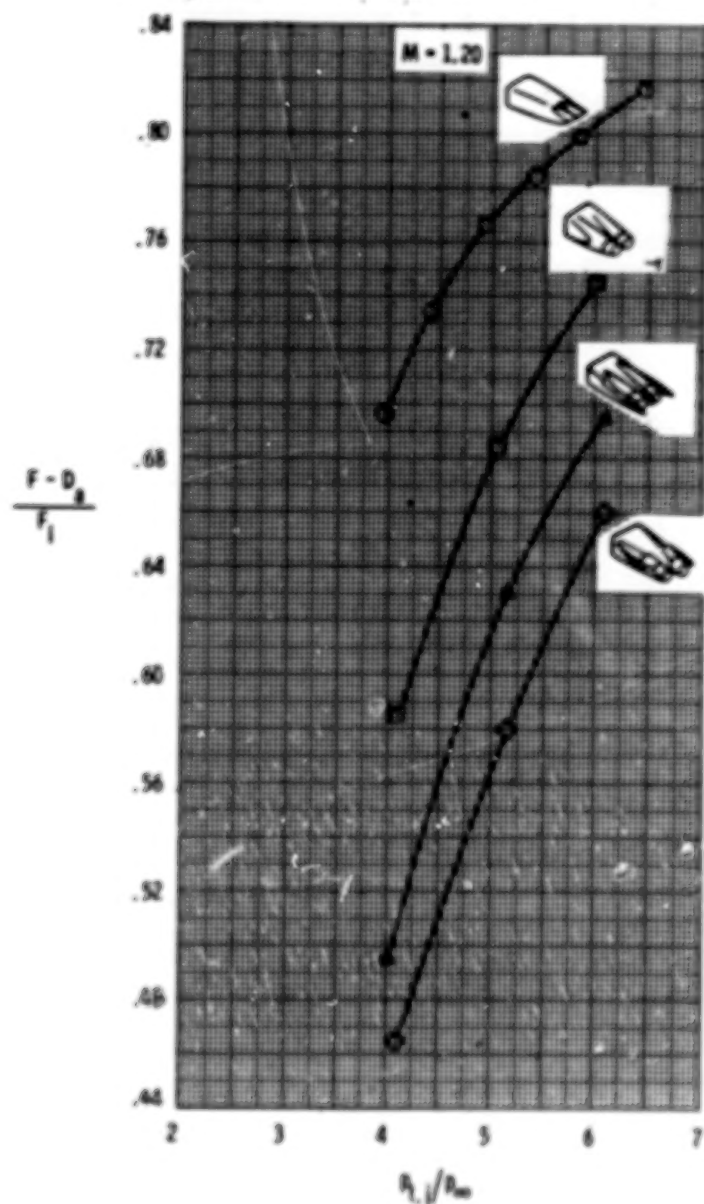
Afterbody	Reference	$A_e/A_t$	$(A_m - A_t)/A_m$
○ Two dimensional	Present study	1.287	0.855
□ Clean	3-(34)	2.710	.886
◇ Short booms	3-(24)	↓	↓
△ Long booms	3-(14)	↓	↓



(a)  $M = 0.80$  and  $0.90$ .

Figure 20.- Comparison of twin two-dimensional wedge nozzle and twin axisymmetric blow-in-door nozzle performance; dry power, close spaced. Parenthetical number refers to configuration of reference 3.

Afterbody	Reference	$A_0/A_1$	$(A_m - A_0)/A_m$
○ Two dimensional	Present study	1.287	0.855
□ Clean	3-(34)	2.710	.886
◇ Short booms	3-(24)	↓	↓
△ Long booms	3-(14)	↓	↓



(b)  $M = 1.20$ .

Figure 20.- Concluded.

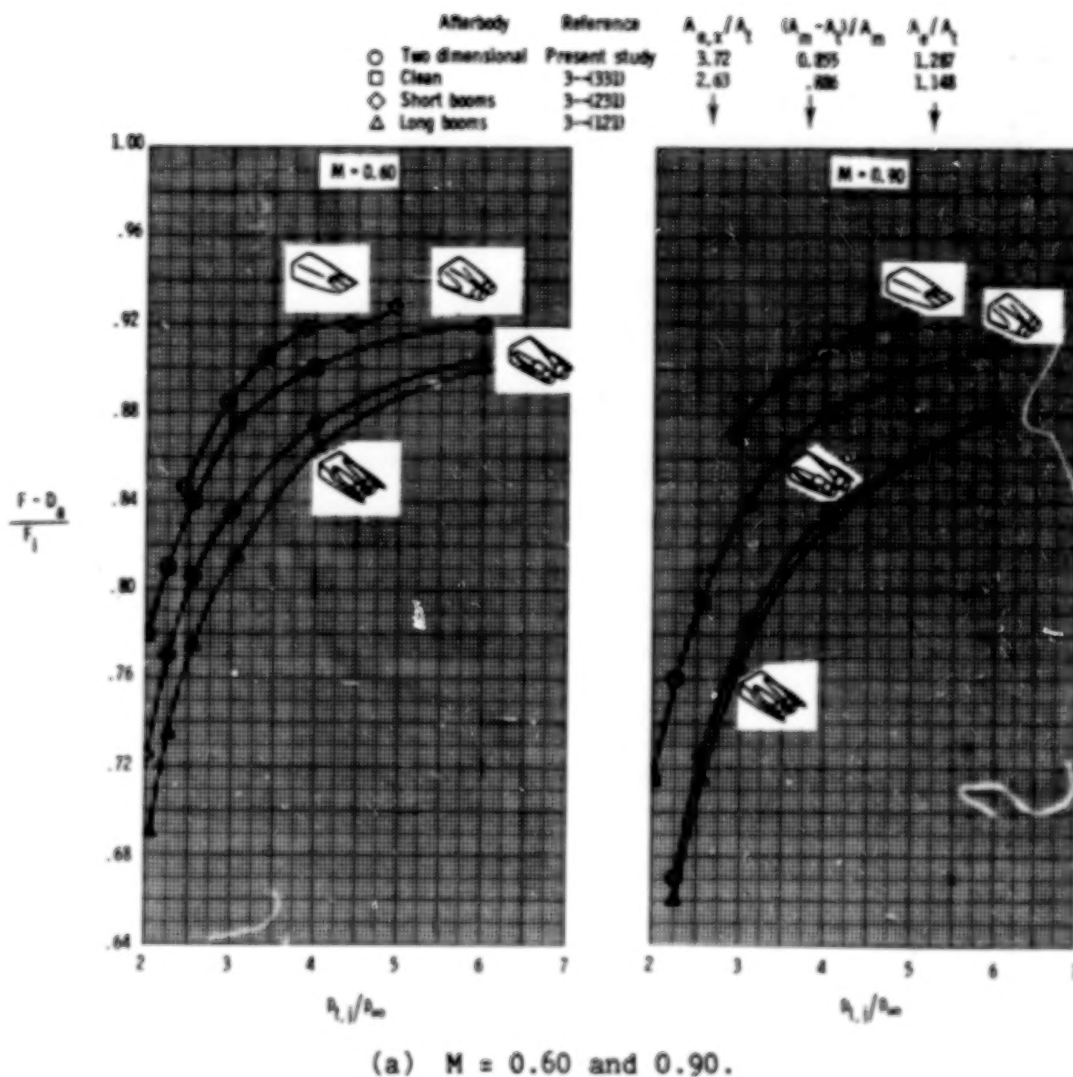
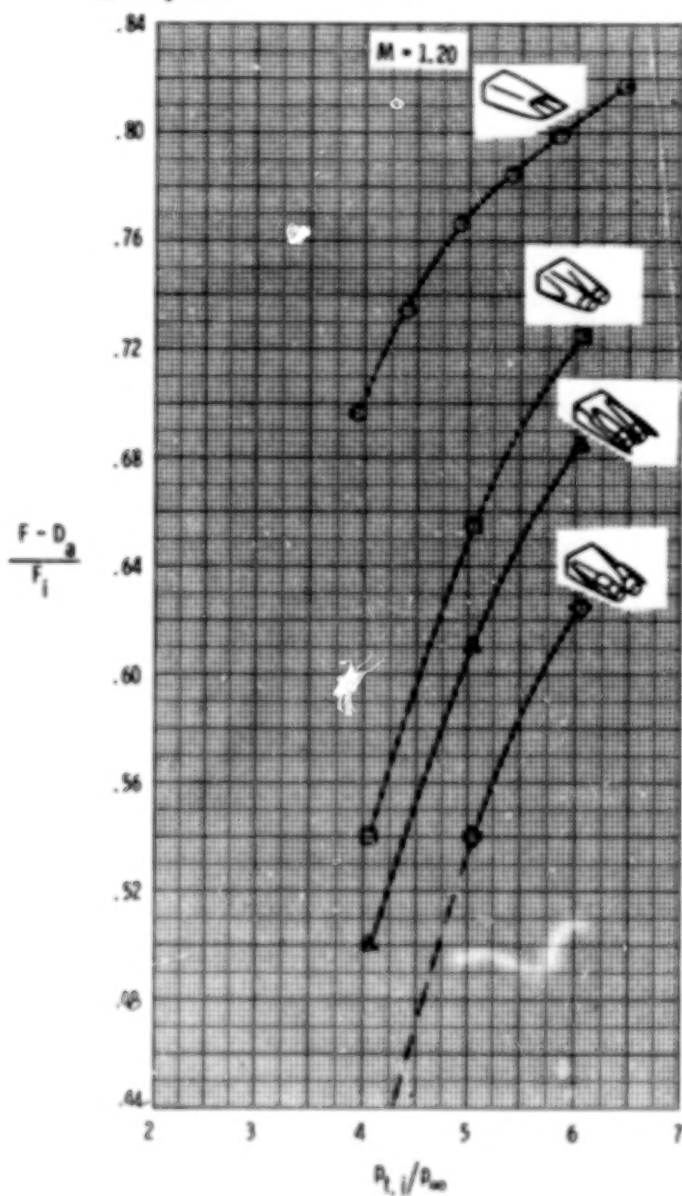


Figure 21.- Comparison of twin two-dimensional wedge nozzle and twin axisymmetric plug nozzle performance; dry power, close spaced. Parenthetical number refers to configuration of reference 3.

Afterbody	Reference	$A_{e,x}/A_t$	$(A_m - A_t)/A_m$	$A_e/A_t$
○ Two dimensional	Present study	3.72	0.855	1.287
□ Clean	3--(331)	2.63	.886	1.148
◇ Short booms	3--(231)	↓	↓	↓
△ Long booms	3--(121)	↓	↓	↓



(b)  $M = 1.20$ .

Figure 21.- Concluded.

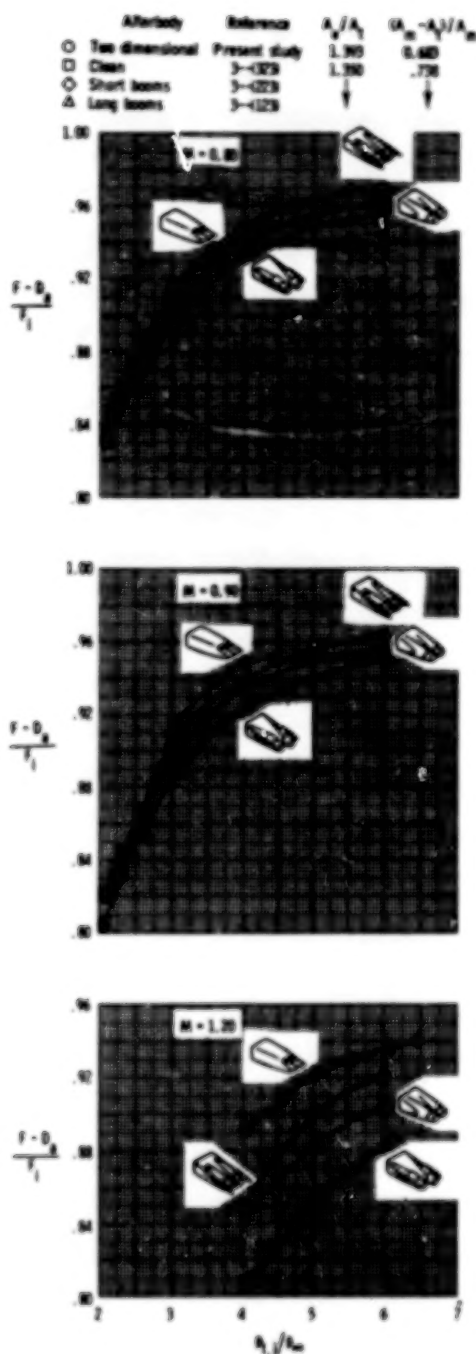


Figure 22.- Comparison of twin two-dimensional wedge nozzle and twin axisymmetric convergent-divergent nozzle performance; afterburner power, close spaced. Parenthetical number refers to configuration of reference 3.

- Nozzle
- Two-dimensional wedge
  - 
  - ◇
  - △ Iris-convergent
  - ▽ Convergent-divergent
  - ▷ Blow-in-door
  - ◻ Axisymmetric plug

Power setting

Dry  
Afterburner

$A_e/A_t$

$A_{e,x}/A_t$

$(A_m - A_t)/A_m$

1.287

3.72

0.855

1.100

1.87

.683

1.393

1.87

.683

1.000

--

.738

1.350

--

--

2.290

--

--

1.323

1.73

--

Clean afterbody  
Close spaced

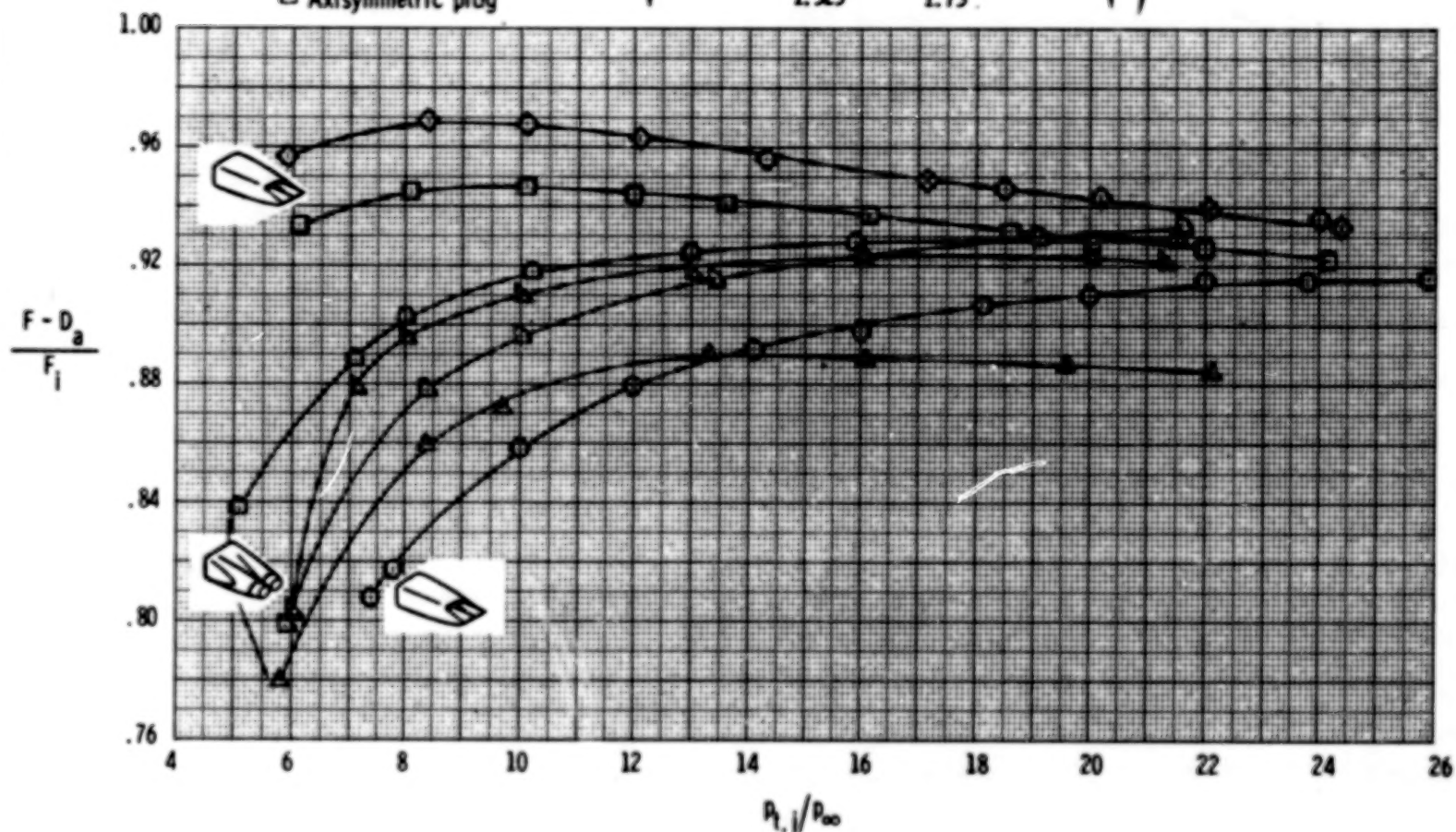


Figure 23.- Comparison of twin two-dimensional wedge nozzle and twin axisymmetric nozzle performance at  $M = 2.20$ .



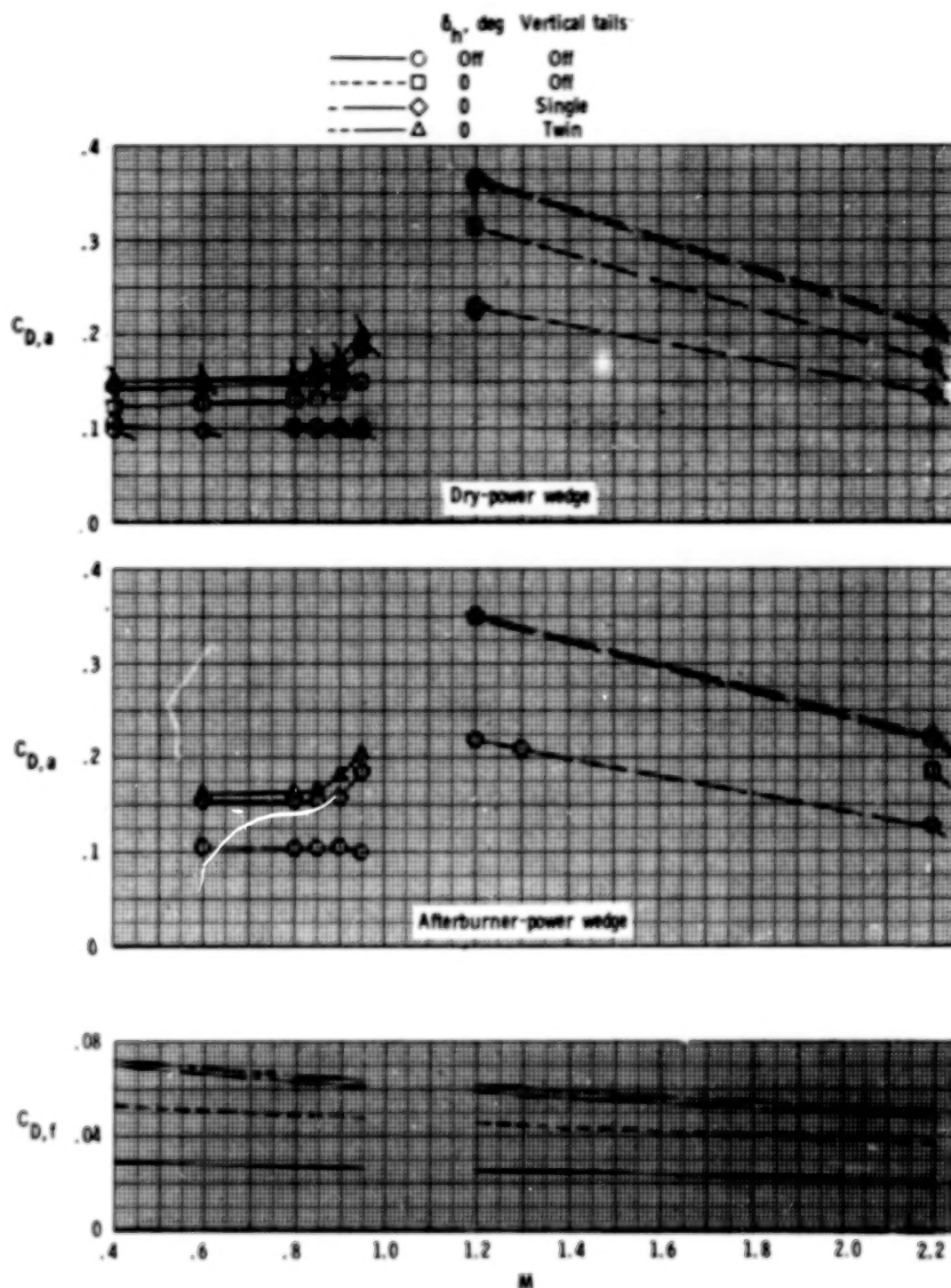
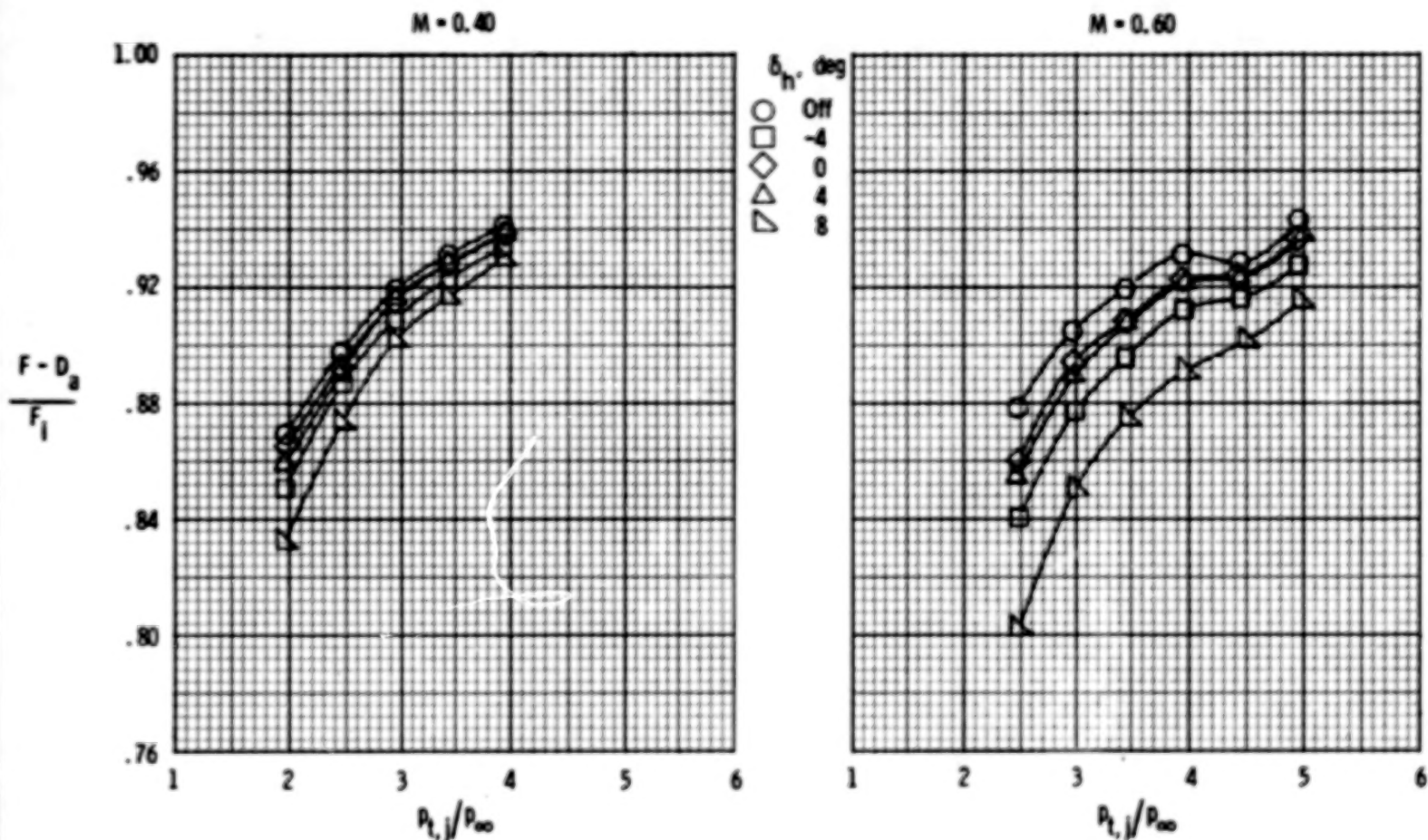
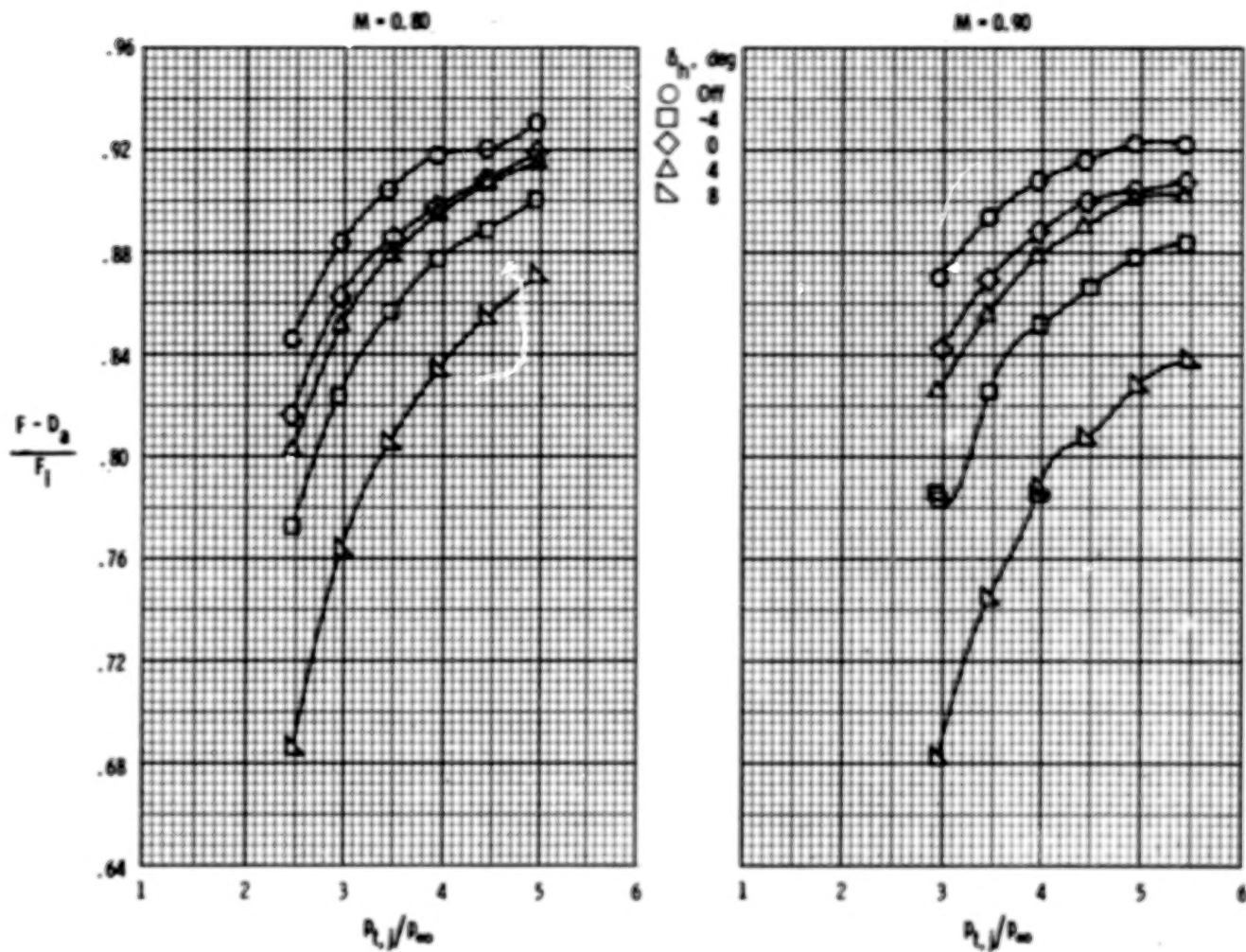


Figure 24.- Variation with Mach number of measured jet-off drag coefficient and computed skin friction drag coefficient. Flagged symbols represent repeat points.



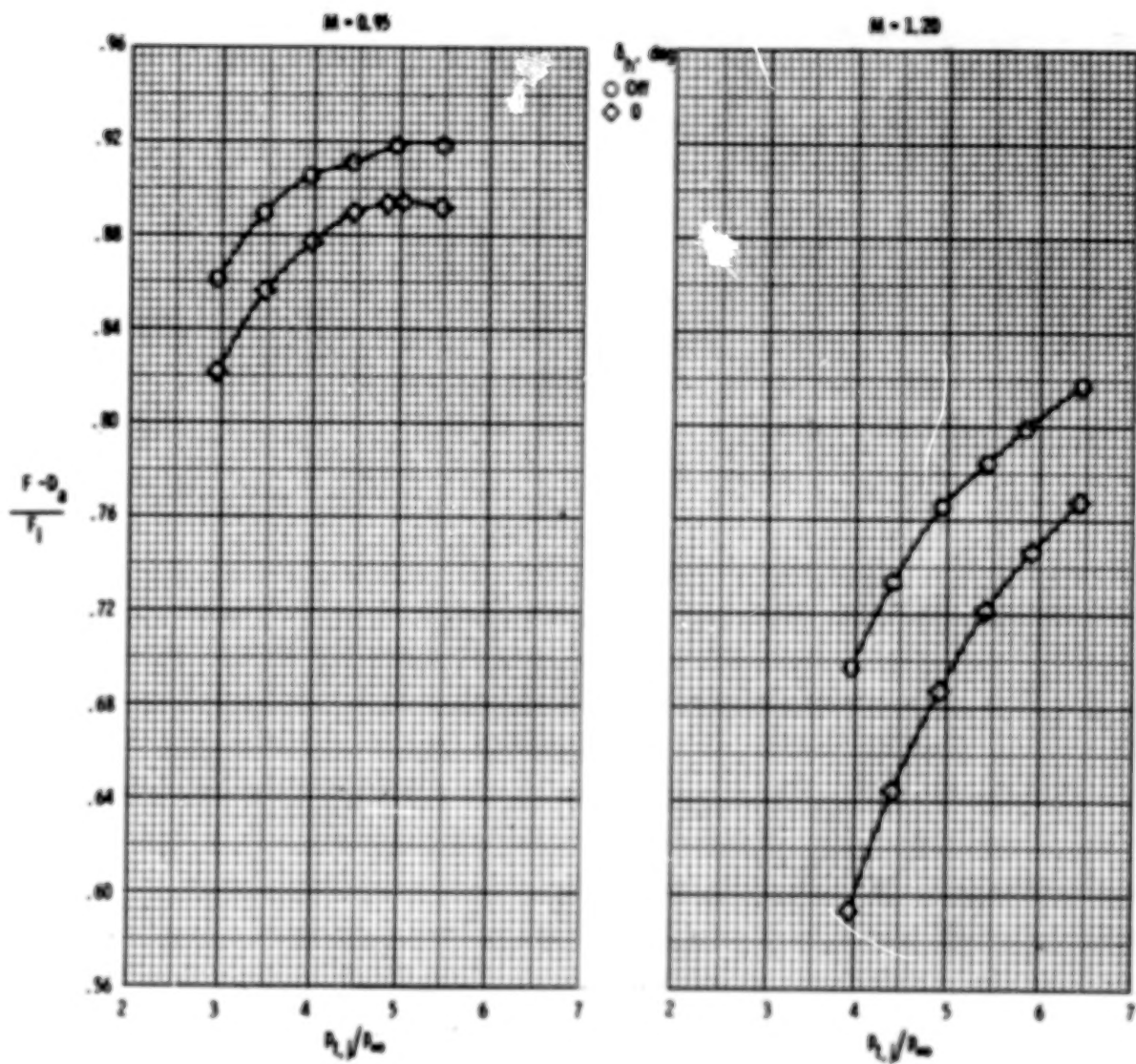
(a)  $M = 0.40$  and  $0.60$ .

Figure 25.- Effect of horizontal-tail deflection on thrust minus drag over a range of pressure ratios and Mach numbers. Vertical tails off. Basic dry power nozzle.



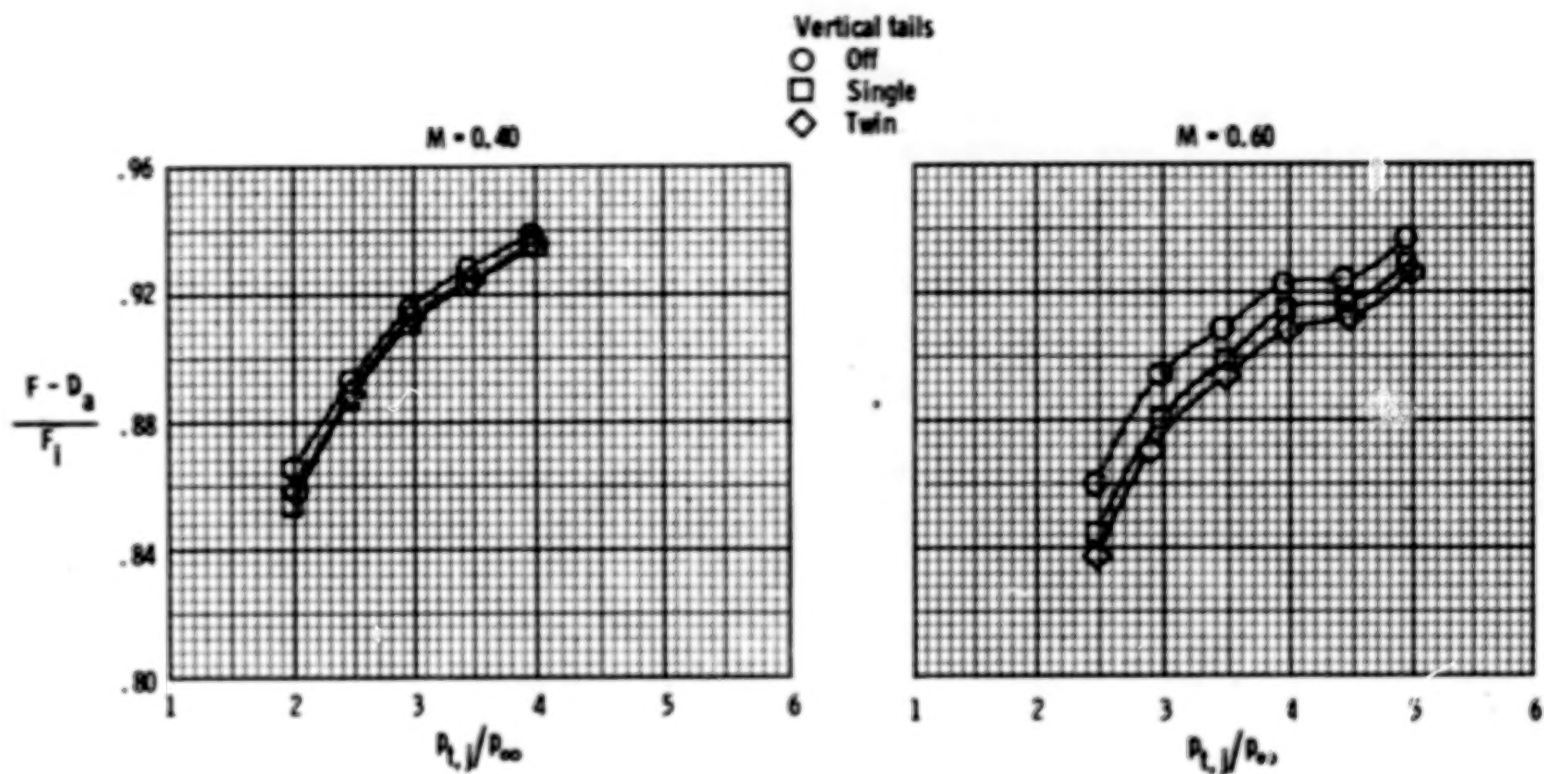
(b)  $M = 0.80$  and  $0.90$ .

Figure 25.- Continued.



(c)  $M = 0.95$  and  $1.20$ .

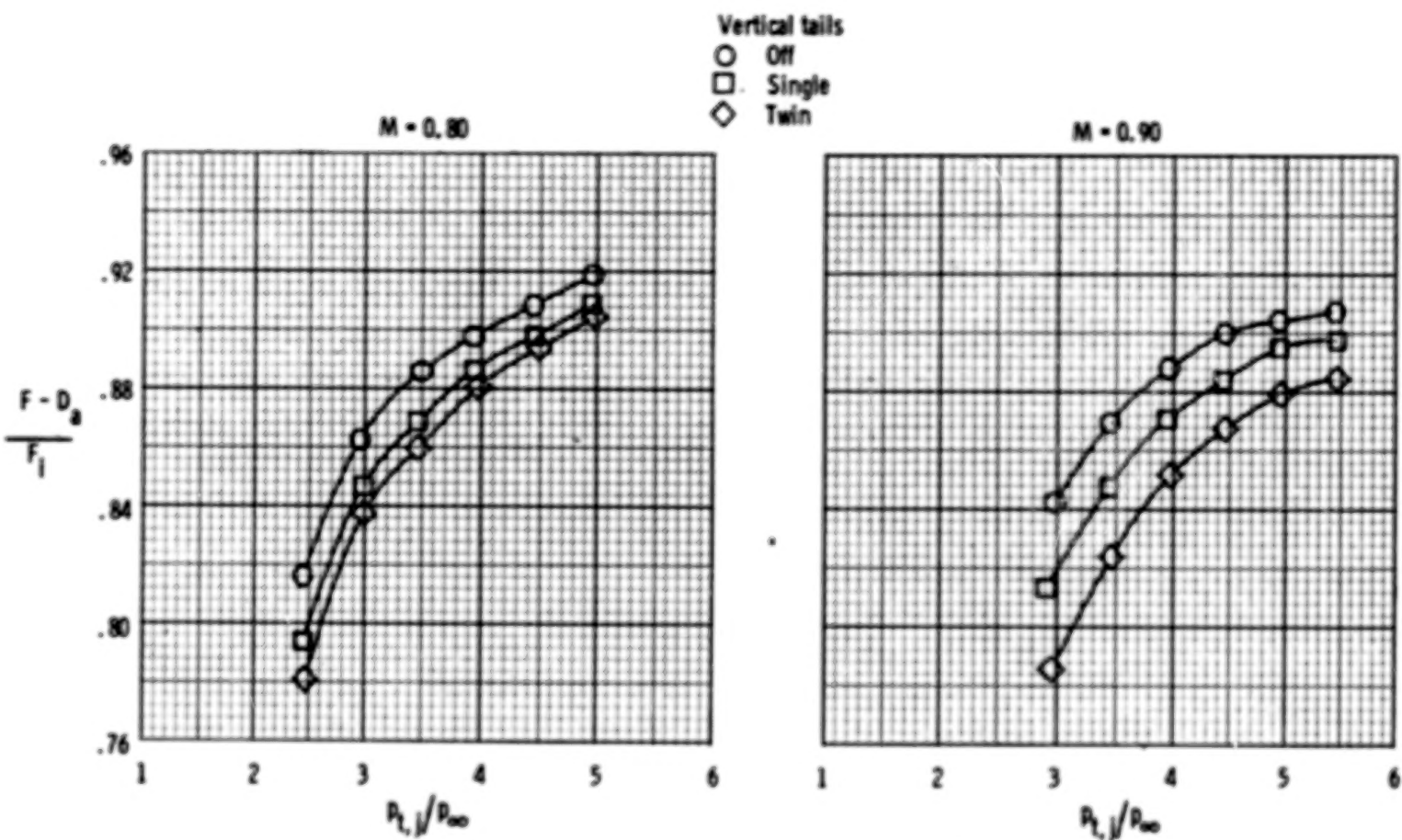
Figure 25.- Concluded.



(a)  $M = 0.40$  and  $0.60$ .

Figure 26.- Effect of vertical tails on thrust minus drag for several pressure ratios and Mach numbers. Basic dry power nozzle.  $\delta_n = 0^\circ$ .

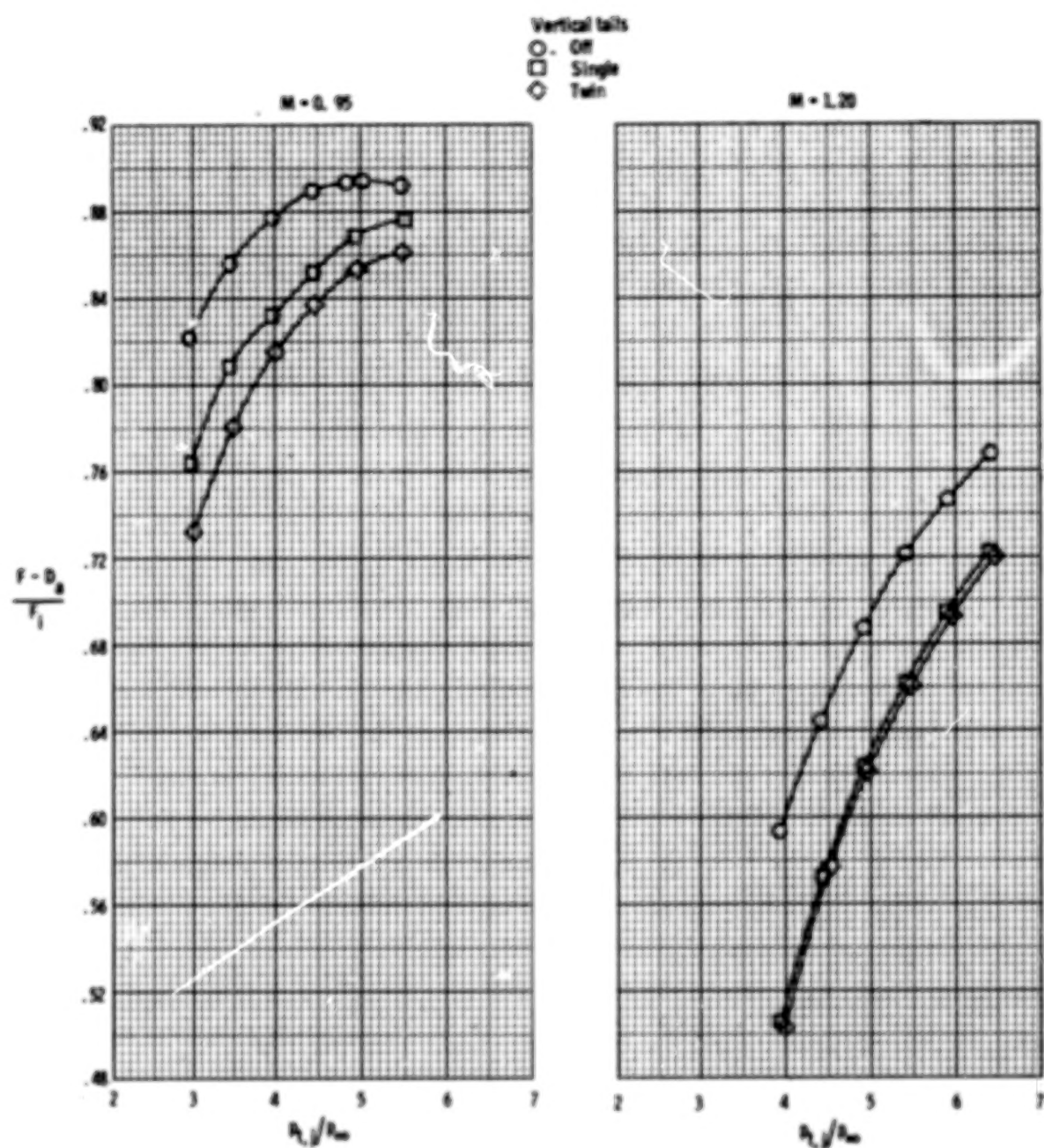




(b)  $M = 0.80$  and  $0.90$ .

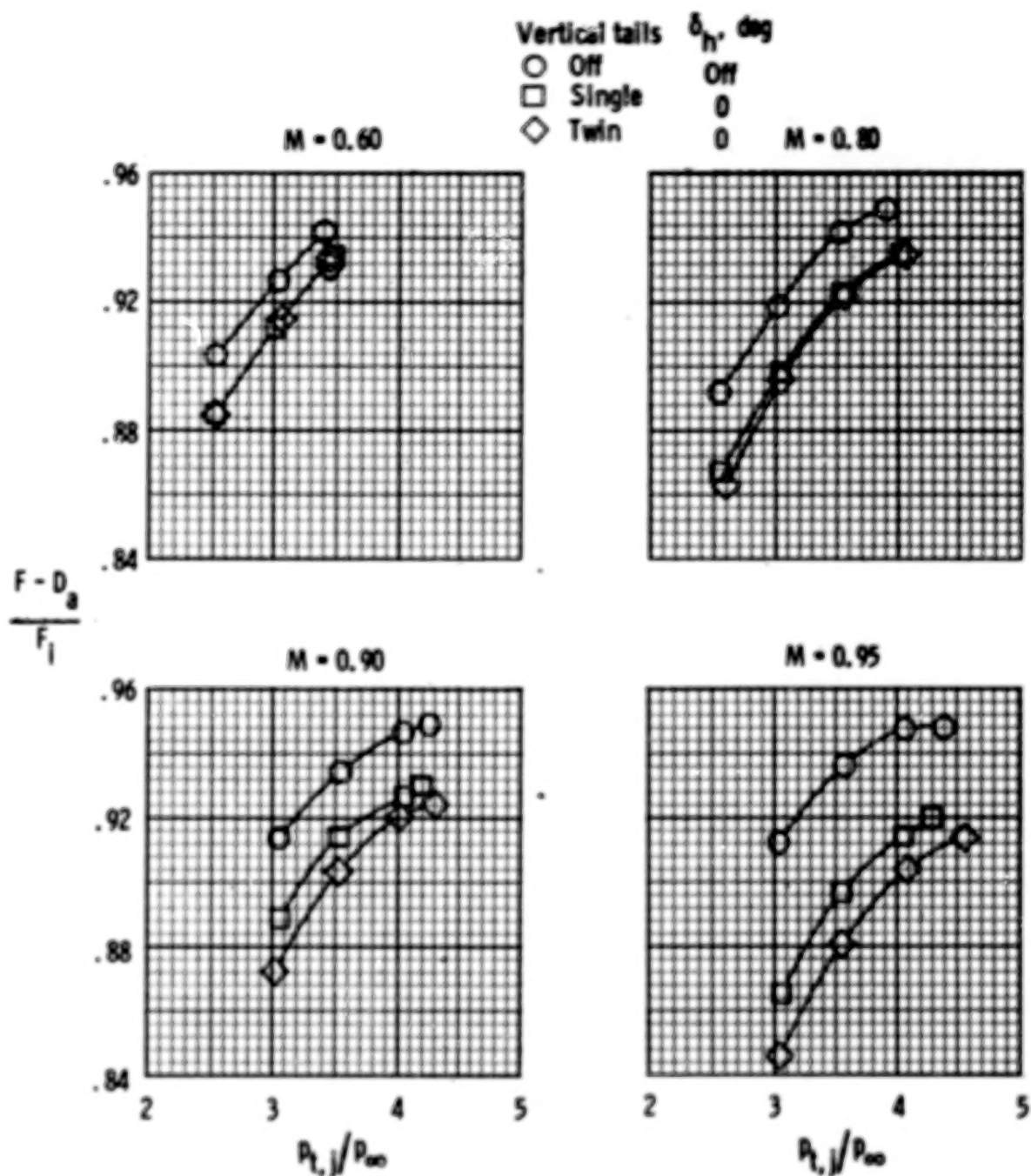
Figure 26.- Continued.





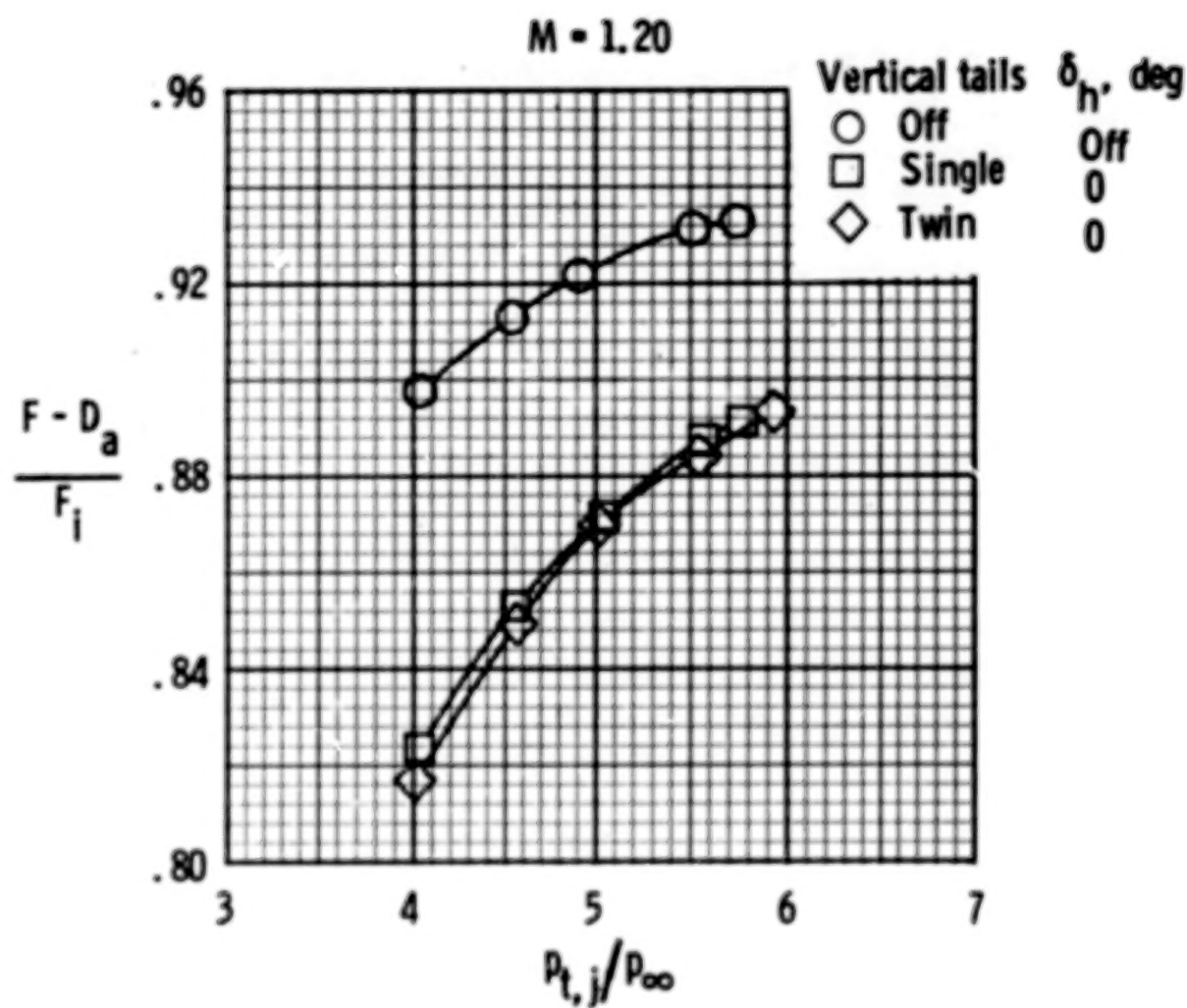
(c)  $M = 0.95$  and  $1.20$ .

Figure 26.- Concluded.



(a)  $M = 0.60, 0.80, 0.90$ , and  $0.95$ .

Figure 27.- Effect of vertical tails on thrust minus drag for several pressure ratios and Mach numbers. Basic afterburner nozzle.



(b)  $M = 1.20$ .

Figure 27.- Concluded.

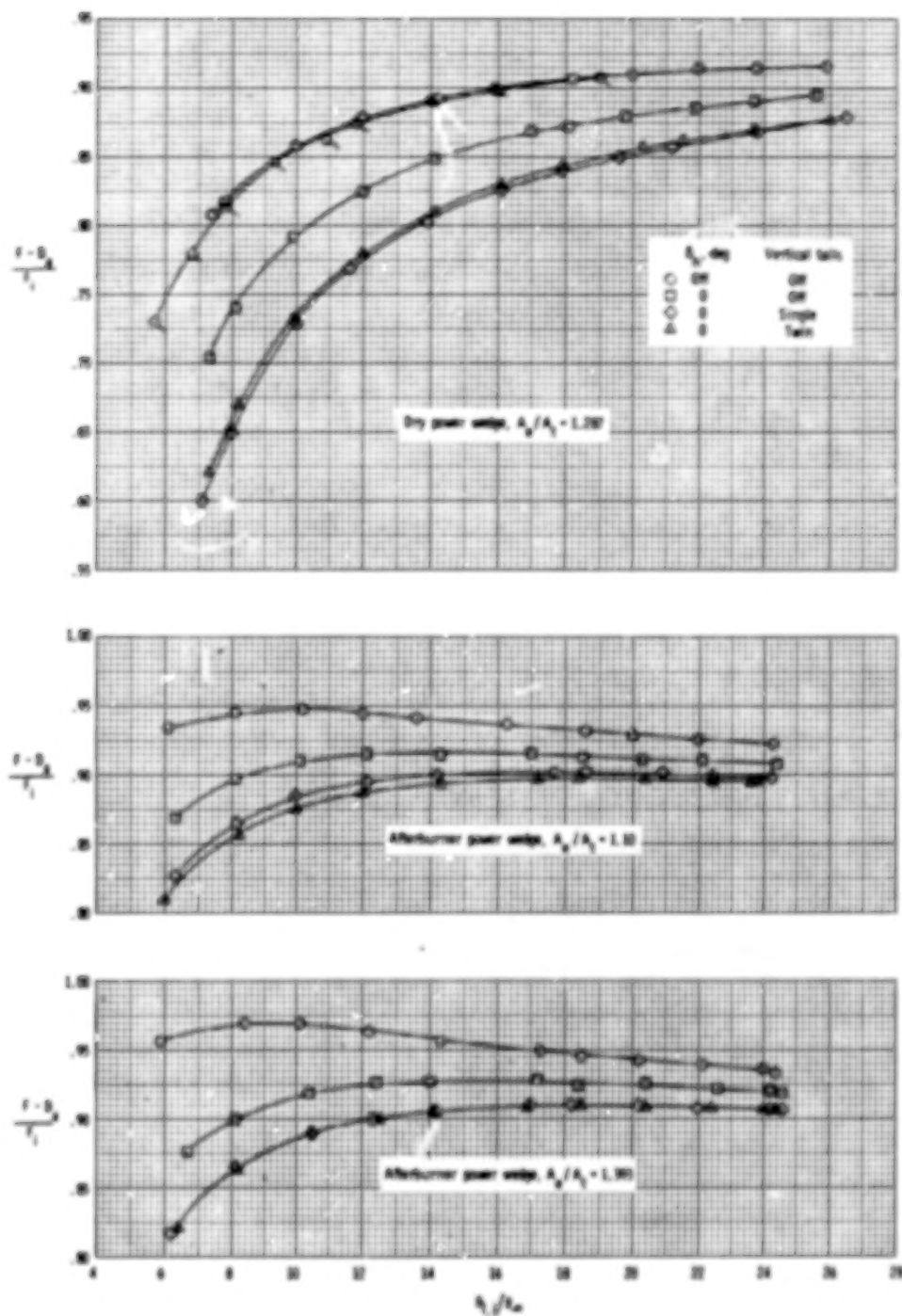
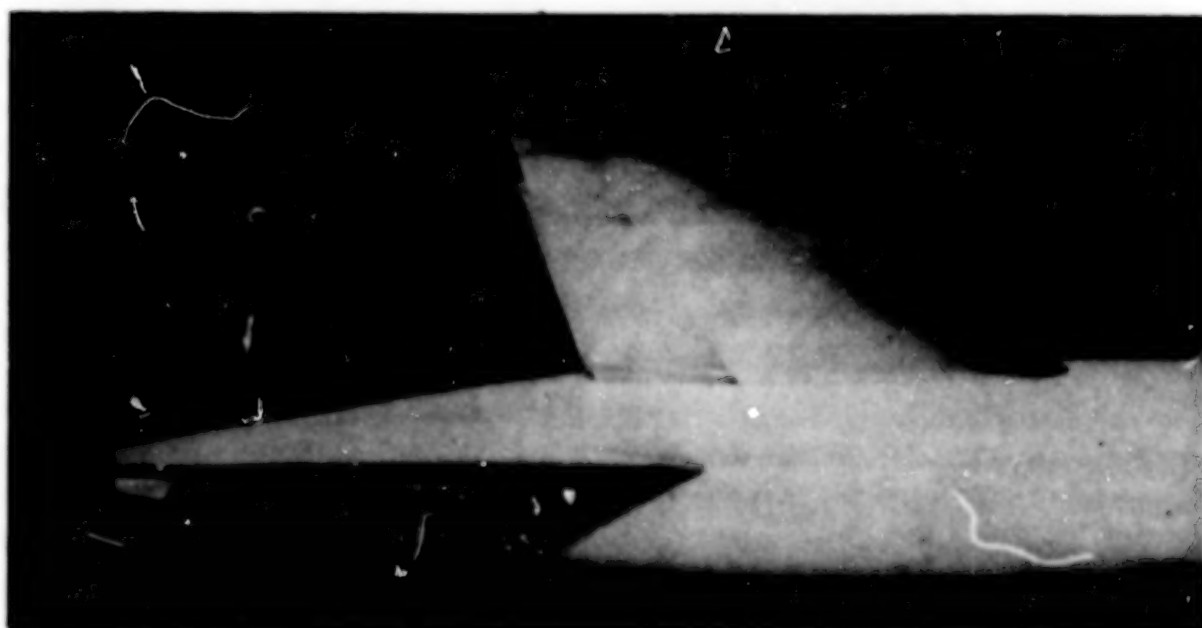
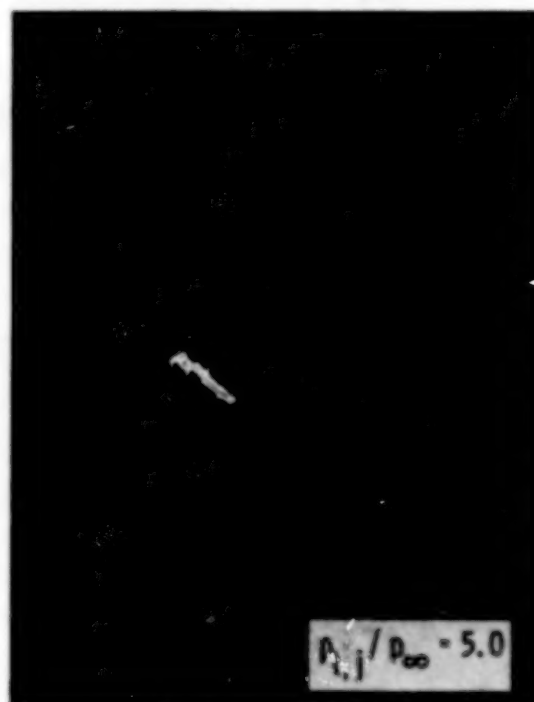
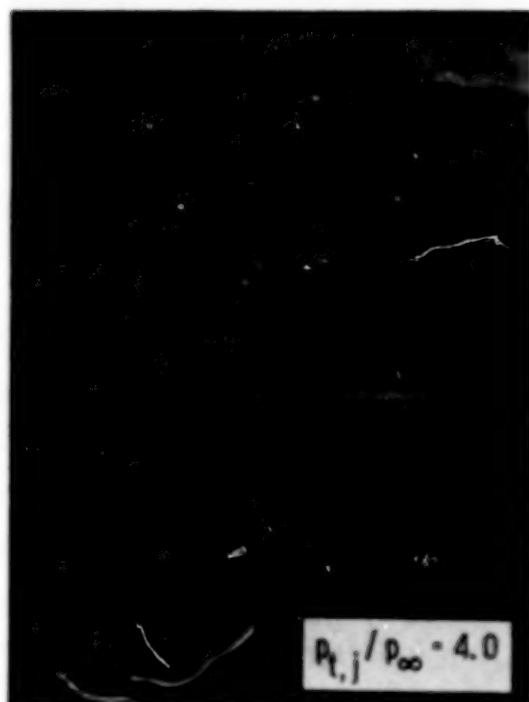


Figure 28.- Thrust-minus-drag performance for various configurations.  $M = 2.20$ . Flagged symbols indicate  $N_{Re} = 16.40 \times 10^6$ .



L-77-205

Figure 29.- Oil-flow visualization of twin tail installation at  $M = 0.90$ .

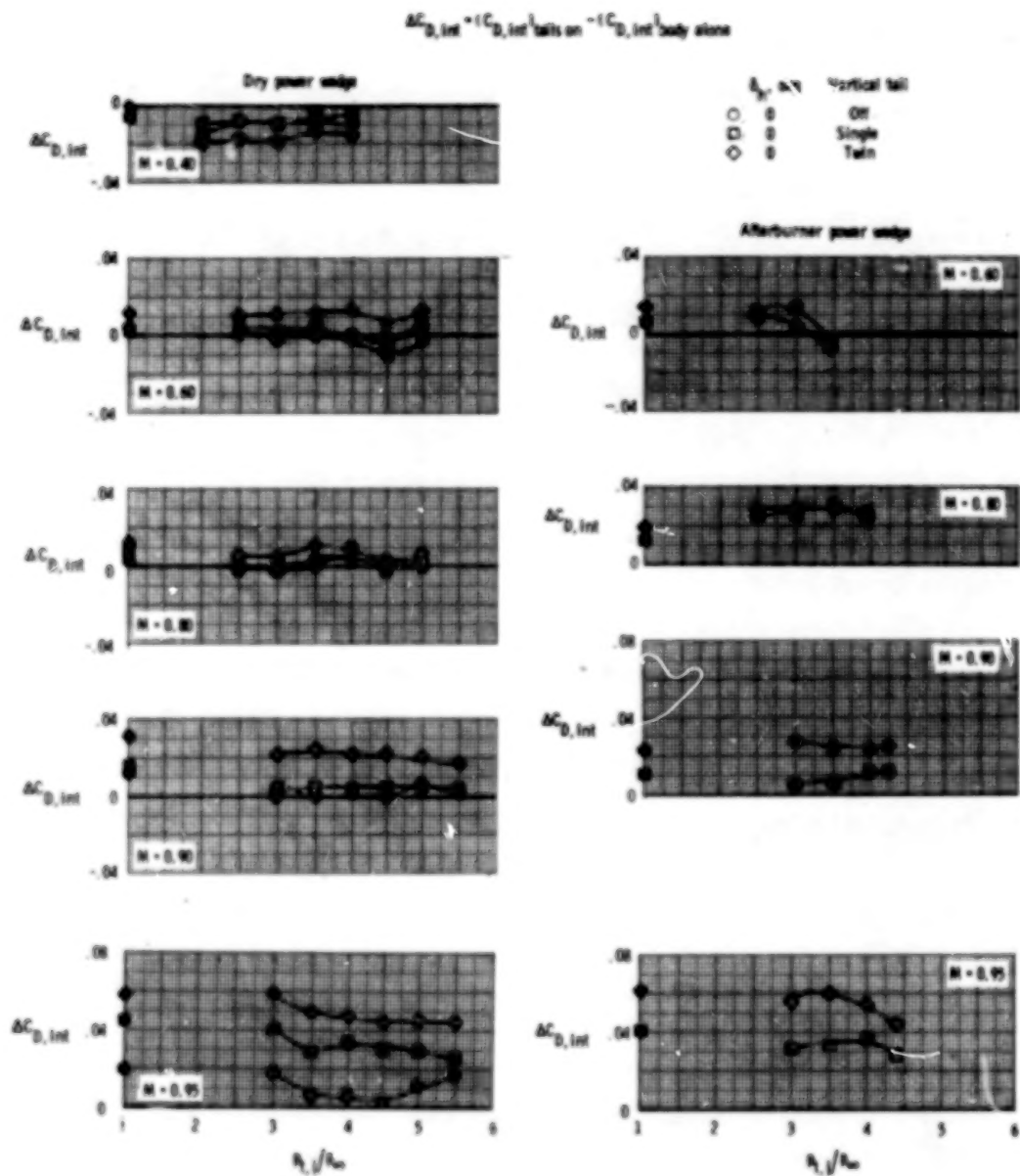


Figure 30.- Variation of subsonic tail interference incremental drag coefficient with pressure ratio. Solid symbols represent jet-off values.

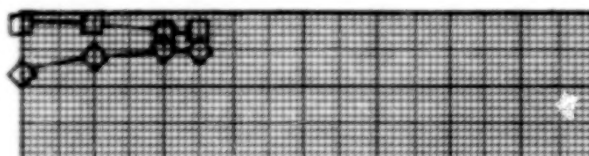
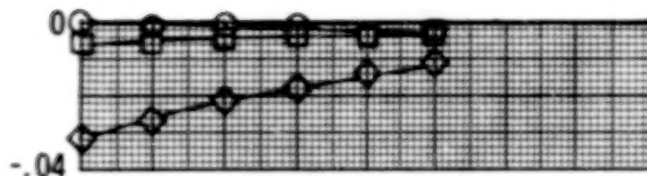


$$\Delta \left( \frac{F - D_{int}}{F_i} \right) = \left( \frac{F - D_{int}}{F_i} \right)_{\text{tails}} - \left( \frac{F - D_{int}}{F_i} \right)_{\text{body}}$$

Dry power wedge

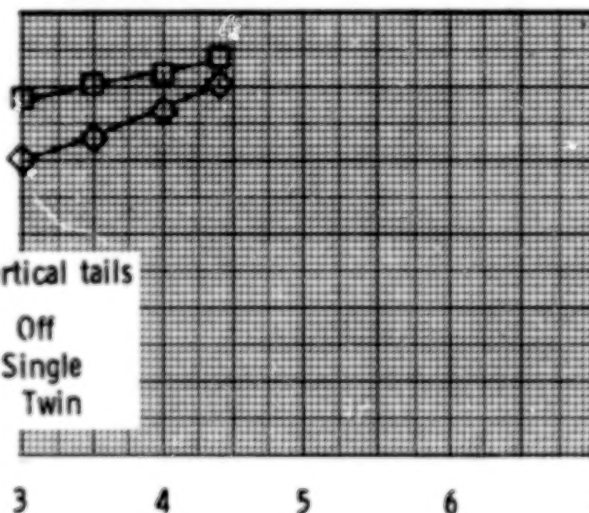
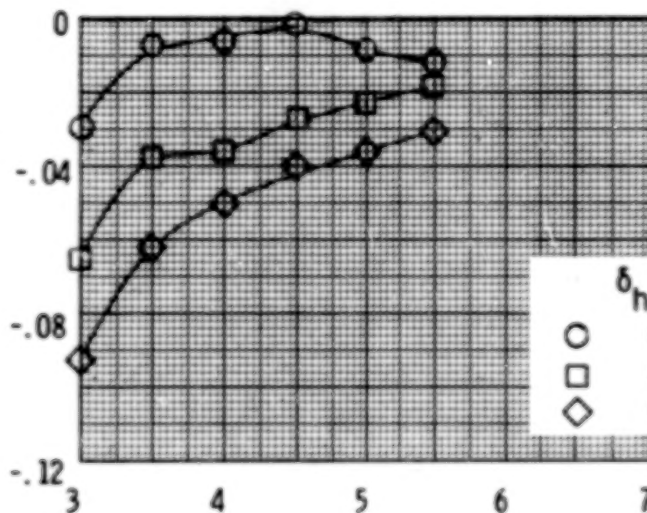
Afterburner power wedge

M = 0.90



M = 0.95

$$\Delta \left( \frac{F - D_{int}}{F_i} \right)$$



δ<sub>h</sub>, deg Vertical tails

- 0
- 0
- ◇ 0

Off  
Single  
Twin

Figure 31.- Variation of subsonic tail interference parameter with pressure ratio.

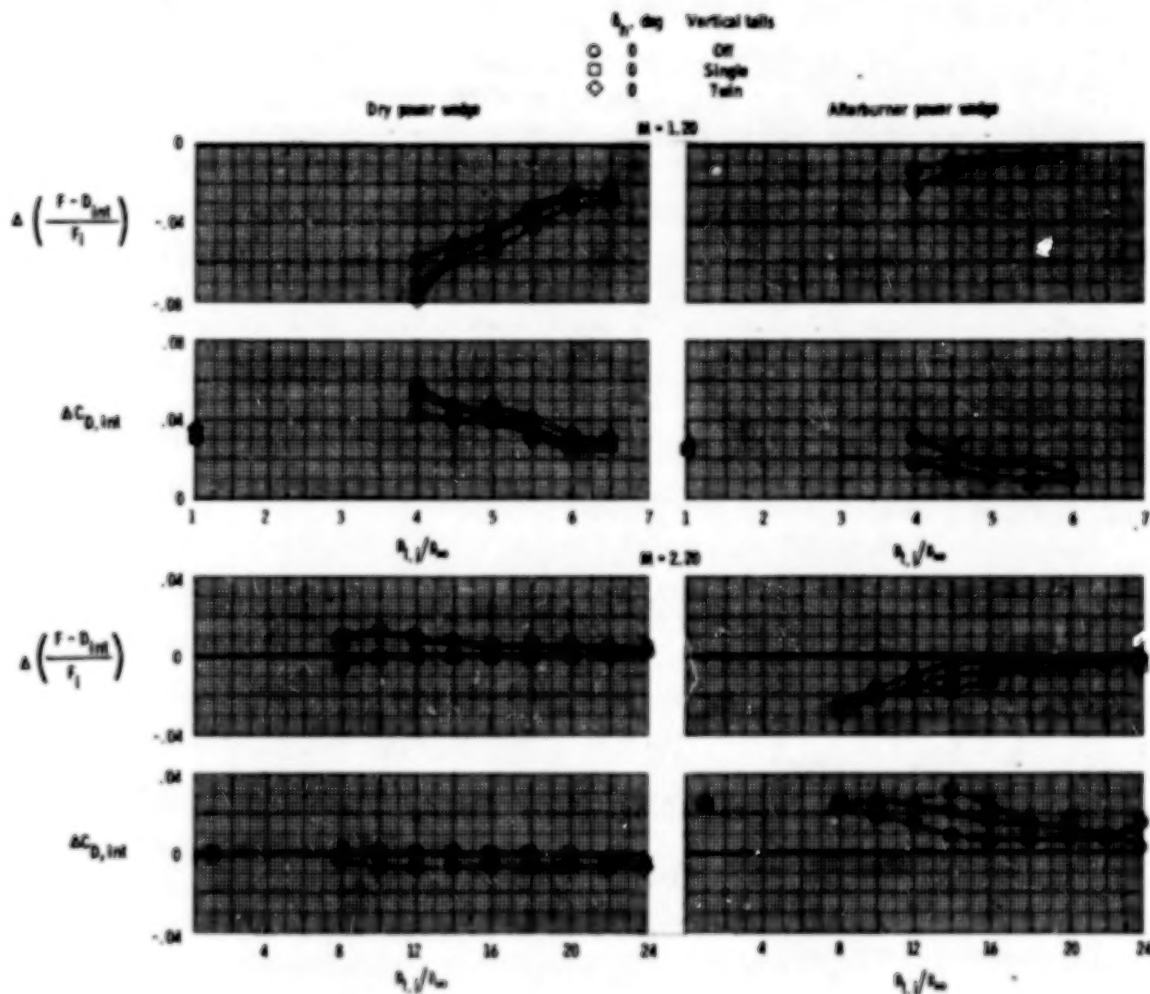
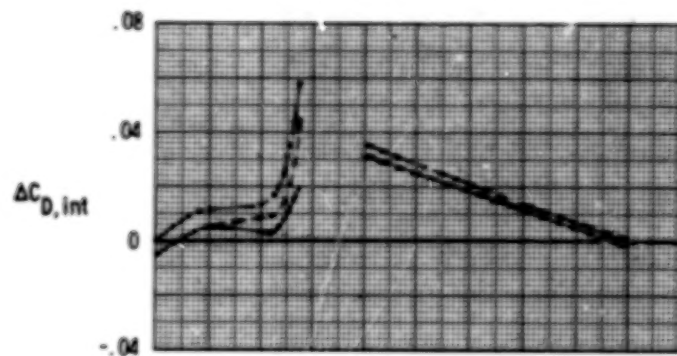


Figure 32.- Variation of tail interference parameter and incremental drag coefficient with pressure ratio for supersonic Mach numbers. Solid symbols represent jet-off values.



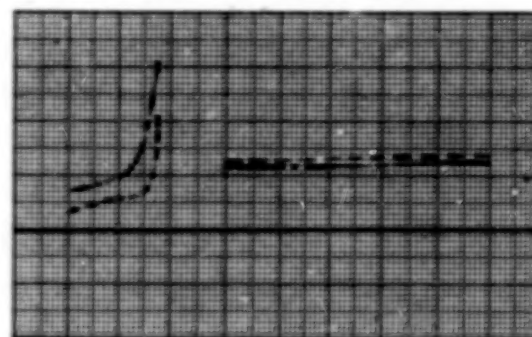
	$\delta_h$ , deg	Vertical tail
—	0	Off
- - -	0	Single
- · -	0	Twin

Dry power wedge



Jet-off

Afterburner power wedge



At scheduled pressure ratio

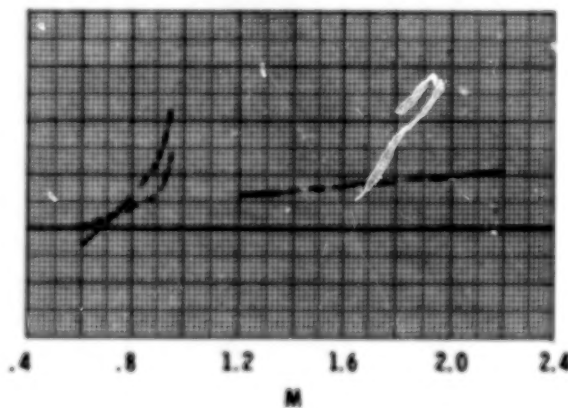
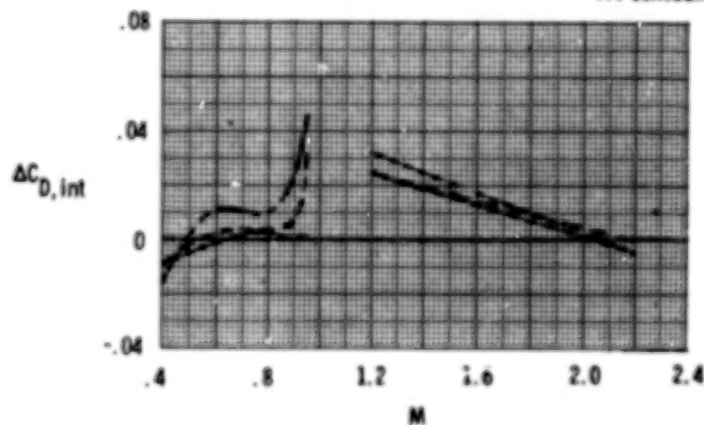
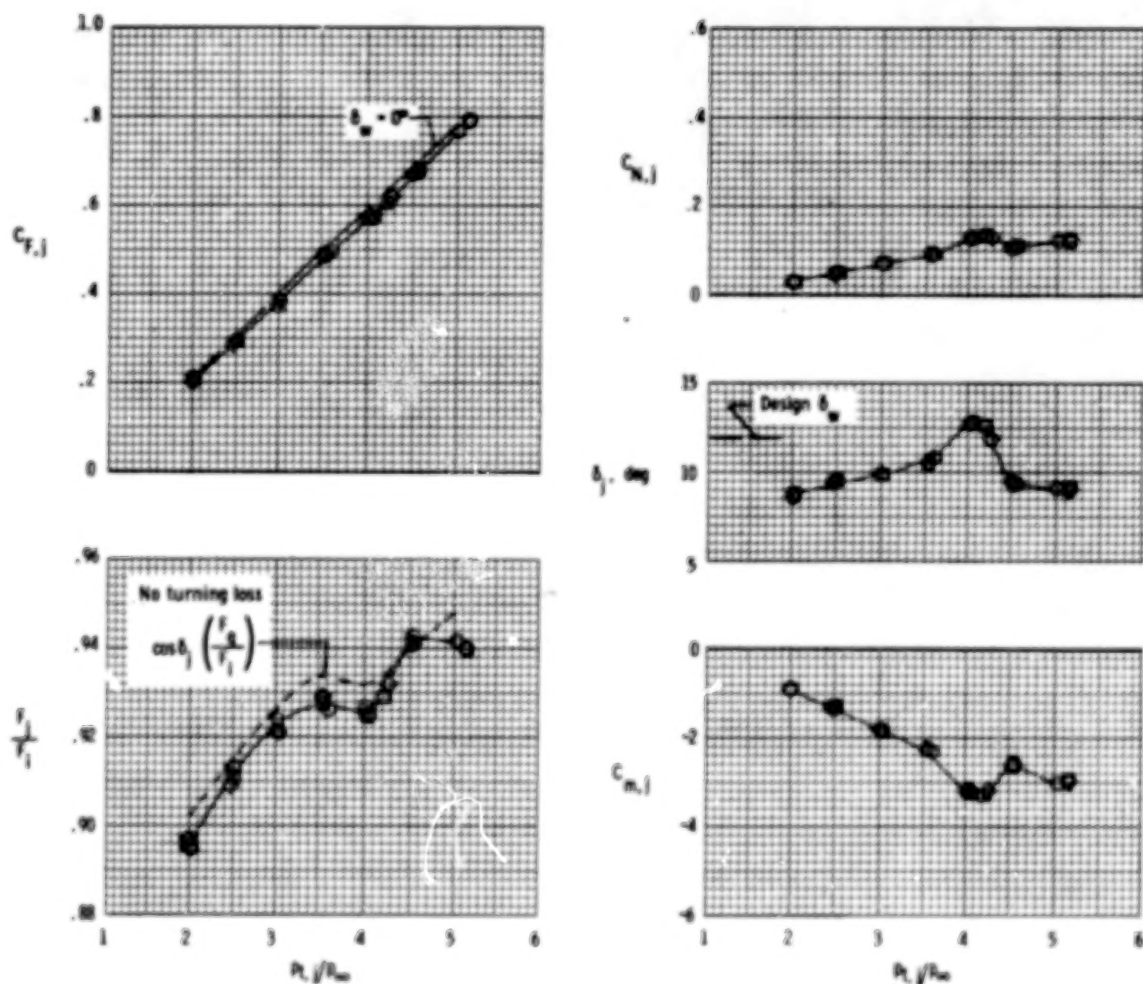
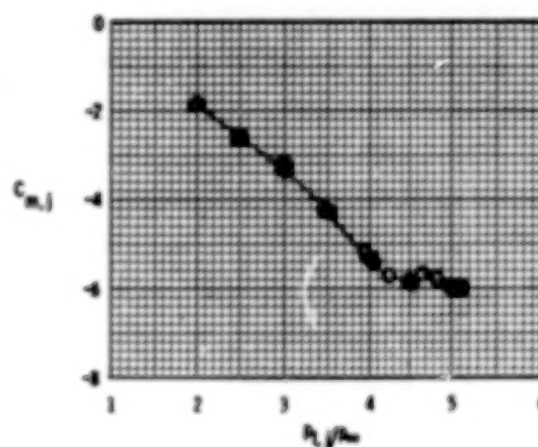
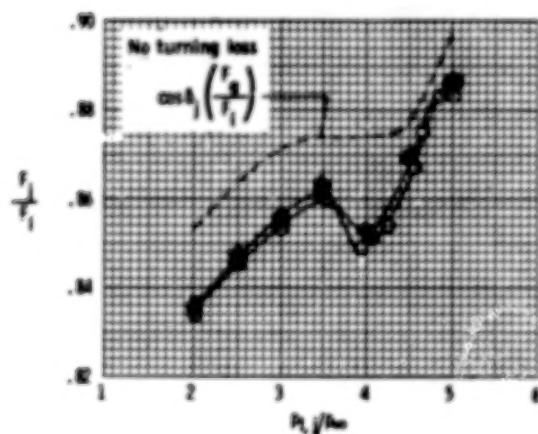
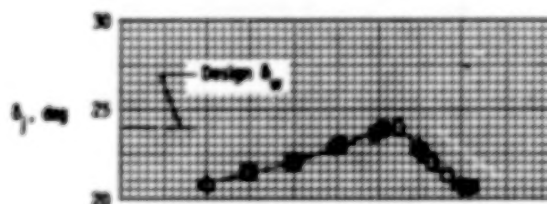
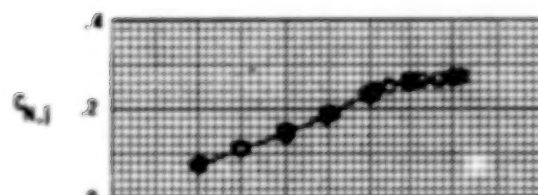
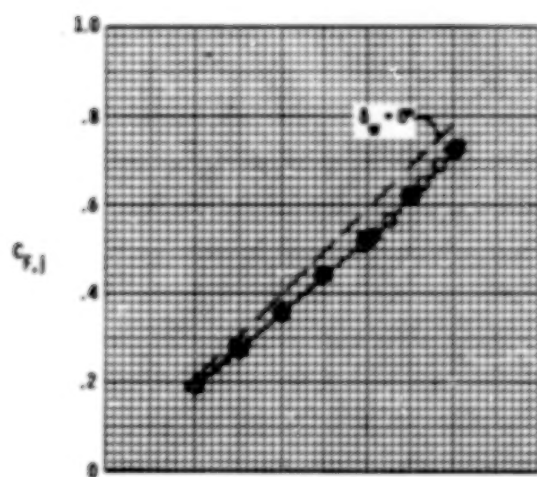


Figure 34.- Effect of tail installation on tail interference.



(a)  $\delta_w = 12^\circ$ .

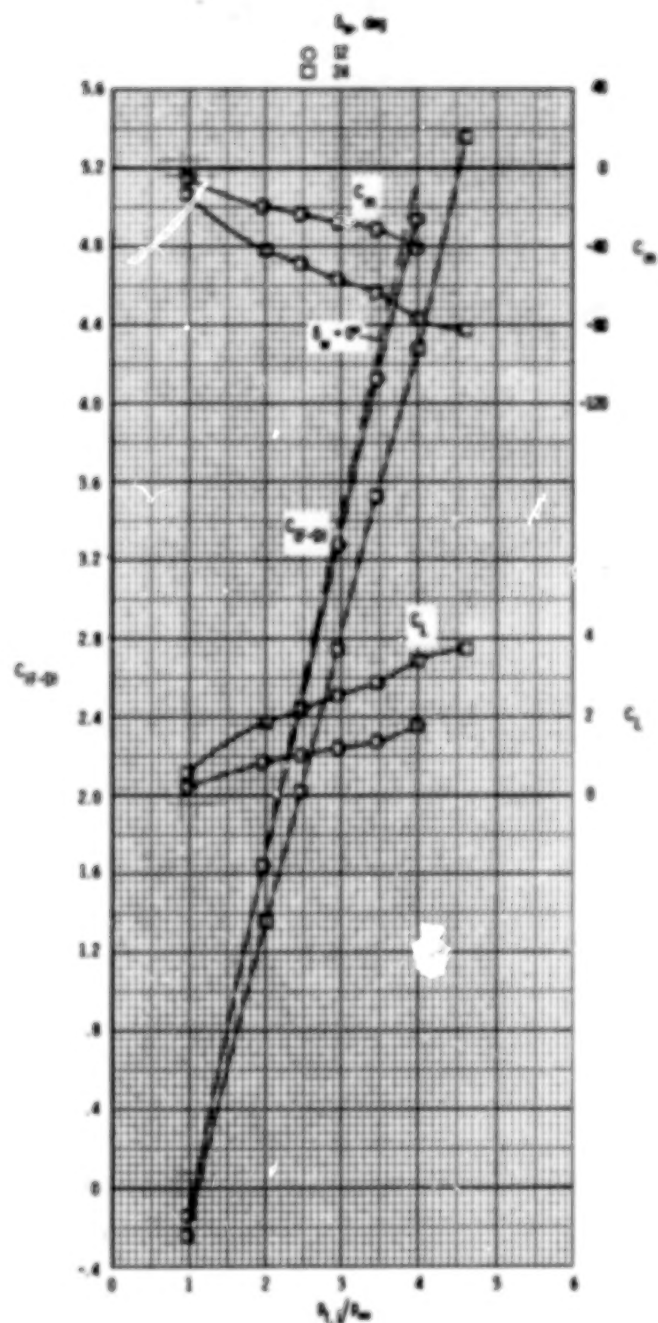
Figure 35.- Static thrust vectoring characteristics for dry power nozzle. Symbols represent various static runs.



(b)  $\delta_w = 24^\circ$ .

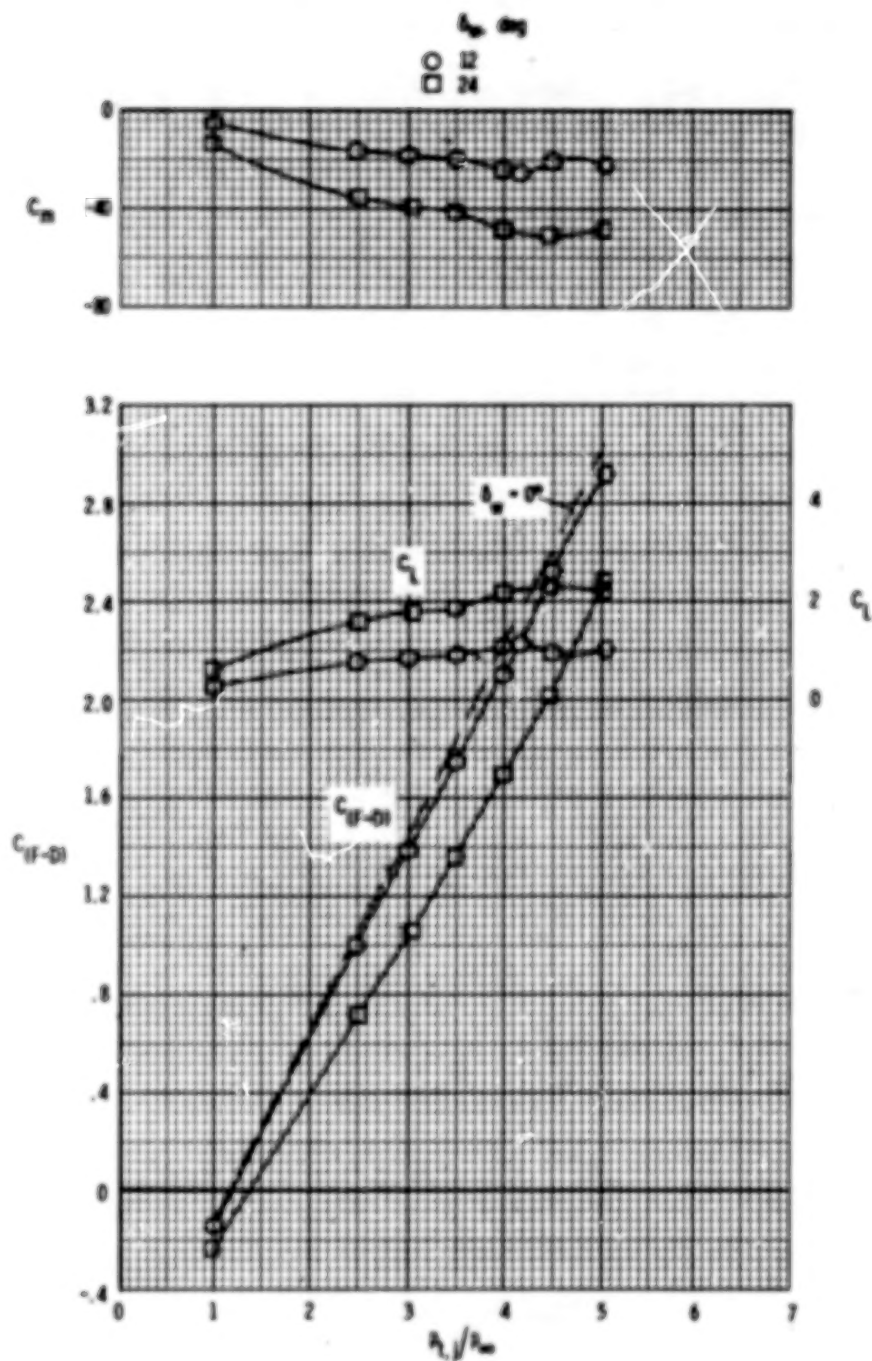
Figure 35.- Concluded.





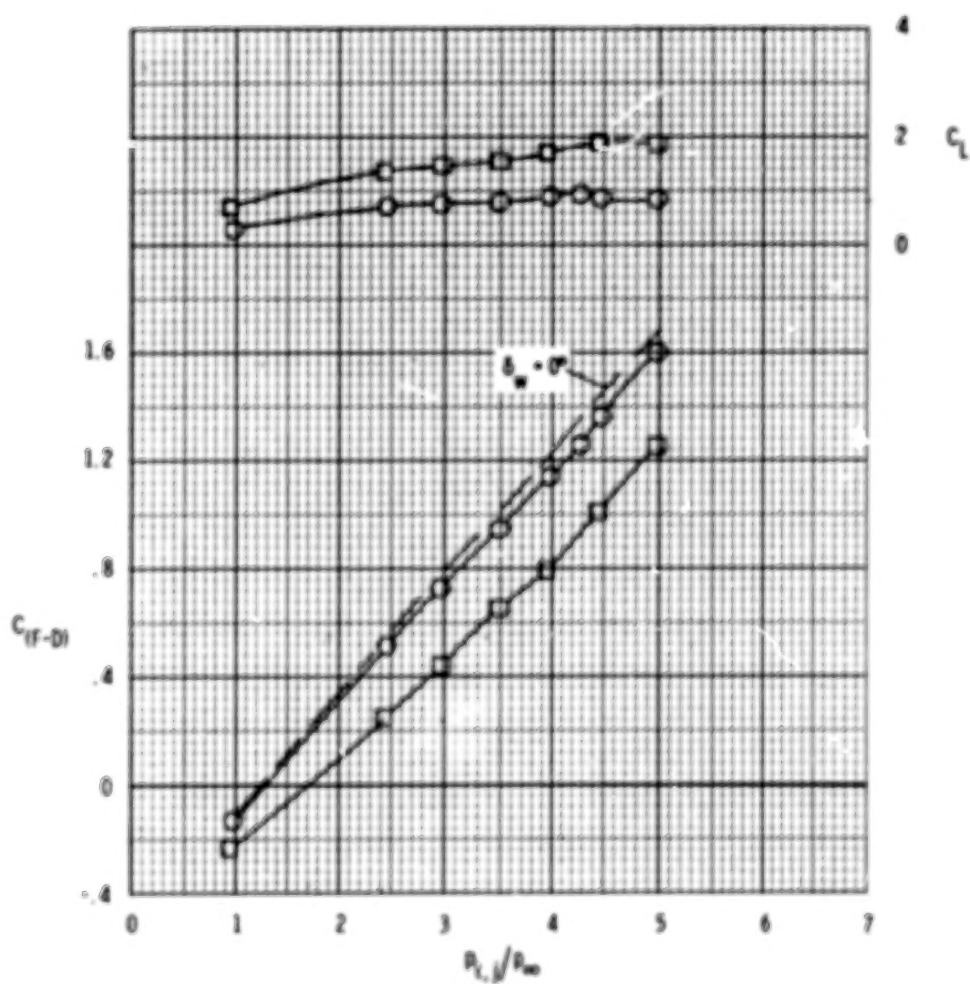
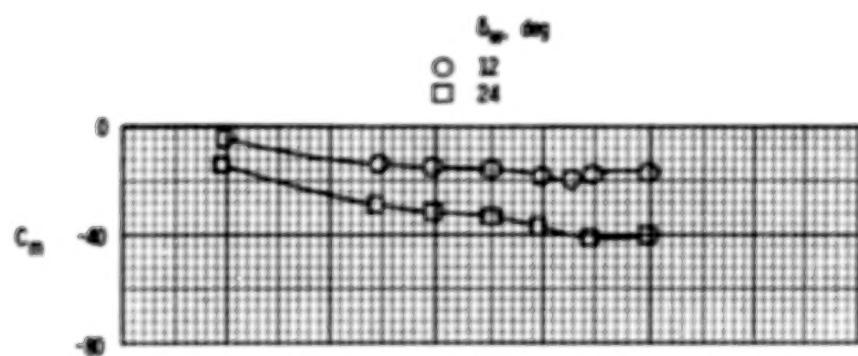
(a)  $M = 0.40$ ;  $\alpha = 0^\circ$ .

Figure 36.- Effect of thrust vectoring on aerodynamic characteristics. No tails.



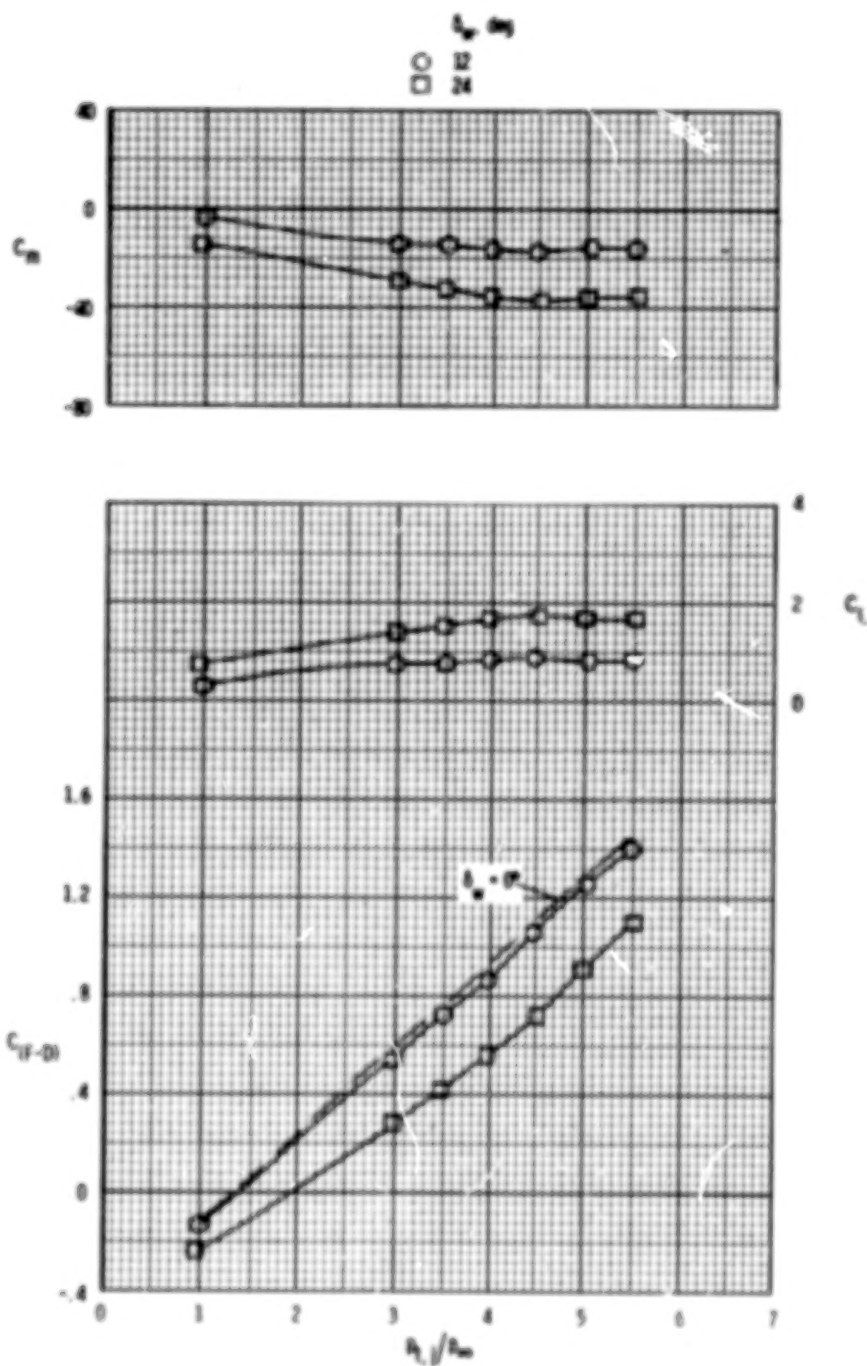
(b)  $M = 0.60$ ;  $\alpha = 0^\circ$ .

Figure 36.- Continued.



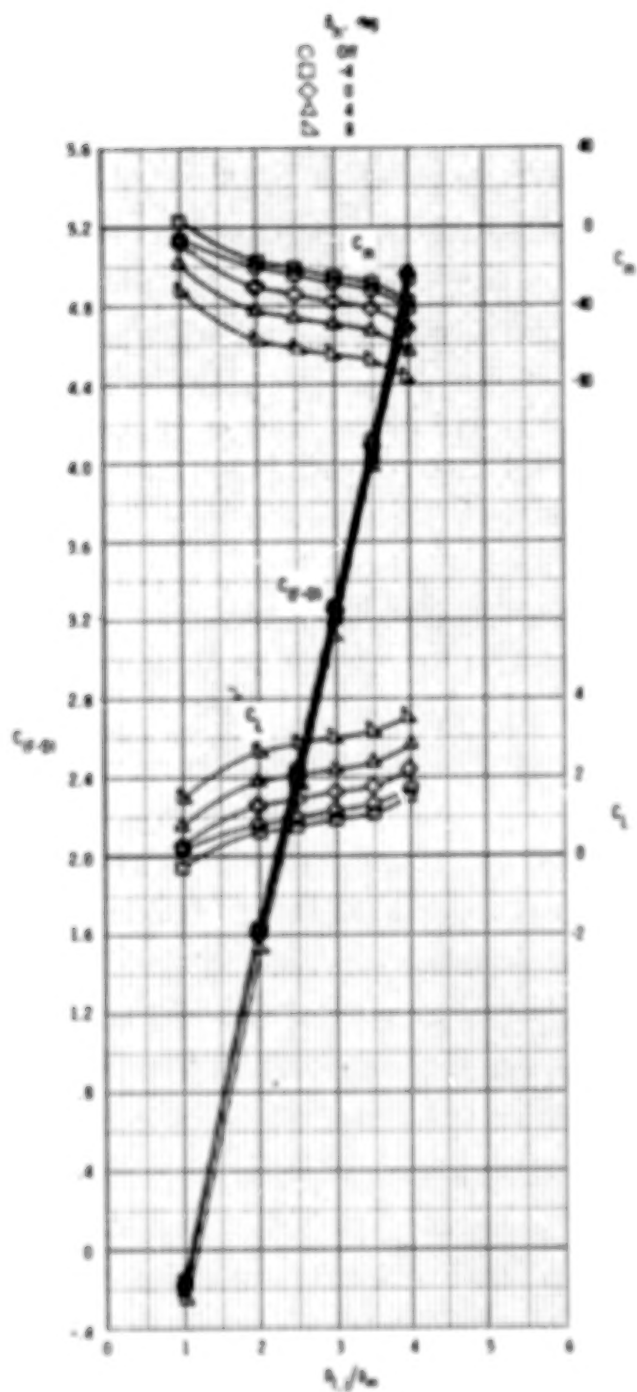
(c)  $M = 0.80$ ;  $\alpha = 0^\circ$ .

Figure 36.- Continued.



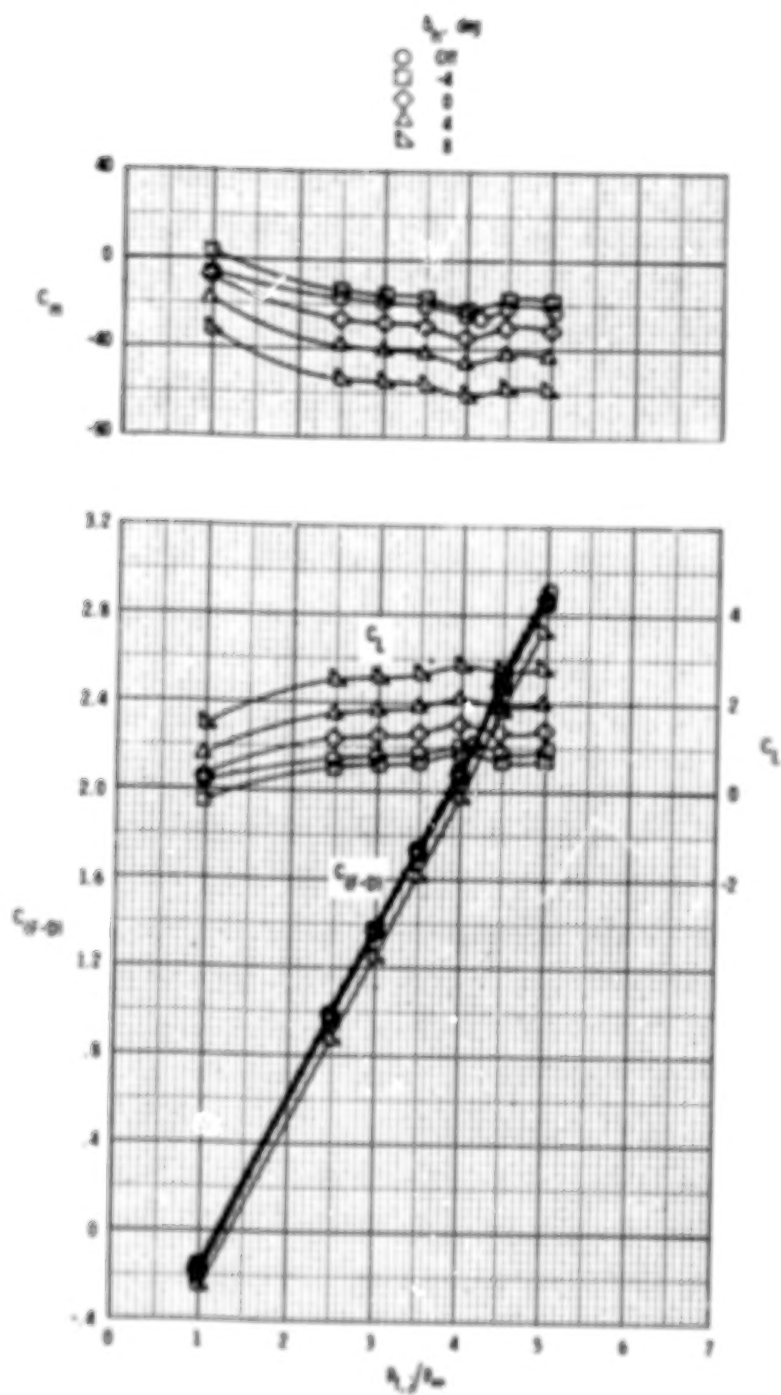
(d)  $M = 0.90$ ;  $\alpha = 0^\circ$ .

Figure 36.- Concluded.



(a)  $M = 0.40$ ;  $\alpha = 0^\circ$ .

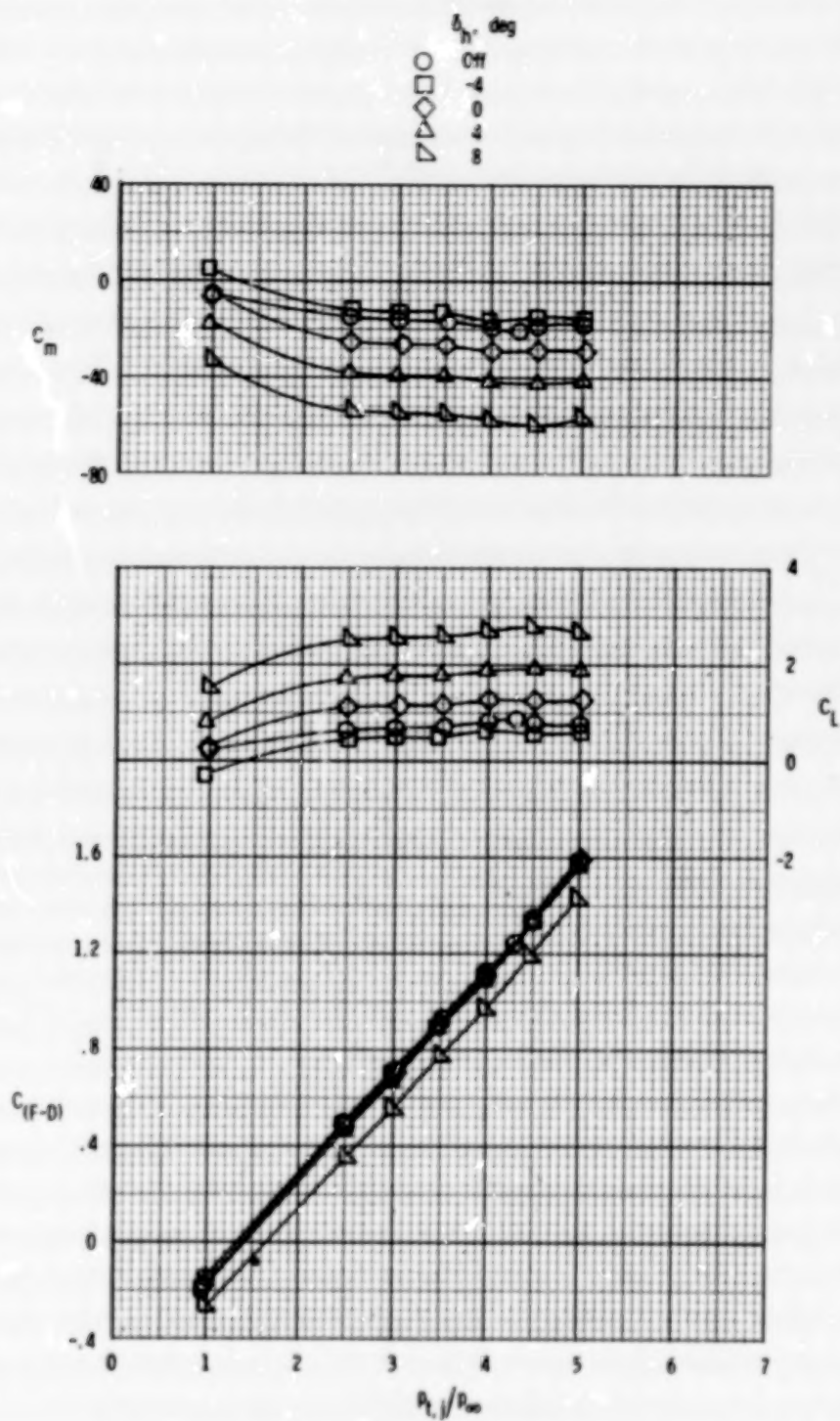
Figure 37.- Effect of horizontal-tail deflection with  $12^\circ$  thrust vectoring. Vertical tails off.



(b)  $M = 0.60$ ;  $\alpha = 0^\circ$ .

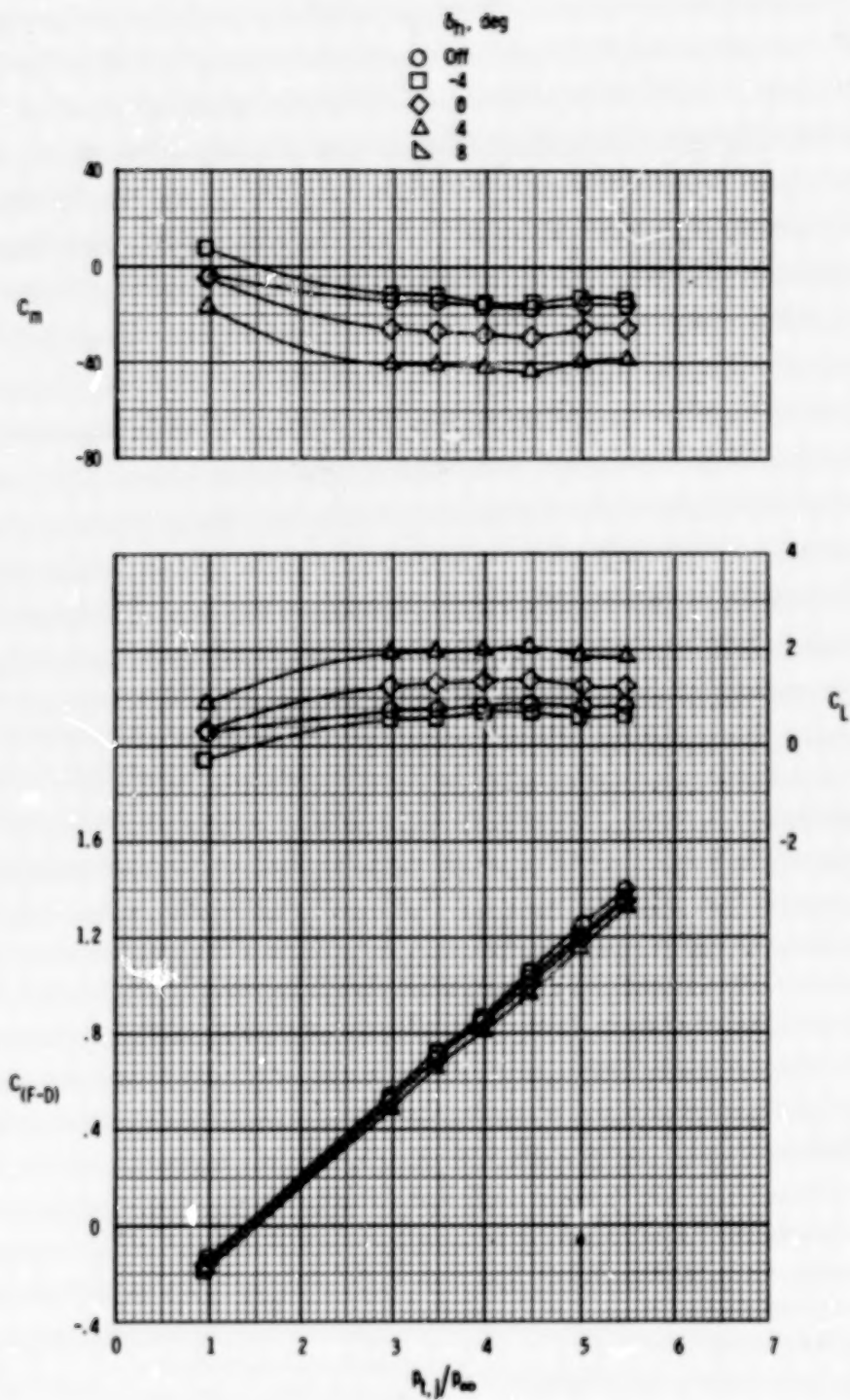
Figure 37.- Continued.





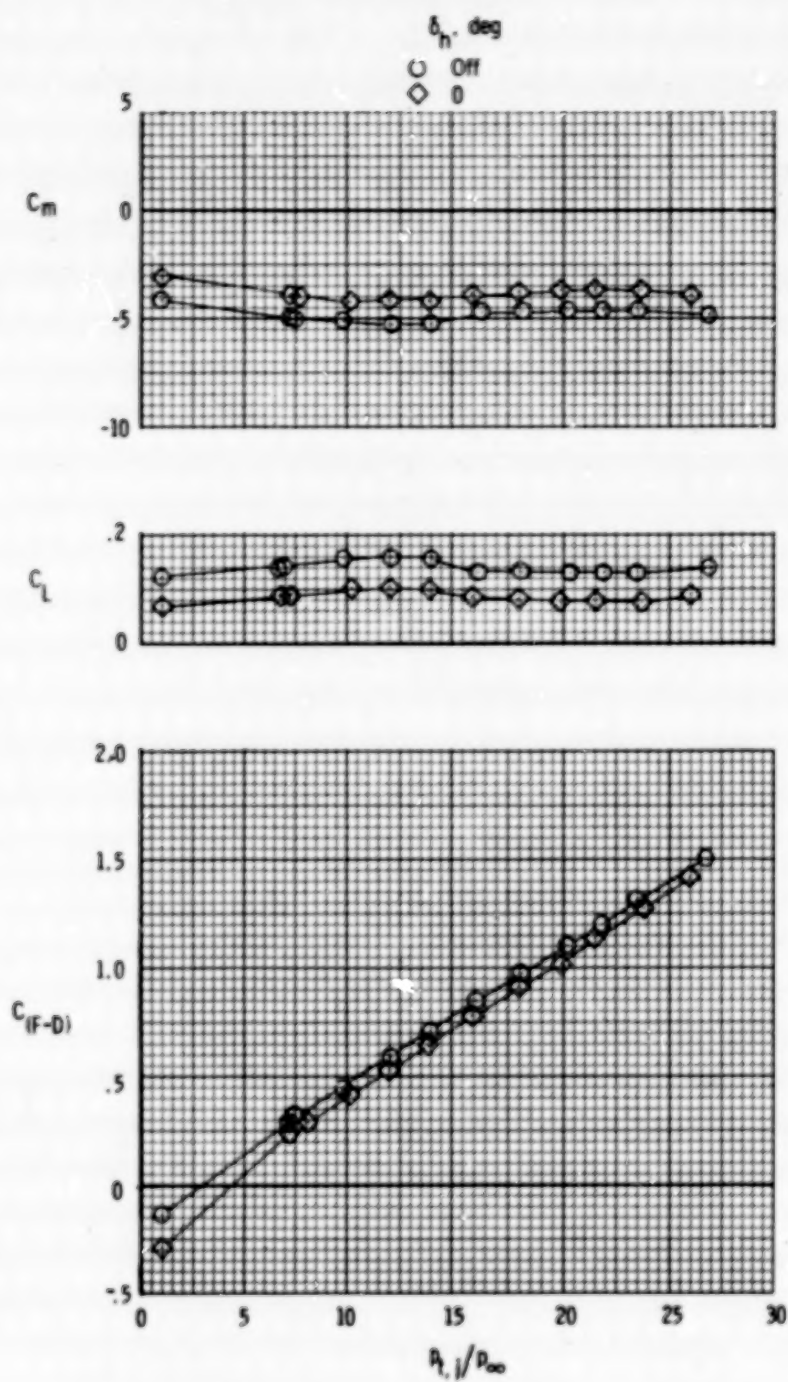
(c)  $M = 0.80$ ;  $\alpha = 0^\circ$ .

Figure 37.- Continued.



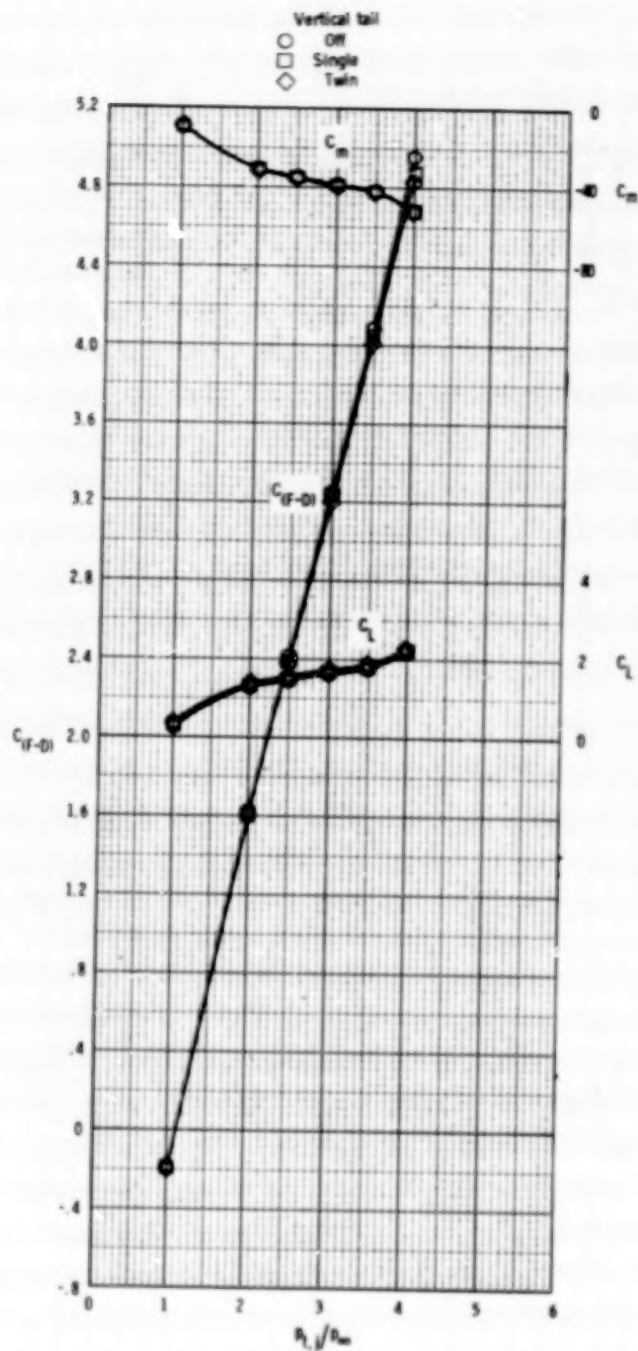
(d)  $M = 0.90$ ;  $\alpha = 0^\circ$

Figure 37.- Continued.



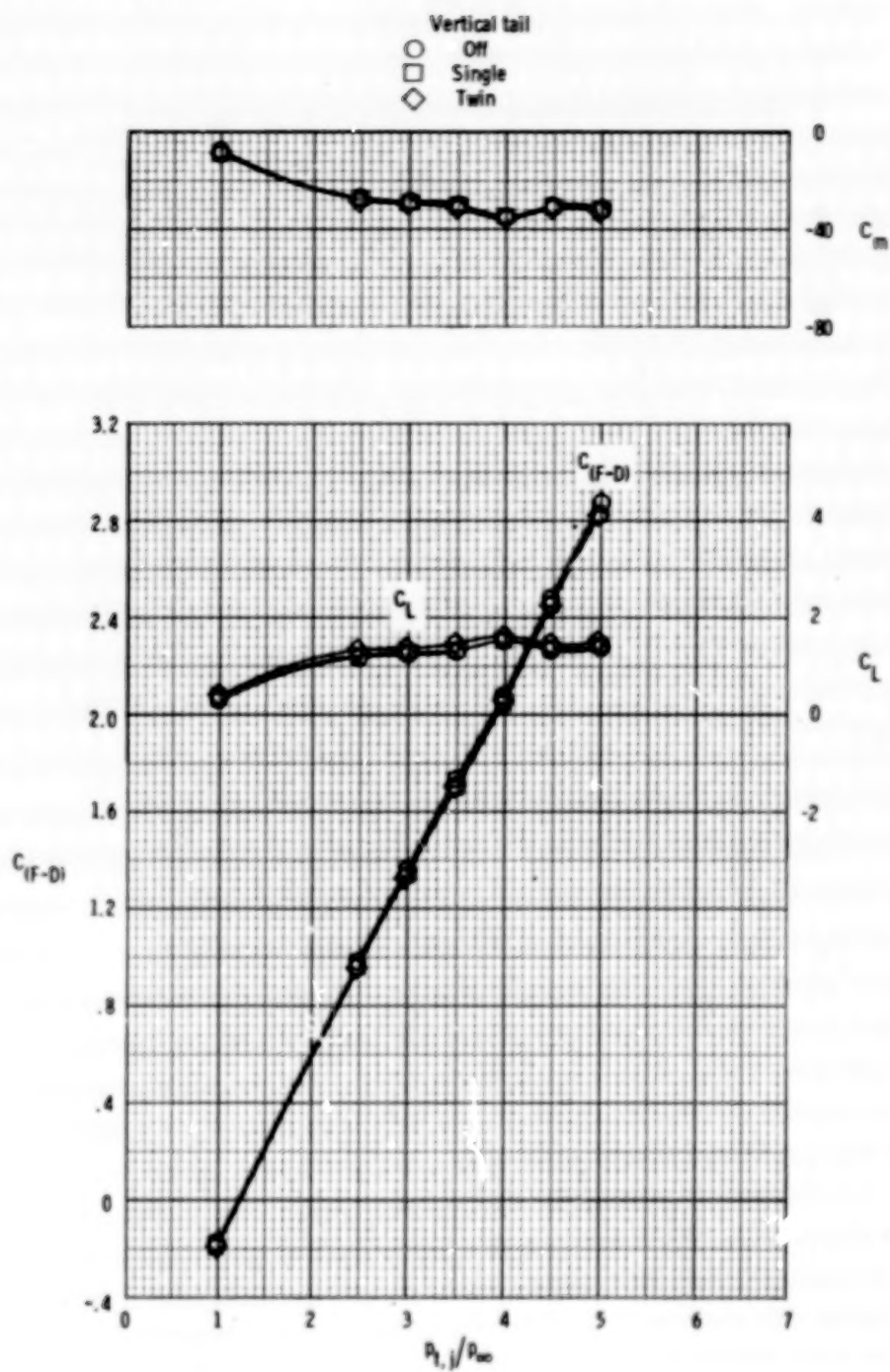
(e)  $M = 2.20$ ;  $\alpha = 0^\circ$ .

Figure 37.- Concluded.



(a)  $M = 0.40$ ;  $\alpha = 0^\circ$ .

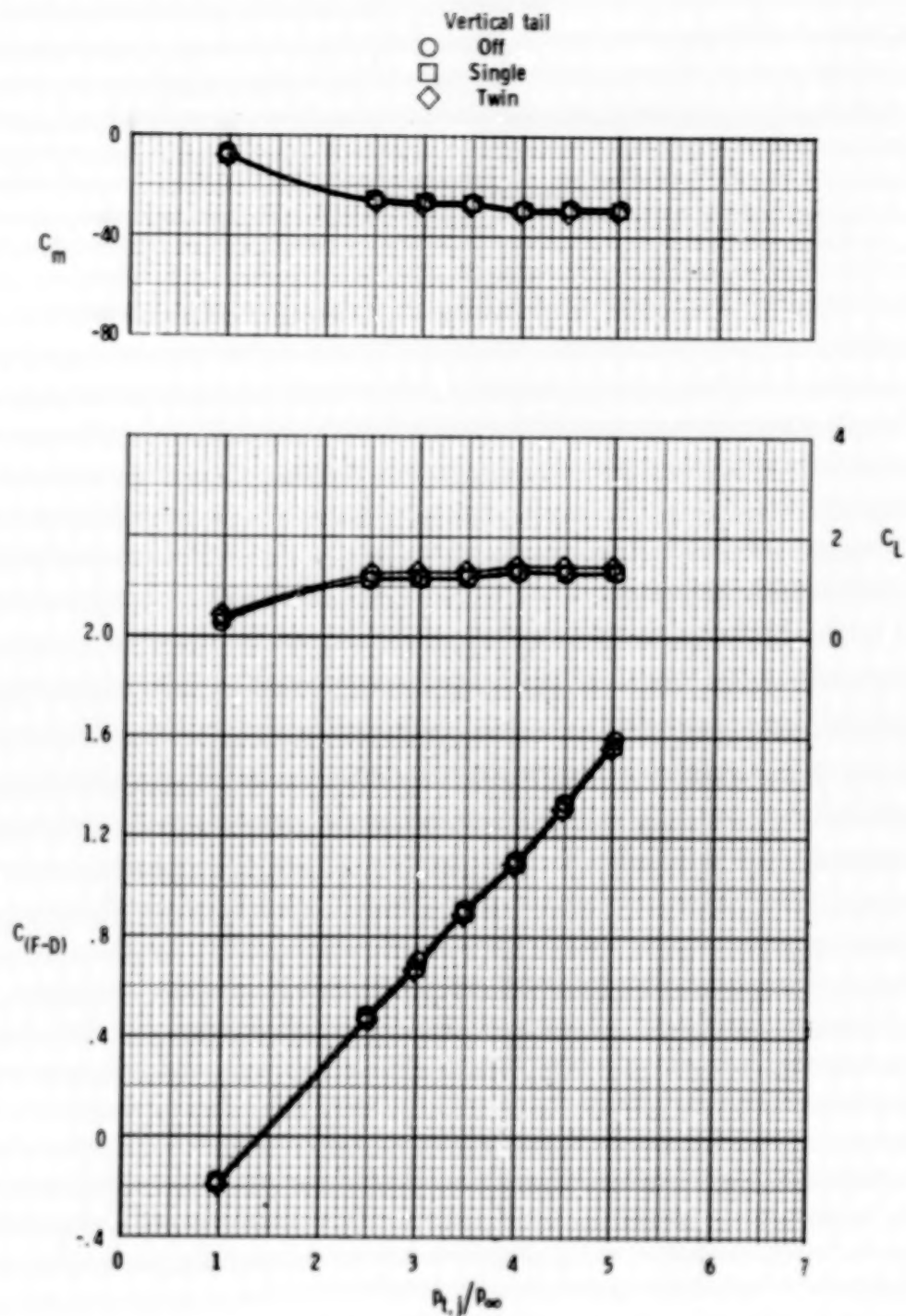
Figure 38.- Effect of vertical-tail installation on  $12^\circ$  wedge thrust vectoring characteristics.



(b)  $M = 0.60$ ;  $\alpha = 0^\circ$ .

Figure 38.- Continued.

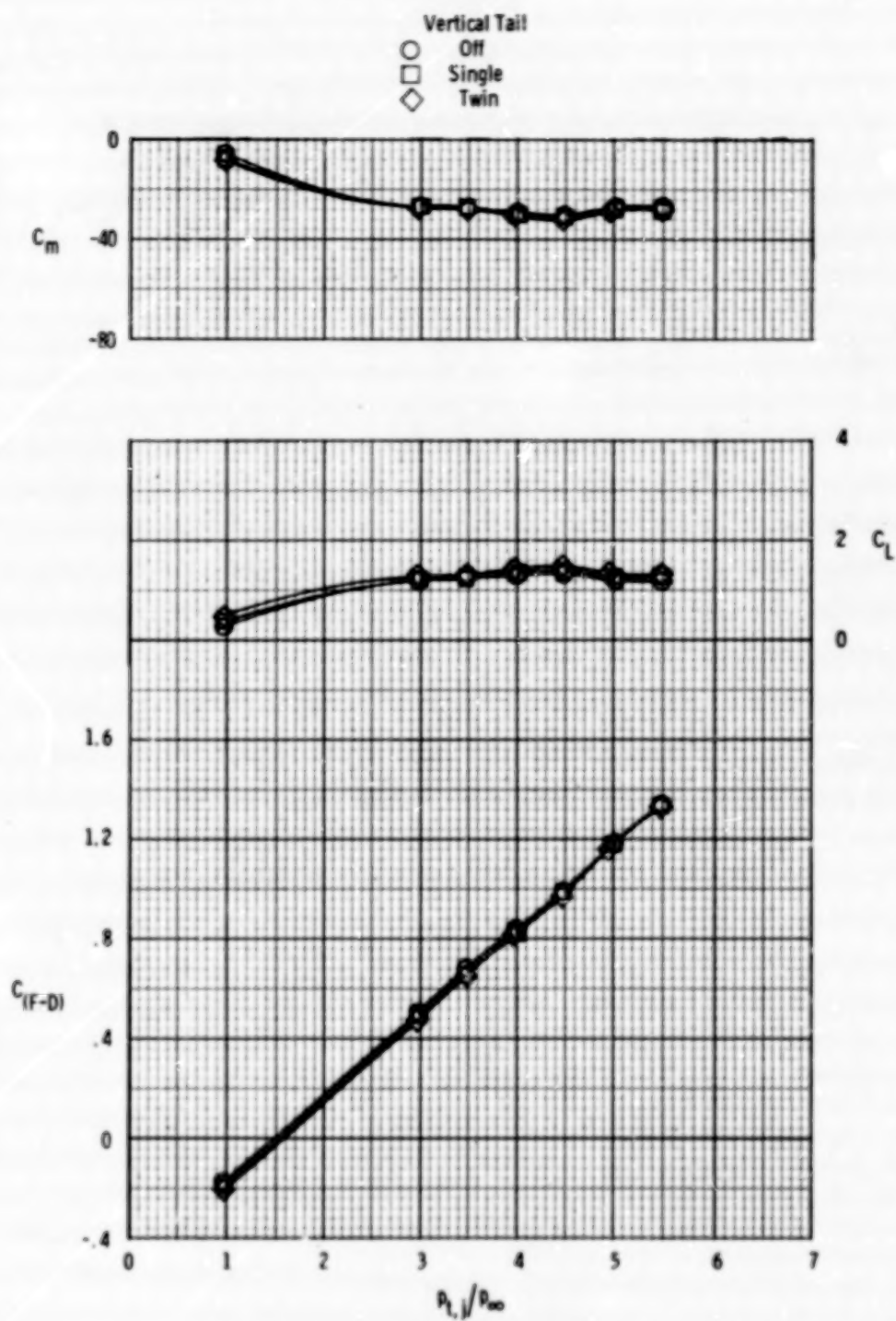




(c)  $M = 0.80$ ;  $\alpha = 0^\circ$ .

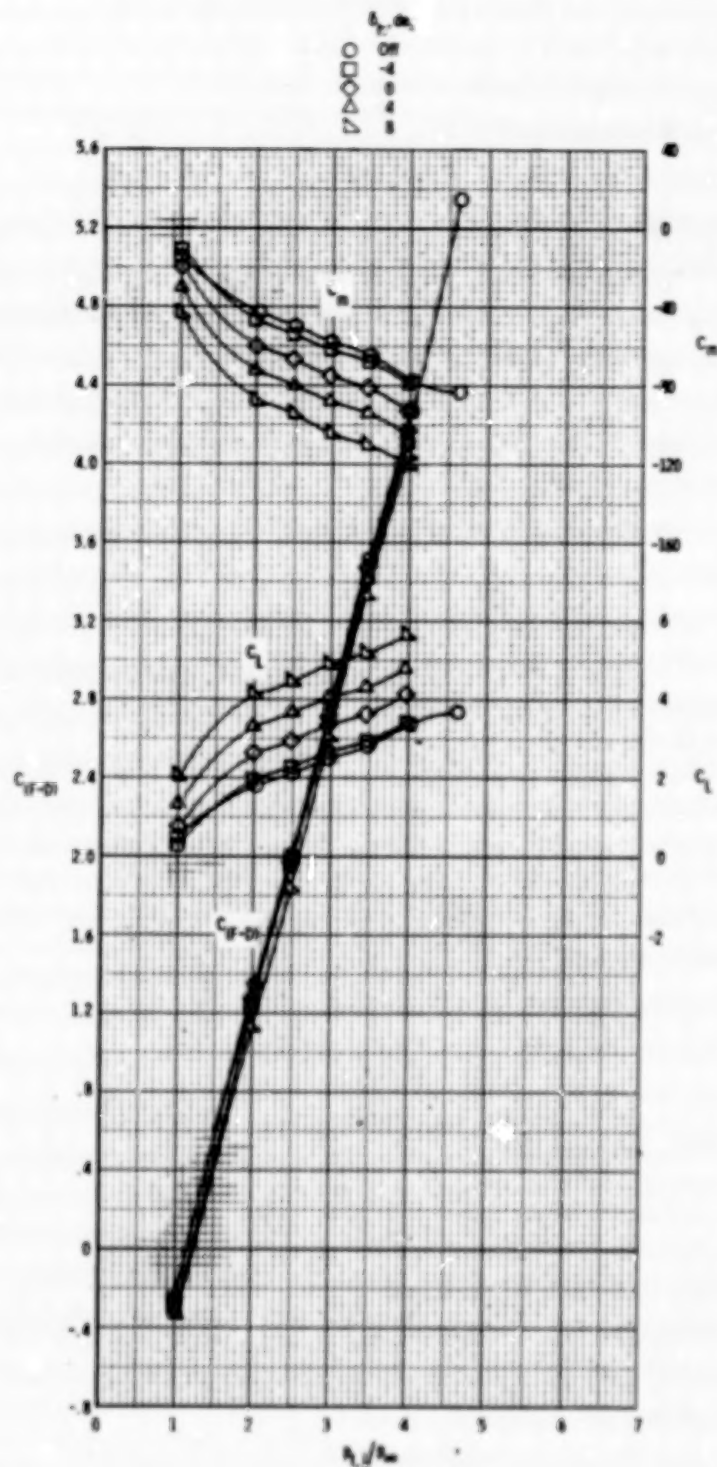
Figure 38.- Continued.





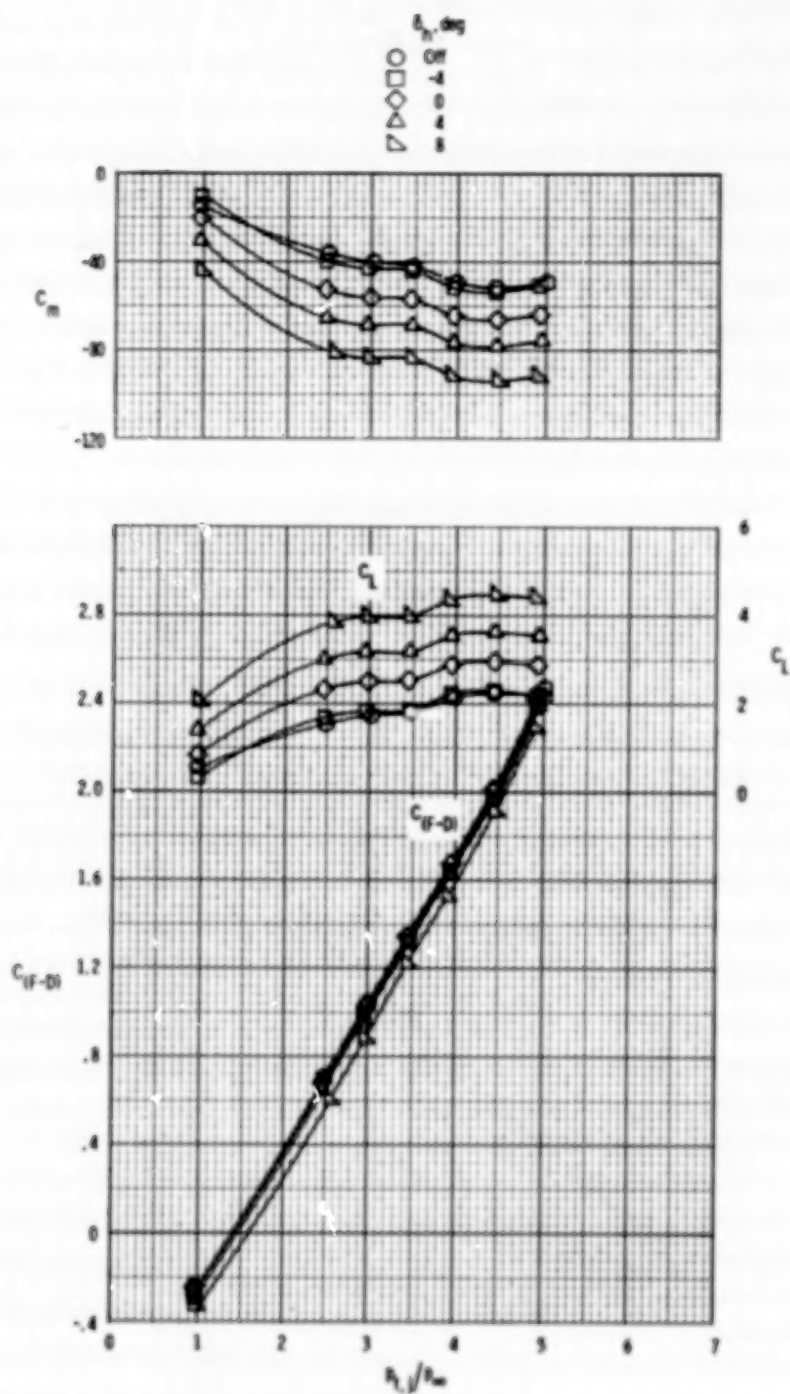
(d)  $M = 0.90$ ;  $\alpha = 0^\circ$ .

Figure 38.- Concluded.



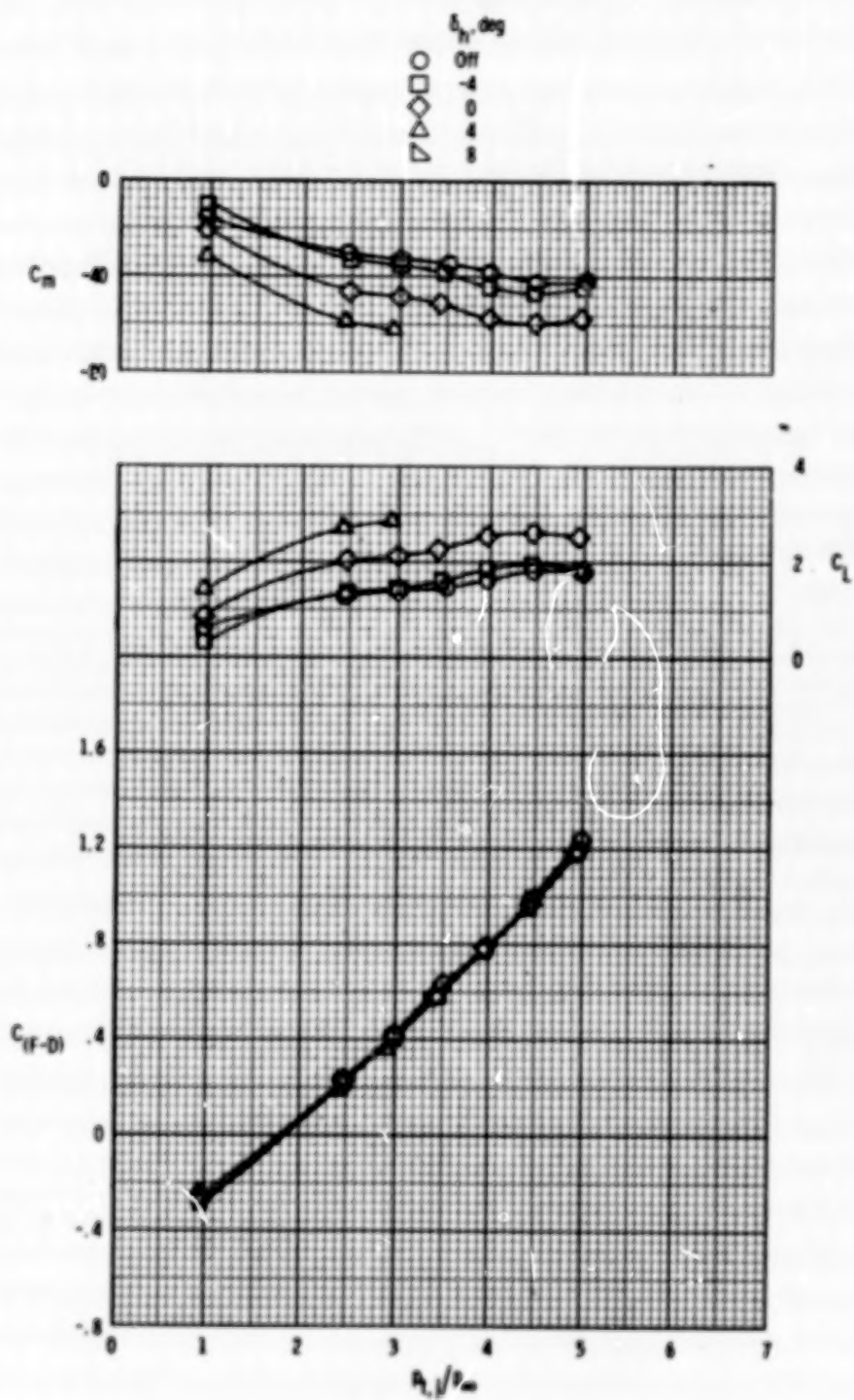
(a)  $M = 0.40$ ;  $\alpha = 0^\circ$ .

Figure 39.- Effect of horizontal-tail deflection on  $24^\circ$  wedge thrust vectoring characteristics.



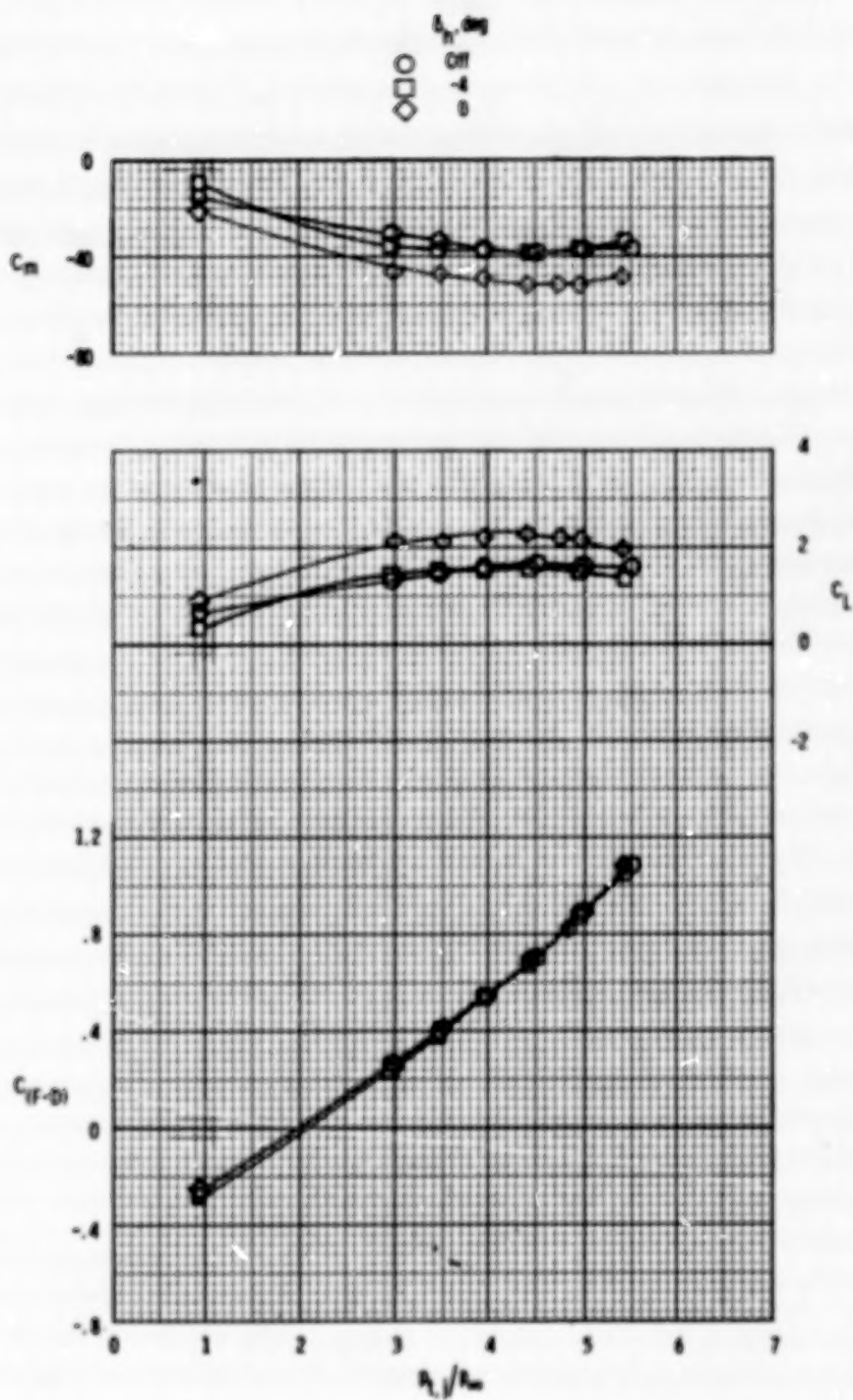
(b)  $M = 0.60$ ;  $\alpha = 0^\circ$ .

Figure 39.- Continued.



(c)  $M = 0.80$ ;  $\alpha = 0^\circ$ .

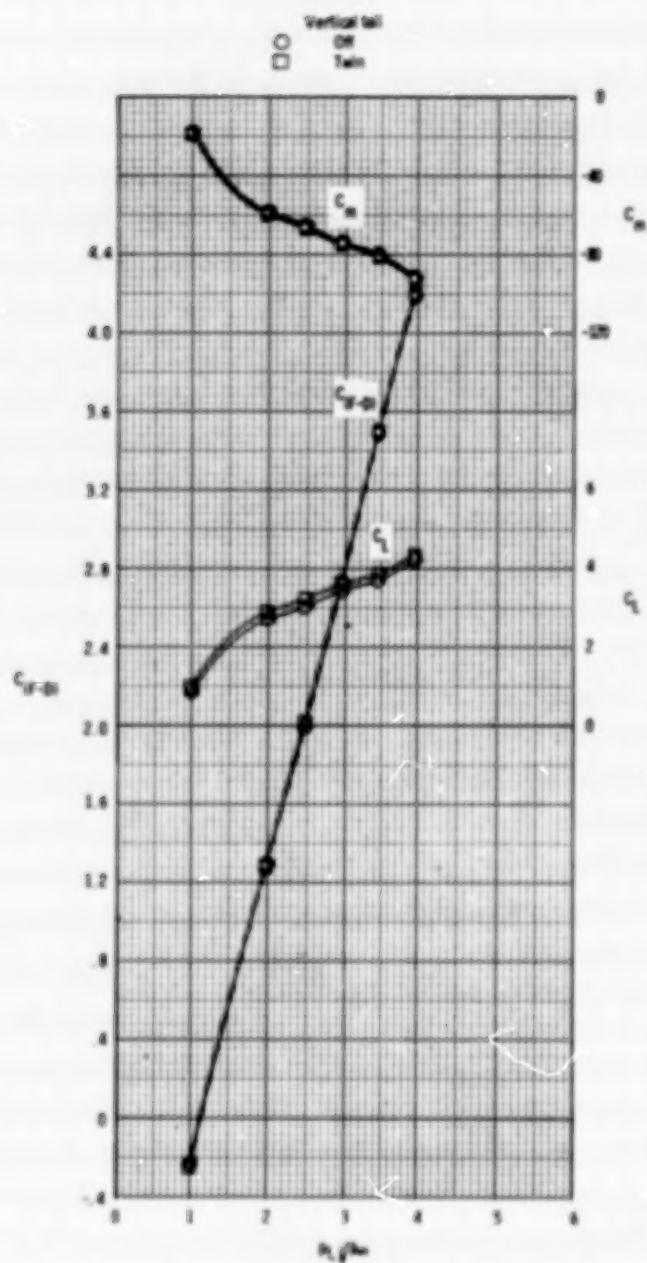
Figure 39.- Continued.



(d)  $M = 0.90$ ;  $\alpha = 0^\circ$ .

Figure 39.- Concluded.

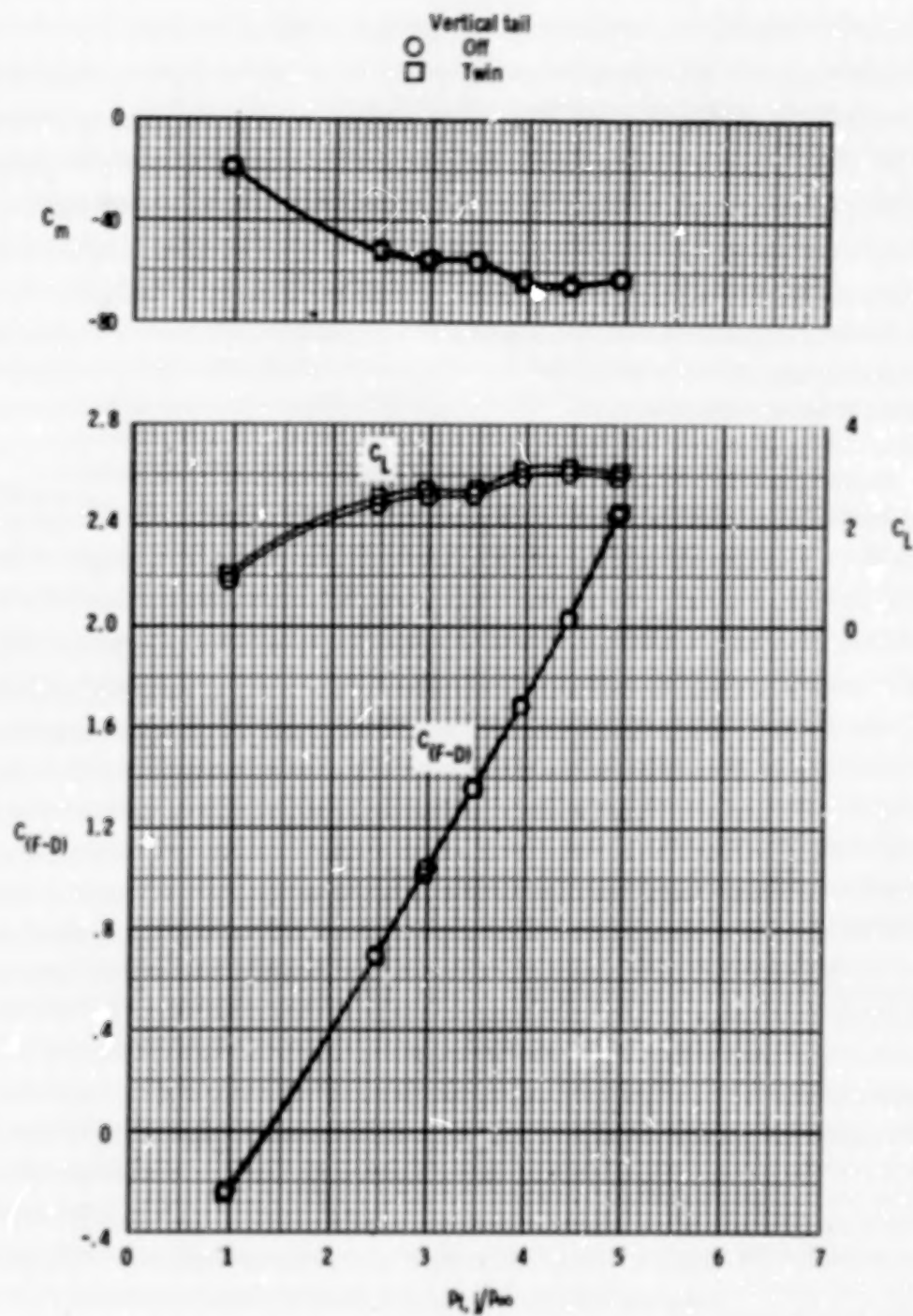




(a)  $M = 0.40$ ;  $\alpha = 0^\circ$ .

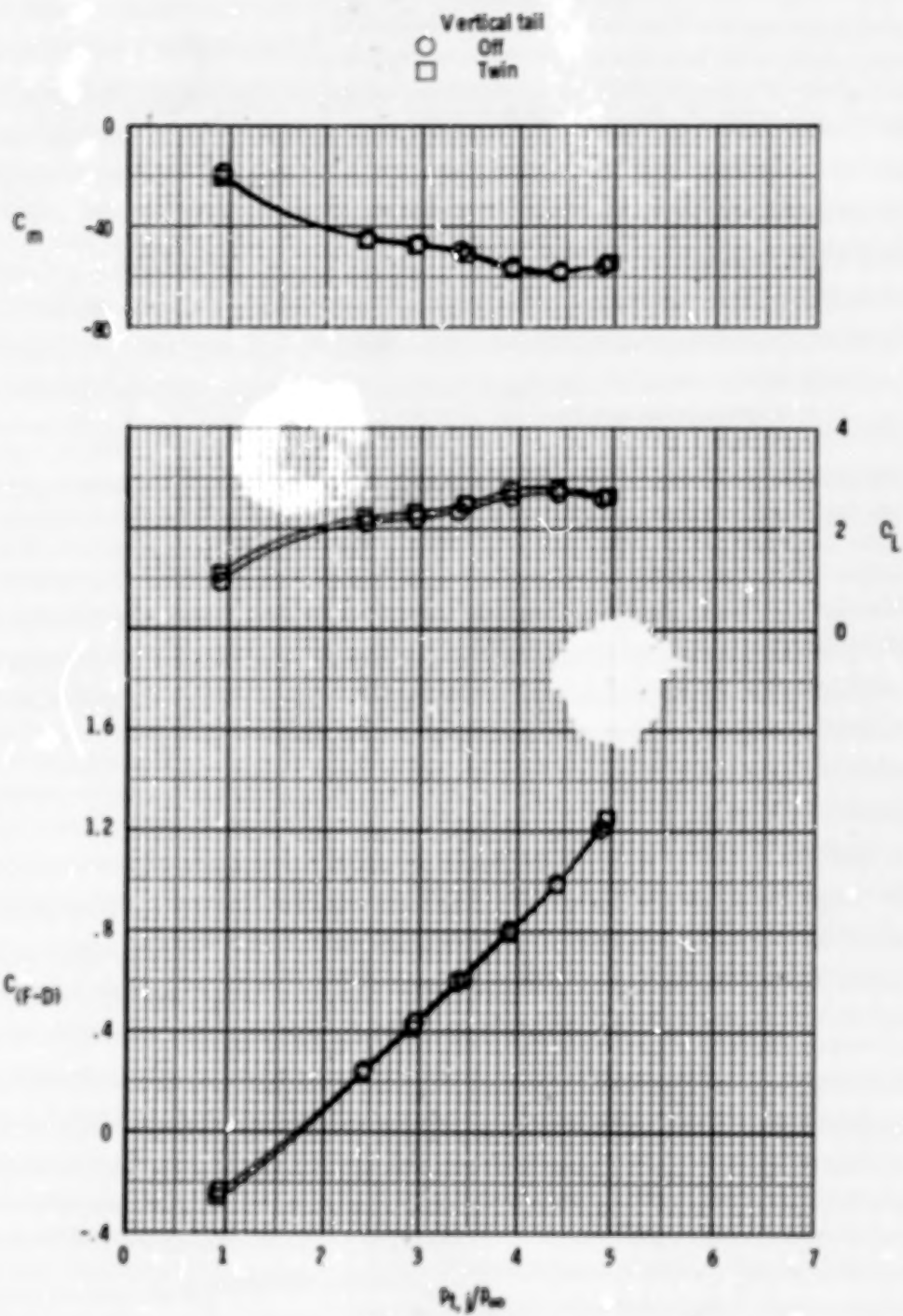
Figure 40.- Effect of twin vertical-tail installation on  $24^\circ$  wedge thrust vectoring characteristics.





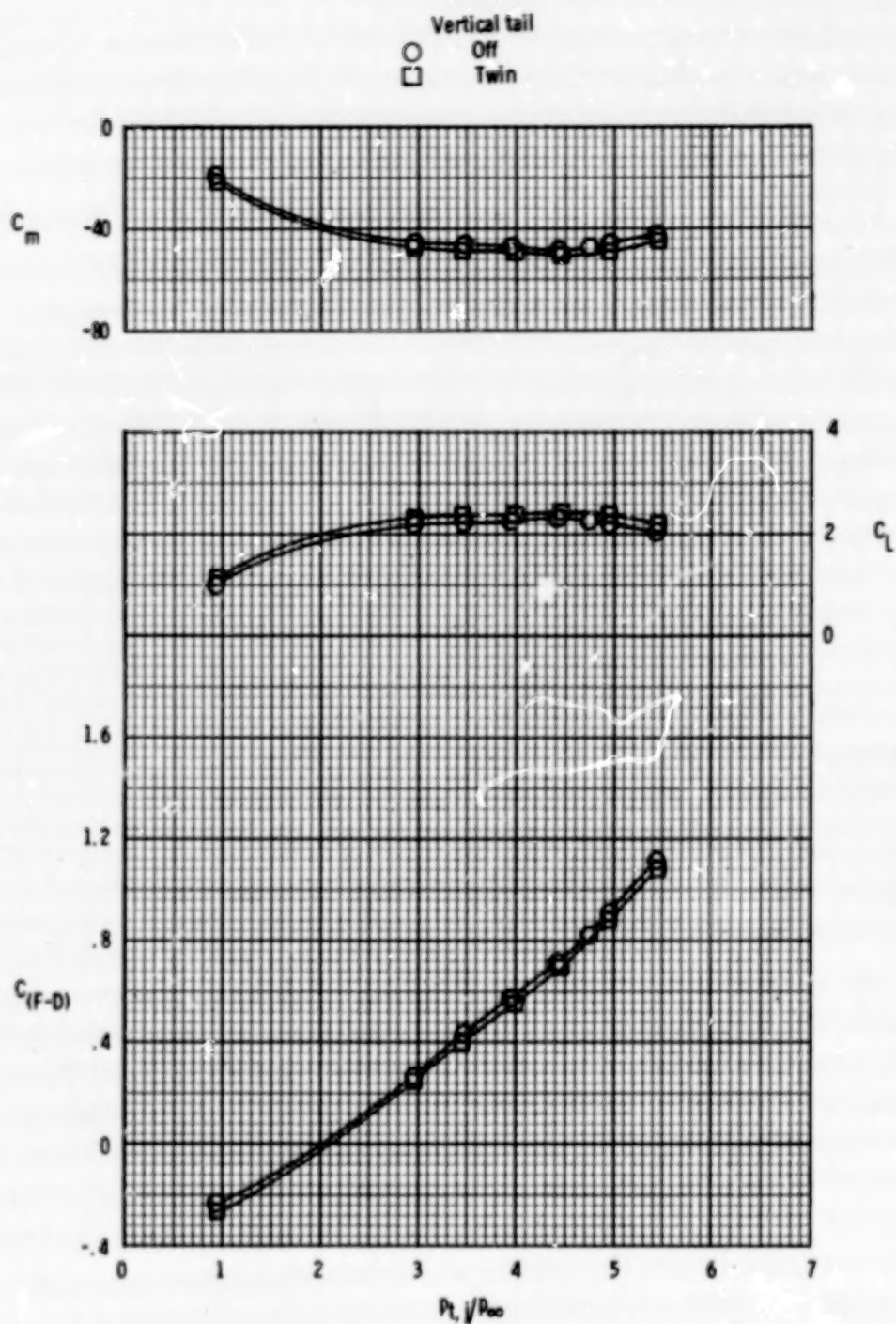
(b)  $M = 0.60$ ;  $\alpha = 0^\circ$ .

Figure 40.- Continued.



(c)  $M = 0.80$ ;  $\alpha = 0^\circ$ .

Figure 40.- Continued.



(d)  $M = 0.90$ ;  $\alpha = 0^\circ$ .

Figure 40.- Concluded.







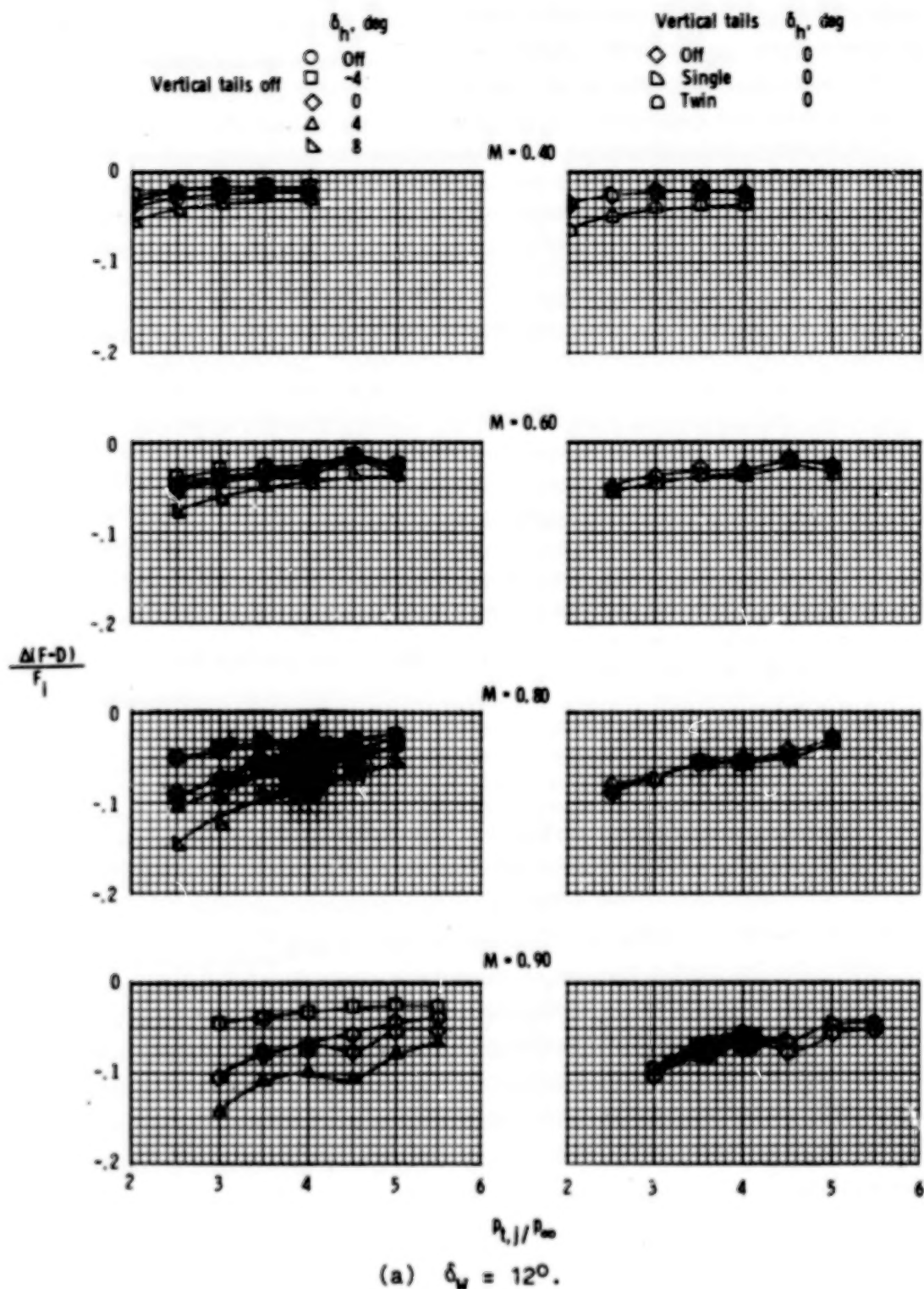
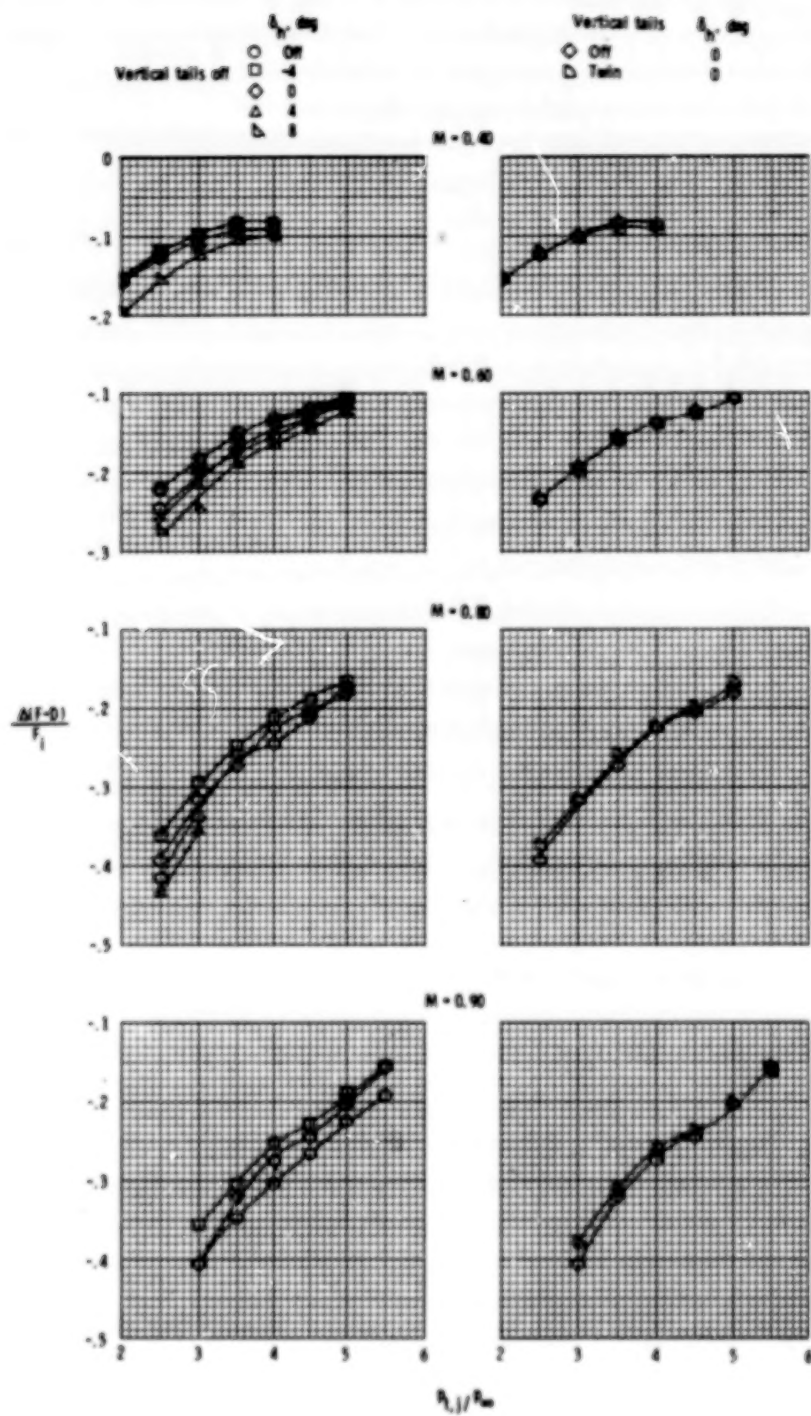


Figure 42.- Effect of thrust vectoring variation on incremental thrust-minus-drag characteristics for various configurations.





(b)  $\delta_w = 24^\circ$ .

Figure 42.- Concluded.

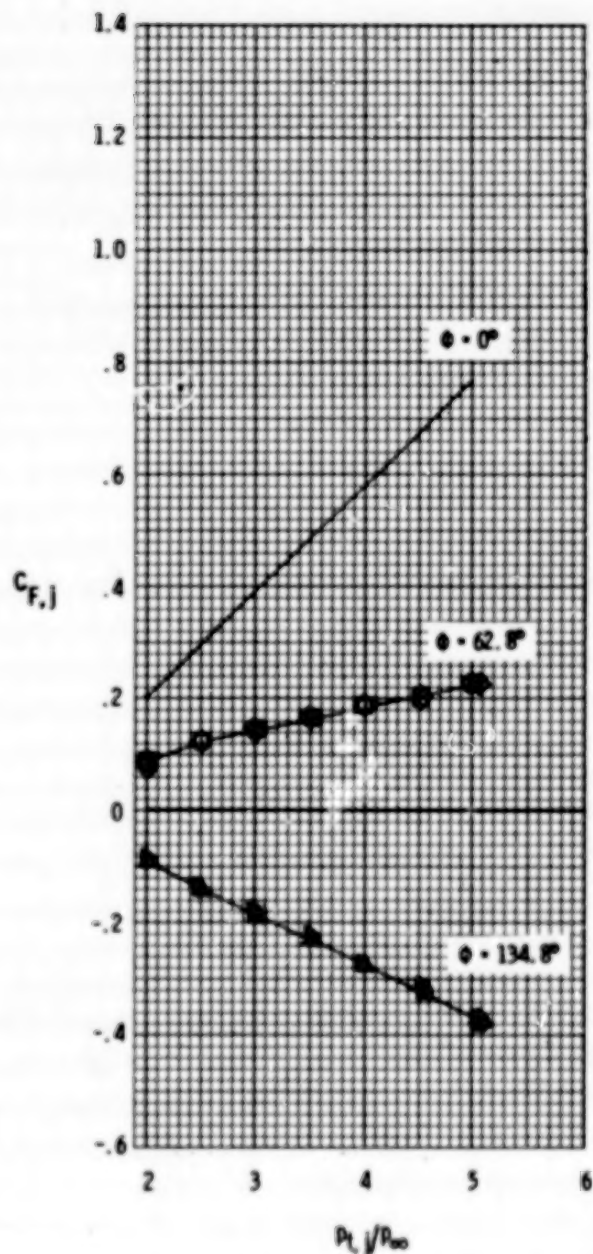
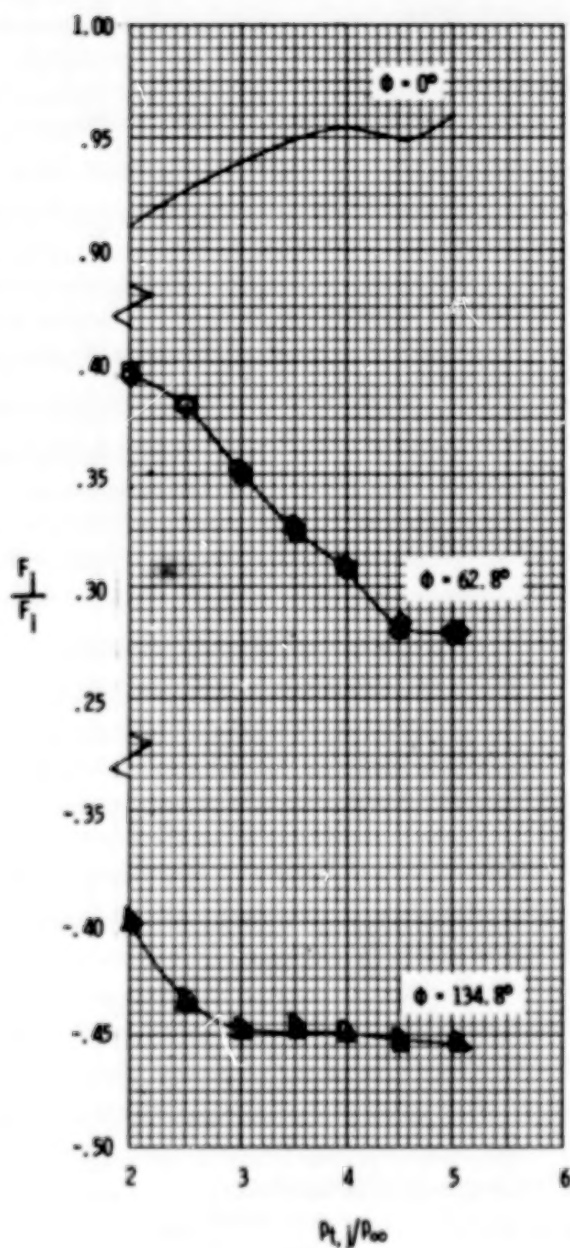


Figure 43.- Static reverse-thrust characteristics for dry power nozzle. Symbols represent various static runs.

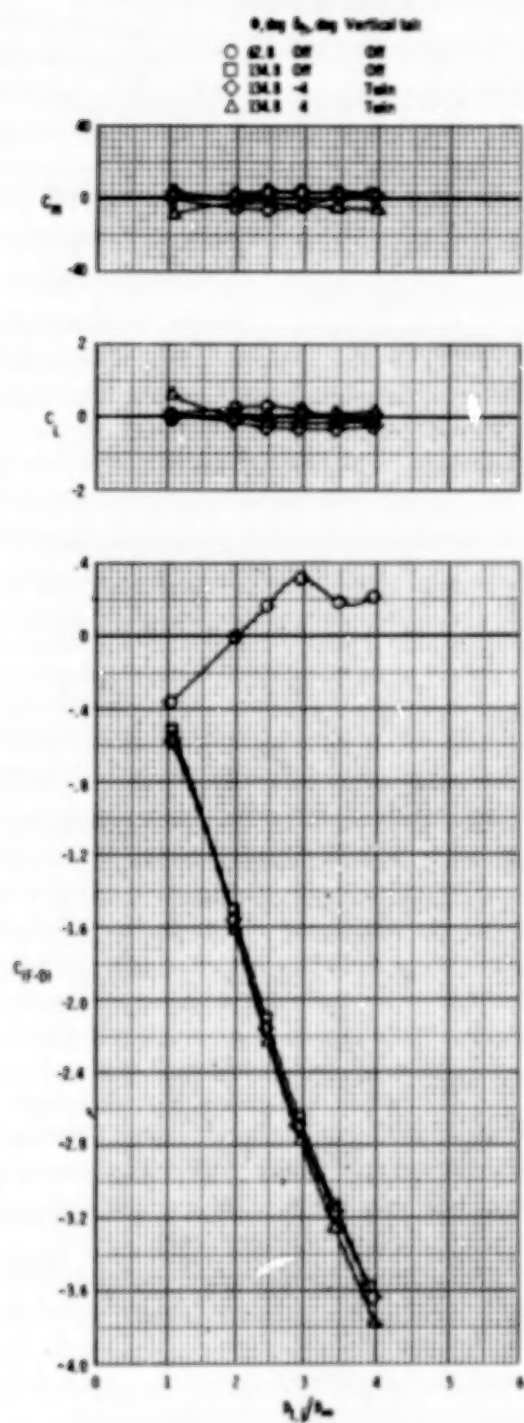
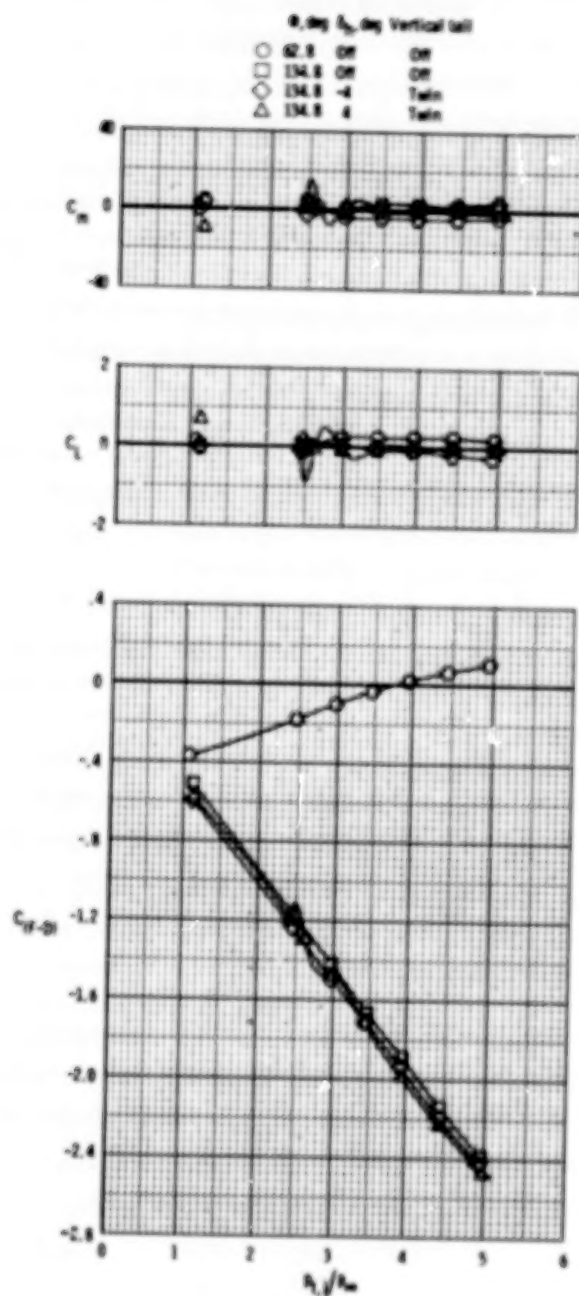
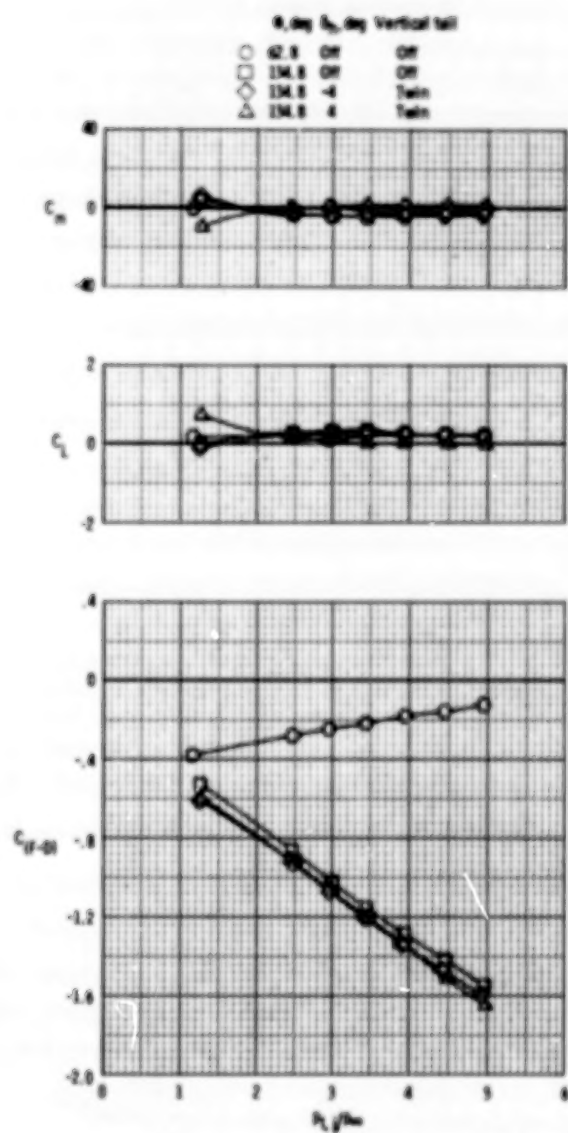


Figure 44.- Effect of thrust reversing on aerodynamic characteristics.



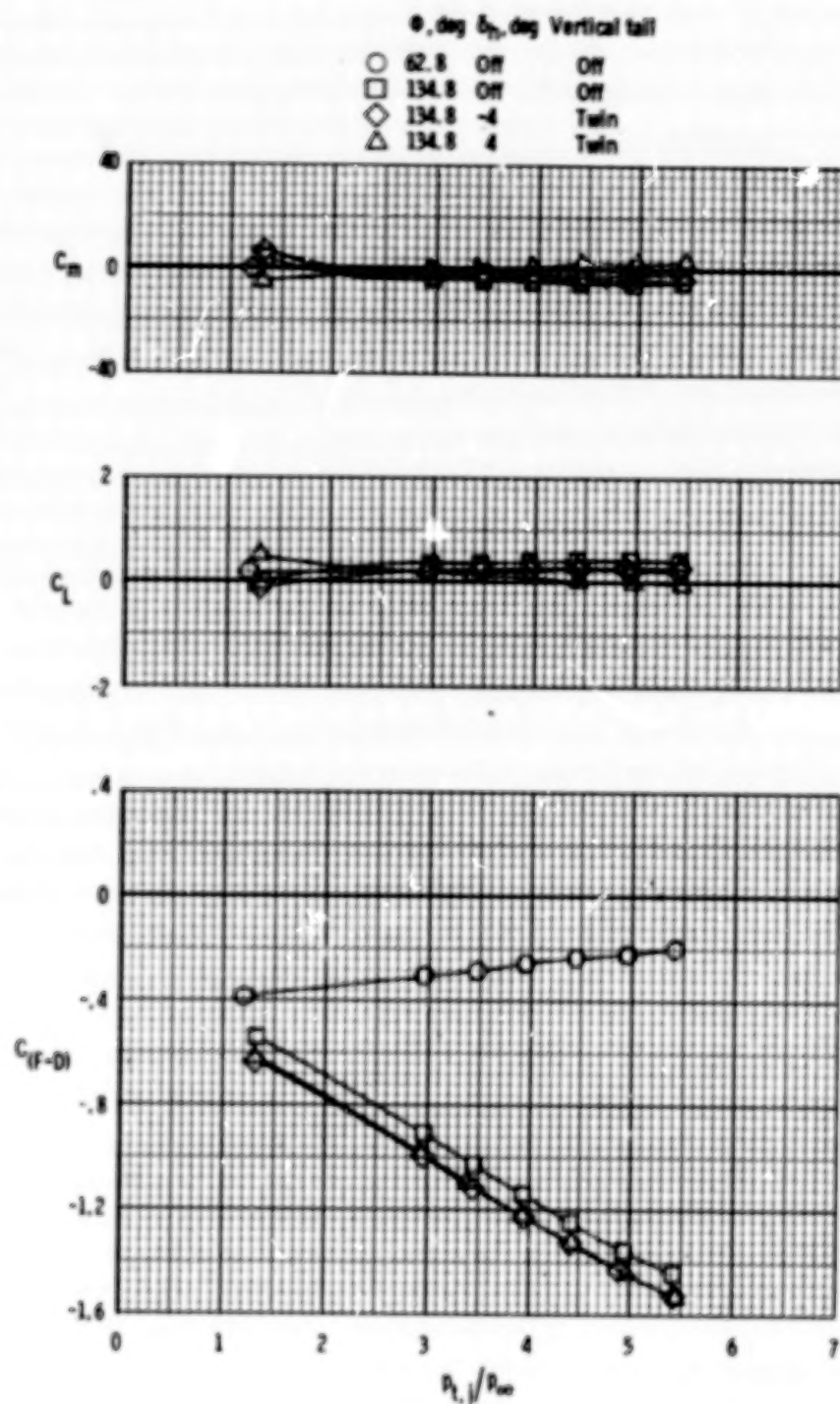
(b)  $M = 0.60$ .

Figure 44.- Continued.



(c)  $M = 0.80$ .

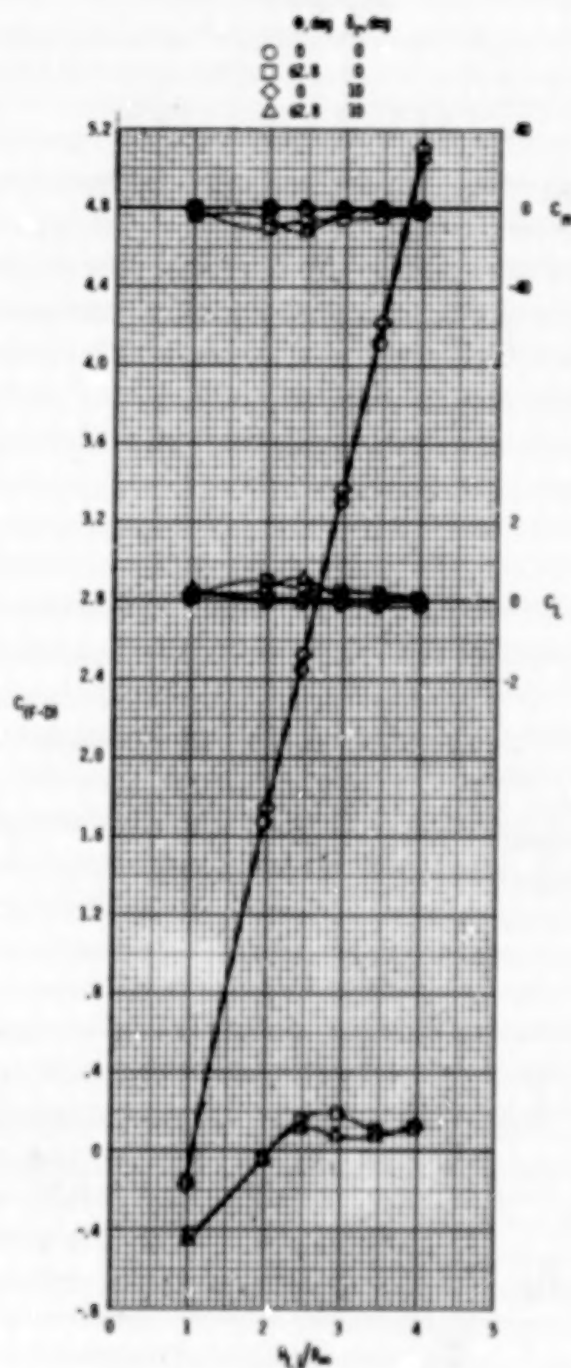
Figure 44.- Continued.



(c)  $M = 0.90$ .

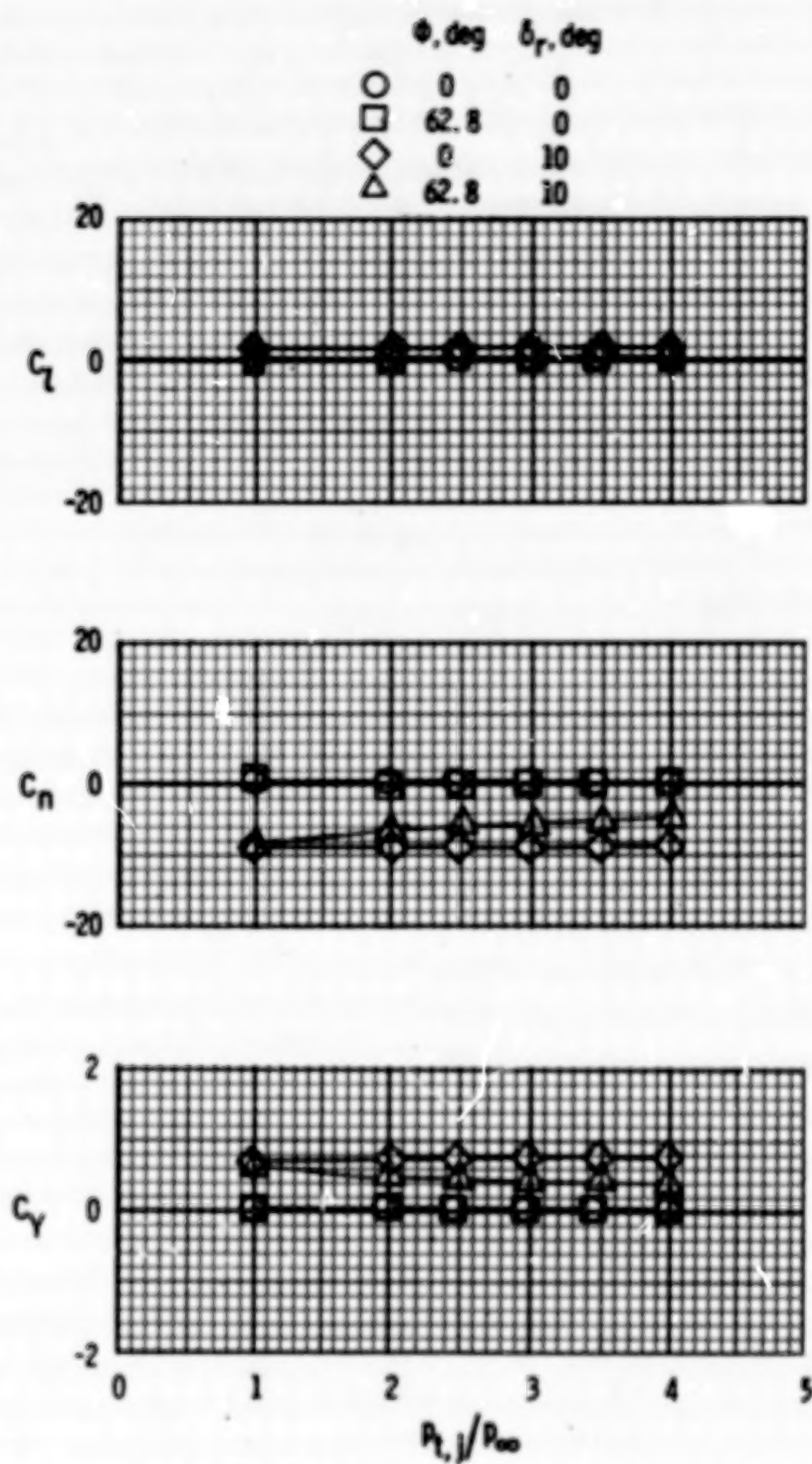
Figure 4A.- Concluded.





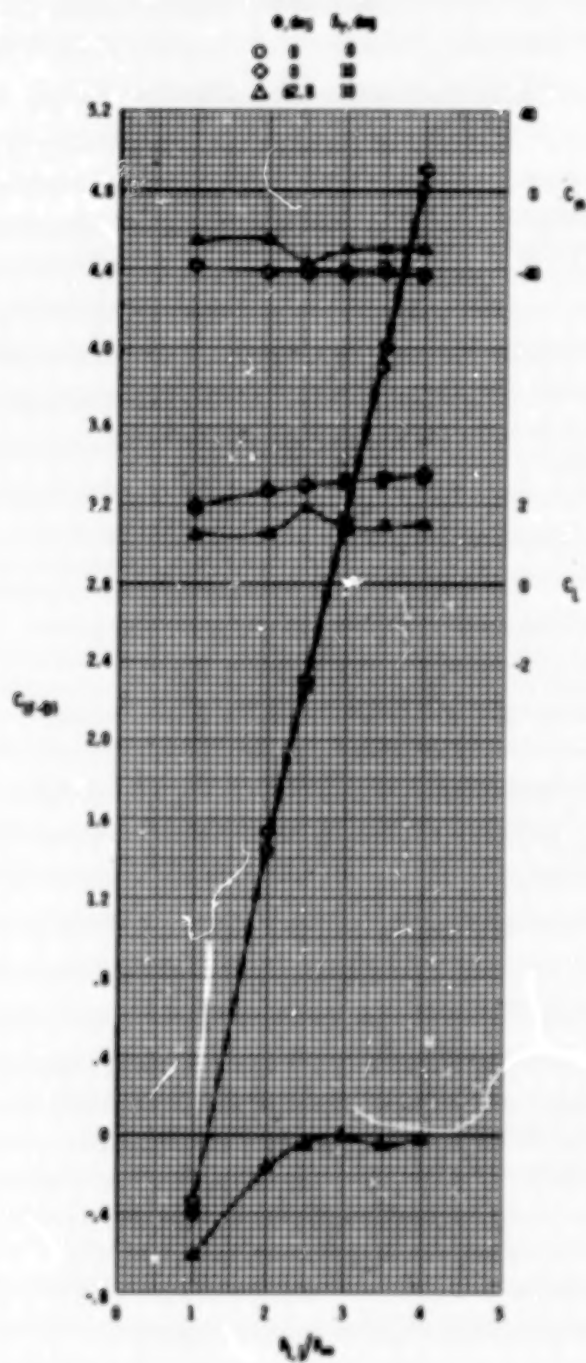
(a)  $M = 0.40$ ;  $\alpha = 0^\circ$ .

Figure 45.- Effect of rudder deflection on aerodynamic characteristics with reverse thrust. Single vertical tail;  $\delta_h = 0^\circ$ .



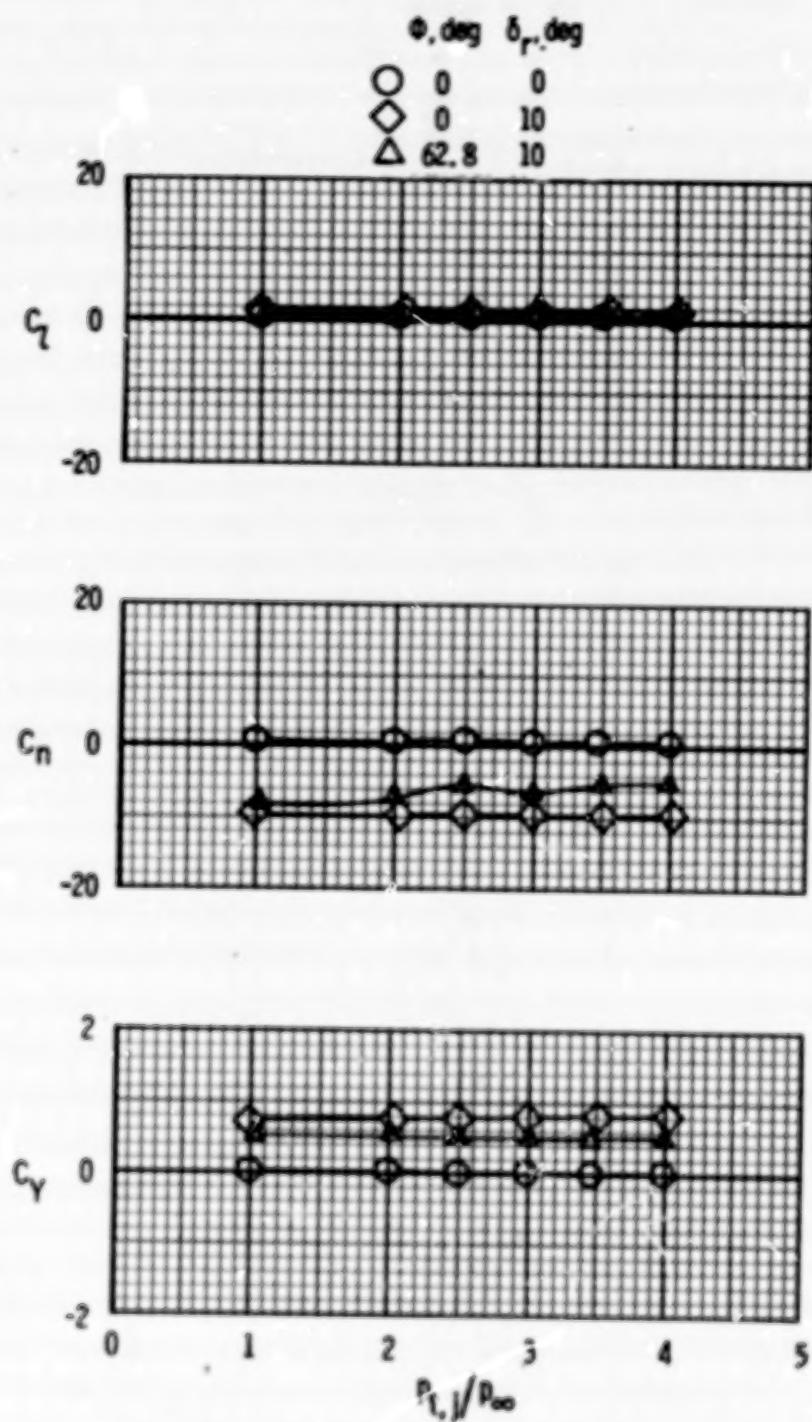
(a)  $M = 0.40$ ;  $\alpha = 0^\circ$ . Concluded.

Figure 45.- Continued.



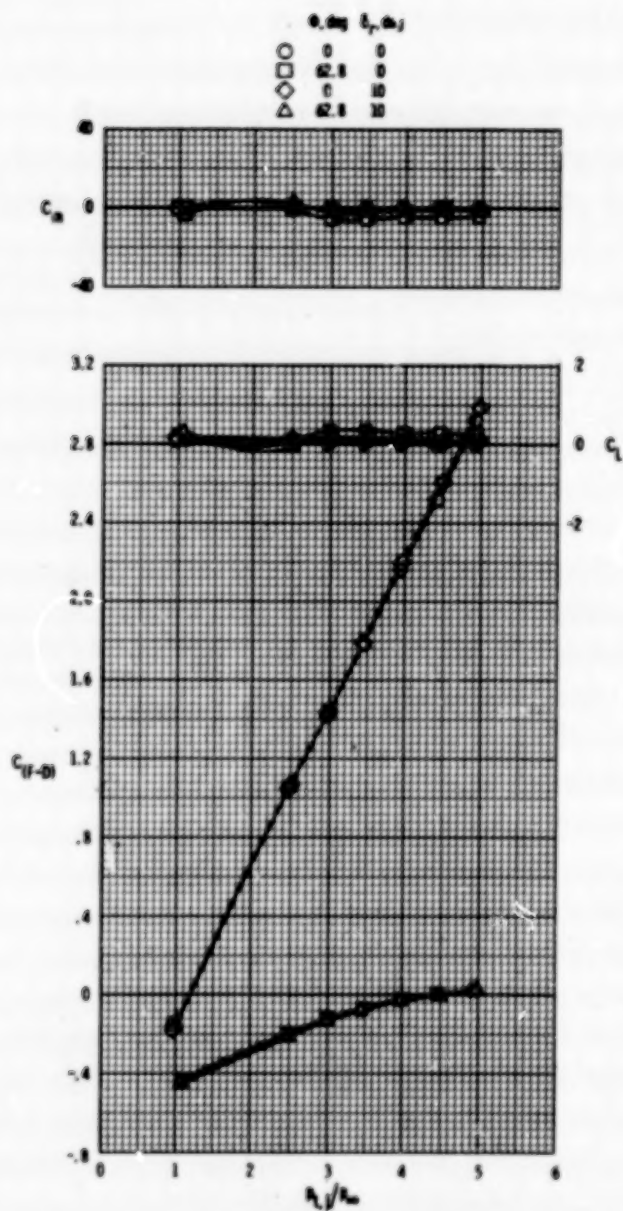
(b)  $M = 0.40$ ;  $\alpha = 80^\circ$ .

Figure 45.- Continued.



(b)  $M = 0.40$ ;  $\alpha = 8^\circ$ . Concluded.

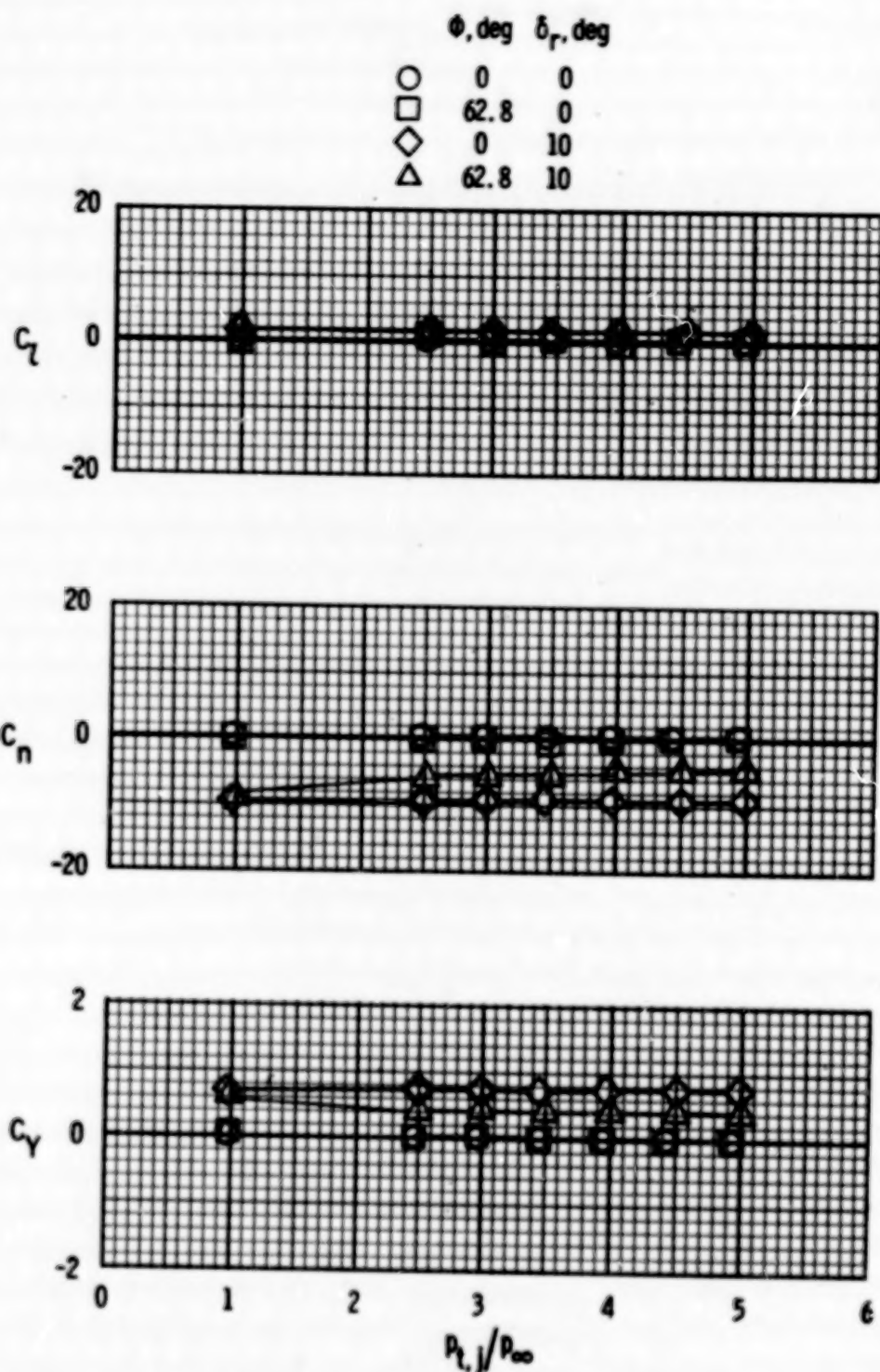
Figure 45.- Continued.



(c)  $M = 0.60$ ;  $\alpha = 0^\circ$ .

Figure 45.- Continued.

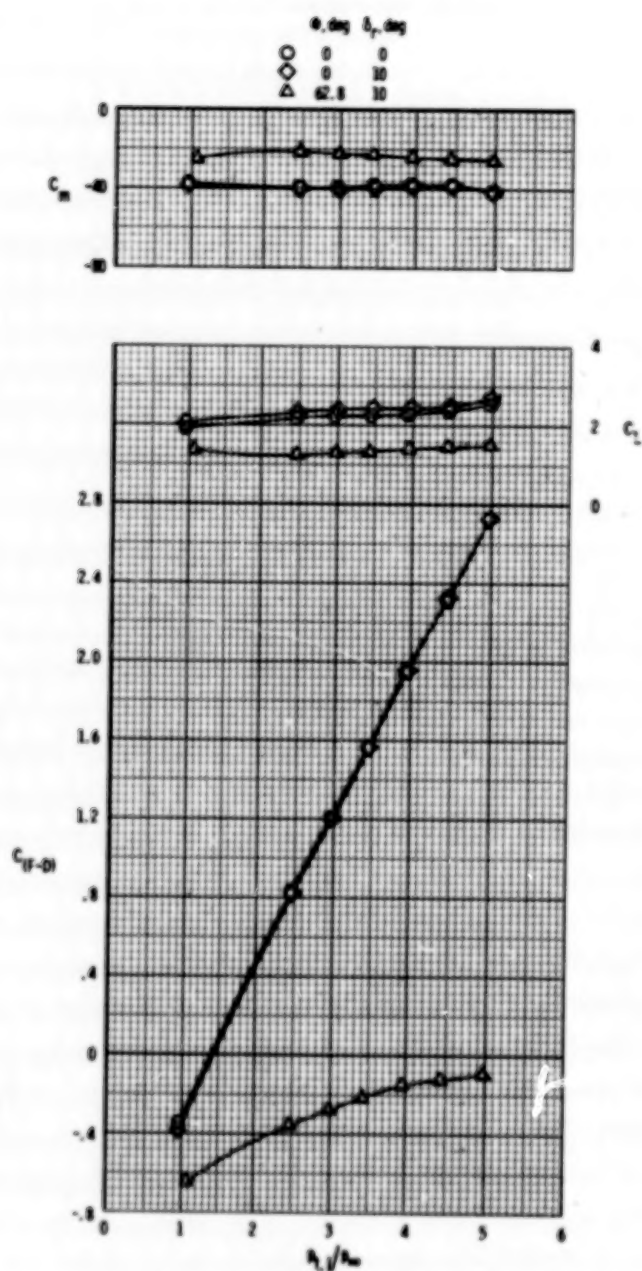




(c)  $M = 0.60$ ;  $\alpha = 0^\circ$ . Concluded.

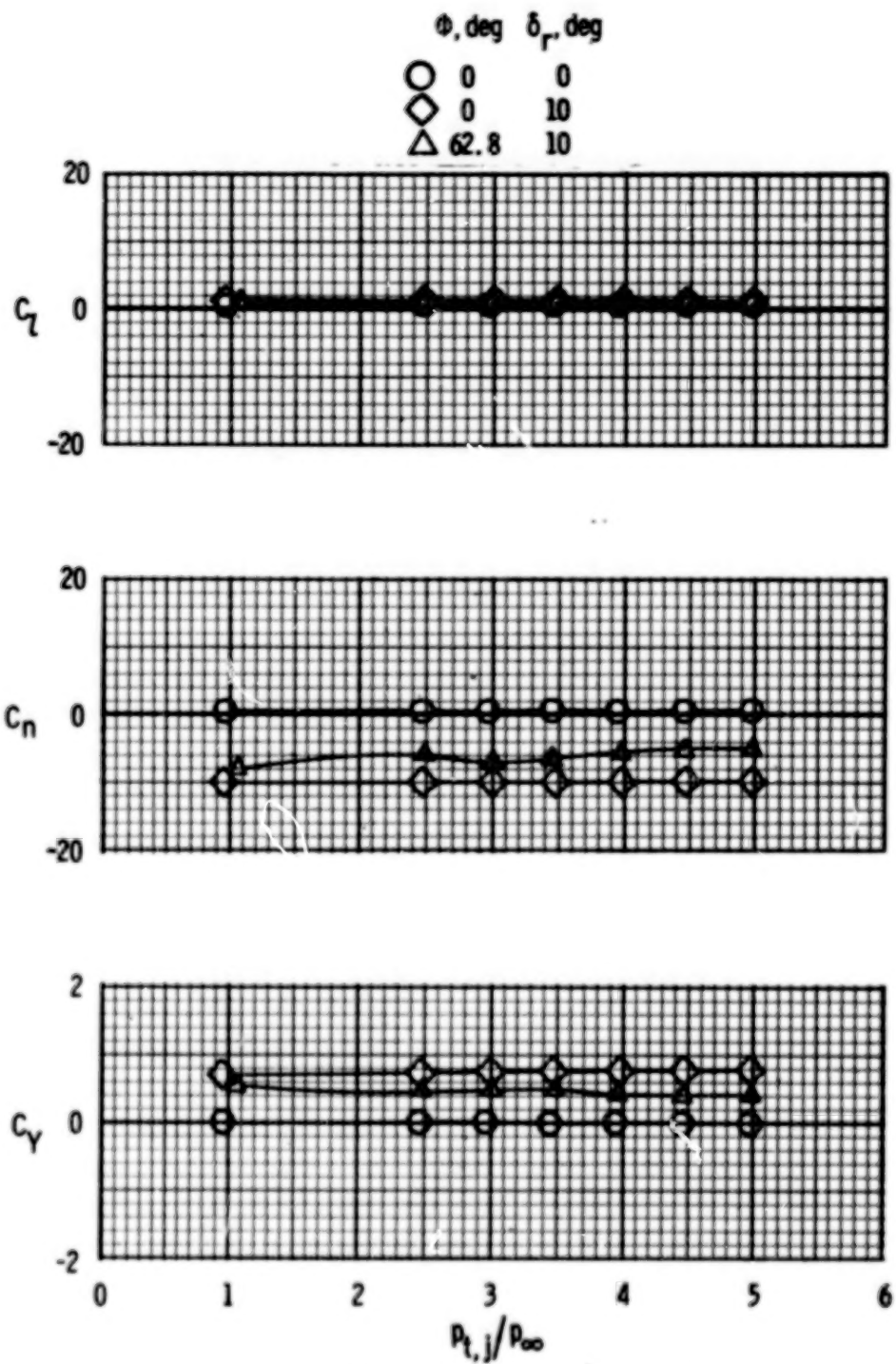
Figure 45.- Continued.





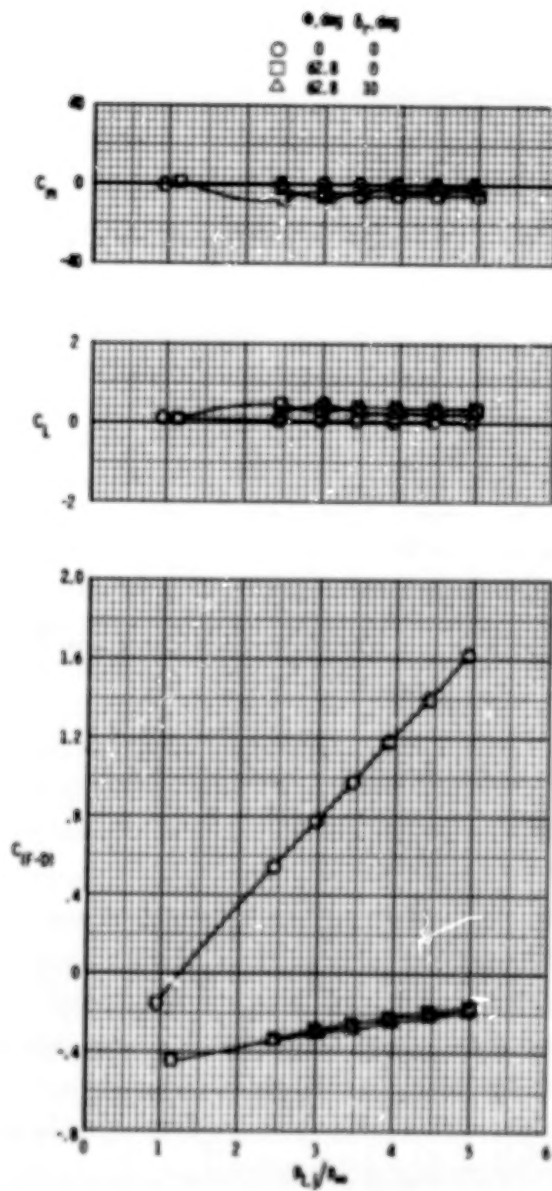
(d)  $M = 0.60$ ;  $\alpha = 8^\circ$ .

Figure 45.- Continued.



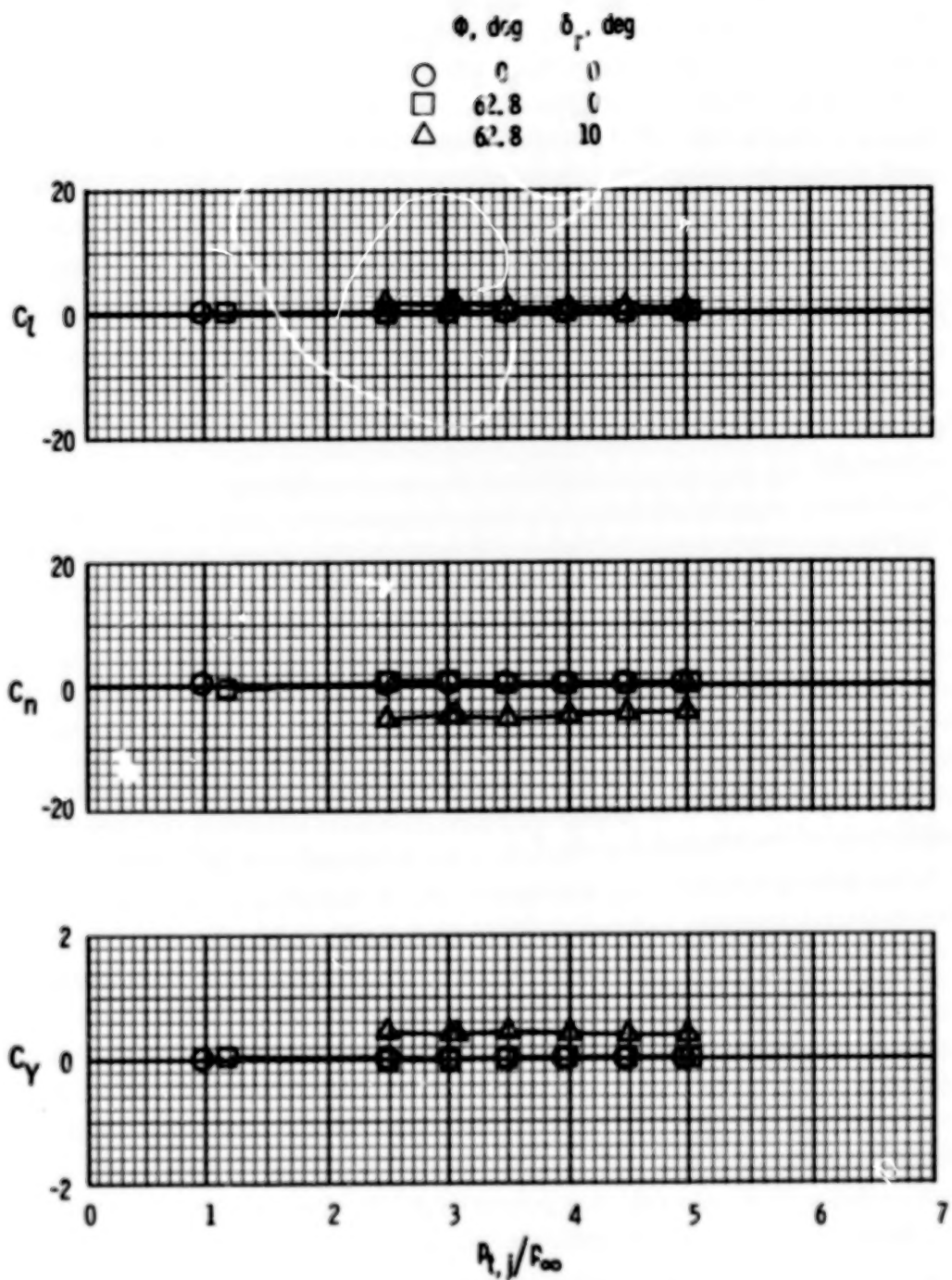
(d)  $M = 0.60$ ;  $\alpha = 8^\circ$ . Concluded.

Figure 45.- Continued.



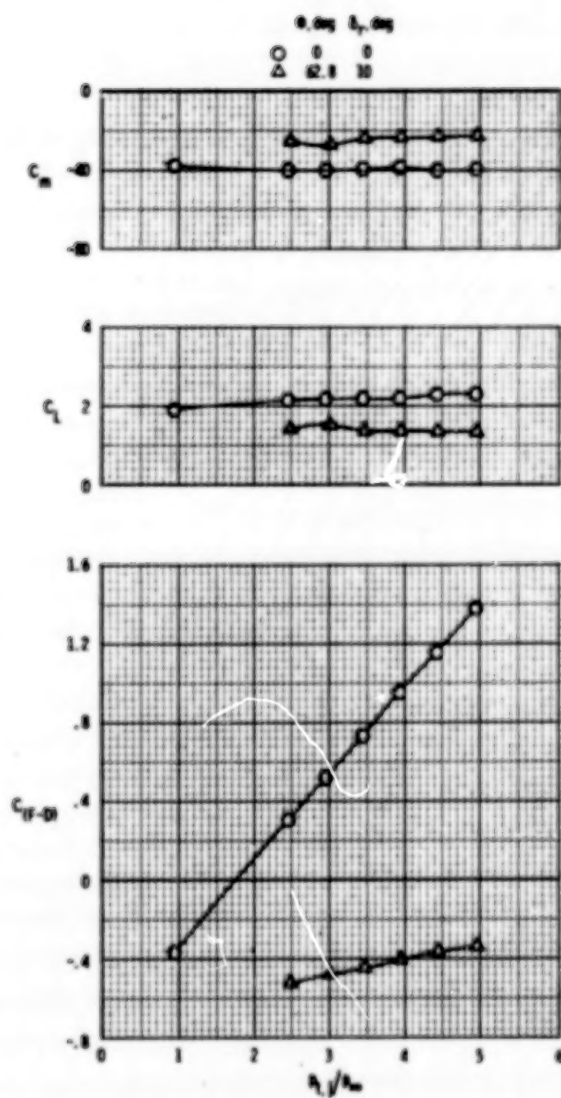
(e)  $M = 0.80$ ;  $\alpha = 0^\circ$ .

Figure 45.- Continued.



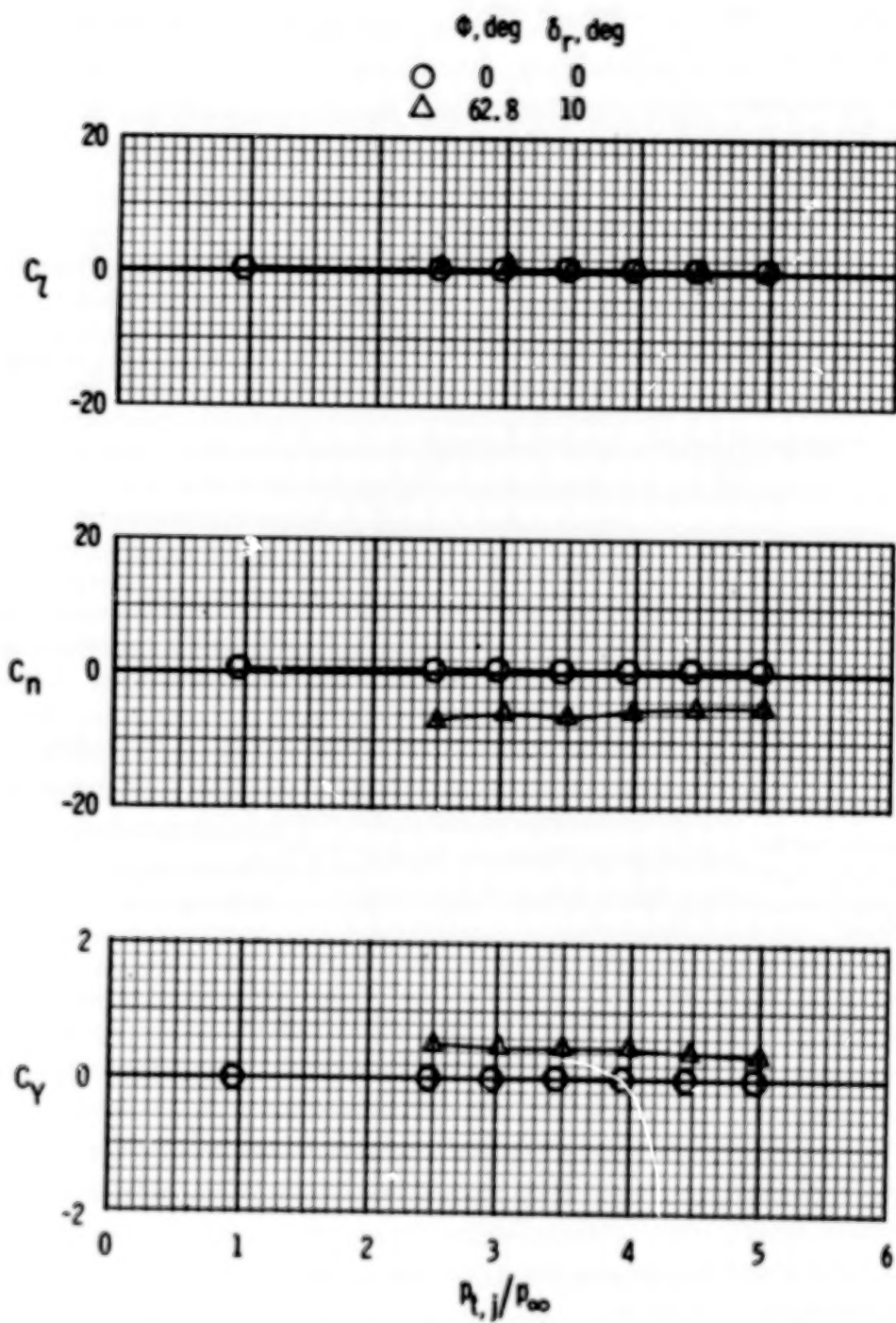
(e)  $M = 0.80$ ;  $\alpha = 0^\circ$ . Concluded.

Figure 45.- Continued.



(f)  $M = 0.80$ ;  $\alpha = 8^\circ$ .

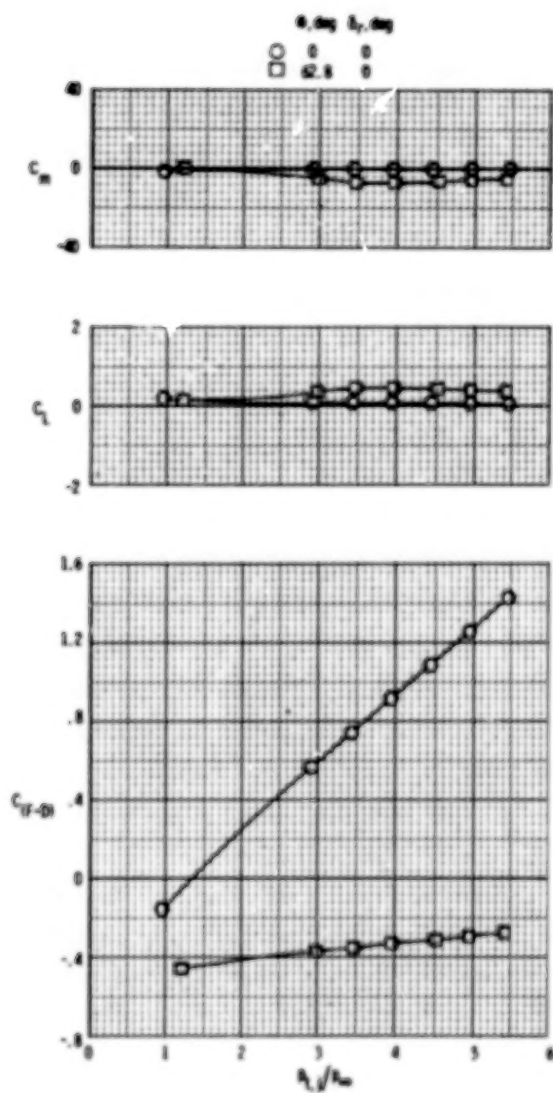
Figure 45.- Continued.



(f)  $M = 0.80$ ;  $\alpha = 8^\circ$ . Concluded.

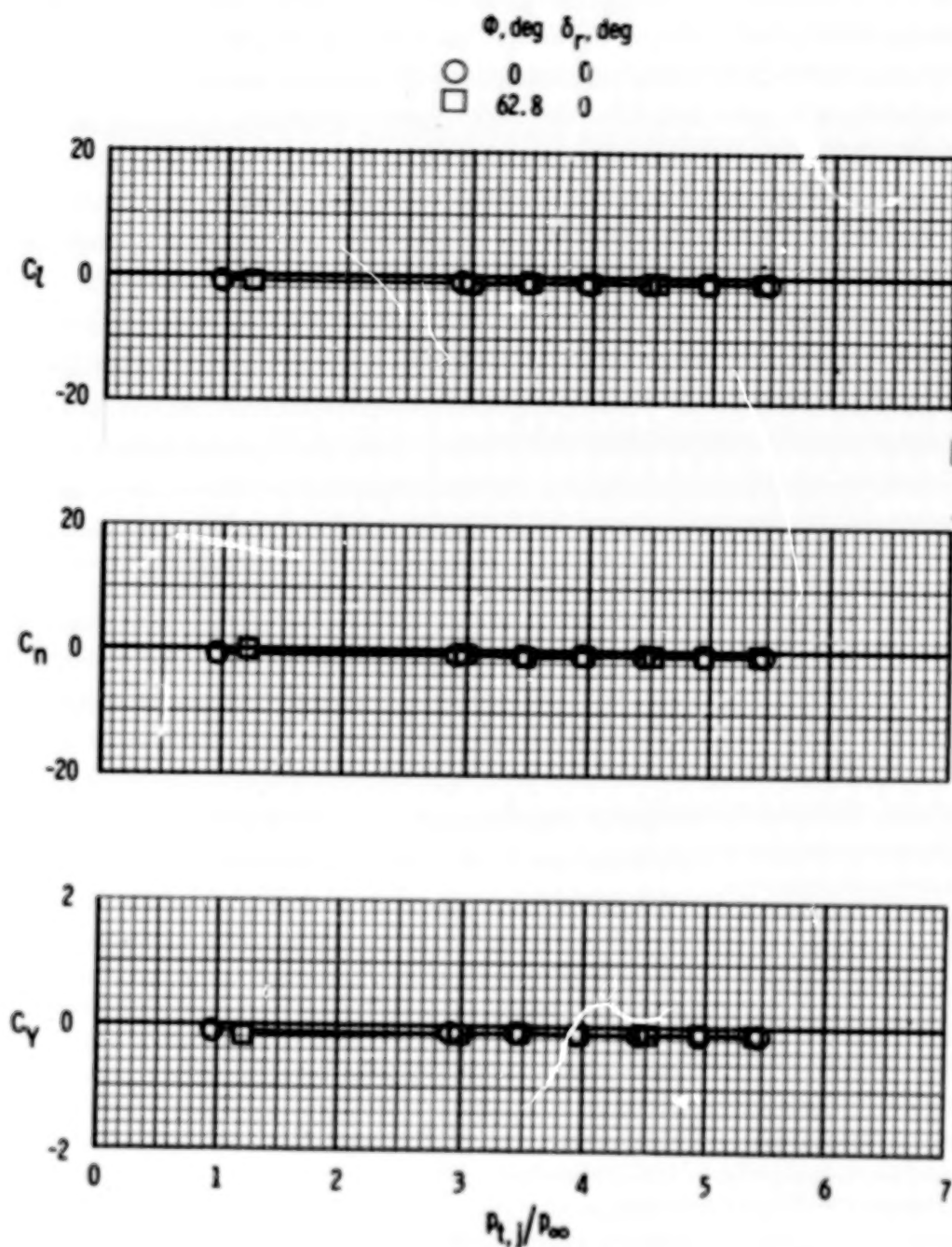
Figure 45.- Continued.





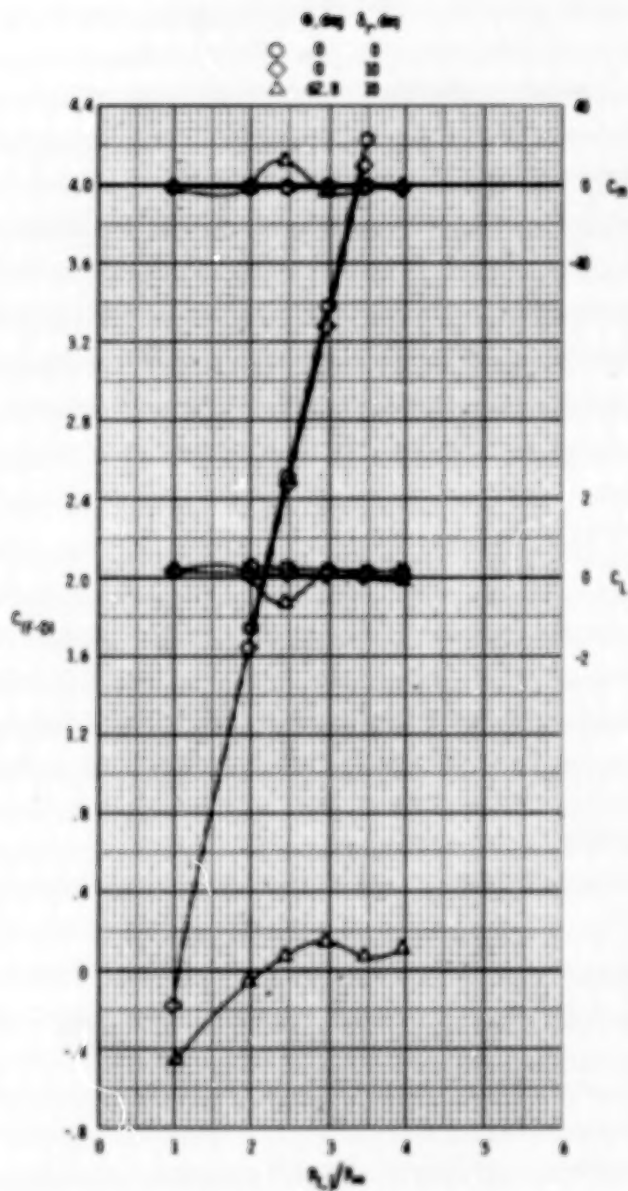
(g)  $M = 0.90$ ;  $\alpha = 0^\circ$ .

Figure 45.- Continued.



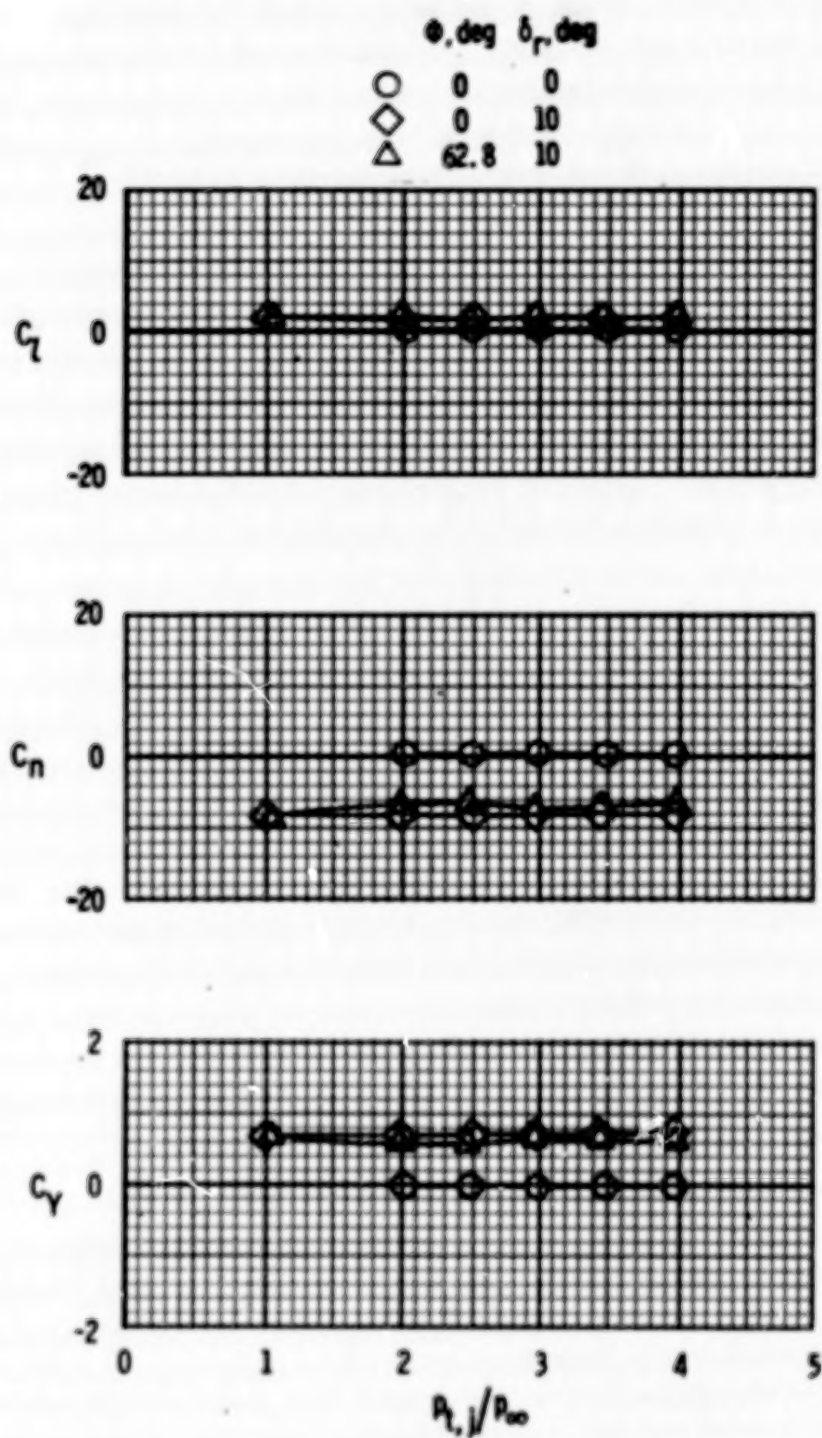
(g)  $M = 0.90$ ;  $\alpha = 0^\circ$ . Concluded.

Figure 45.- Concluded.



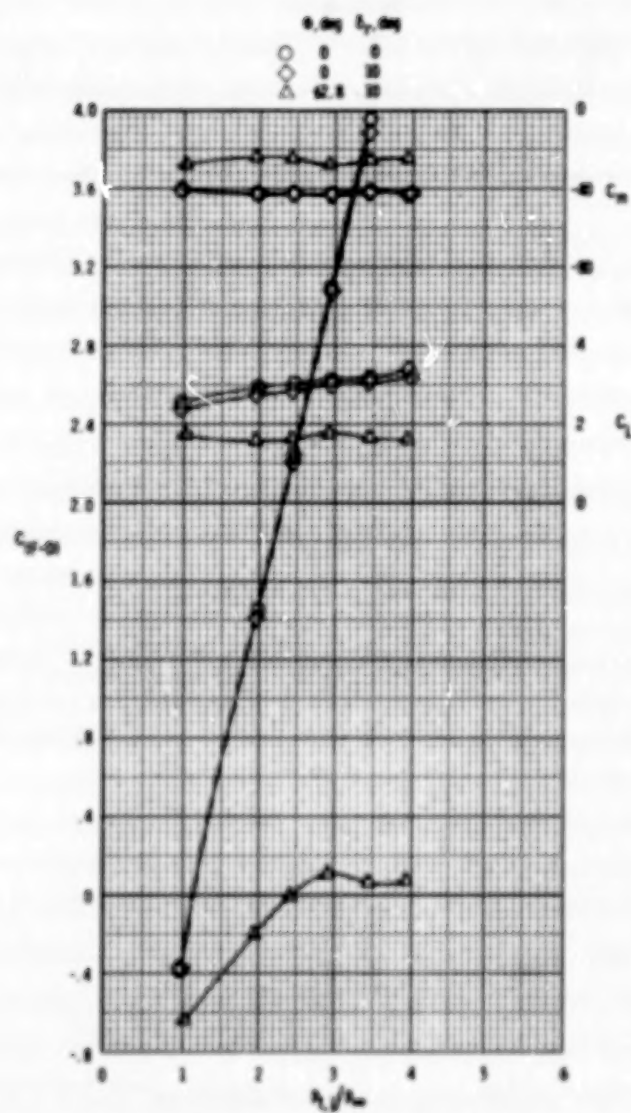
(a)  $M = 0.40$ ;  $\alpha = 0^\circ$ .

Figure 46.- Effect of rudder deflection and reverse thrust on aerodynamic characteristics. Twin vertical tails;  $\delta_h = 0^\circ$ .



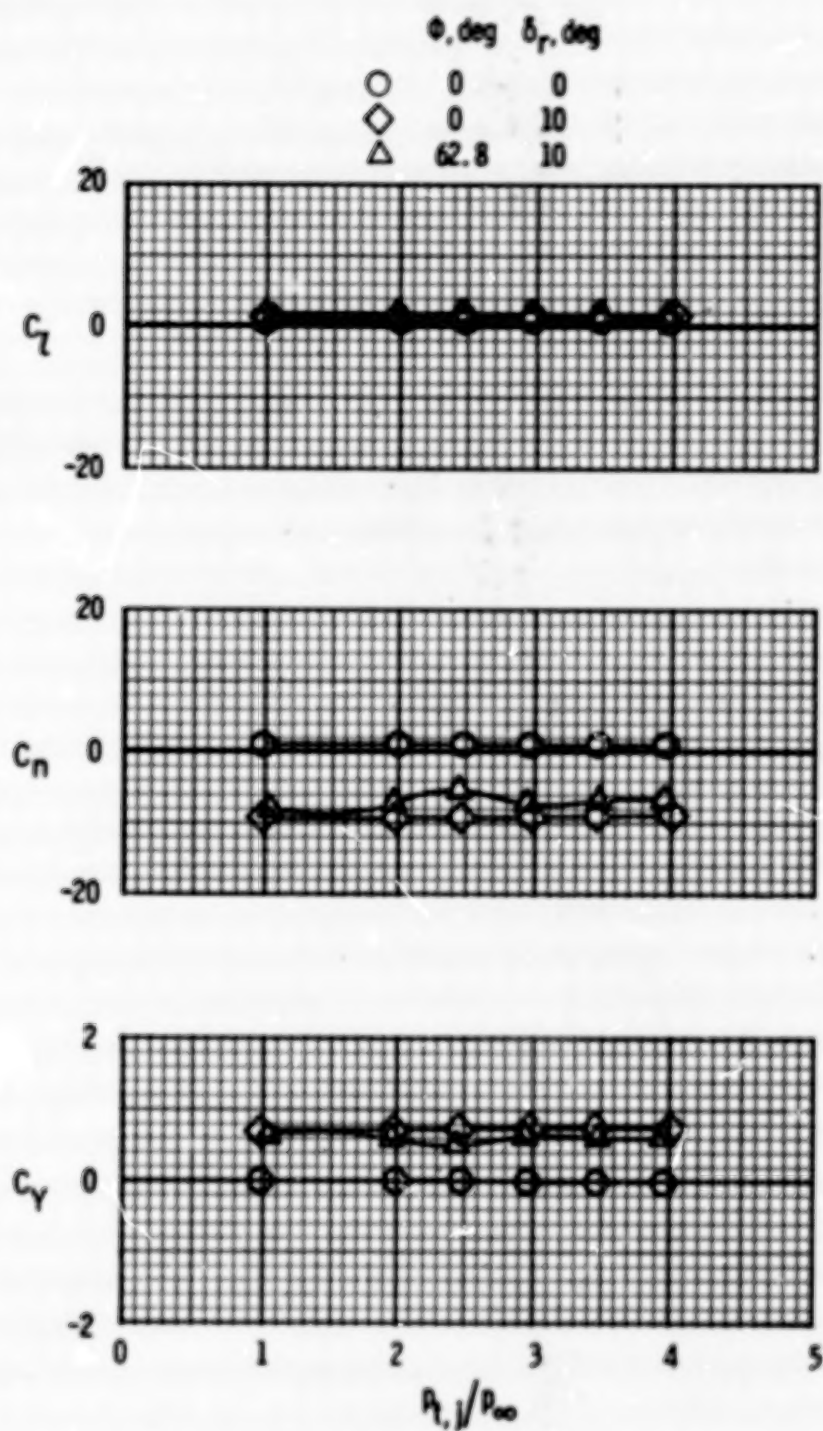
(a)  $M = 0.40$ ;  $\alpha = 0^\circ$ . Concluded.

Figure 4f.- Continued.



(b)  $M = 0.40$ ;  $\alpha = 80^\circ$ .

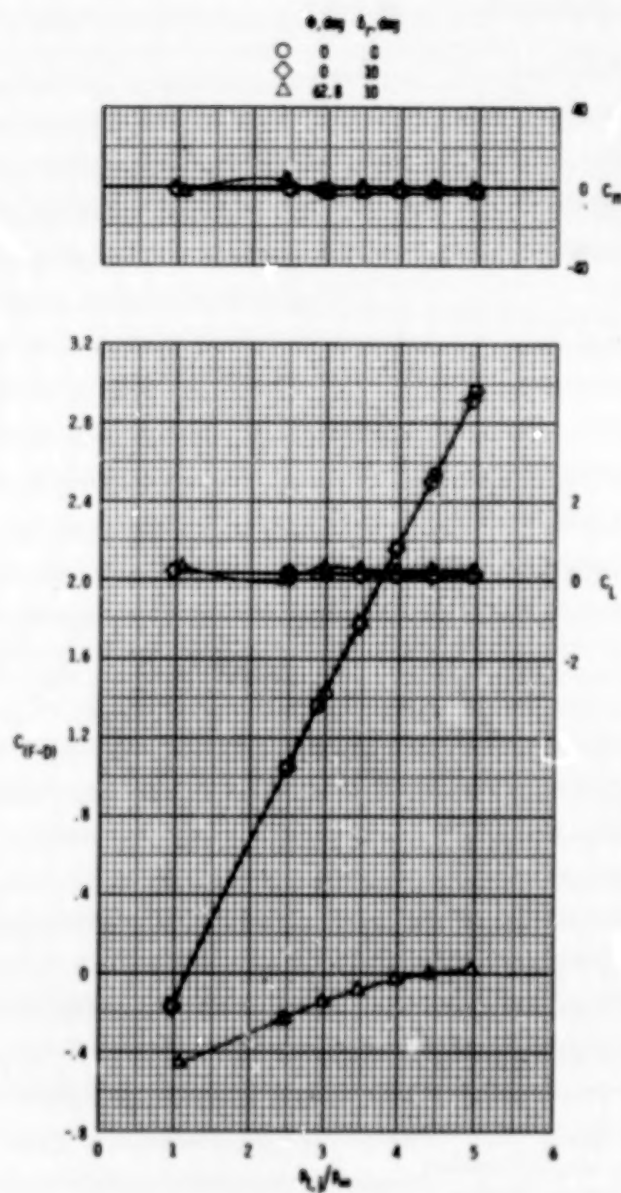
Figure 46.- Continued.



(b)  $M = 0.40$ ;  $\alpha = 8^\circ$ . Concluded.

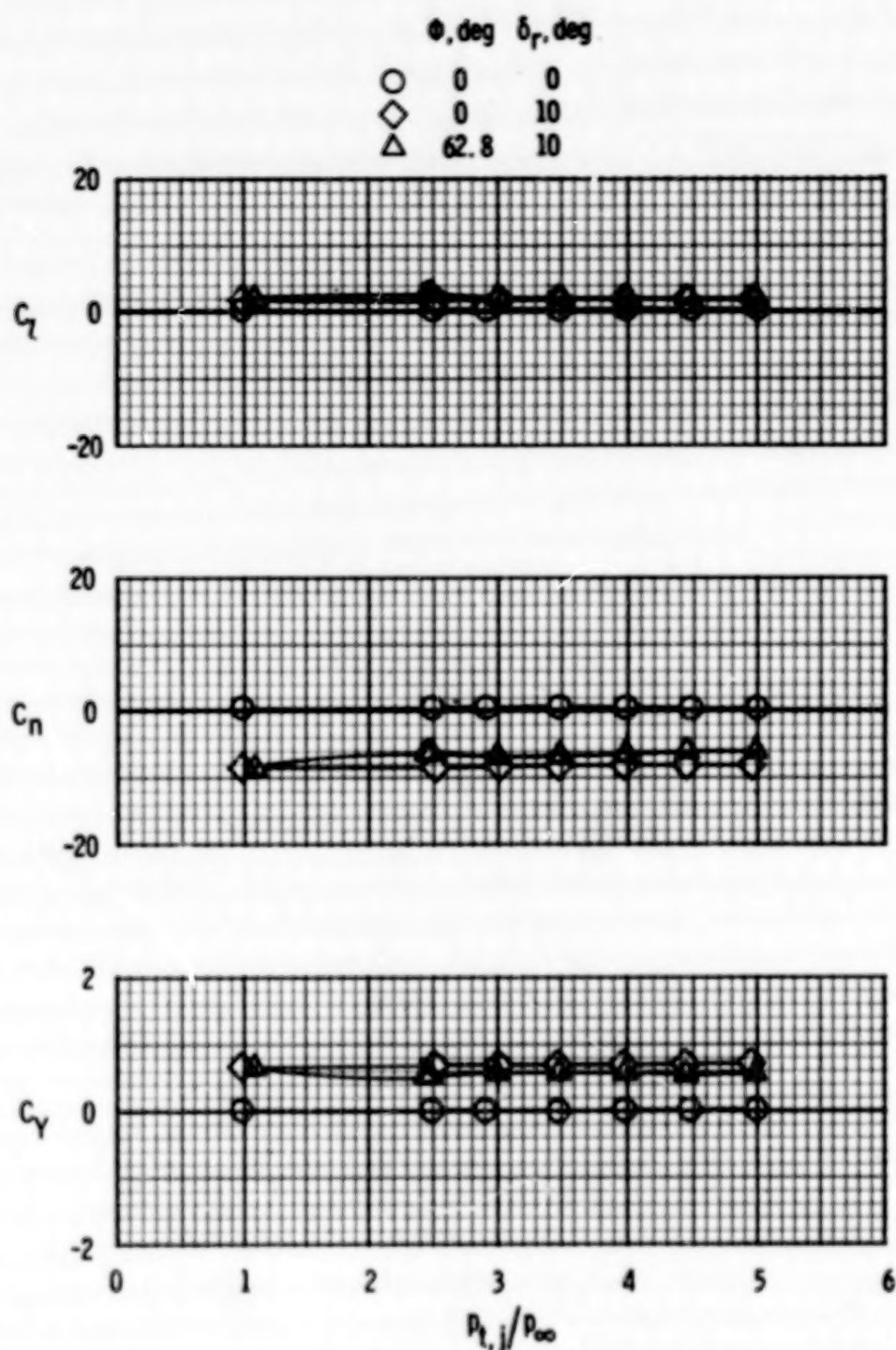
Figure 46.- Continued.





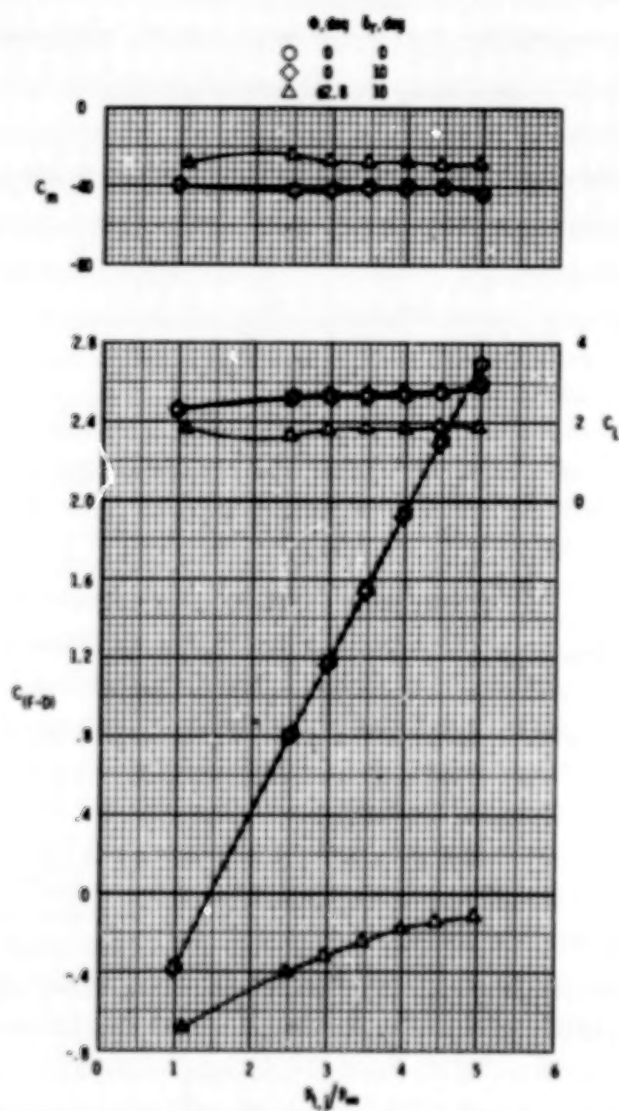
(c)  $M = 0.60$ ;  $\alpha = 0^\circ$ .

Figure 46.- Continued.



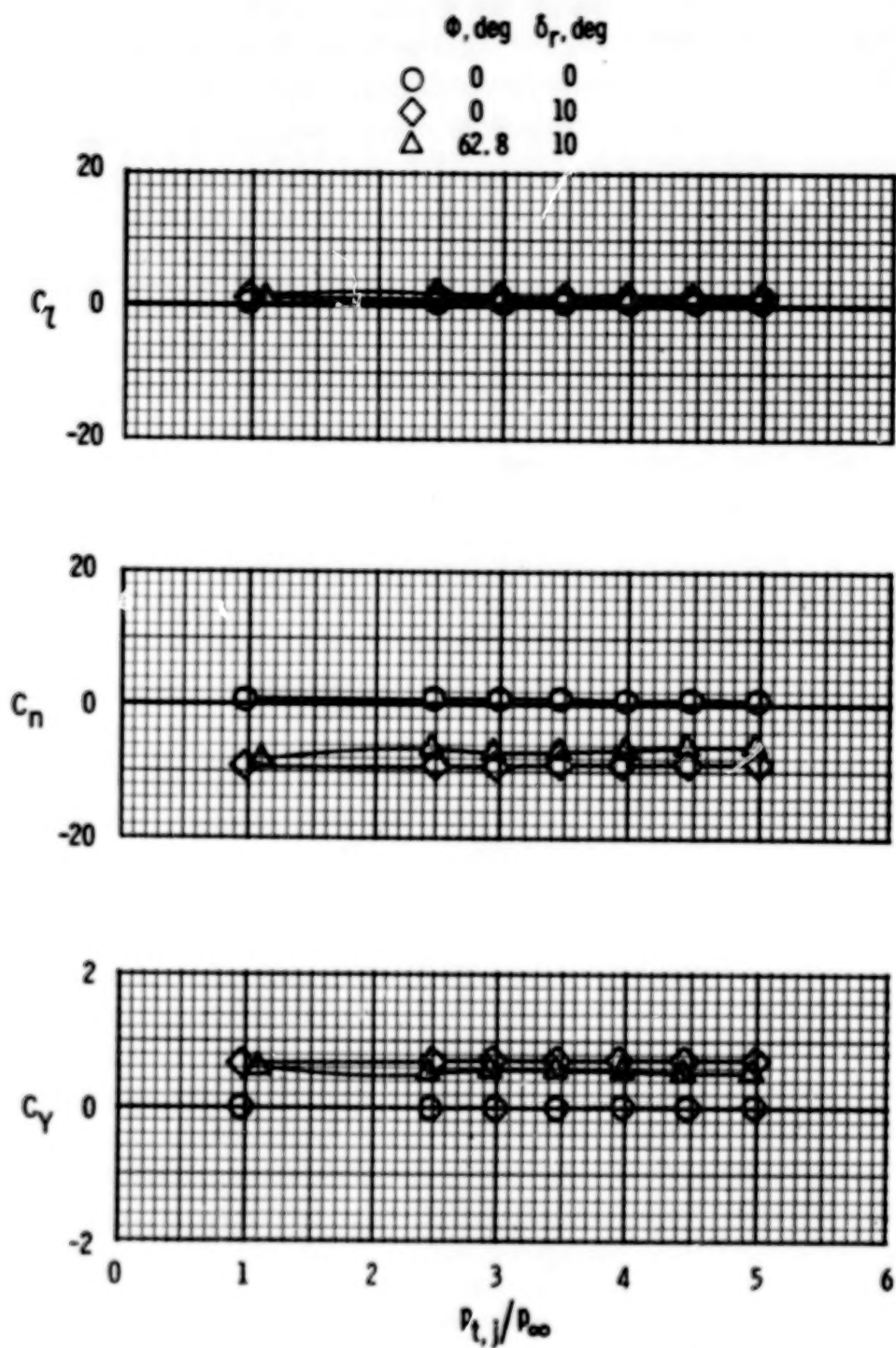
(c)  $M = 0.60$ ;  $\alpha = 0^\circ$ . Concluded.

Figure 46.- Continued.



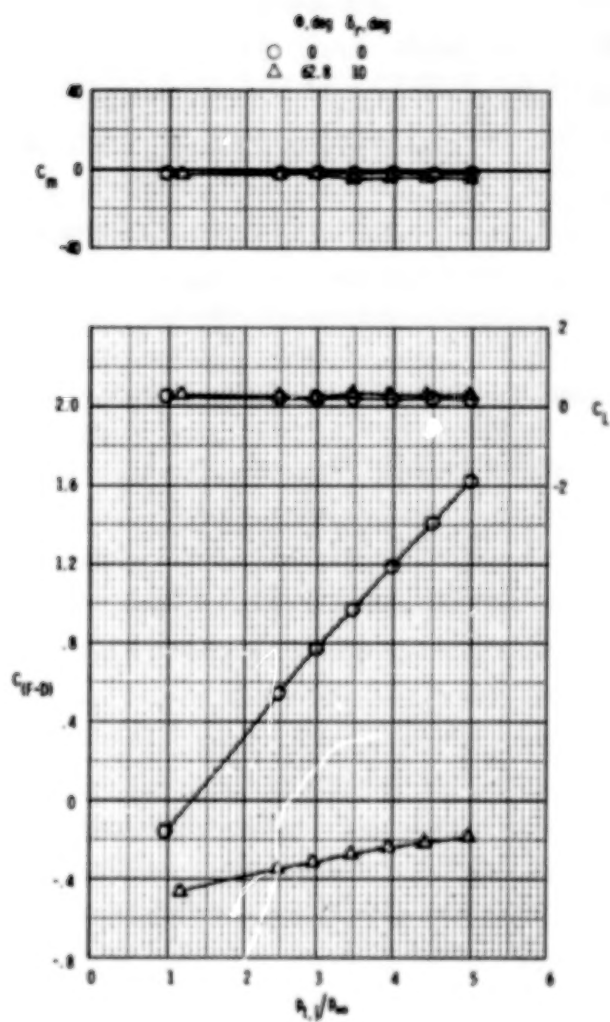
(d)  $M = 0.60$ ;  $\alpha = 80^\circ$ .

Figure 46.- Continued.



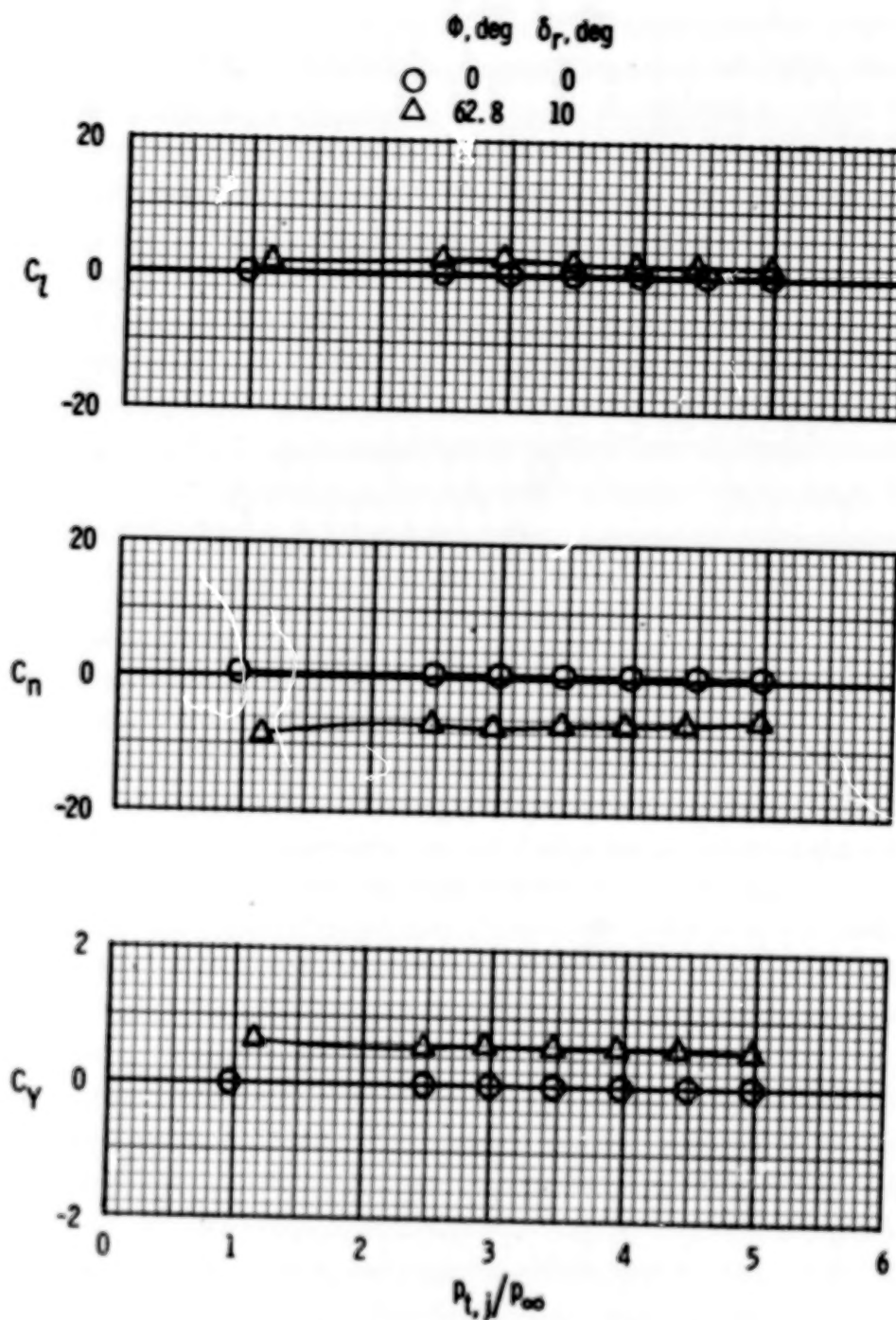
(d)  $M = 0.60$ ;  $\alpha = 8^\circ$ . Concluded.

Figure 46.- Continued.



(e)  $M = 0.80$ ;  $\alpha = 0^\circ$ .

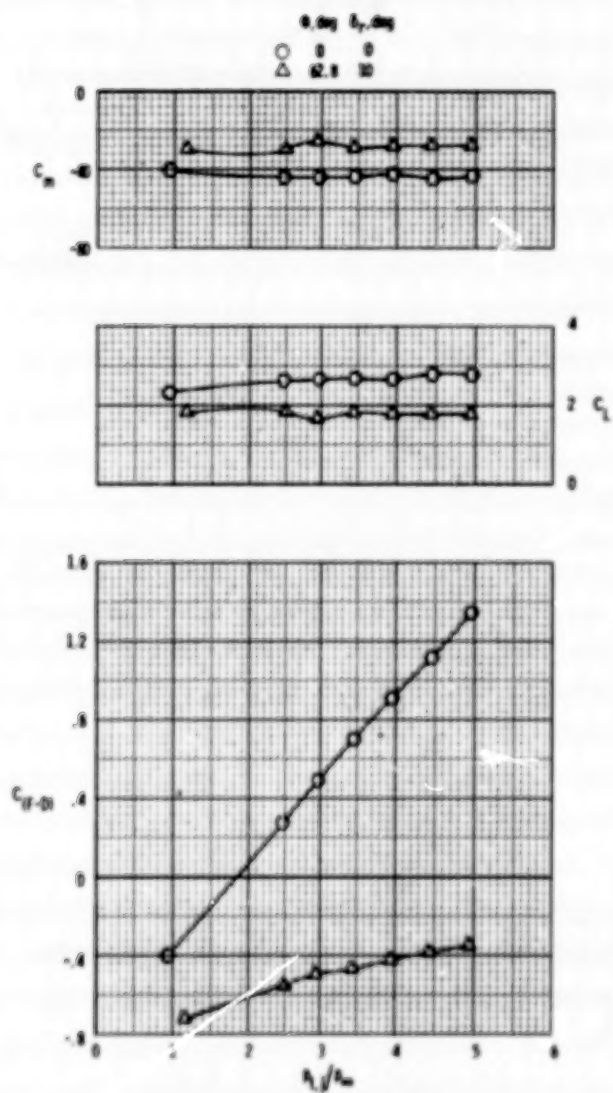
Figure 46.- Continued.



(e)  $M = 0.80$ ;  $\alpha = 0^\circ$ . Concluded.

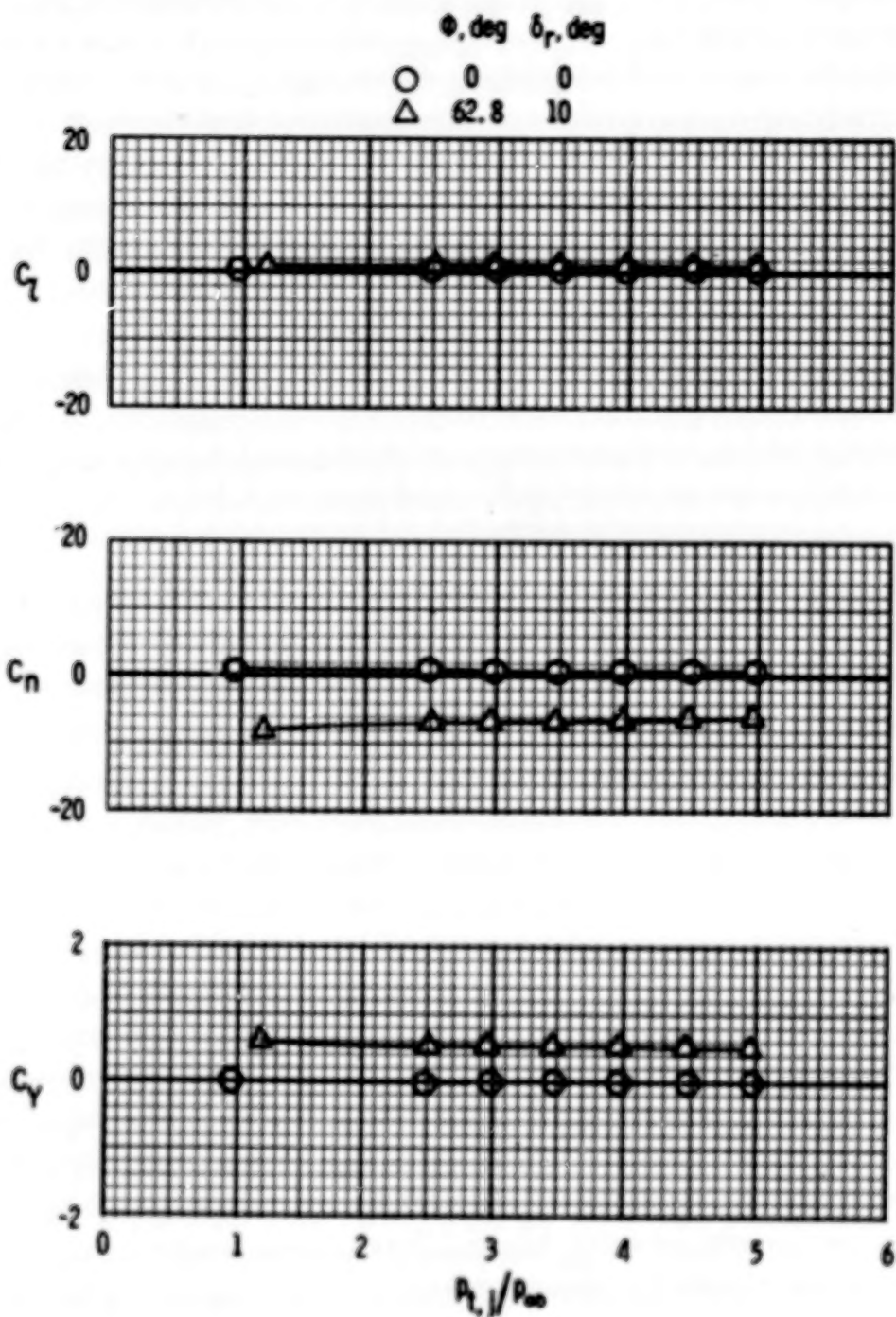
Figure 46.- Continued.





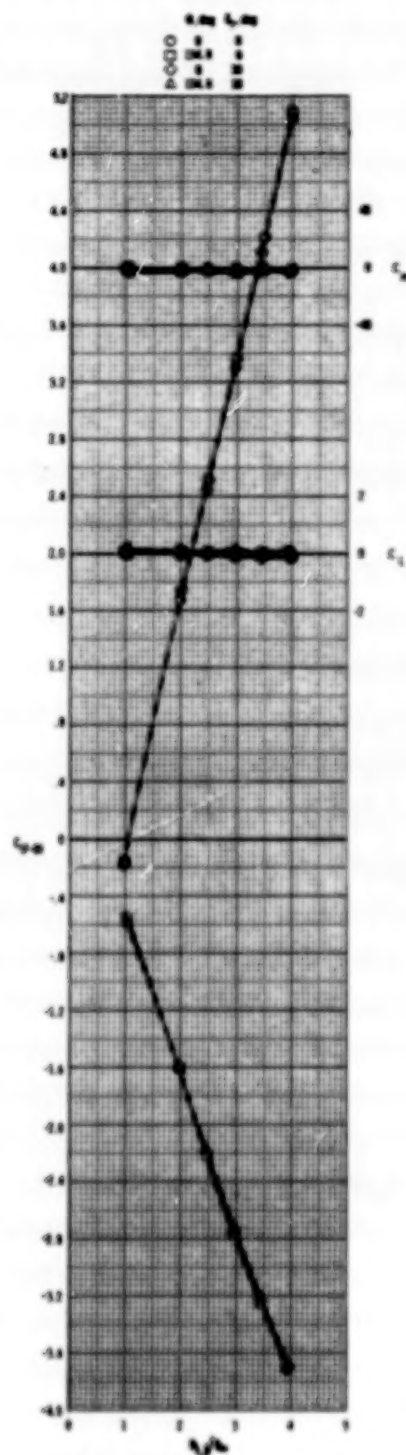
(f)  $M = 0.80$ ;  $\alpha = 8^\circ$ .

Figure 46.- Continued.



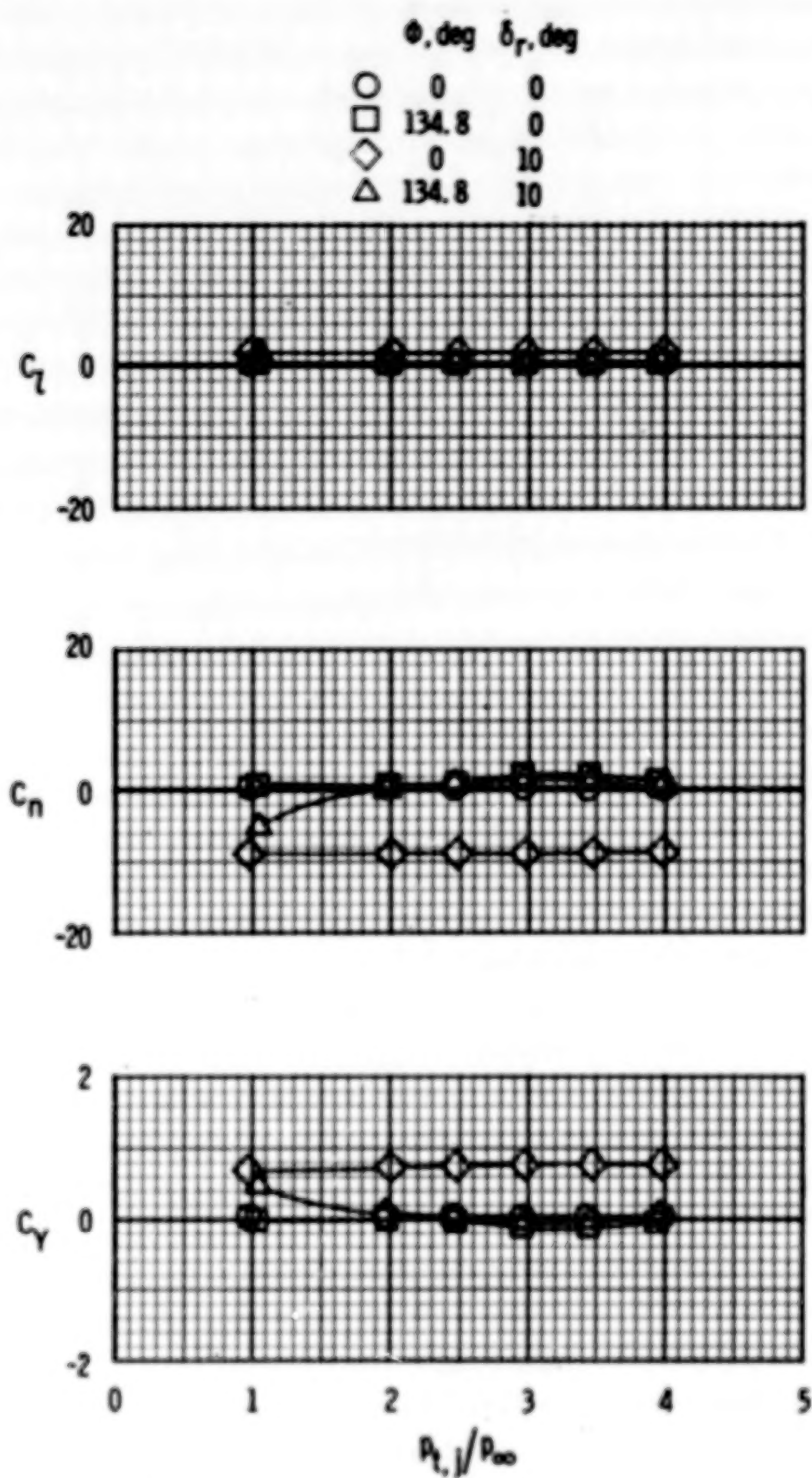
(f)  $M = 0.80$ ;  $\alpha = 8^\circ$ . Concluded.

Figure 46.- Concluded.



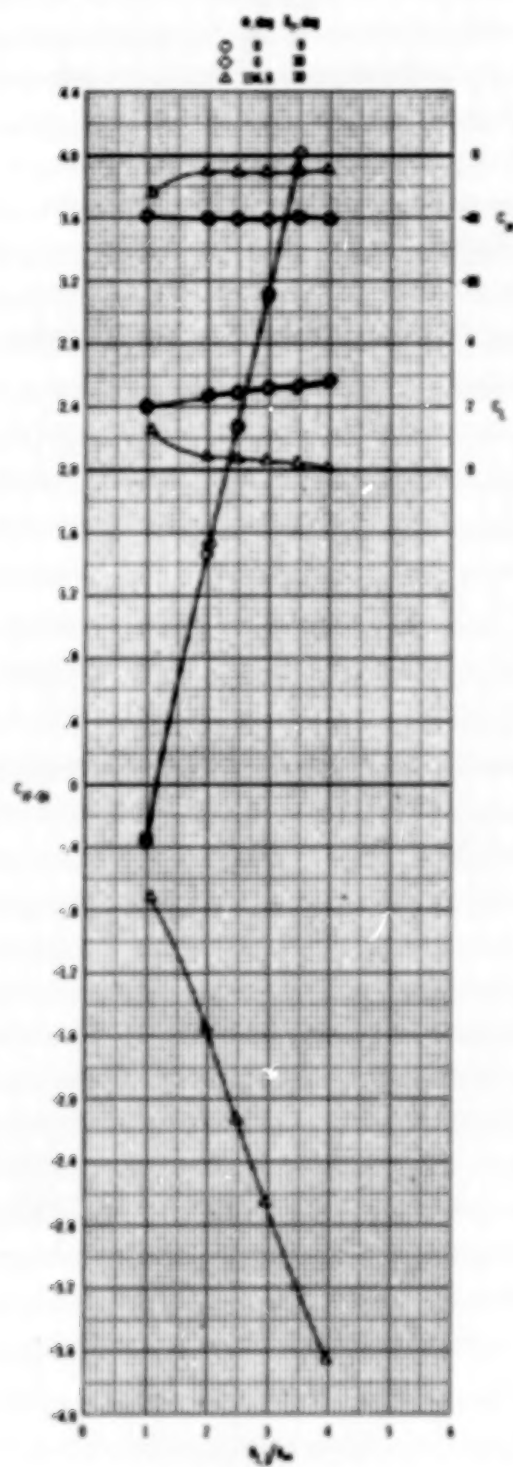
(a)  $M = 0.40$ ;  $\alpha = 0^\circ$ .

Figure 47.- Effect of rudder deflection and reverse thrust on aerodynamic characteristics. Single vertical tail;  $\delta_h = 0^\circ$ .



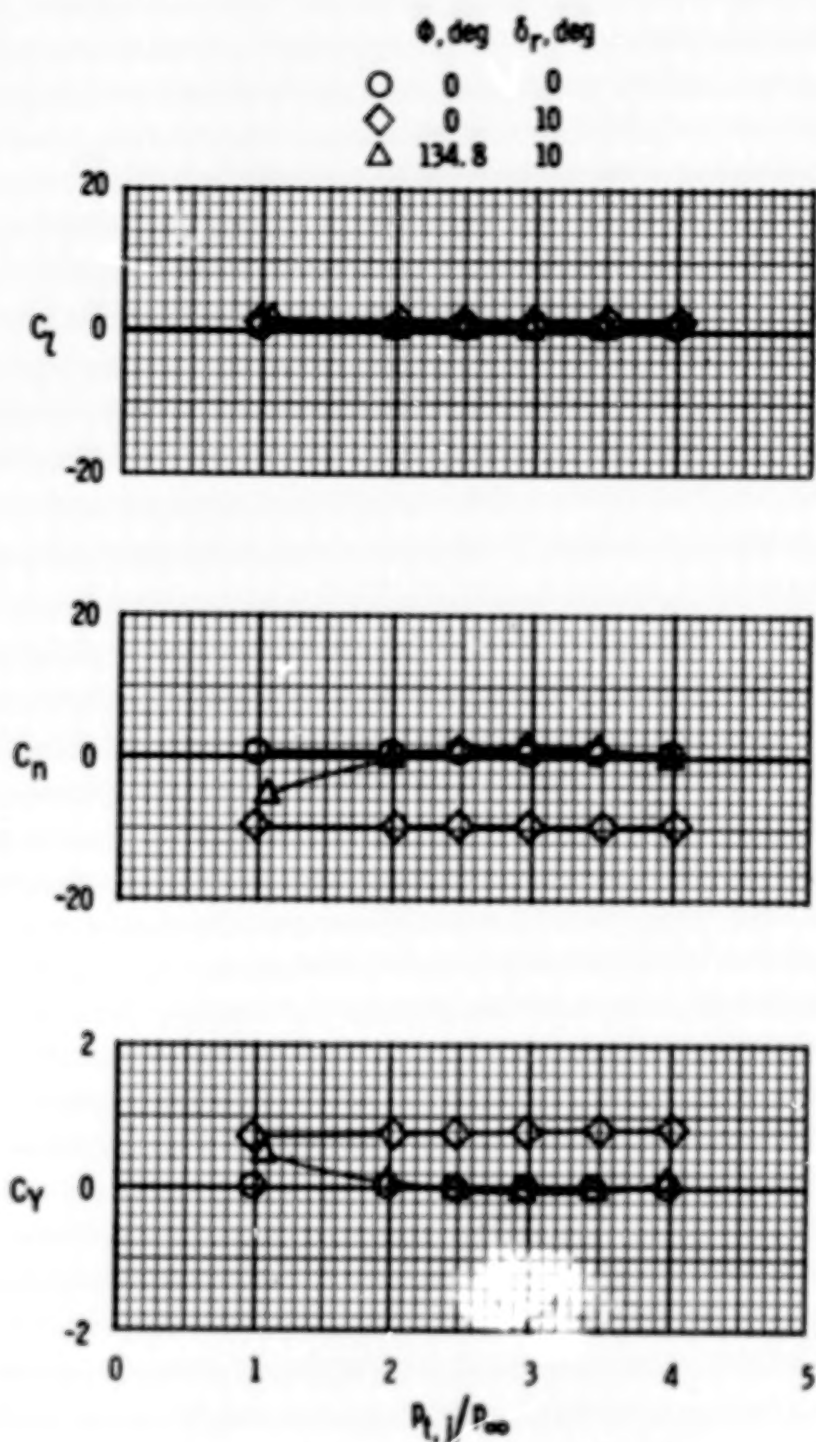
(a)  $M = 0.40$ ;  $\alpha = 0^\circ$ . Concluded.

Figure 47.- Continued.



(b)  $M = 0.40$ ;  $\alpha = 8^\circ$ .

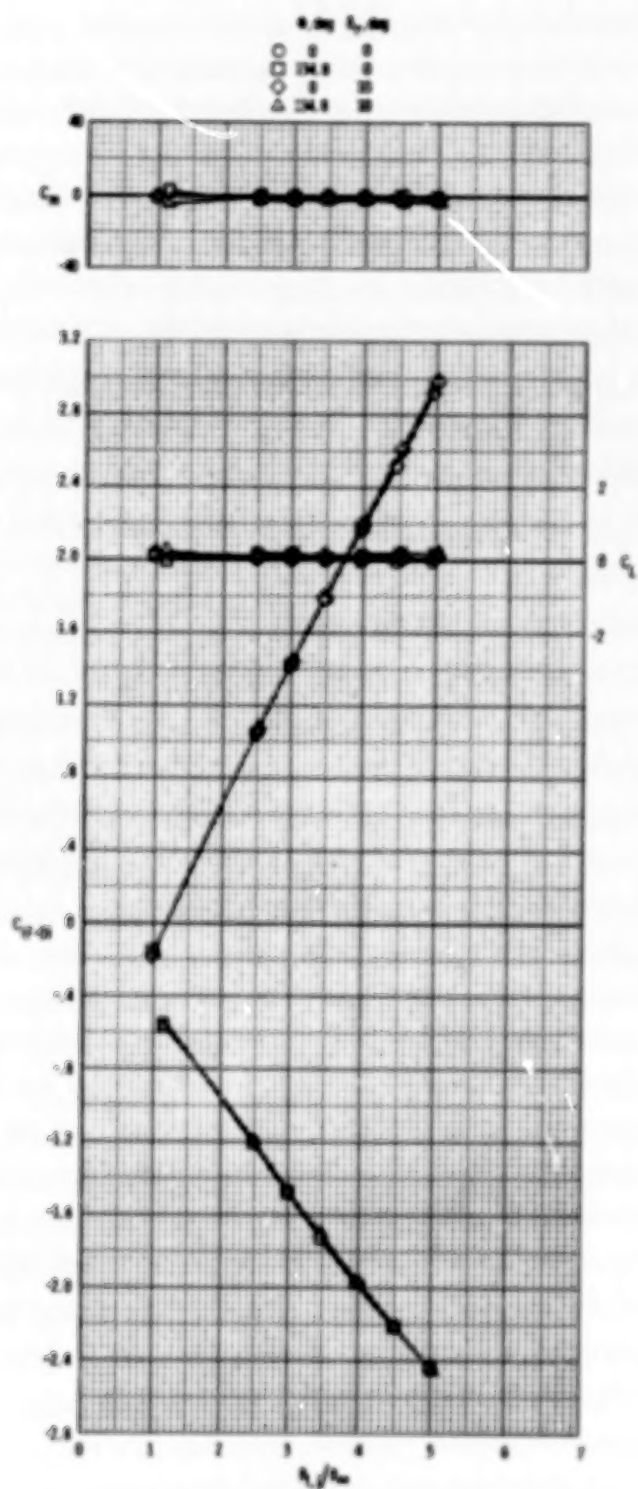
Figure 47.- Continued.



(b)  $M = 0.40$ ;  $\alpha = 8^\circ$ . Concluded.

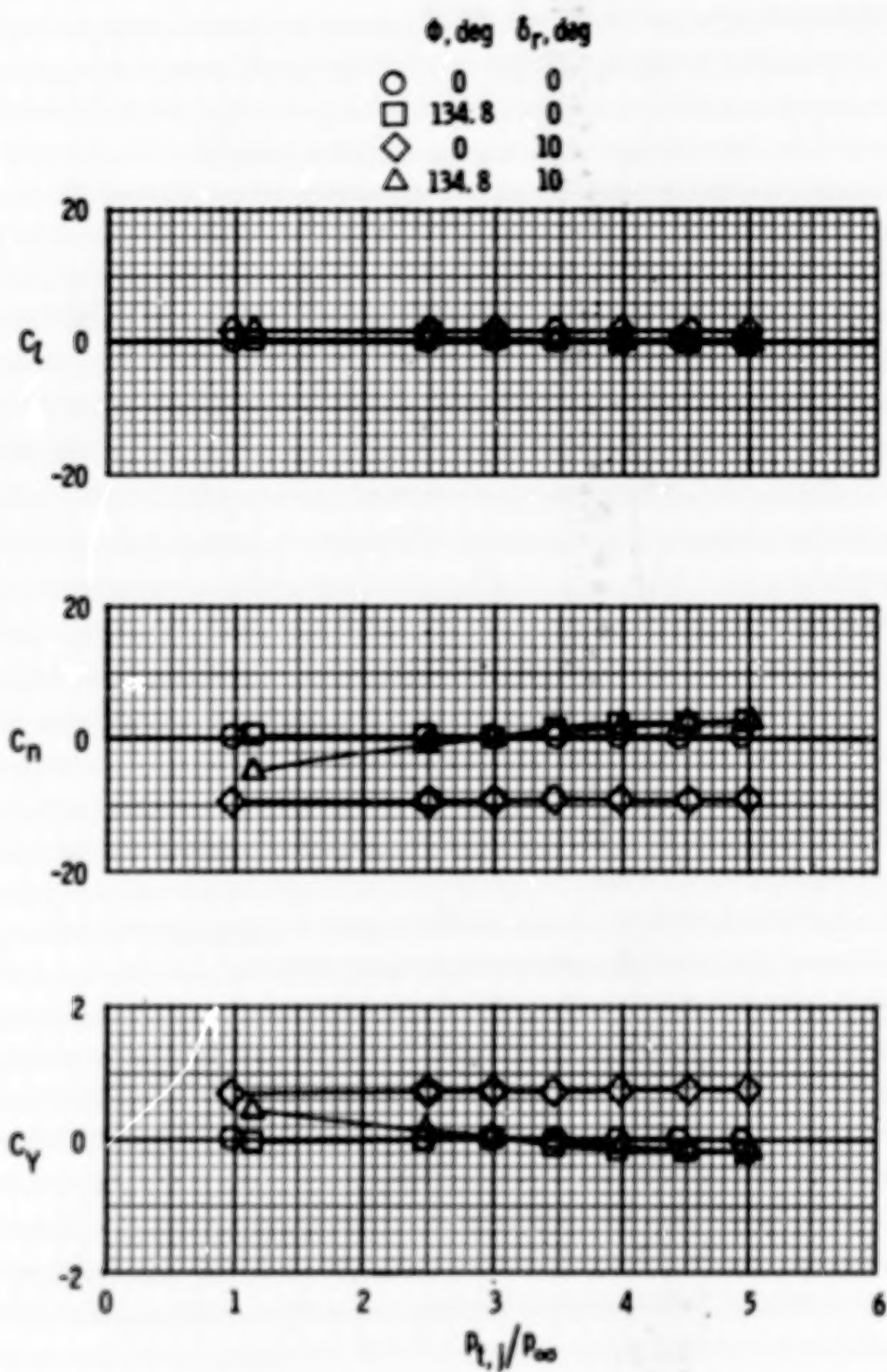
Figure 47.- Continued.





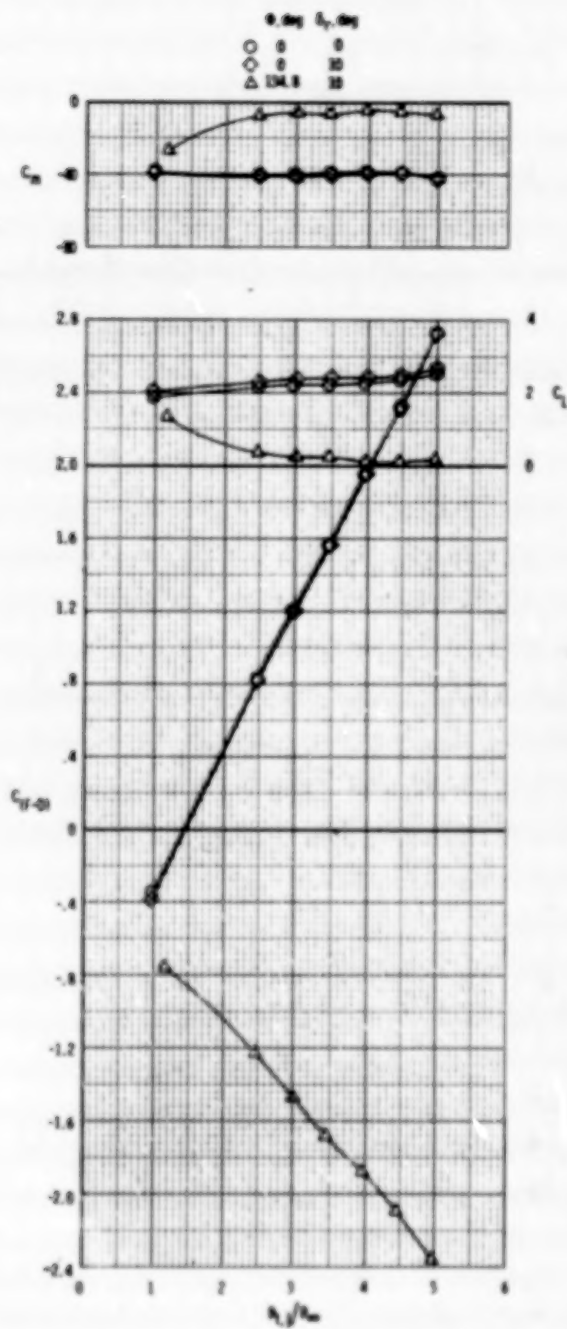
(c)  $M = 0.60$ ;  $\alpha = 0^\circ$ .

Figure 47.- Continued.



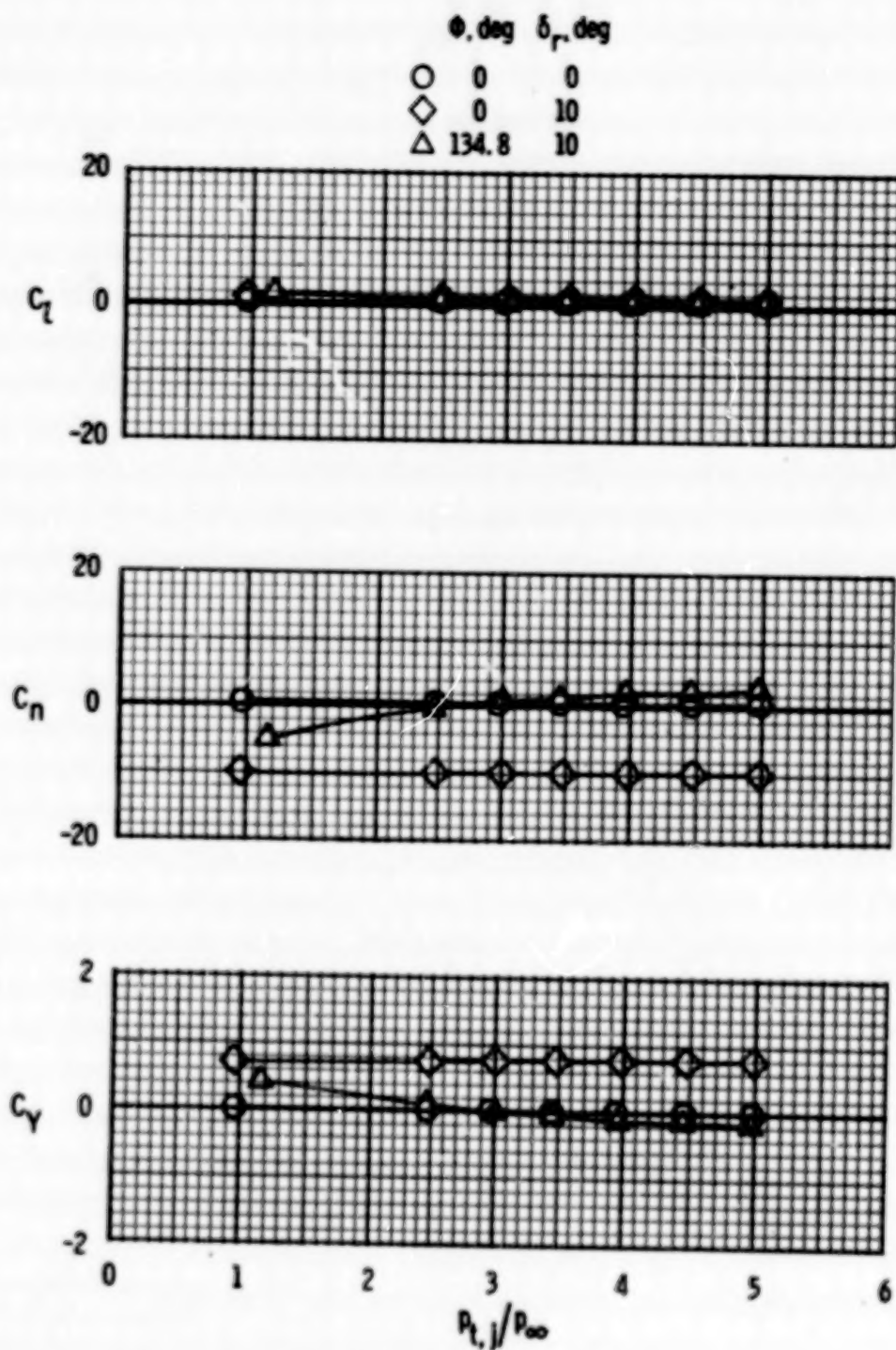
(c)  $M = 0.60$ ;  $\alpha = 0^\circ$ . Concluded.

Figure 47.- Continued.



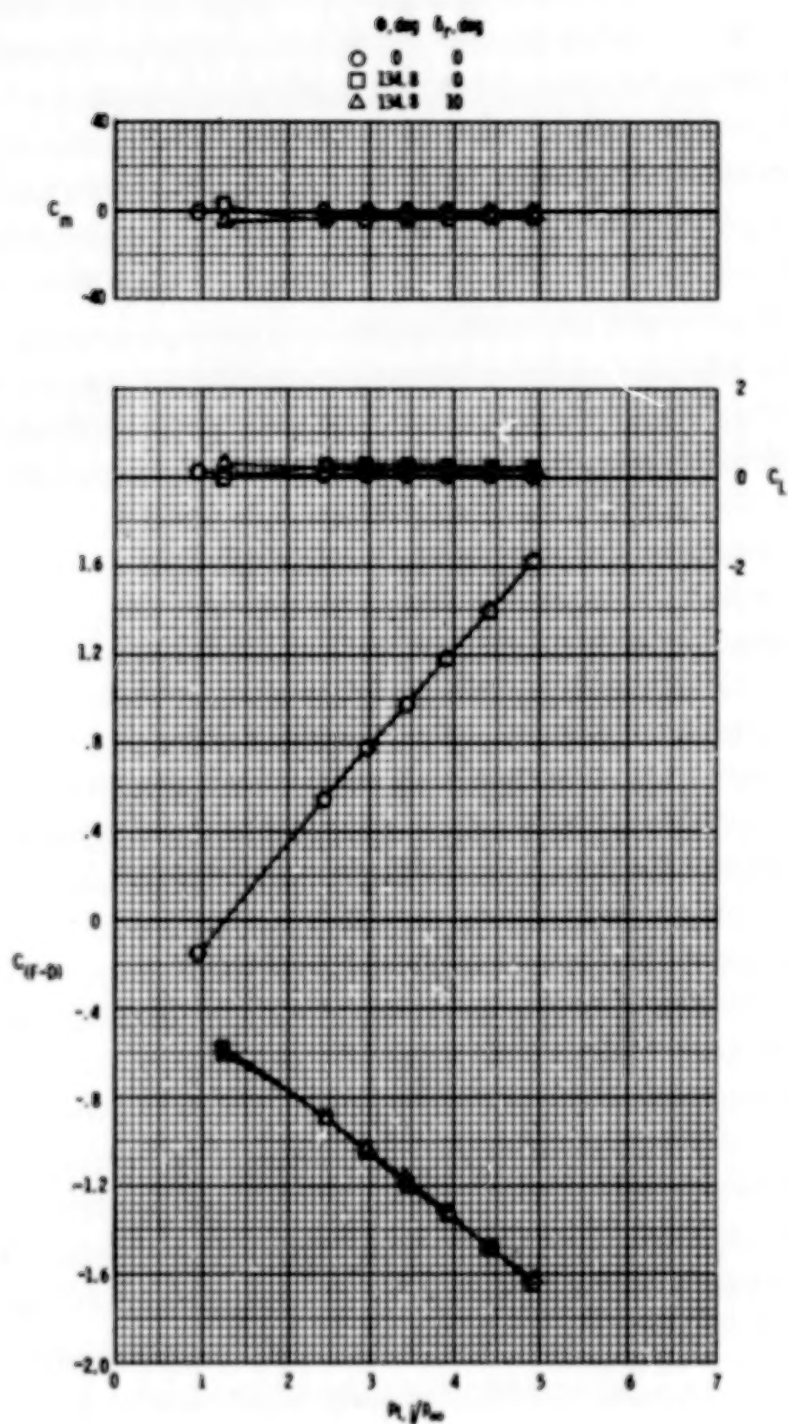
(d)  $M = 0.60$ ;  $\alpha = 8^\circ$ .

Figure 47.- Continued.



(d)  $M = 0.60$ ;  $\alpha = 8^\circ$ . Concluded.

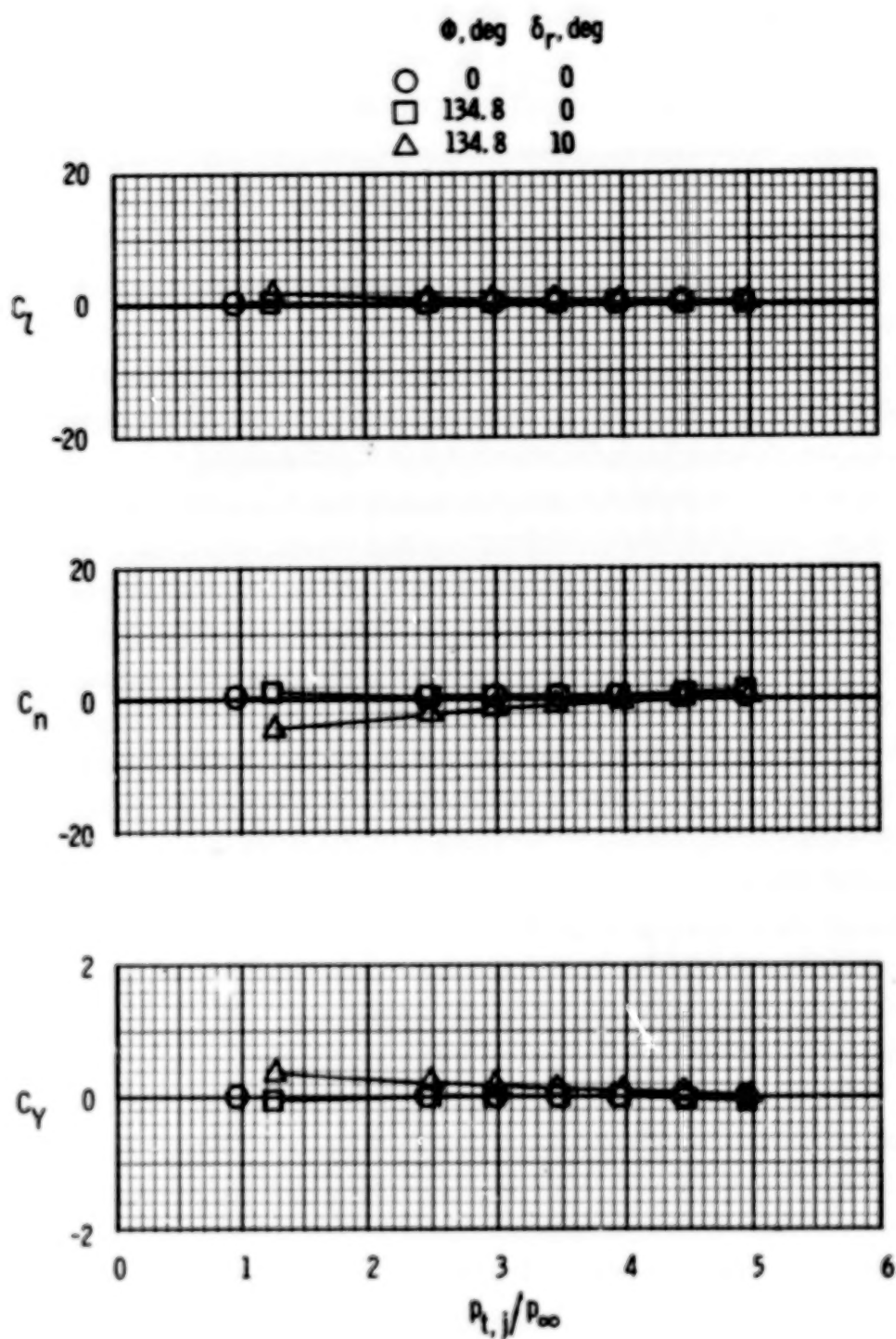
Figure 47.- Continued.



(e)  $M = 0.80$ ;  $\alpha = 0^\circ$ .

Figure 47.- Continued.

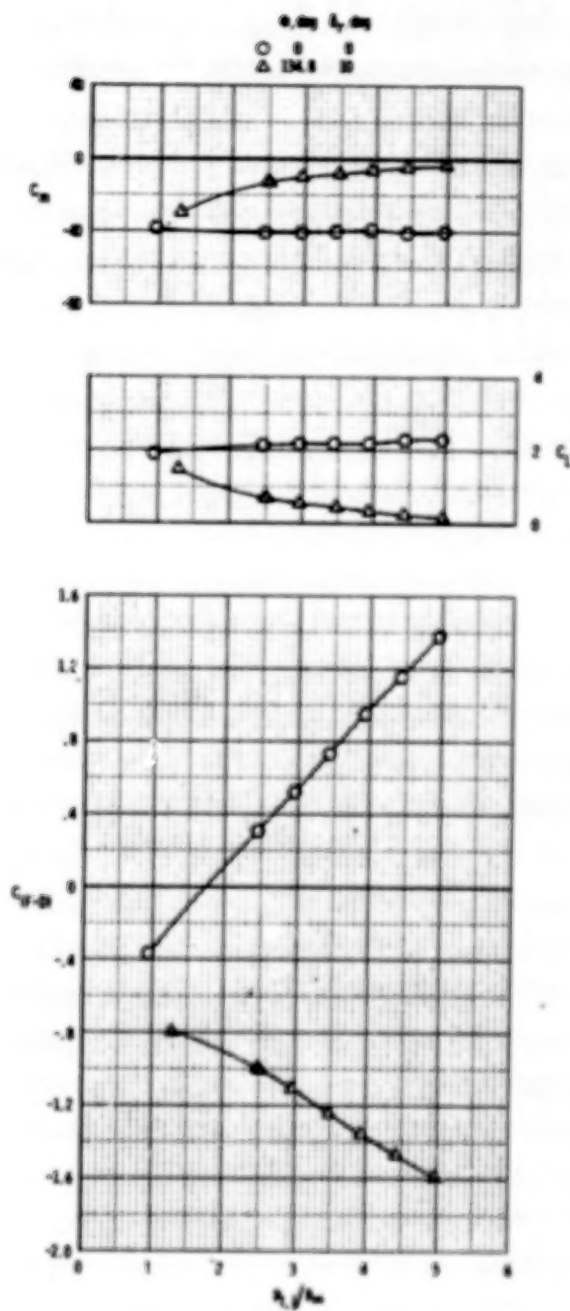




(e)  $M = 0.80$ ;  $\alpha = 0^\circ$ . Concluded.

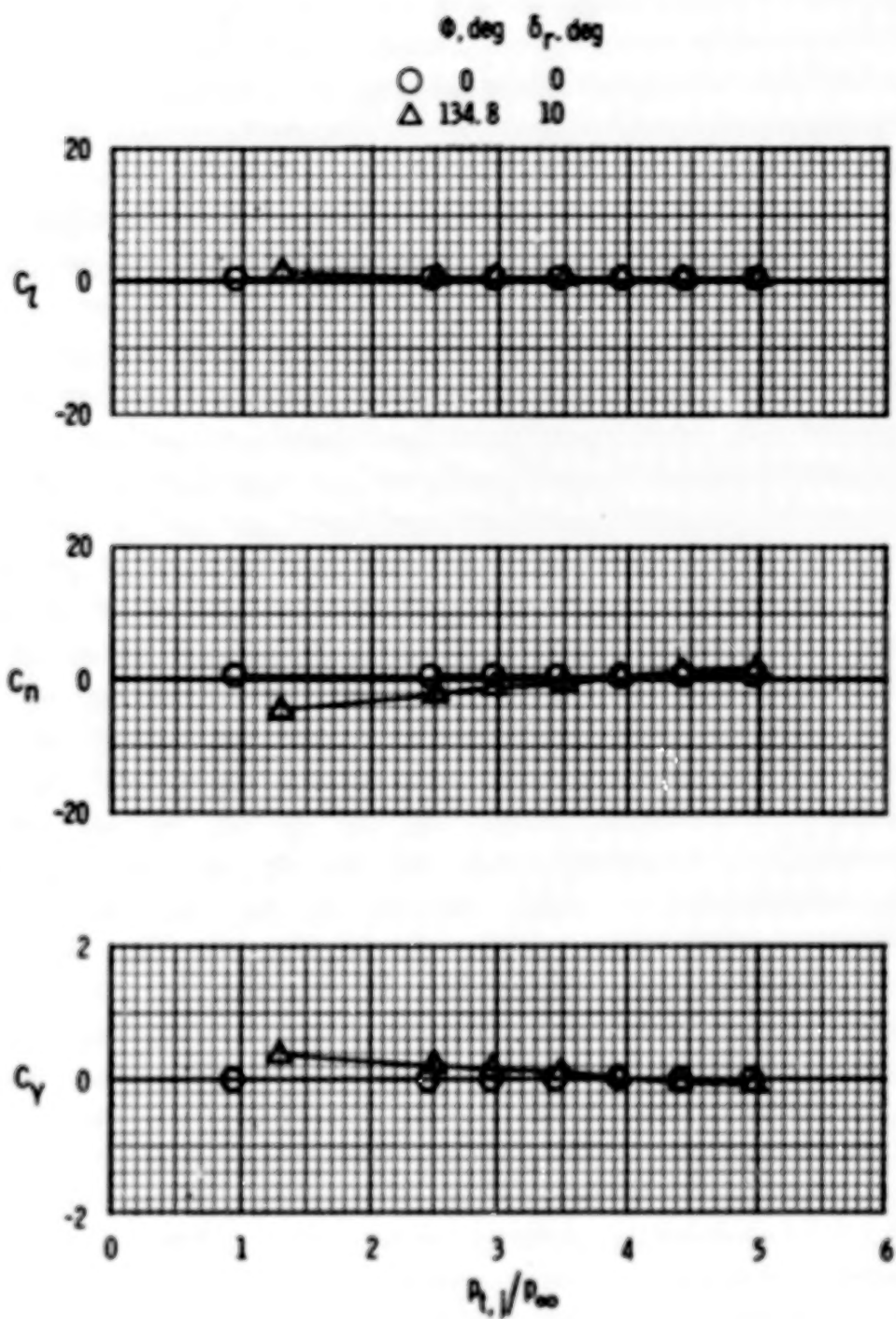
Figure 47.- Continued.





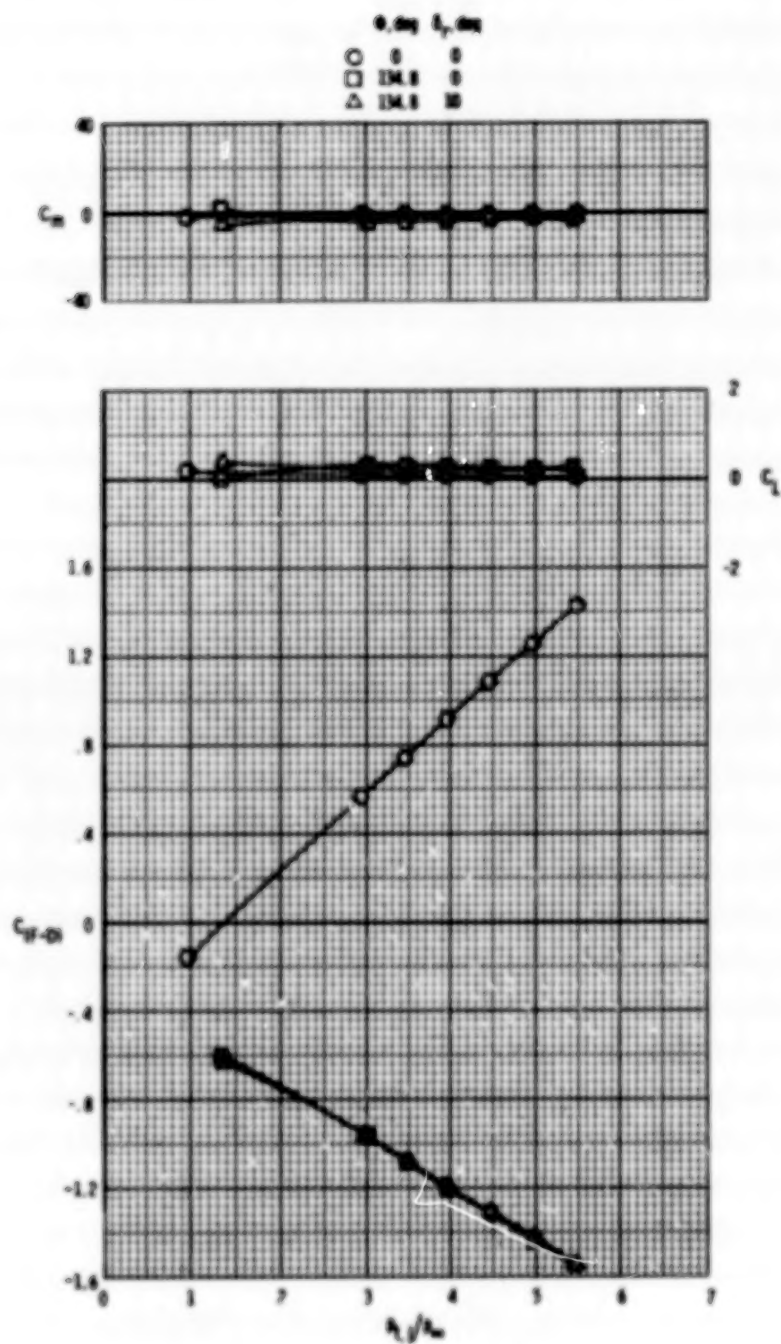
(f)  $M = 0.80$ ;  $\alpha = 80^\circ$ .

Figure 47.- Continued.



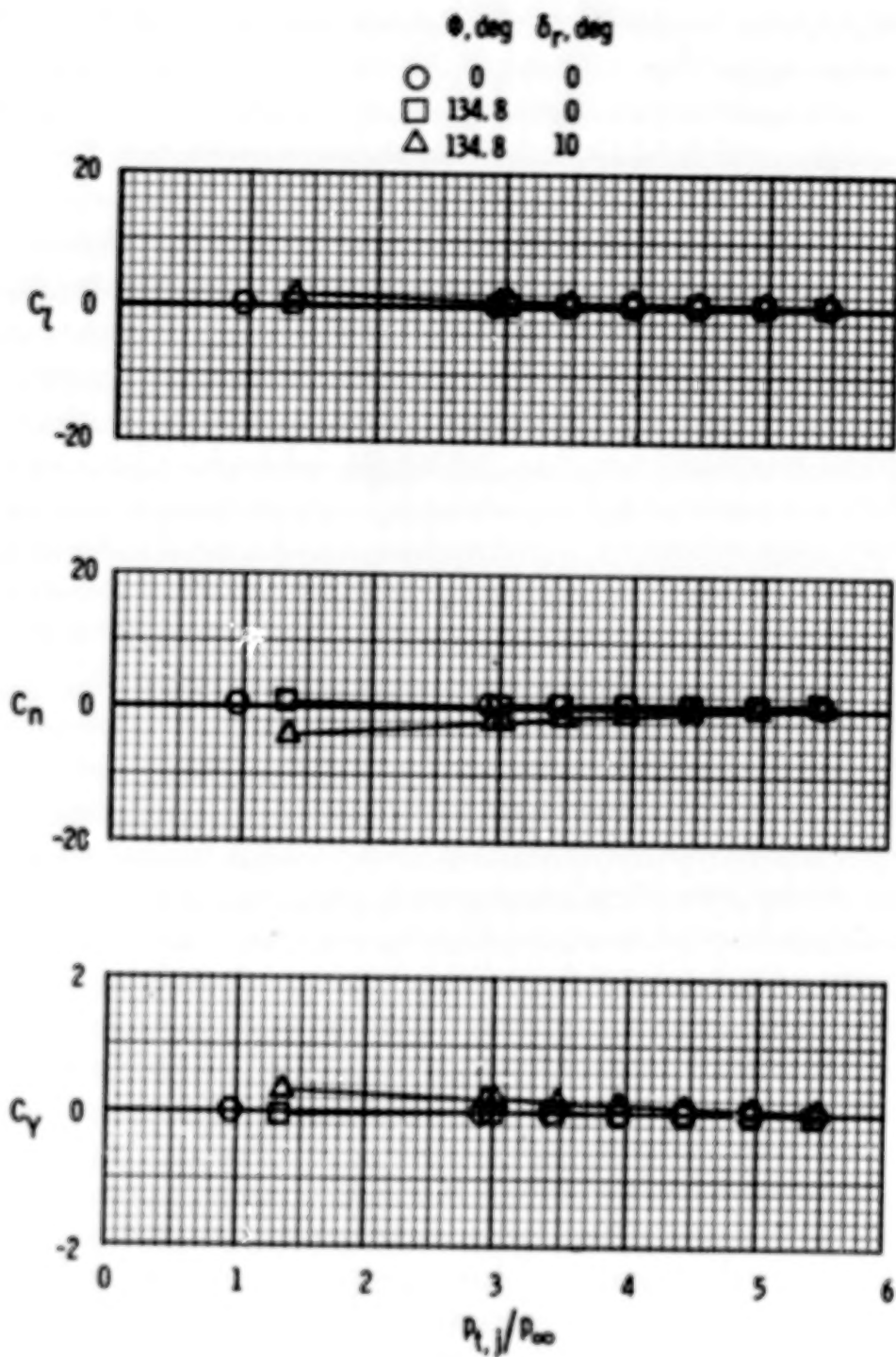
(f)  $M = 0.80$ ;  $\alpha = 8^\circ$ . Concluded.

Figure 47.- Continued.



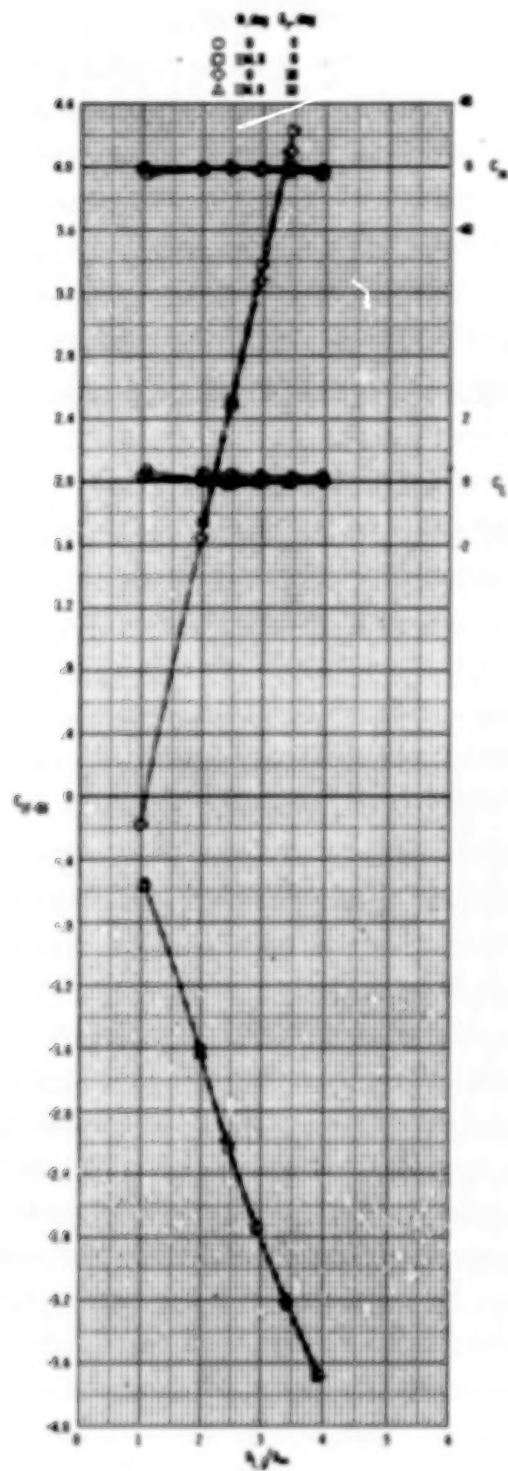
(g)  $M = 0.90$ ;  $\alpha = 0^\circ$ .

Figure 47.- Continued.



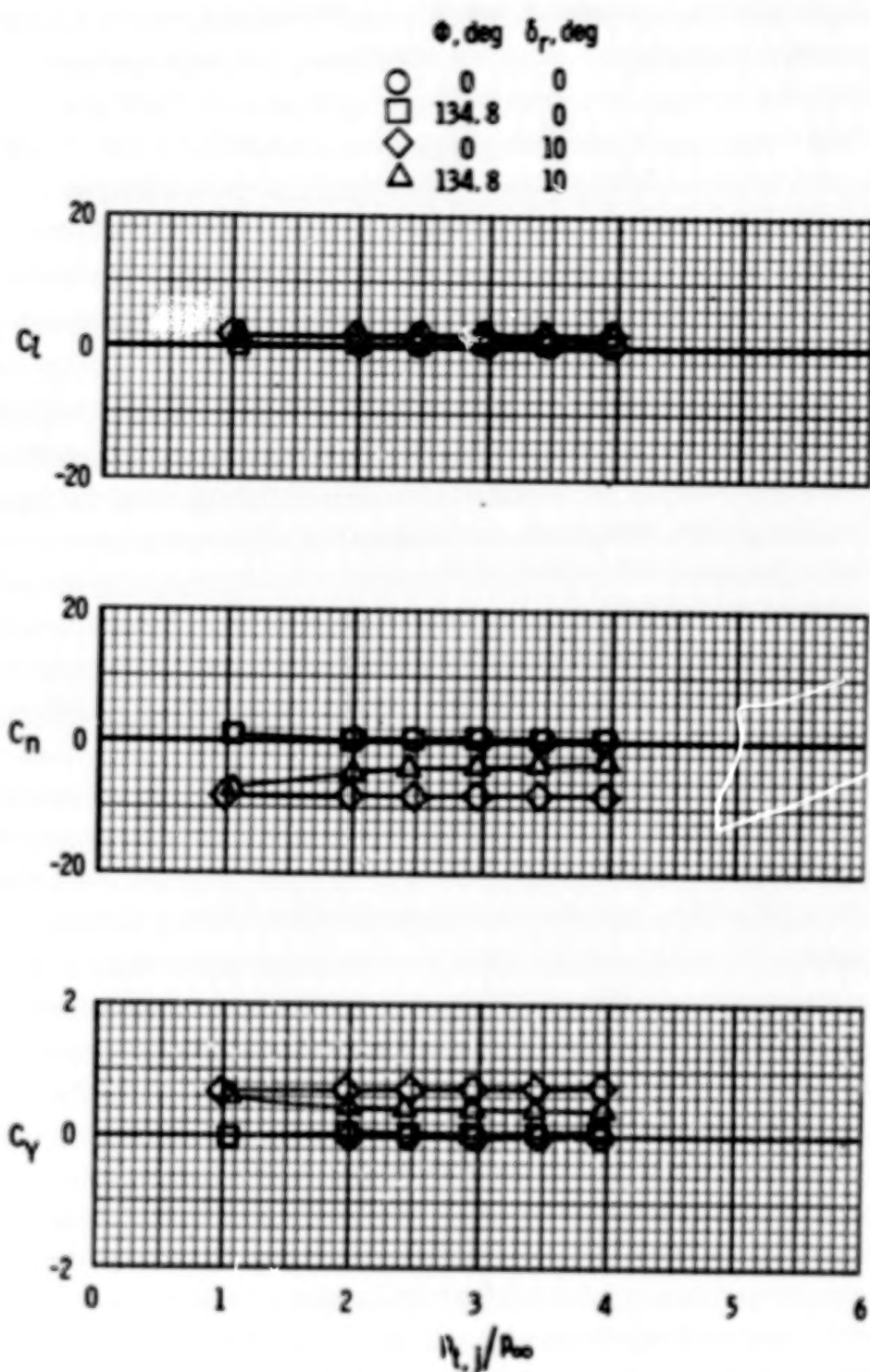
(g)  $M = 0.90$ ;  $\alpha = 0^\circ$ . Concluded.

Figure 47.- Concluded.



(a)  $M = 0.40$ ;  $\alpha = 0^\circ$ .

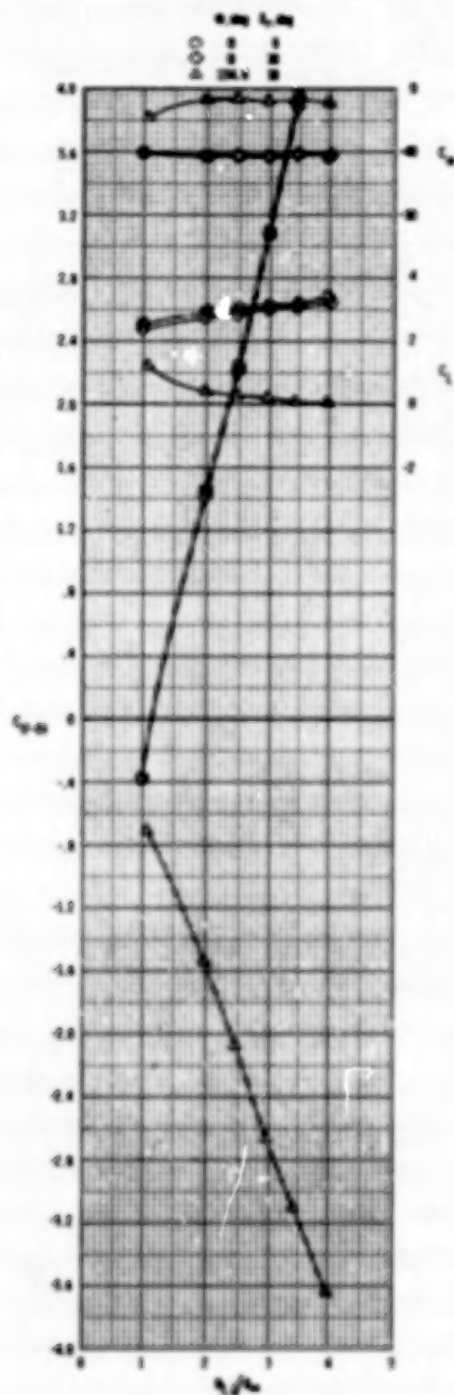
Figure 48.- Effect of rudder deflection and reverse thrust on aerodynamic characteristics. Twin vertical tails;  $\delta_h = 0^\circ$ .



(a)  $M = 0.40$ ;  $\alpha = 0^\circ$ . Concluded.

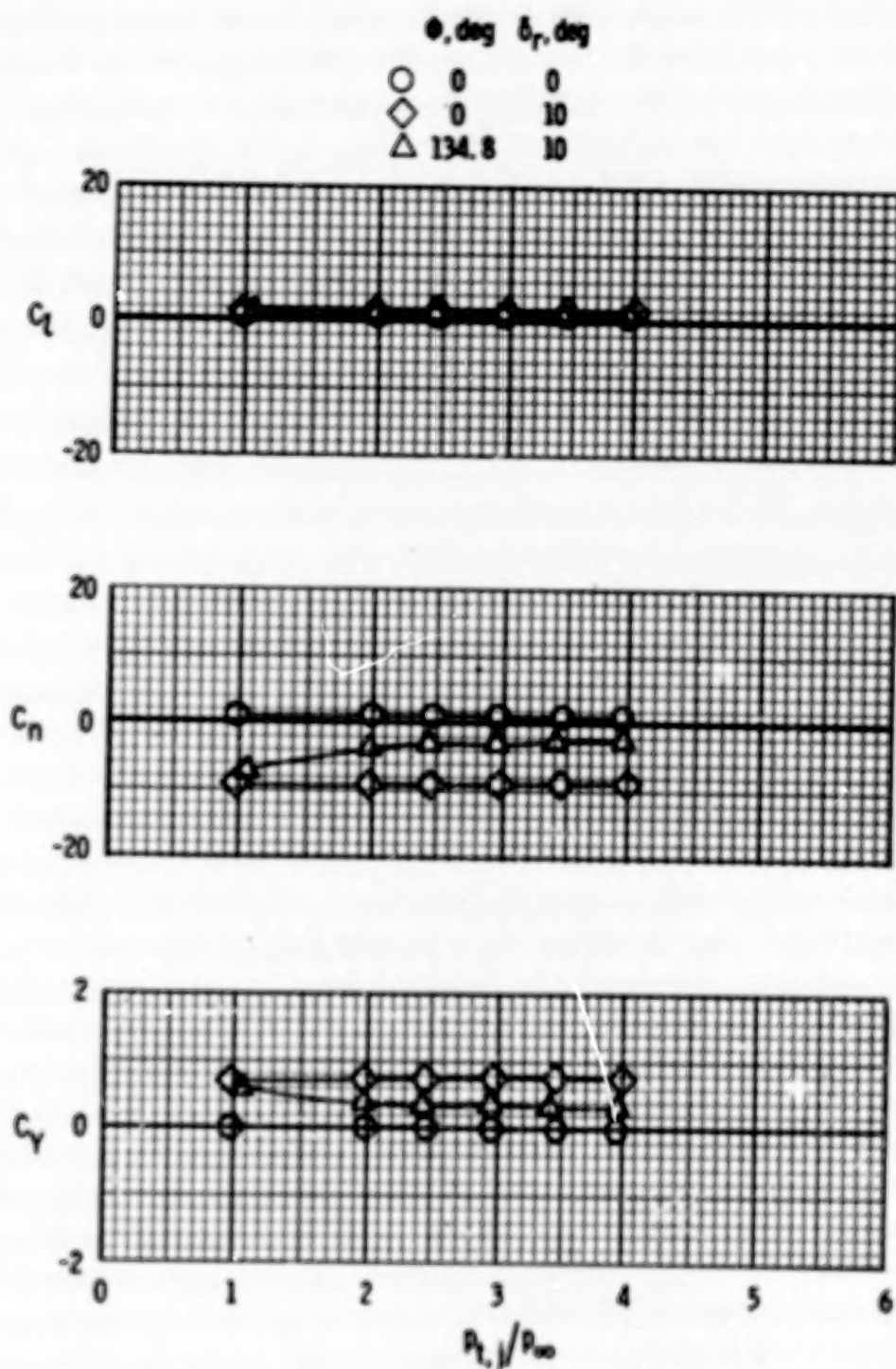
Figure 48.- Continued.





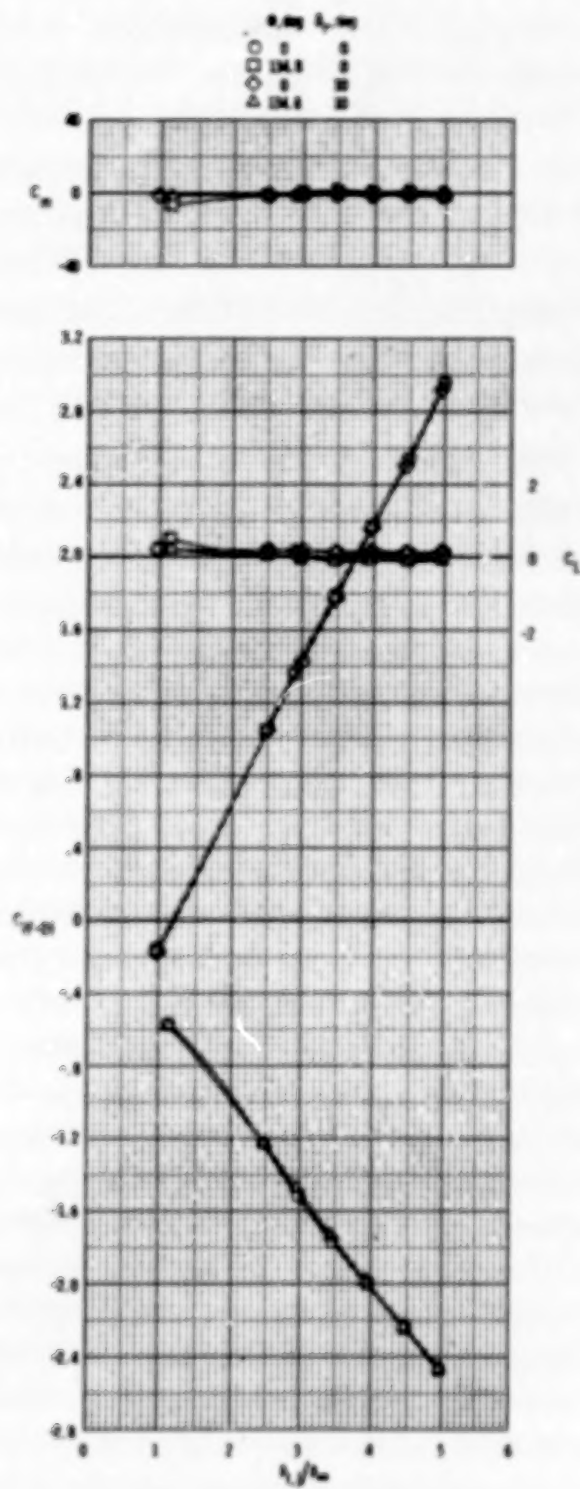
(b)  $M = 0.40$ ;  $\alpha = 8^\circ$ .

Figure 48.- Continued.



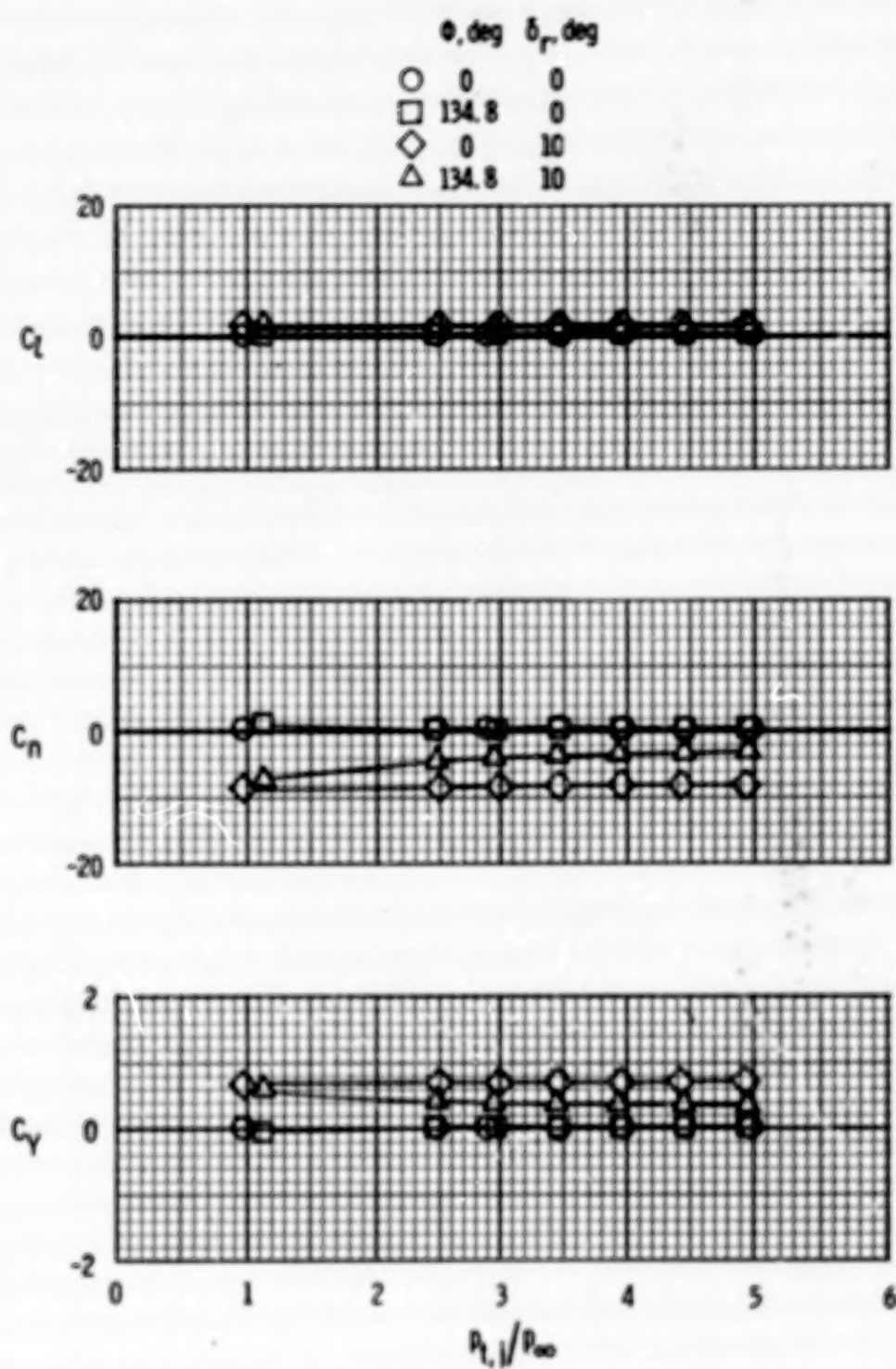
(b)  $M = 0.40$ ;  $\alpha = 8^\circ$ . Concluded.

Figure 48.- Continued.



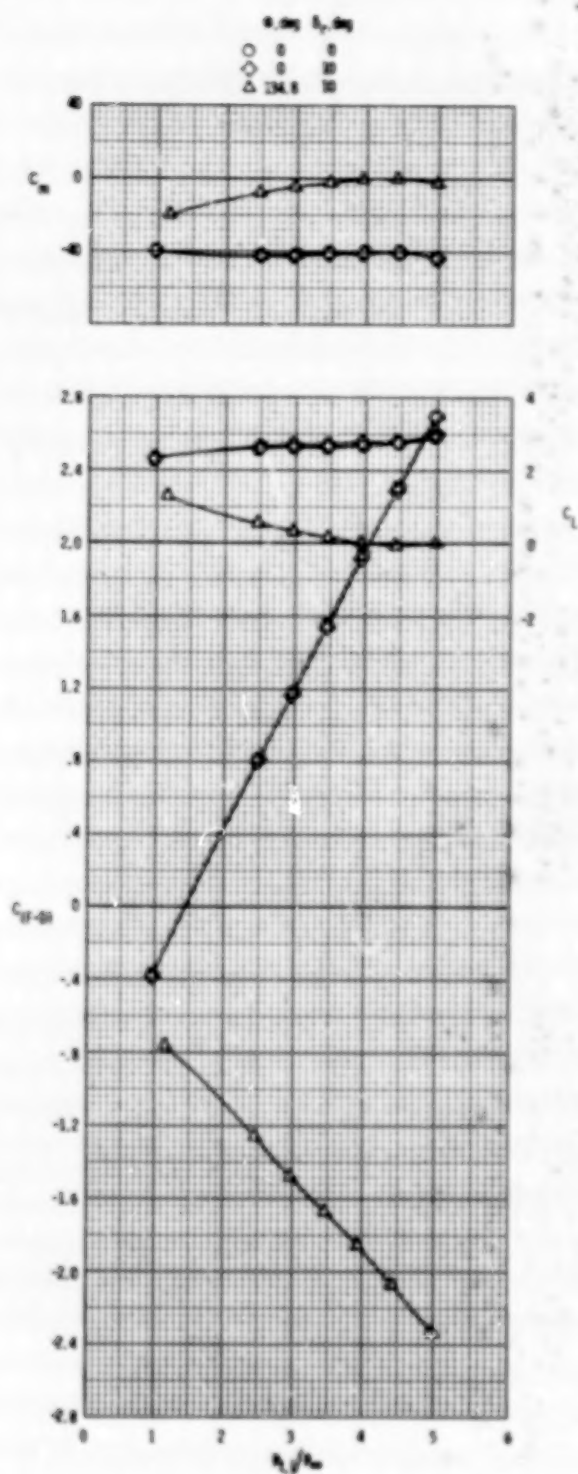
(c)  $M = 0.60$ ;  $\alpha = 0^\circ$ .

Figure 48.- Continued.



(c)  $M = 0.60$ ;  $\alpha = 0^\circ$ . Concluded.

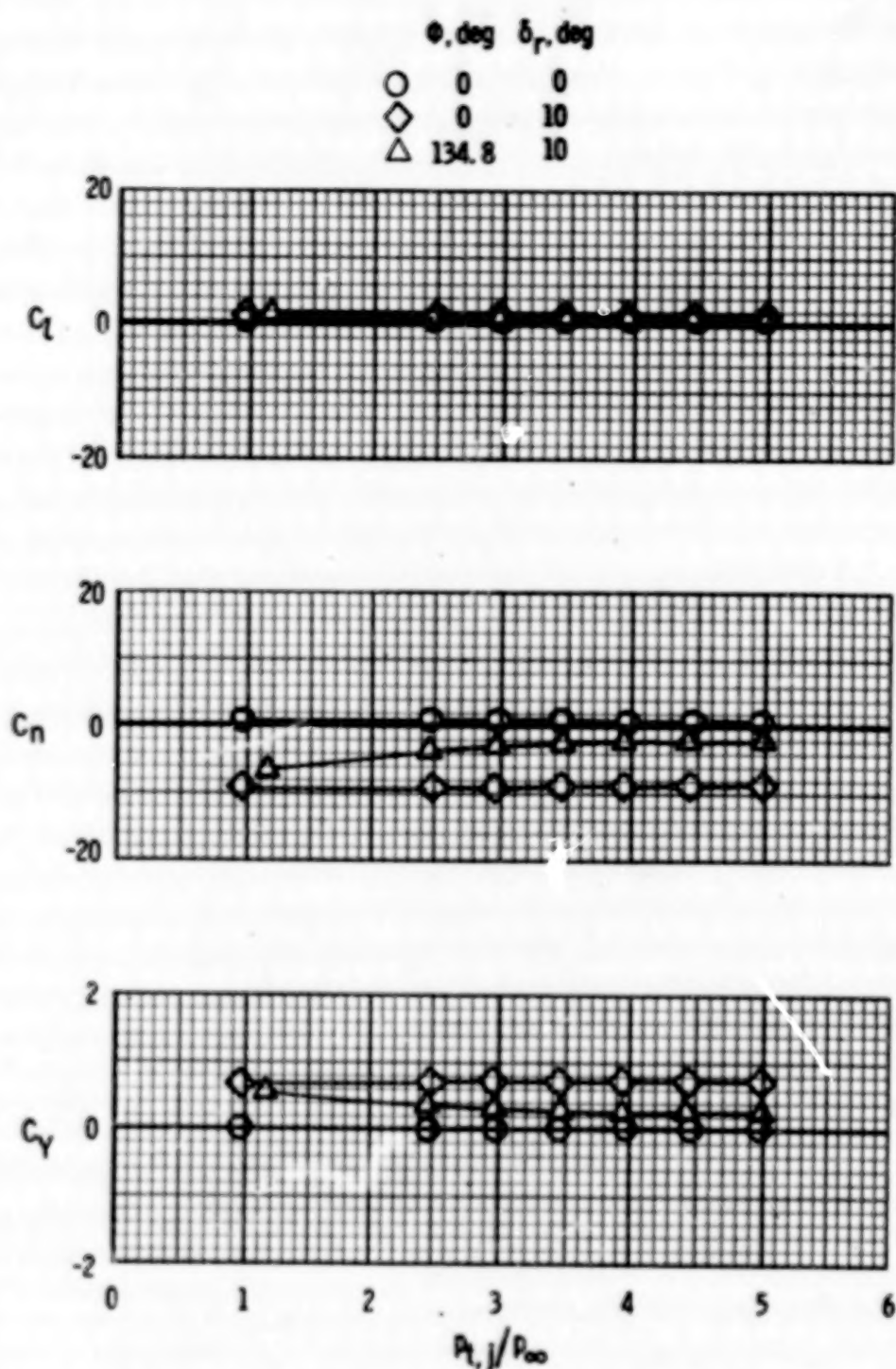
Figure 48.- Continued.



(d)  $M = 0.60$ ;  $\alpha = 80^\circ$ .

Figure 48.- Continued.

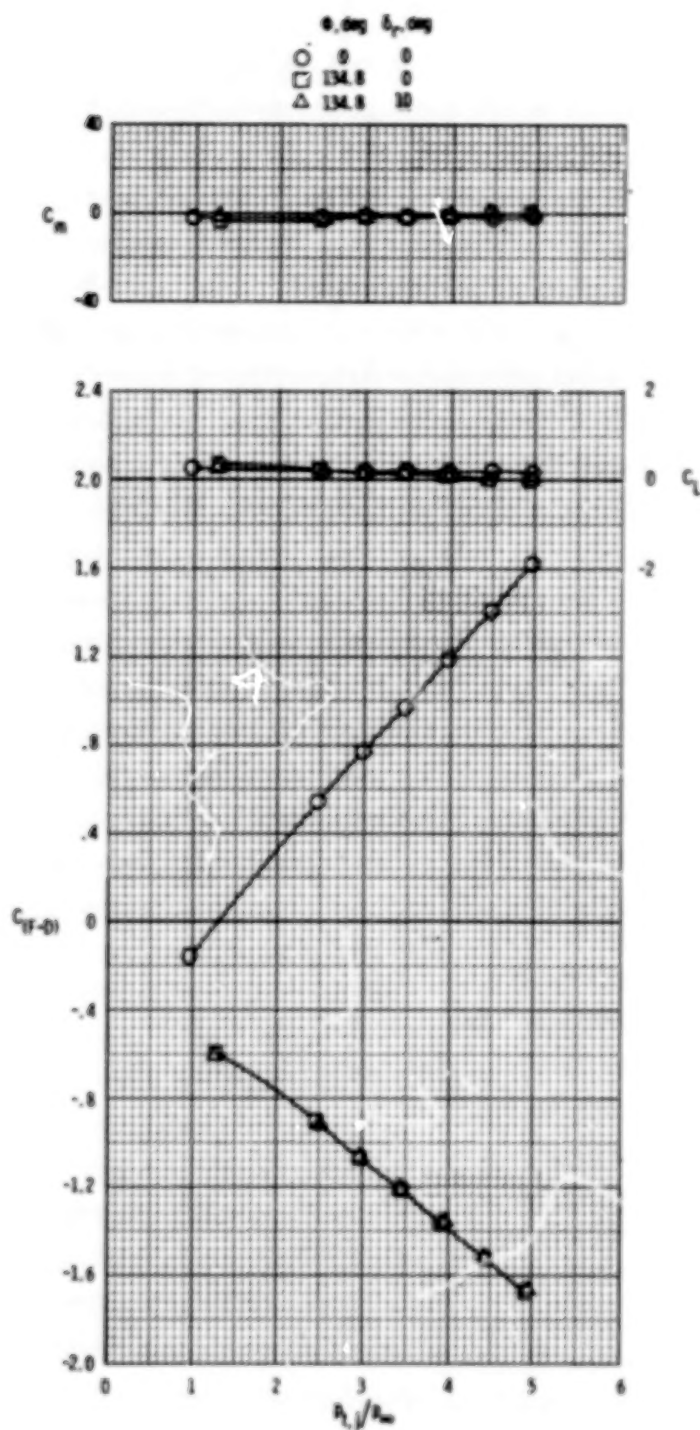




(d)  $M = 0.60$ ;  $\alpha = 8^\circ$ . Concluded.

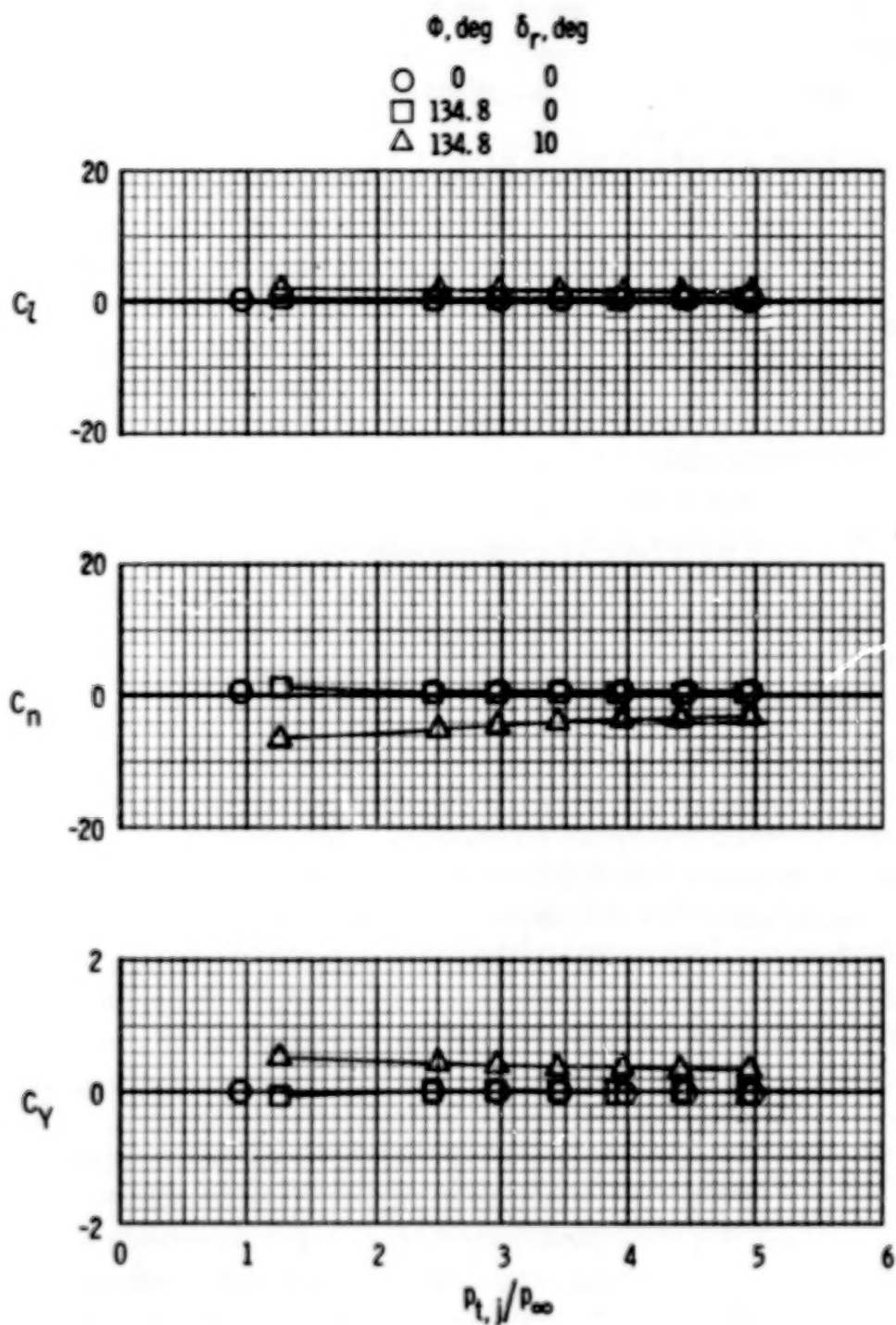
Figure 48.- Continued.





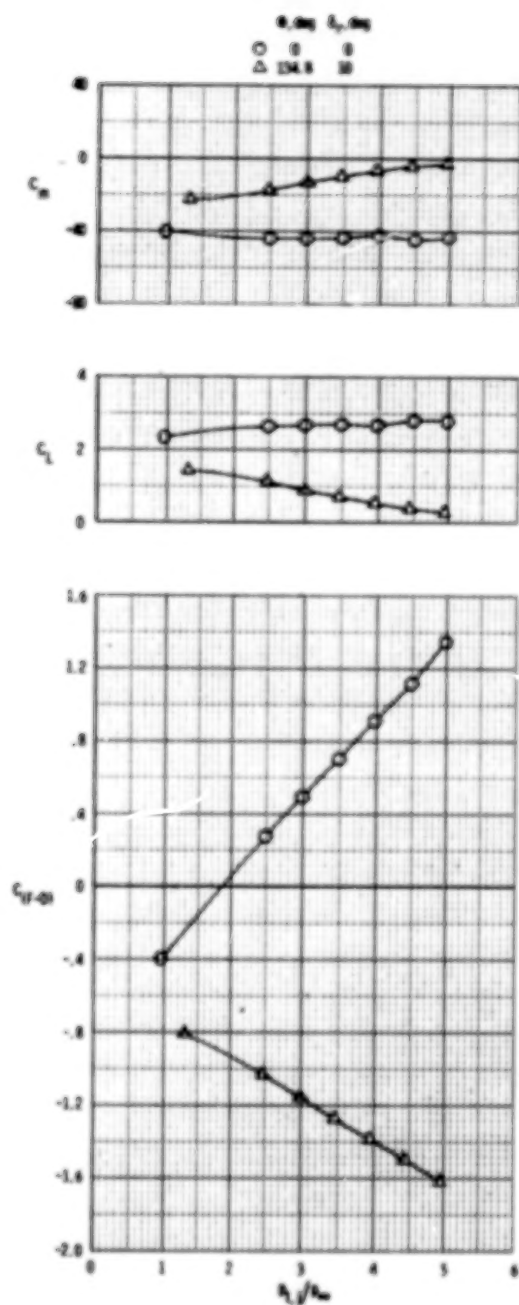
(e)  $M = 0.80; \alpha = 0^\circ.$

Figure 48.- Continued.



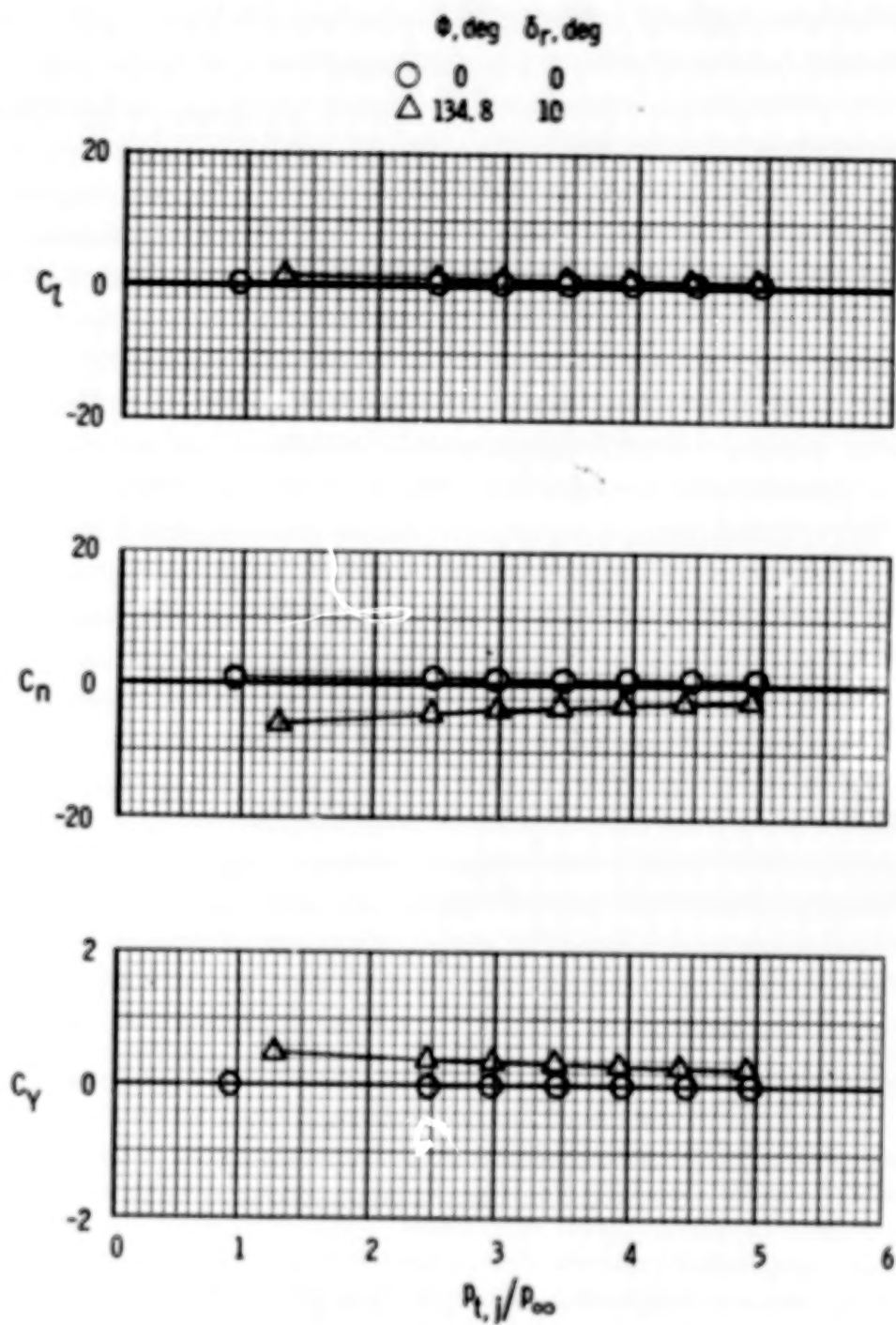
(e)  $M = 0.80$ ;  $\alpha = 0^\circ$ . Concluded.

Figure 48.- Continued.



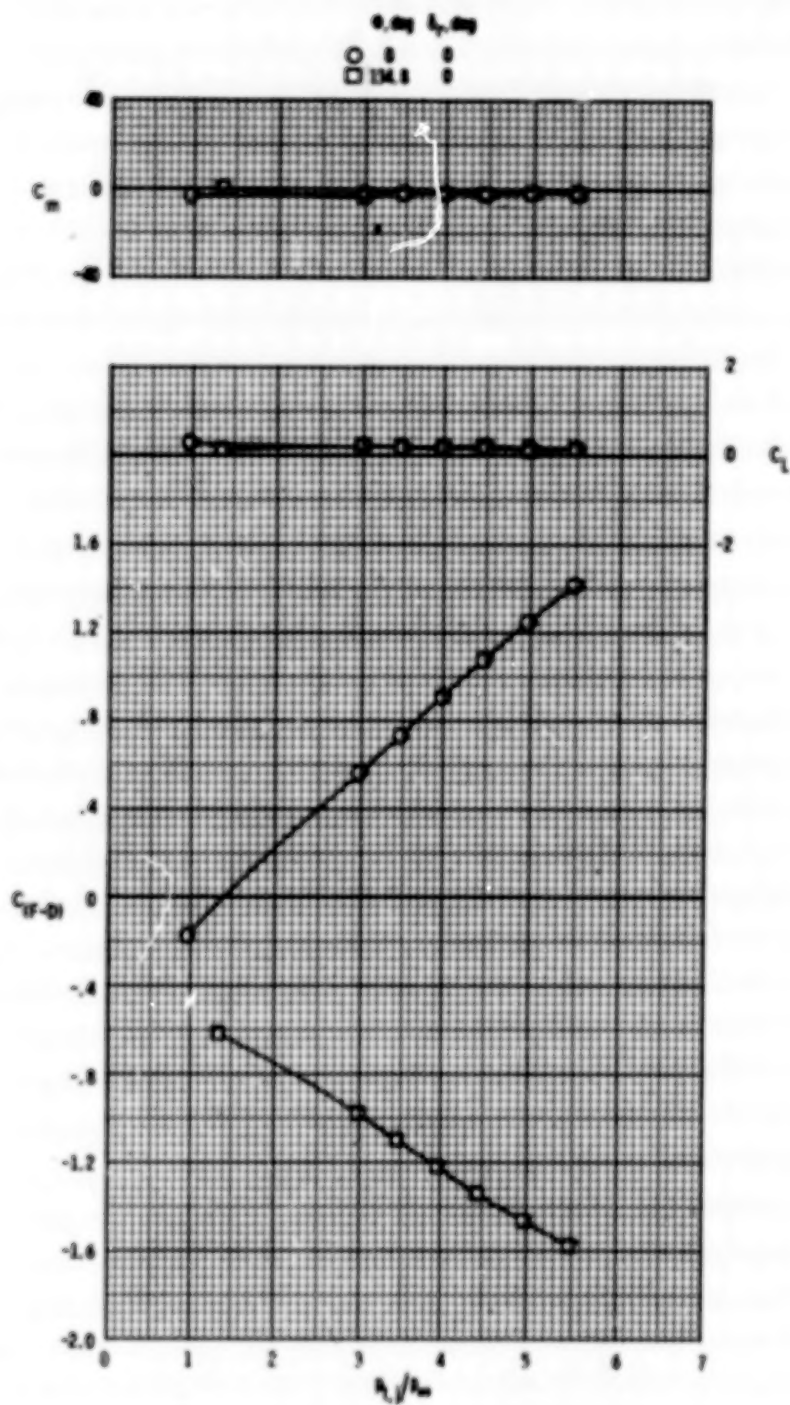
(f)  $M = 0.80, \alpha = 8^\circ$ .

Figure 48.- Continued.



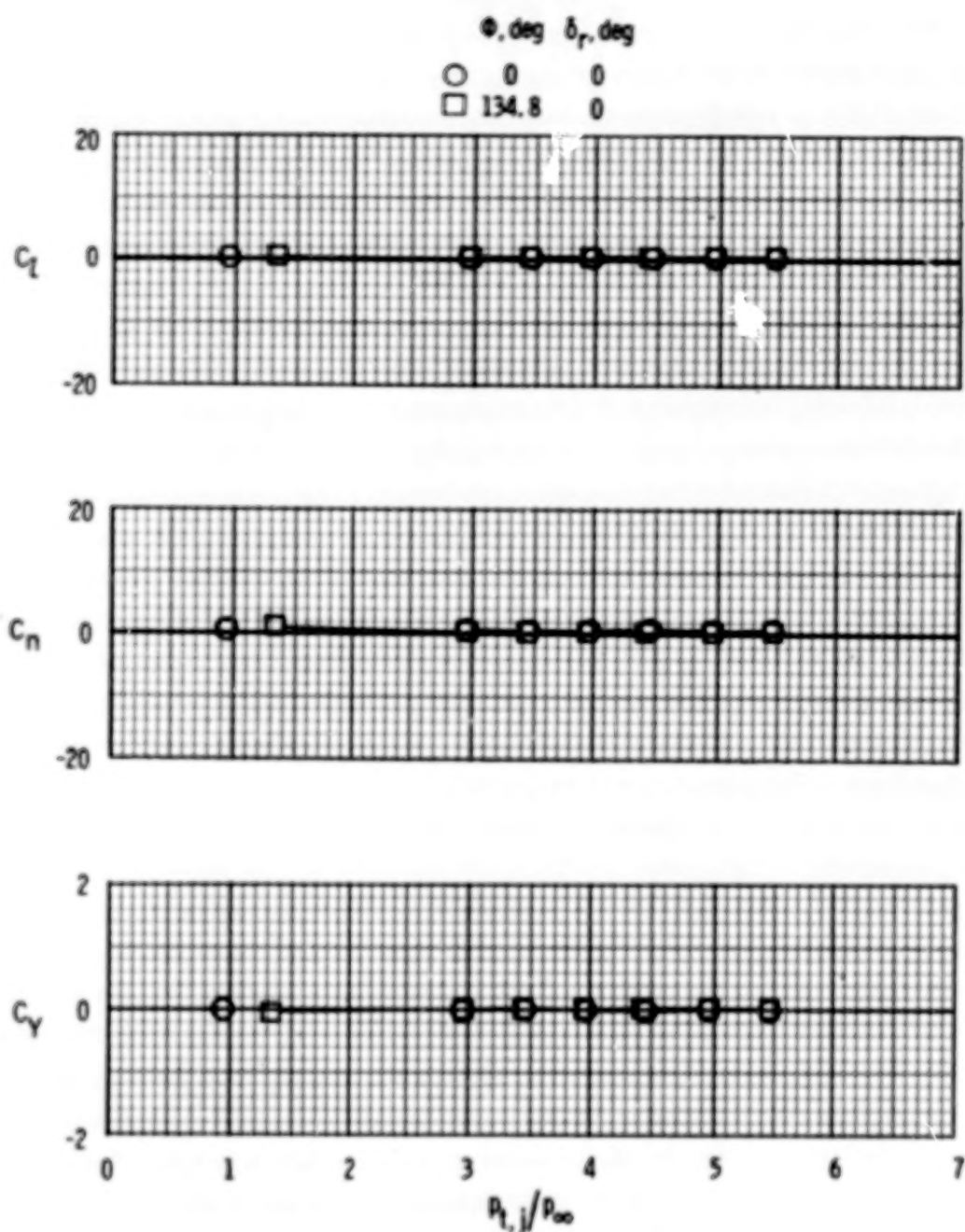
(f)  $M = 0.80$ ,  $\alpha = 8^\circ$ . Concluded.

Figure 48.- Continued.



(g)  $M = 0.90$ ,  $\alpha = 0^\circ$ .

Figure 48.- Continued.



(g)  $M = 0.90$ ,  $\alpha = 0^\circ$ . Concluded.

Figure 48.- Concluded.



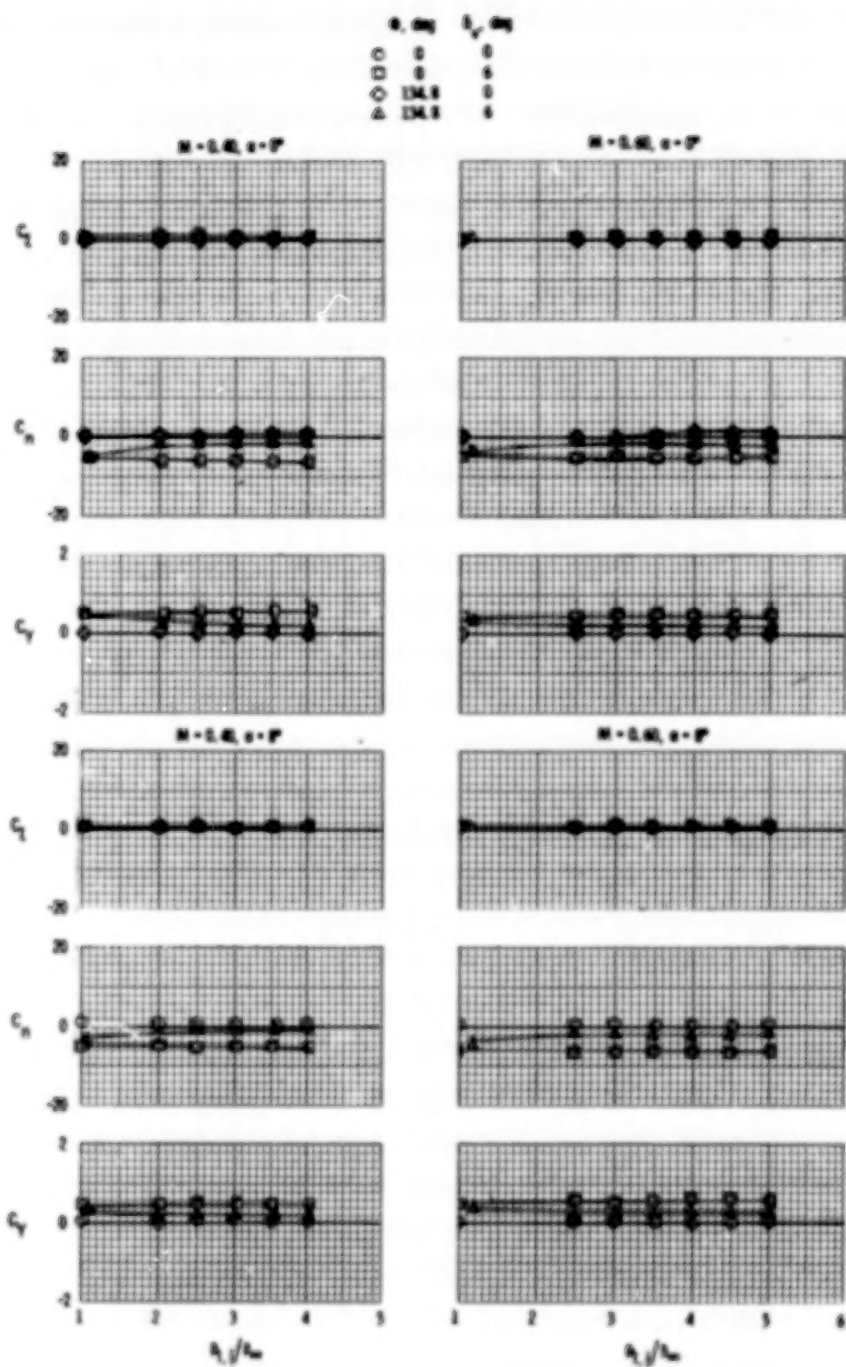


Figure 49.- Effect of single vertical-tail deflection on lateral aerodynamic characteristics with reverse thrust.  $\delta_h = 0^\circ$ .

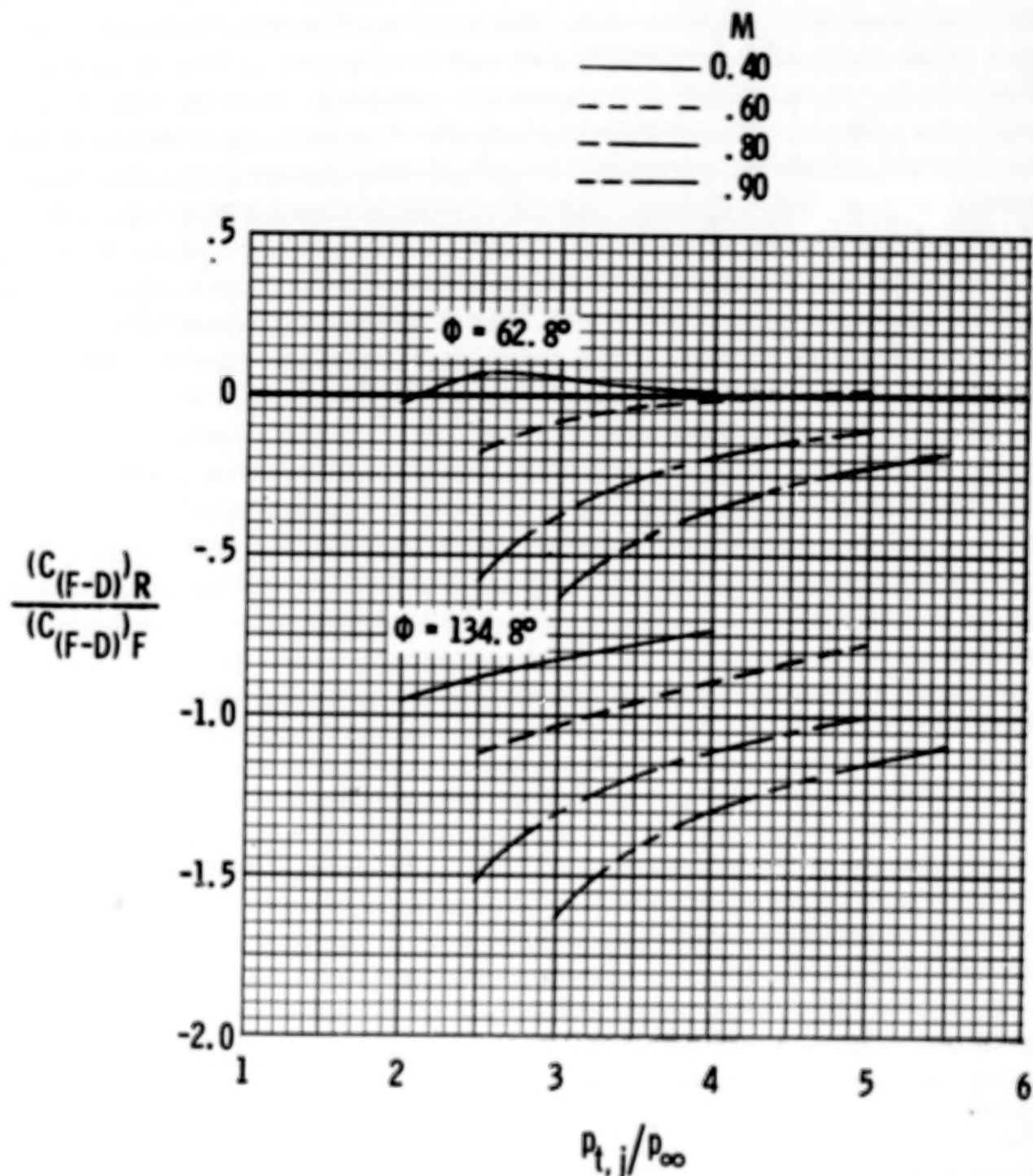


Figure 50.- Effect of nozzle pressure ratio on thrust reverser effectiveness.  
Single vertical tail;  $\delta_h = 0^\circ$ .

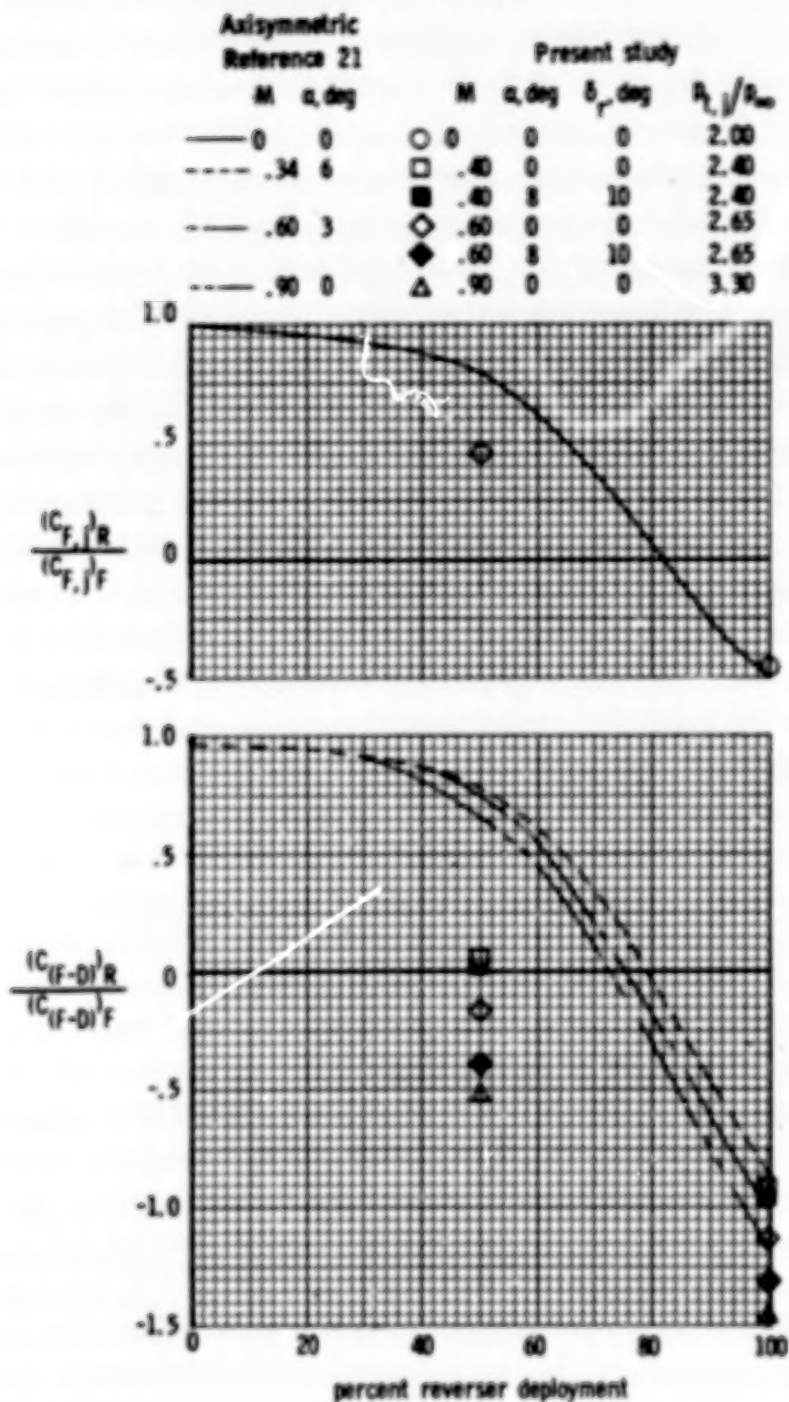


Figure 51.- Thrust modulation performance as function of percent reverser deployment. Single tail;  $\delta_h = 0^\circ$  for present study.

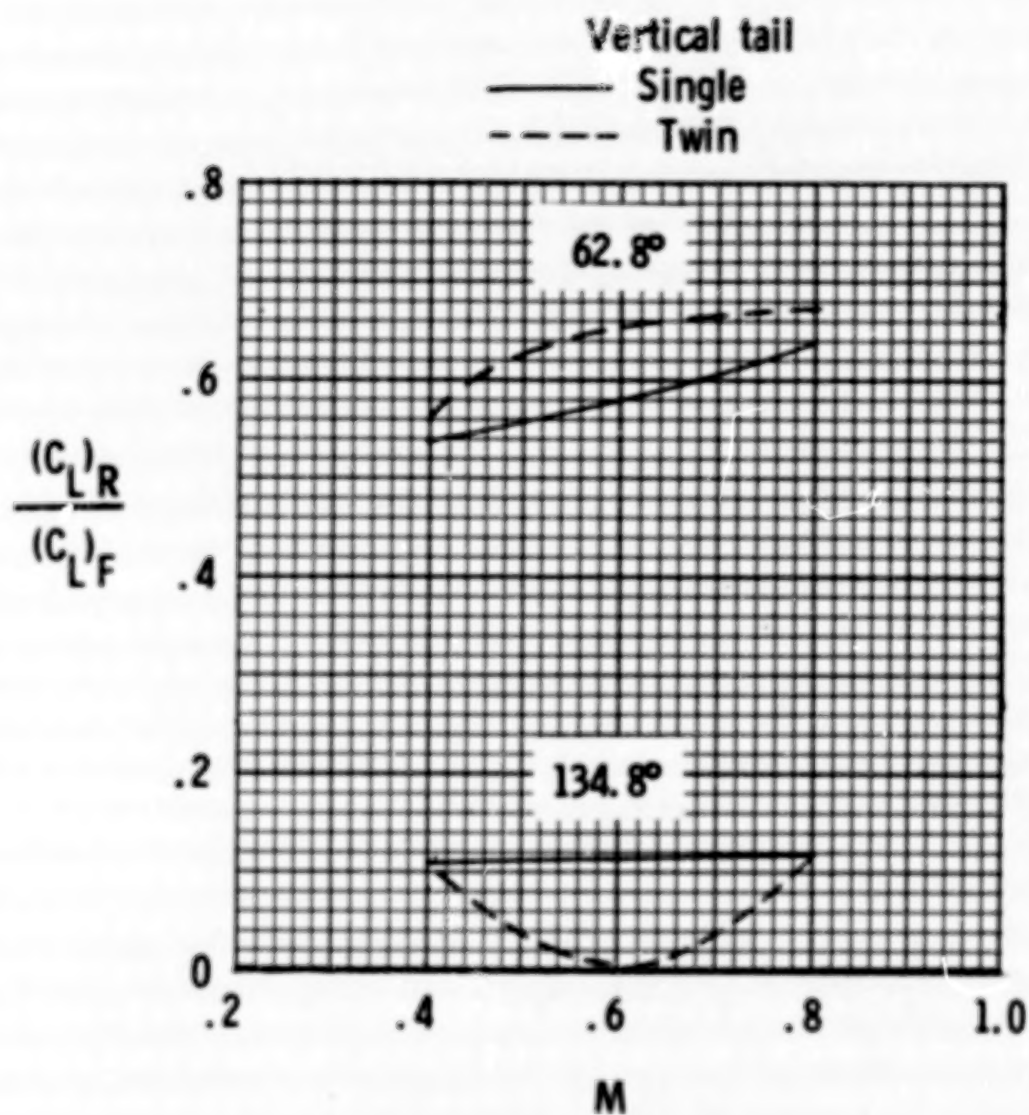


Figure 52.- Variation of  $(C_L)_R / (C_L)_F$  with Mach number.  $\alpha = 8^\circ$ .

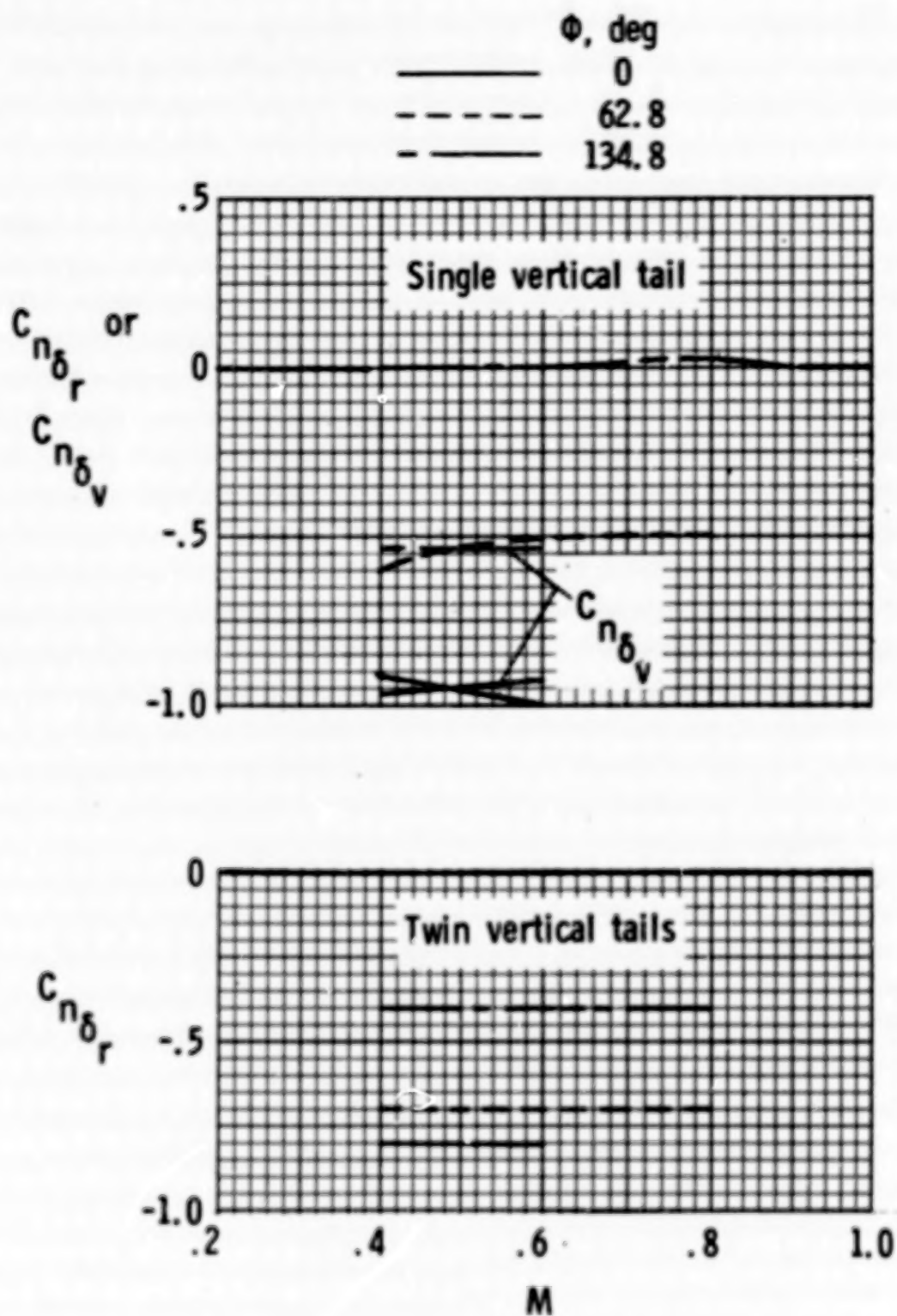
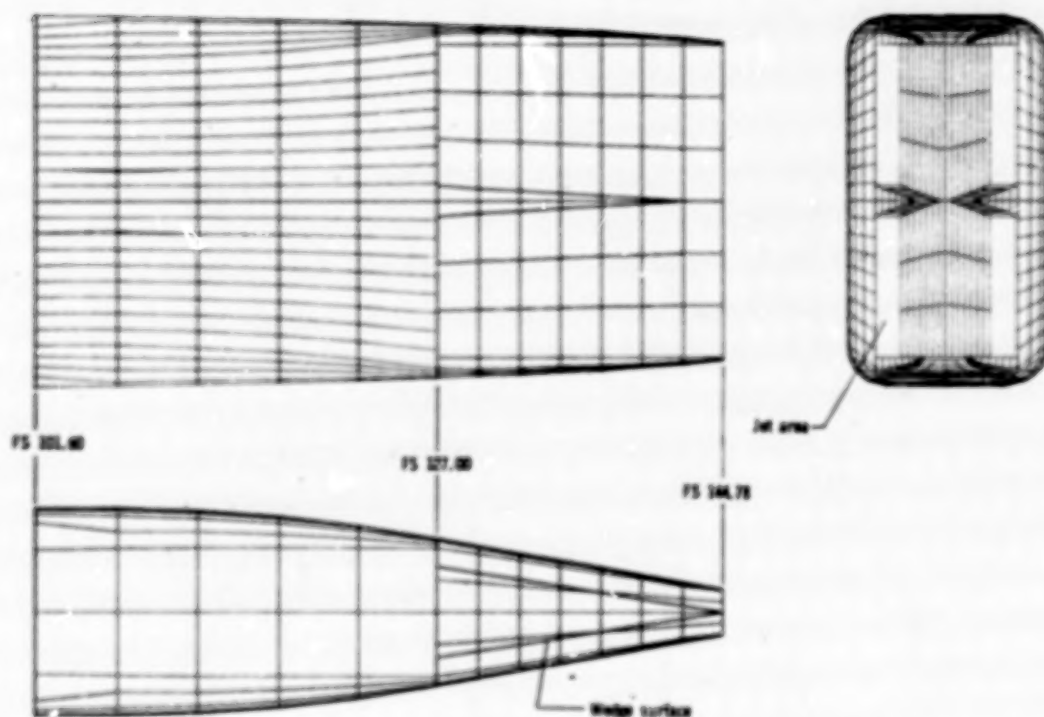


Figure 53.- Effect of thrust reversing on rudder or vertical-tail effectiveness.  $\delta_h = 0^\circ$ ;  $\alpha = 0^\circ$ .

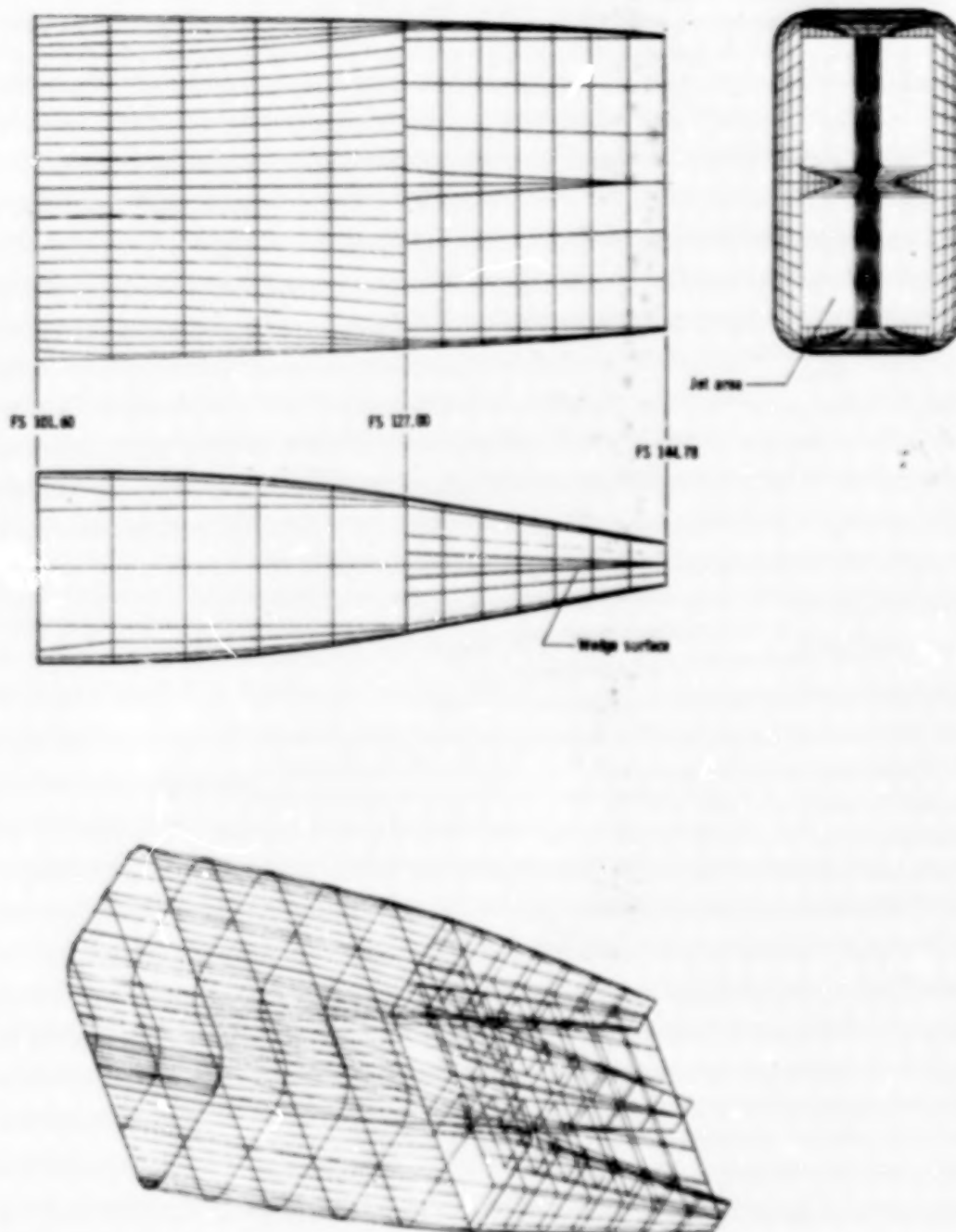




(a) Dry power wedge.

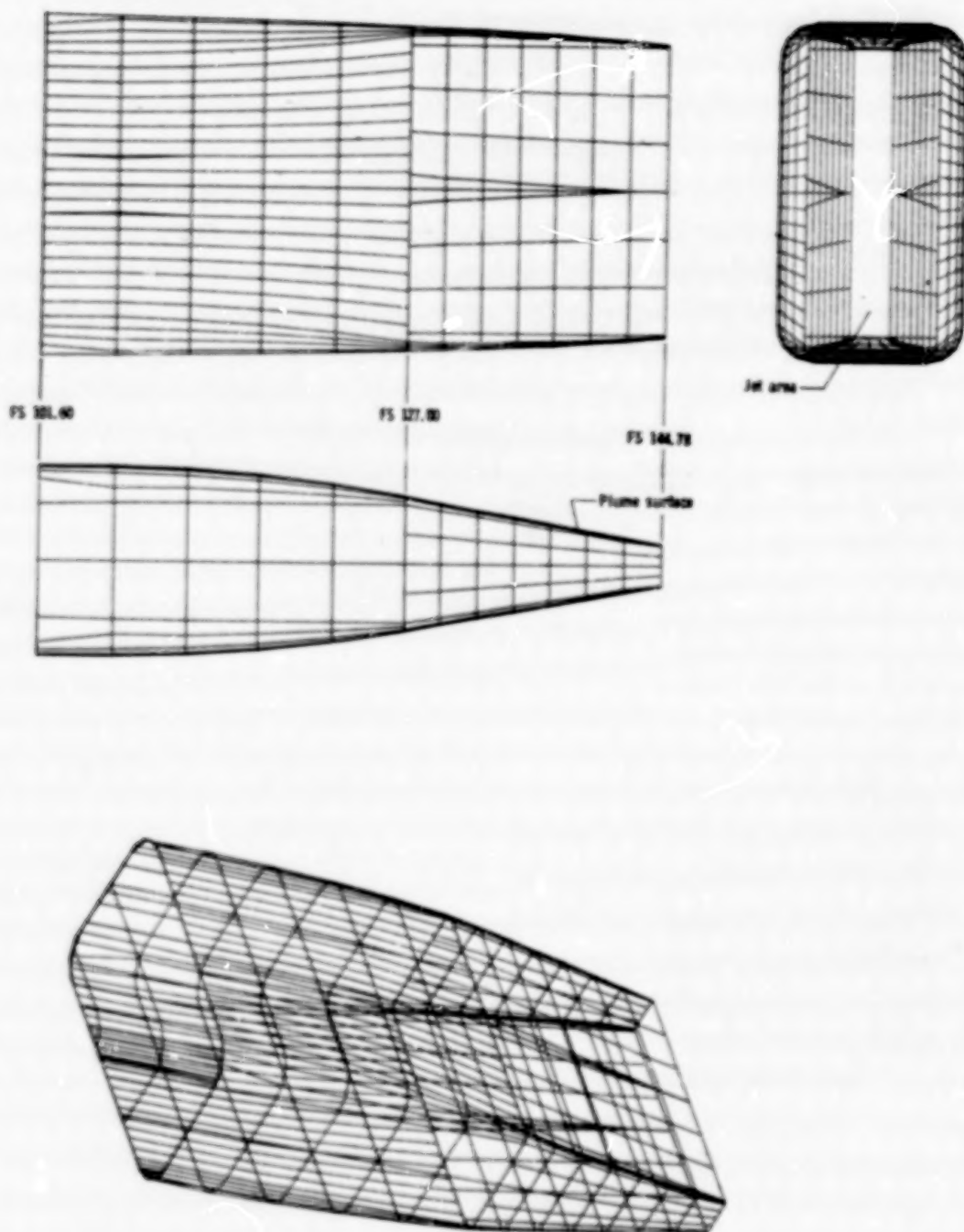
Figure 54.- Computer-generated drawings of various mathematical models used for calculating wave drag. Fuselage stations are in centimeters.





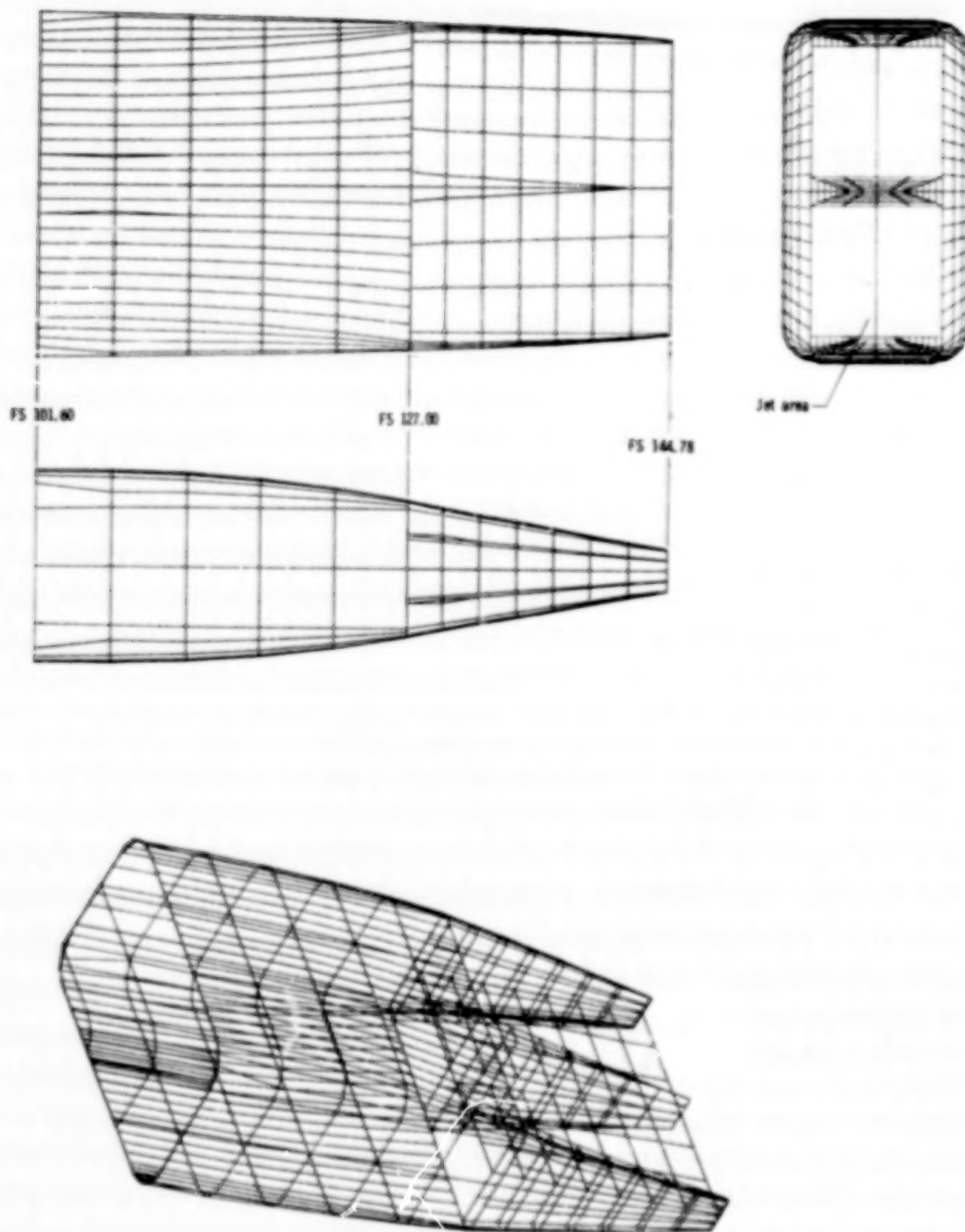
(b) Afterburner power wedge.

Figure 54.- Continued.



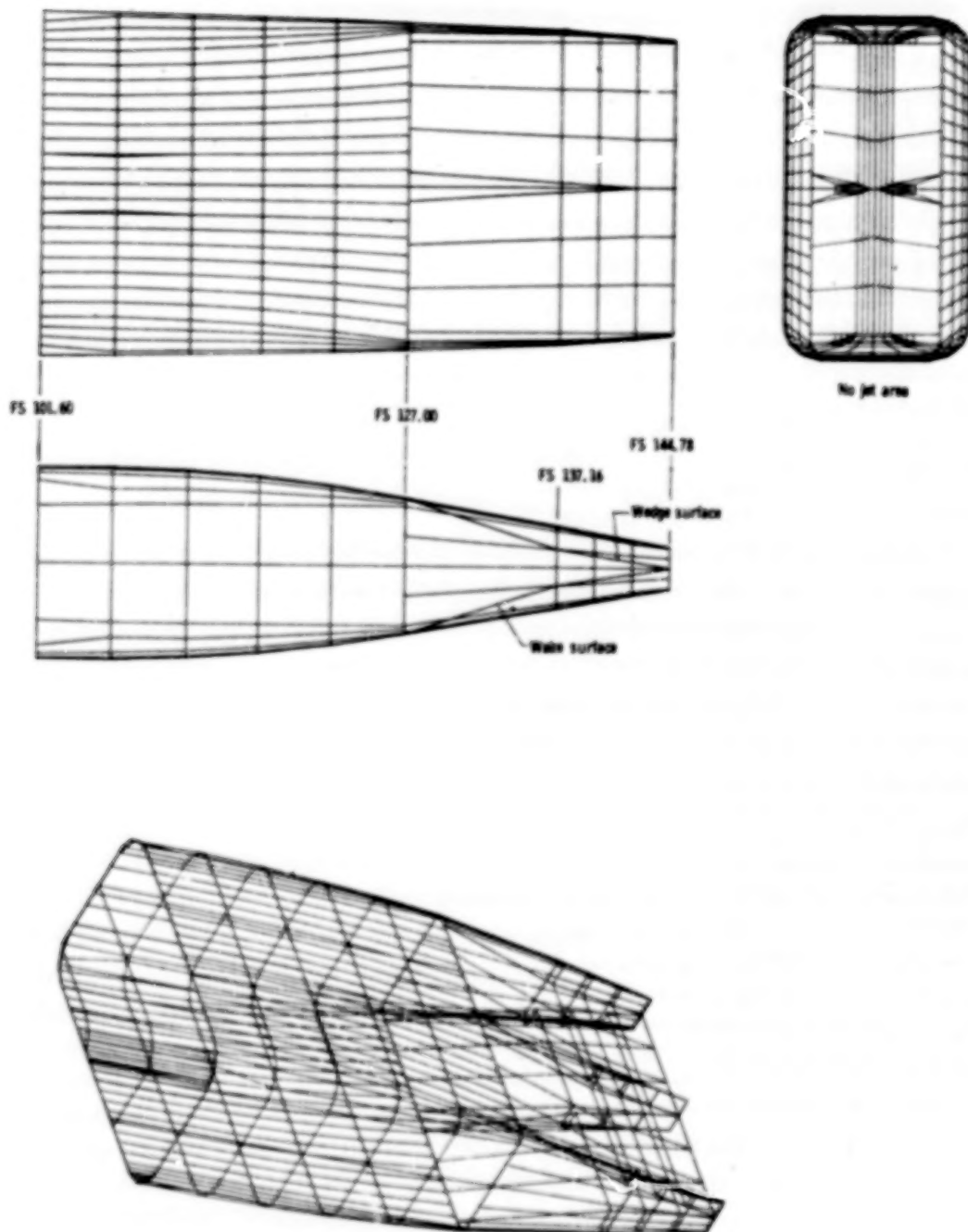
(c) Simulated jet plume.

Figure 54.- Continued.



(d) No wedge.

Figure 54.- Continued.



(e) Wake impinging at FS 137.16.

Figure 54.- Concluded.

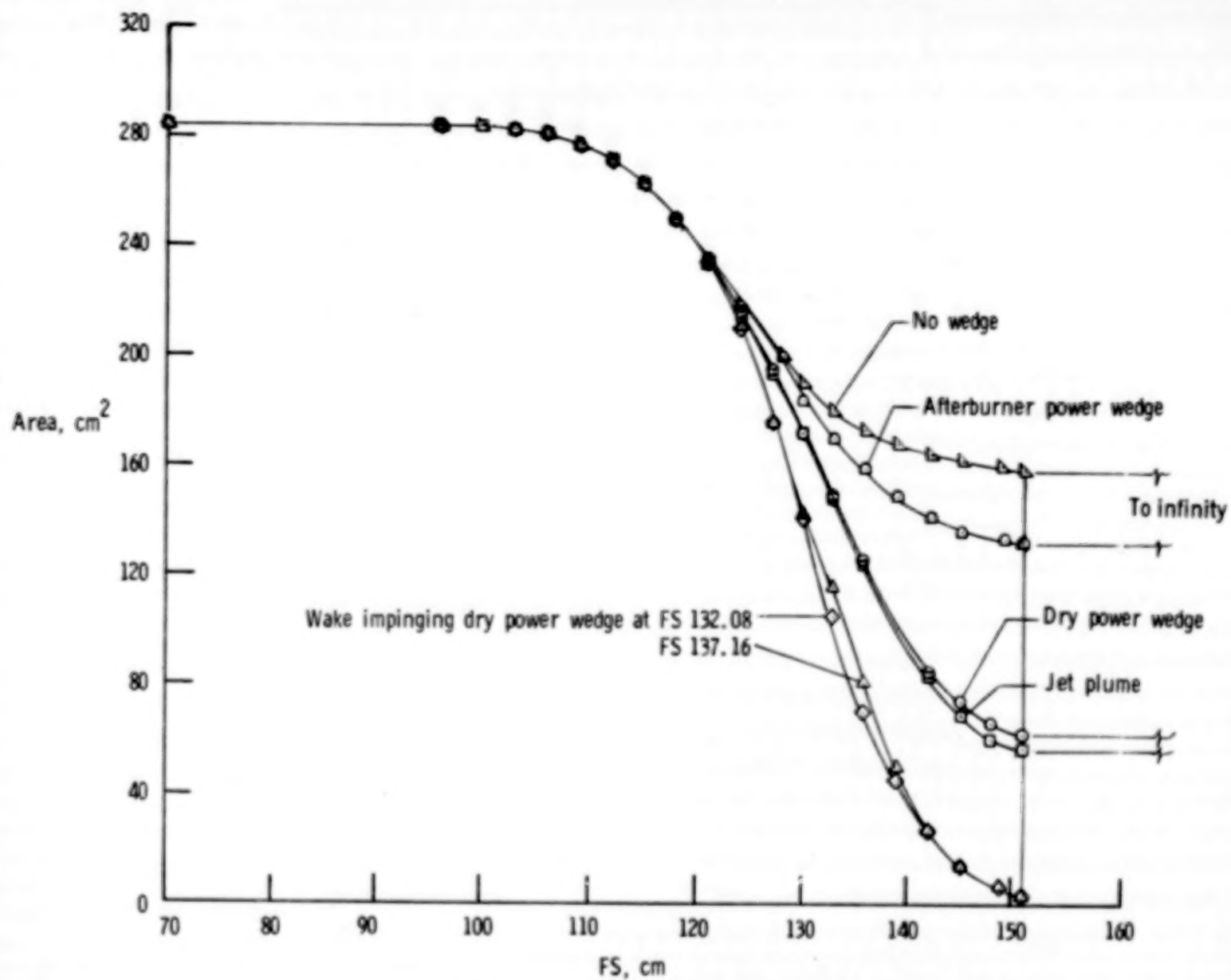


Figure 55.- Area distributions for various mathematical models.  
Fuselage stations are in centimeters.

— Dry power wedge  
 — Afterburner power wedge  
 - - - Jet plume  
 — No wedge



Wake impinging dry power wedge  
from FS 132.08 to 142.24

$C_{D,a}$  for

○ Dry power, jet off  
 ● Dry power,  $p_{t,j}/p_{\infty} = 5.9$   
 □ Afterburner power, jet off

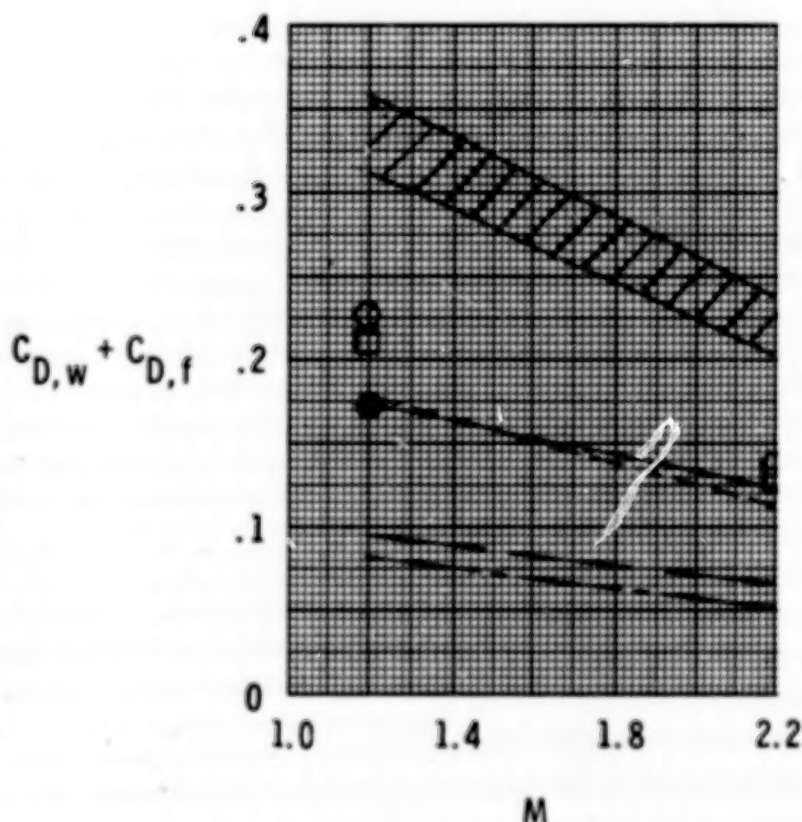
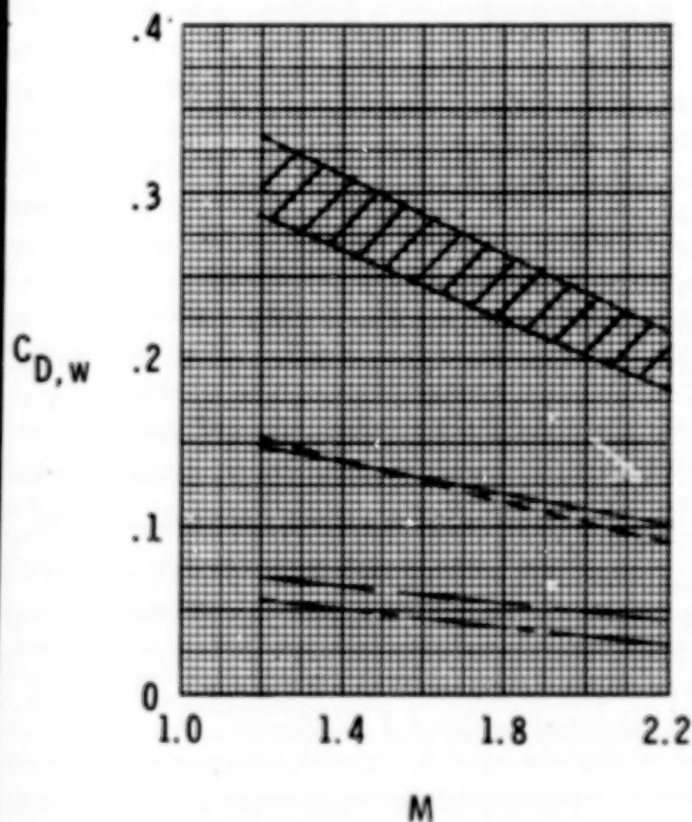


Figure 56.- Comparison of wave drag and wave-plus-friction drag coefficient computed for various mathematical models, body alone. Fuselage stations are in centimeters.



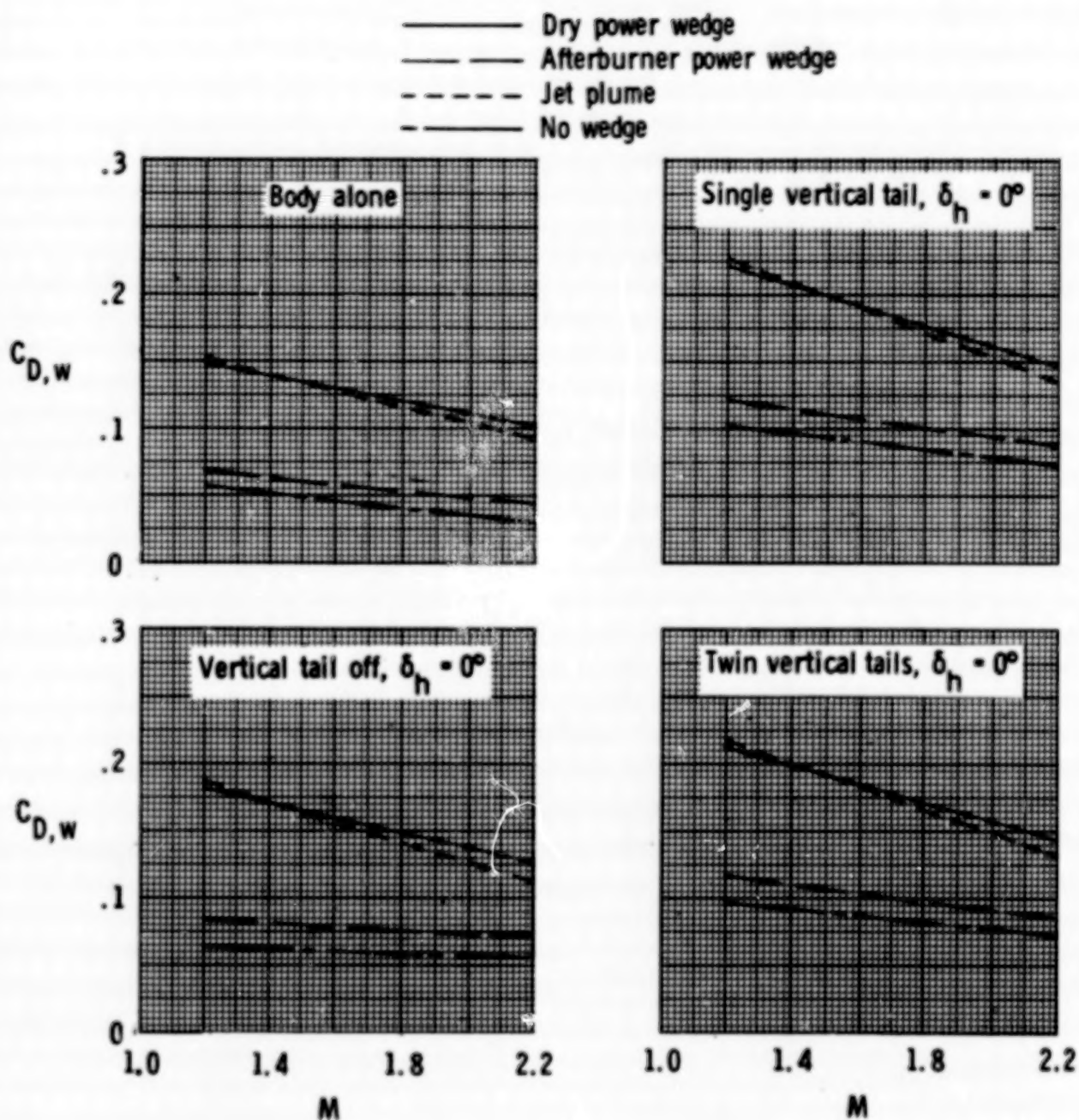


Figure 57.- Computed wave drag for various tail installations.

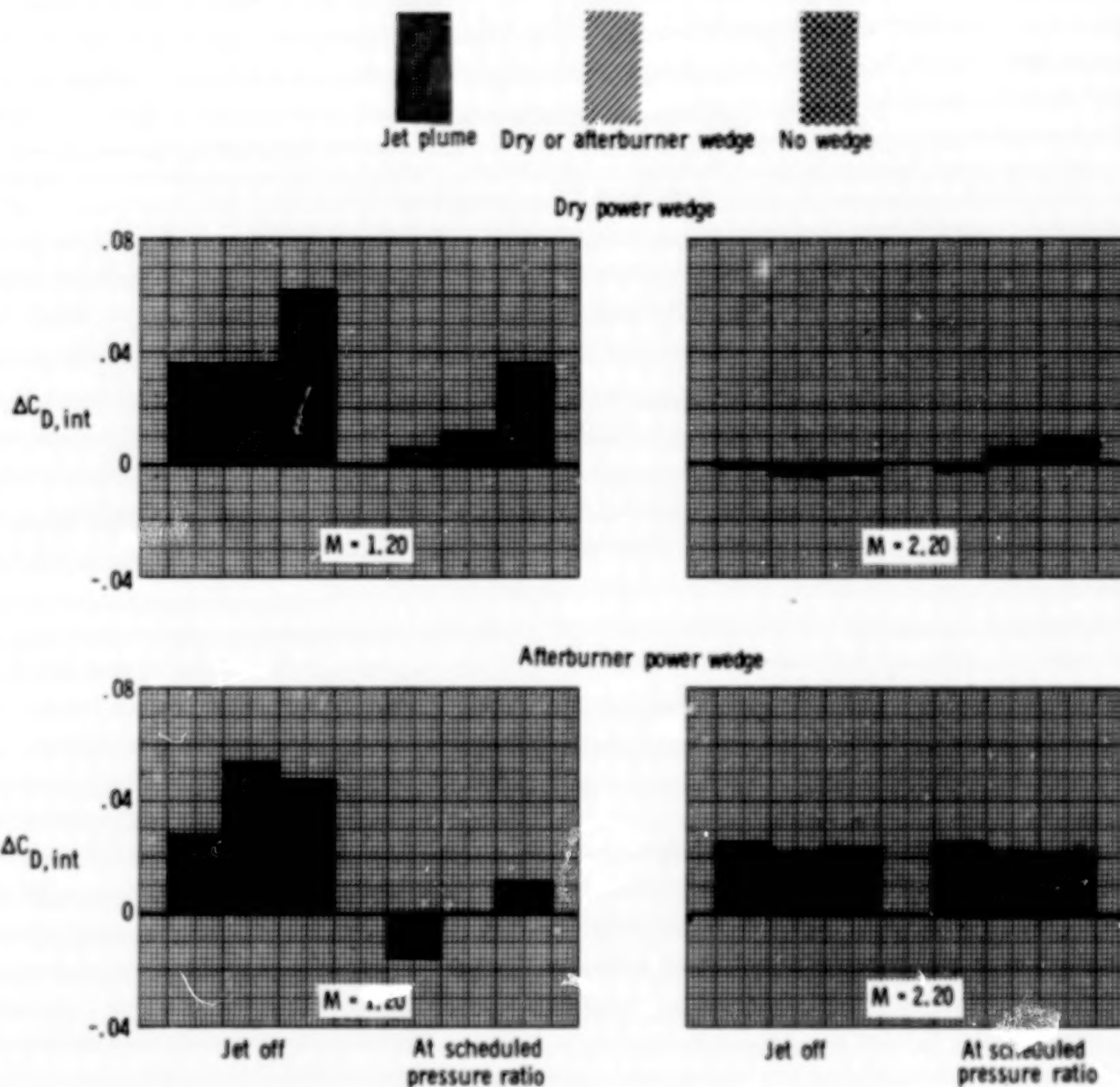


Figure 58.- Sensitivity of incremental interference drag coefficient to mathematical model used to compute wave drag for model with twin vertical tails and  $\delta_h = 0^\circ$ .



**END**

**1.4.78**